

Report

R-19-23

July 2019



Structural control on stress variability at Forsmark

Matti Hakala

Jesse Ström

Jouni Valli

Jani Juvani

SVENSK KÄRNBRÄNSLEHANTERING AB

SWEDISH NUCLEAR FUEL
AND WASTE MANAGEMENT CO

Box 3091, SE-169 03 Solna
Phone +46 8 459 84 00
skb.se

SVENSK KÄRNBRÄNSLEHANTERING

ISSN 1402-3091

SKB R-19-23

ID 1858172

July 2019

Structural control on stress variability at Forsmark

Matti Hakala, Jesse Ström, Jouni Valli, Jani Juvani
Rock Mechanics Consulting Finland Oy

Keywords: 3D modelling, In-situ stress, Mean stress, Stress variability, Deformation zones.

This report concerns a study which was conducted for Svensk Kärnbränslehantering AB (SKB). The conclusions and viewpoints presented in the report are those of the authors. SKB may draw modified conclusions, based on additional literature sources and/or expert opinions.

A pdf version of this document can be downloaded from www.skb.se.

© 2019 Svensk Kärnbränslehantering AB

Abstract

The *in-situ* stress state is one of the key rock mechanics parameters and it must be well understood for the design of an underground repository of spent nuclear fuel. The current stress state in the Fennoscandia area is dominated and driven by Mid-Atlantic ridge push and collision of the Eurasian and African plates in the Alps. Additionally, earlier glaciation cycles have changed stress conditions remarkably and promoted the shear of brittle fault zones thereby causing changes in the stress field. In the thrust fault conditions that have been dominant for a long time, shallow dipping faults have been, and are still, prone to slip.

The Swedish Nuclear Fuel and Waste Management Company (SKB) has selected the Forsmark site for the construction of a repository at a depth of –470 m. So far approximately 130 overcoring and 240 hydraulic stress measurements have been completed and interpreted by Martin (2007) while also making use of borehole breakout, core diking and non-linear strain rock sample data. This interpretation indicated notable variation in both horizontal stress components but did not address the variability.

This study aimed at examining the interaction of brittle deformation zones (DZ) and the *in-situ* stress state in the Forsmark area using the discontinuous numerical simulation tool 3DEC. The primary goal was to understand the observed and expected variation in stress magnitudes and orientations at repository depth, but also to verify rock parameters. The work was performed in two phases and the results of the first phase guided the second phase. In the first phase the main studied factors were the brittle fault surface geometry and shear strength; planar geometry versus the interpreted undulating surfaces. The second phase involved only the undulating faults and the *in-situ* stress was established by normal velocity boundary conditions, the thrust orientation relative to fault geometry was varied by ± 20 degrees. A glaciation cycle with pore pressure changes was added to all the simulations and two different fault shear strength values were tested.

The results indicated that the simulation of the realistic variation of *in-situ* stress measurements requires that the stress state is established by boundary thrust conditions and includes disturbances caused by the latest major glaciation cycle. The use of undulating DZ surface geometry was also found to be more realistic. Additionally, a good match with the measurement results was obtained with simple constant thrust boundary conditions. When the stress state is established by thrust, the resulting mean stresses are fairly insensitive to the studied DZ parameter values. If the DZ parameters are in a realistic range, the lower shear strength will mainly increase the resulting variation in stress magnitudes and orientations.

Some thrust model cases resulted in a fairly good statistical correlation with overcoring measurement results although very large differences did exist in point to point comparison. Above the 300 m level the variation matched observations fairly well. Very low magnitudes are, however, common in the simulation results indicating that low stress measurement results could be possible and should thus not be discarded per se. Conversely, simulation result variation also indicates higher magnitudes, but not to the level of observed extremely high measurement results which probably have suffered from thermal effects induced by heating associated with overcoring.

This study demonstrated that it is possible to construct a 3DEC model with very complicated non-planar DZ geometry, including over a hundred faults, and compute solutions in reasonable timeframes.

Sammanfattning

Spänningsförhållandet *in-situ* är en av de viktigaste bergmekaniska parametrarna. En god förståelse för detta är viktigt i dimensionering och design av underjordsförvar för slutförvaring av använt kärnbränsle. Det nuvarande spänningsfältet i Fennoskandien tros vara orsakat av tektonisk plattförskjutning via Mittatlantiska ryggen och kollisionen mellan den Eurasiska och Afrikanska plattan. Tidigare glaciationer har lett till markant ändrade spänningsförhållanden vilket också främjat glidning längs spröda strukturer och i förlängningen en förändring i spänningsfältet. Under dessa förhållanden (motsvarande ”reversförkastning”) som dominerat under lång tid, har glidning längs flackt stupande strukturer skett. Sådana strukturer är fortfarande benägna att glida.

Svensk Kärnbränslehantering AB (SKB) har valt Forsmark som plats för anläggandet av slutförvaret på ett tänkt djup av 470 m. Hittills har 130 bergspänningsmätningar med överborrning och 240 mätningar med hydrauliska metoder utförts. Dessa har tolkats av Martin (2007) där också information om borrhålsskador (”borehole breakouts”), uppsprickning i kärnor (”core diskings”) och icke-linjära töjningsdata inkluderats. Denna tolkning indikerade en signifikant variation i båda de horisontella spänningskomponenterna, men diskuterade inte någon förklaring till dessa variationer.

Föreliggande studie syftar till att undersöka samverkan mellan spröda deformationszoner (DZ) och *in-situ* spänningsförhållandena i Forsmark, med nyttjande av numerisk diskontinuum-analys med programmet 3DEC. Det primära målet var att söka förstå de observerade och förväntade variationerna i magnitud och orientering på spänningarna på förvarsdjup, men också att verifiera bergparametrarna. Arbetet utfördes i två steg där resultaten från det första steget nyttjades för att styra arbetet i steg 2. I det första steget studerades främst geometri och skjuvhållfasthet på de spröda zonerna – plan geometri kontra en undulerande yta. I det andra steget analyserades endast undulerande ytor på deformationszonerna och *in-situ* spänningsfältet simulerades via en pålagd förskjutning på modellränderna. Riktningen på pålagd förskjutning relativt geometrin på deformationszonerna varierades med $\pm 20^\circ$. En glaciationscykel med förändringar i porttryck adderades till alla simuleringar och två olika skjuvhållfastheter för deformationszonerna testades.

Resultaten indikerade att simulering av en realistisk variation i spänningsdata kräver att spänningsförhållandena genereras via en förskjutning applicerad på modellränderna samt att påverkan från den senaste glaciationen inkluderas. Användandet av en undulerande geometri på deformationszonernas begränsningsytor var också mer realistiskt jämfört med en plan geometri. En god överensstämmelse med mätdata erhålls för en konstant förskjutning applicerad på modellränderna. För detta fall är de resulterande medelspänningarna relativt okänsliga för variationer i parametervärden för deformationszonerna. En lägre skjuvhållfasthet leder exempelvis huvudsakligen till en ökning i variationen i magnitud och riktning för spänningarna.

En del av beräkningsfallen resulterade i en relativt god statistisk korrelation med resultat från överborrningsmätningar, även om stora skillnader förekom punktvis. Ovan 300 m nivå var överensstämmelsen i variation relativt god. Beräkningsresultaten visade dock på delvis mycket små spänningsmagnituder, vilket indikerar att sådana spänningar kan vara möjliga också i verkligheten, och således inte med automatik skall förkastas från mätdata. Resultaten indikerade också bitvis högre spänningar, men inte motsvarande en del av de extremt höga värden som uppmätts, där de senare sannolikt är termiskt påverkade (vid mätningarna).

Denna studie har demonstrerat att det är möjligt att konstruera en 3DEC-modell med mycket komplicerade, icke-plana geometrier för deformationszoner, inkluderande mer än hundra sådana zoner, men fortfarande erhålla beräkningsresultat på rimlig tid.

Contents

1	Introduction	7
1.1	Background	7
1.2	Goals	8
2	Initial data	9
2.1	Deformation zones	9
2.2	In-situ stress	10
2.3	Rock properties	10
3	Simulation approach and input data	11
3.1	Approach	11
3.2	Geometry	11
	3.2.1 Planar model	11
	3.2.2 Undulating model	13
3.3	Rock mass properties	15
3.4	Deformation zones	16
3.5	In-situ state of stress and ground water	16
3.6	Glaciation	19
3.7	Simulation cases	21
	3.7.1 Simulation Phase 1	21
	3.7.2 Simulation Phase 2	21
4	Simulation results	25
4.1	Presentation of results	25
4.2	First simulation phase	26
4.3	Second simulation phase	34
5	Discussion and conclusions	43
	References	45
	Appendix 1a Simulation Phase 1 – DZ total shear displacements	47
	Appendix 1b Simulation Phase 2 – DZ total shear displacements	51
	Appendix 2a Simulation Phase 1 – lower hemisphere equal angle projections of sheared zones	55
	Appendix 2b Simulation Phase 2 – lower hemisphere equal angle projections of sheared zones	59
	Appendix 3a Simulation Phase 1 – change in σ_1 magnitude	63
	Appendix 3b Simulation Phase 2 – change in σ_1 magnitude	71
	Appendix 4a Simulation Phase 1 – change in σ_1 trend	79
	Appendix 4b Simulation Phase 2 – change in σ_1 trend	87
	Appendix 5a Simulation Phase 1 – mean and variation of σ_1 magnitude, trend and σ_1/σ_2 ratio for hundred meter intervals (90 % variation interval)	95
	Appendix 5b Simulation Phase 2 – pre/post glacial mean and variation of σ_1 magnitude, trend and σ_1/σ_2 ratio for hundred meter intervals (90 % variation interval)	99
	Appendix 6a Simulation Phase 1 – frequency of σ_1 trend and magnitude variation at repository depth	105
	Appendix 6b Simulation Phase 2 – pre/post glacial frequency of σ_1 trend and magnitude variation at repository depth	109
	Appendix 7a Simulation Phase 1 – σ_1 magnitude and trend correlation with stress measurements	115

Appendix 7b	Simulation Phase 2 – post glacial σ_1 and σ_2 and σ_3 magnitude correlation with stress measurements	119
Appendix 8a	Simulation Phase 1 – σ_1 trend frequency based on stress measurements and stress tensors at the same location in the models	133
Appendix 8b	Simulation Phase 2 – σ_1 trend frequency based on stress measurements and stress tensors at the same location in the models	137
Appendix 9	Case 2-15	143

1 Introduction

1.1 Background

The design of a deep bedrock nuclear waste repository hinges on safe final disposal, which is affected by several factors, one of which is the stability of any deformation zones (DZ) that are present in the rock mass of a selected site. The Swedish Nuclear Fuel and Waste Management Company (SKB) has selected the Forsmark site for the construction of a repository at a target depth of -470 m. The Forsmark candidate site is located in Northern Uppland approximately 100 km north of Stockholm (Figure 1-1). The site is approximately 6 km in length and 2 km in width. A wealth of data has been collected from site investigations resulting in the development of regional and local geological models, which describe the geological features of the site, including its DZs. At a regional scale, the site hosts ca 110 DZs, with ca 57 zones at a local scale (Stephens and Simeonov 2015).

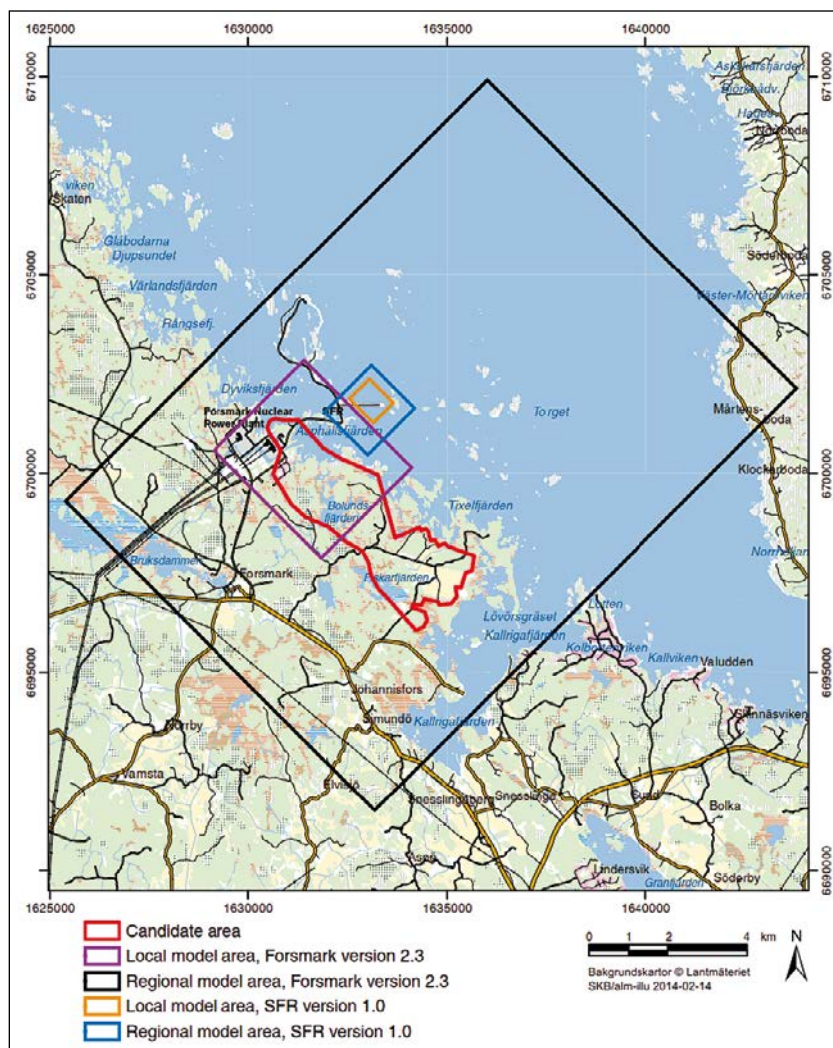


Figure 1-1. The Forsmark site with the local and regional model areas (Stephens and Simeonov 2015).

1.2 Goals

This study aimed to examine the interaction of large structures such as DZs with the *in-situ* stress state in the Forsmark area, limited to the area as defined by the local geological model. The formation of the existing *in-situ* stress state was studied along with how the geology and stress state may respond to glacial loading, as defined in Hökmark et al. (2010). The tool used in this study is 3DEC, a 3-dimensional discontinuum code (Itasca 2019). 3DEC is specifically developed for the simulation of rock mechanics problems. The simulation results included:

- The shear displacements of the DZs as a result of imposing the *in-situ* stress state. In simulation Phase 1 the *in-situ* stress was set directly in the model whereas in simulation Phase 2 it was established by boundary thrust conditions and followed by the most recent glacial cycle.
- The variation of the *in-situ* stress state for both points above.
- The correlation with the *in-situ* stress measurements.
- The sensitivity of the results to changes in DZ parameters.
- The sensitivity of the results to the orientation of applied thrust.

2 Initial data

The initial data used for the study consisted of the Forsmark stage 2.3 deterministic model for DZs (Stephens and Simeonov 2015), the *in-situ* stress state interpretations defined in Martin (2007), as well as the properties defined in Glamheden et al. (2007) and Glamheden et al. (2008).

2.1 Deformation zones

The DZs in the stage 2.3 deterministic model were based initially on the pre-existing models (Stephens and Simeonov 2015) as well as the geological single-hole interpretations for all Forsmark boreholes detailed in the Sicada database. These were then updated using data acquired after a data freeze in 2007, which included data from site investigations such as single hole interpretations and high-resolution ground magnetic data. DZs that are 1 000 m or longer but less than 3 000 m in trace length at the ground surface have been included in the local geological model. Any DZs exceeding this length have been included in the regional model, although any identified gently dipping DZs have also been included in the regional model regardless of their size. A total of 110 DZs have been identified in the regional and local models together, with the local model including 57 DZs (Figure 2-1).

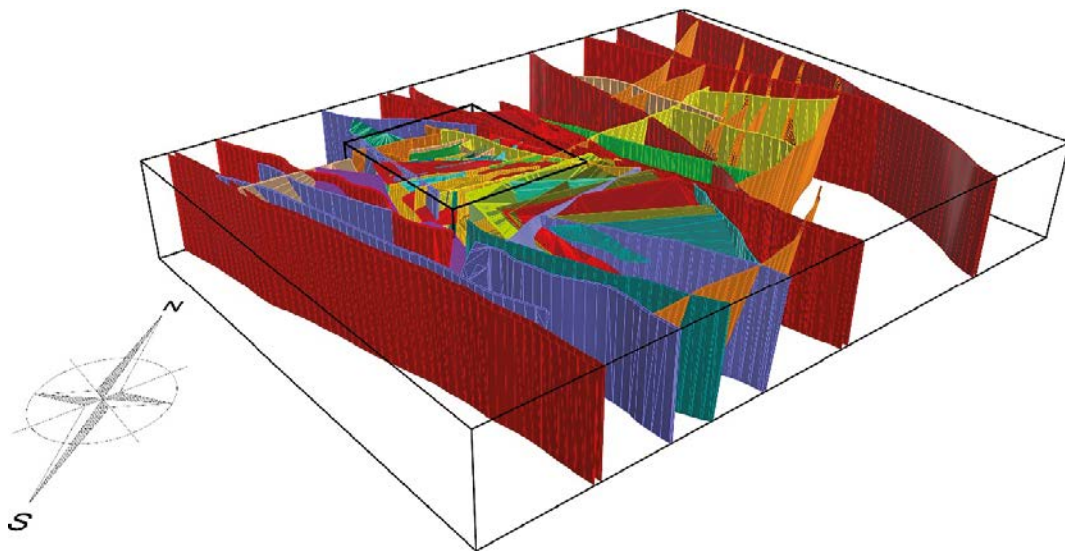


Figure 2-1. The DZs in the stage 2.3 model, with the local model boundaries visible inside the regional boundary volume.

2.2 In-situ stress

The basis for *in-situ* stress interpretation for the Forsmark site was established in 1991 when Stephansson et al. (1991) used data in a Rock Stress Database to evaluate the stress state in Fennoscandia. This Database contained roughly 500 entries from sites in Sweden, Finland and Norway. It was concluded that in the first 1 000 meters there is a high horizontal stress component and both the maximum and minimum horizontal stress components exceed the vertical stress, assuming that the vertical stress is proportional to the weight of the overburden (Martin 2007).

After the Database evaluation, several stress measurement campaigns have been carried out in Forsmark, consisting of overcoring (~130 measurements), hydraulic fracturing (~70 measurements) and hydraulic tests on pre-existing fractures – HTPF (~170 measurements). The results of these campaigns support the conclusions of Stephansson et al. (1991). In addition to stress measurements, other studies were conducted to aid in the interpretation of *in-situ* stress including survey programs of borehole breakouts and core dishing, evaluation of nonlinear strains in laboratory samples and determination of stress magnitudes to cause core dishing (Martin 2007). Based on the measurements and studies above, the *in-situ* stress state in the Forsmark area has been defined in detail in Martin (2007) and presented in modelling stage 2.2 (Glamheden et al. 2007).

Whether using direct or indirect *in-situ* stress state measurements, both clearly point towards a NW-SE orientation of the major horizontal stress. Based on measurements and indirect damage observations, the magnitude variation can be constrained. Based on modelling stage 2.2 and considering the presumption within, the mean magnitudes of major and minor horizontal stresses at a depth of 500 m are approximately 41 MPa and 23 MPa, respectively. Discrete fractures can, according to Glamheden et al. (2007) cause spatial variability of ± 9 degrees in orientation and ± 5 MPa in magnitude.

Since Martin (2007), additional studies of breakout frequency and orientations were conducted in holes KFM08A, KFM08C, KFM09A and KFM09B. The results are fairly similar to those reported by Martin (2007) and support the stress model presented in modelling stage 2.2 (Glamheden et al. 2007). According to these studies, there is no observed increase in borehole breakouts with depth. Increasing Young's modulus as a function of depth in a finite difference model shows a gradual increase in the *in-situ* stress magnitude which is in reasonable agreement with the observed state of *in-situ* stress, but the measured data has a larger variation. Modelling stage 2.3. was performed to confirm the influence of increase in rock mass quality with depth on the *in-situ* stress – no distinct local heterogeneities or geological features were modelled. This resulted in shifting the *in-situ* stresses towards a higher magnitude and actually in less agreement with the measured data than the previous numerical modelling presented in stage 2.2 (Glamheden et al. 2008).

2.3 Rock properties

The multidisciplinary characterization of the Forsmark site including geology, surveying and measurement programs, laboratory tests and interpretation of intact rock, fracture and rock mass mechanical properties are given in Glamheden et al. (2007) and Glamheden et al. (2008). Based on the laboratory tests of rock samples and fractures and hydrological and lithological models, the rock mass quality in Forsmark is good, with stiff, strong and homogeneous rock. In modelling stage 2.2 the rock mass properties have been estimated with empirical and theoretical methods and integrated through a process called harmonization (Glamheden et al. 2007). Tensile tests conducted both parallel and perpendicular to foliation and theoretical analysis of rock mass properties parallel and perpendicular to the major principal stress resulted in similar values regardless of direction, indicating a reasonably isotropic rock mass. Volumes with lower rock mass quality are mainly related to the increased fracture intensity in DZs (Glamheden et al. 2007).

3 Simulation approach and input data

3.1 Approach

The current stress state in the Fennoscandia area is dominated and driven by Mid-Atlantic ridge push and collision of the Eurasian and African plates in the Alps. Additionally, earlier glaciation cycles have changed stress conditions remarkably and promoted the slip of brittle fault zones thereby causing changes in the stress field. In the thrust fault conditions that have been dominant for a long time, shallow dipping faults have been, and are still, prone to slip. As a result, the *in-situ* stress state is altered which has been studied by numerical simulations of the interaction of geological features and the stress state (Tonon et al. 2001, Tonon and Amadei 2003, Hakami 2006, Hakami and Min 2009, Valli et al. 2011, 2016). This study applies a similar analysis method to previous studies by modelling the interpreted deformation zones in the focus area and applying the current stress state interpretation, simulating the stages leading up to the currently interpreted stress state. Simulation results are then interpreted using a number of methods similar to previous studies but also using novel methods.

The work consisted of two phases of numerical simulations. In the first phase the simulation of interaction between stress and the geological structures was performed with two different 3DEC models: one where the geometry of the DZs was simplified to planar best fit planes (Planar model) and one where the DZs were modelled as undulating best fit surfaces (Undulating model). Although the DZs are undulating in reality, this approach was selected to study whether they can be simplified to best fit planes without affecting the resulting stress state. In the first phase the *in-situ* stress state was set directly in the model and the sensitivity to changes in the DZ parameters and *in-situ* stress regime was studied (Hakami 2006, Hakami and Min 2009, Valli et al. 2011, 2016).

Work continued in the second phase with only the undulating model. Unlike in phase one, the *in-situ* stress state was thrust driven, established by velocity boundary conditions. It was reasoned that if DZ shear deformation starts during the thrust boundary process, it could lead to a larger amount of total shear deformation as thrust continues until the target stress state is reached. This could therefore lead to larger variations in the resulting stress state. This approach was also used to determine if the measured low stress magnitudes near the surface (up to a depth of about 200 m) could solely be a result of DZ shear deformation, or if achieving the low stresses requires modified boundary conditions. The second stage also included the introduction of a glaciation cycle, and its effects and the sensitivity to thrust orientation were investigated.

3.2 Geometry

3.2.1 Planar model

The model dimensions matched the dimensions of Forsmark stage 2.3 deterministic model (Stephens and Simeonov 2015) fairly well with some fine tuning of the outer surfaces performed to be certain that the DZs intersect the boundaries of the model. The DZs were simplified to best fit planar planes, with dimensions limited according to the respective intersections with their bounding zones or the model boundaries (Figure 3-1). The model was divided into five volumes, with the innermost encompassing all the Forsmark underground facilities. The zoning density of each volume decreases with increasing distance from the facilities, from 30 meters to 420 meters (Figure 3-2).

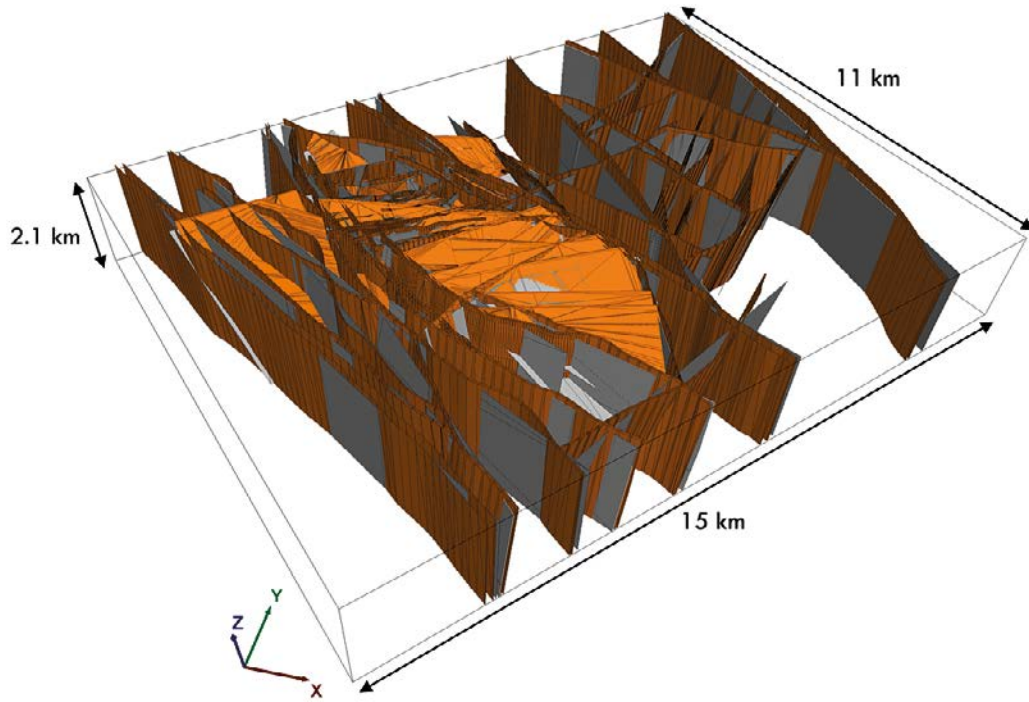


Figure 3-1. The DZs from Forsmark stage 2.3 deterministic model in orange and the best fit planar planes in grey.

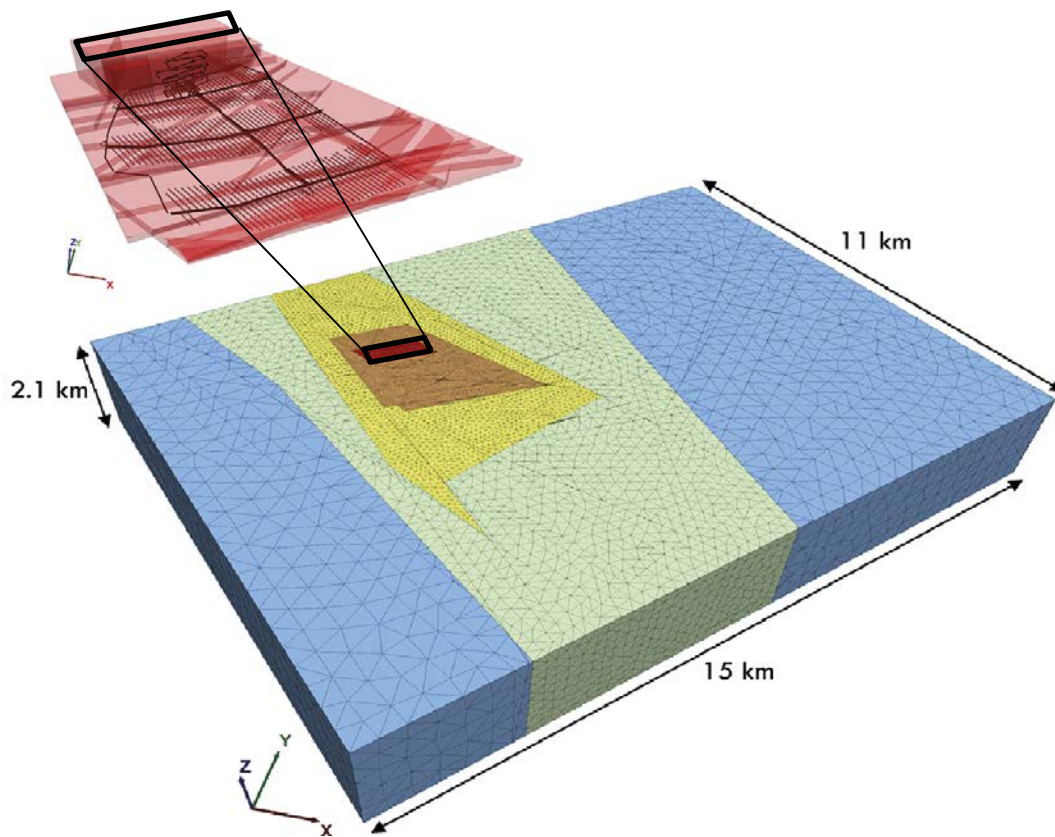


Figure 3-2. Five volumes with various zoning densities and the geometry of the innermost volume encompassing the underground facilities (red). Planar model.

3.2.2 Undulating model

The model attributes matched the planar model described earlier with the exception that the DZs were modelled with undulating surfaces that aim to match the originals as closely as possible while still being computationally reasonable (Figure 3-3). Only large-scale undulation was modelled, small-scale asperities were not included. The maximum deviation from the original DZ-surfaces further away from the underground facilities was allowed to be about 50 meters and the closer the location is to the underground facilities, the more accurately the model surface matched the original. The maximum deviation around the facilities is approximately 5 meters. Due to geometrical issues with intersecting DZs leading to very narrow and bad quality elements, some additional simplification to the undulating surfaces was necessary. Some small parts of the surfaces were removed, mostly near the rock surface (Figure 3-4). The trimmed surfaces are either co-planar with other DZs in close vicinity or form very slim “pockets” near the surface with contacts with other DZs. Due to the very limited area of these surfaces compared to the overall model size, the effect of their absence can be considered negligible to the large-scale behaviour of the stress field. Zoning of the model was done with the same principles as in the planar model – undulating surfaces caused some differences at the DZ surface boundaries (Figure 3-5).

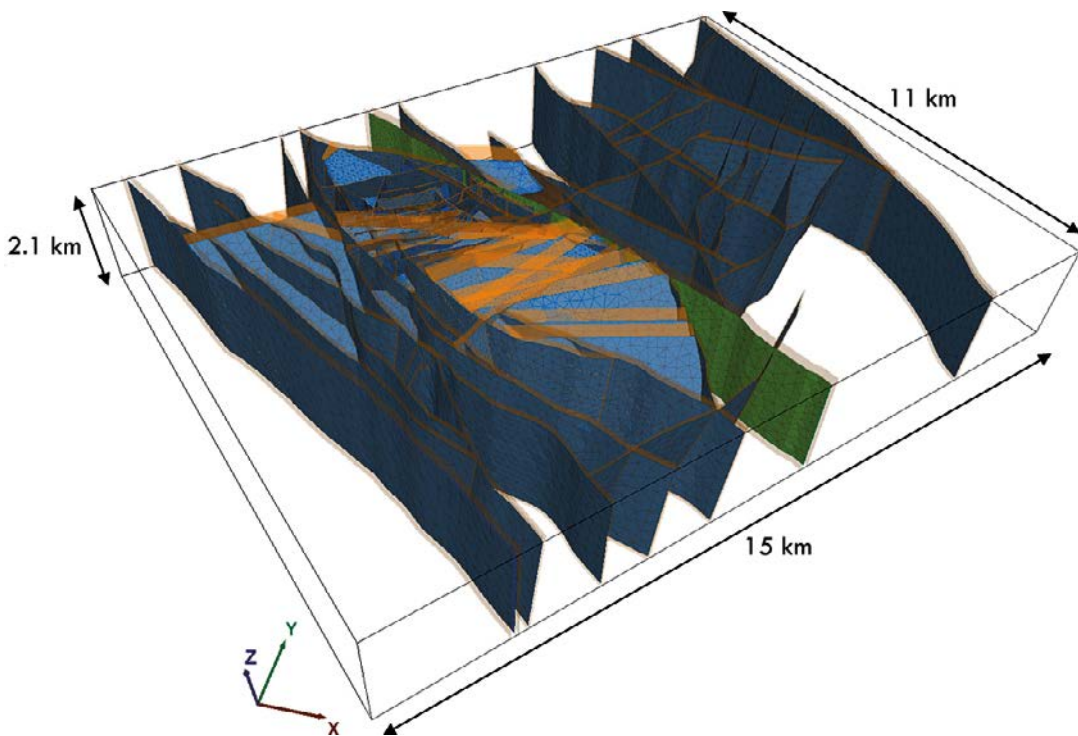


Figure 3-3. The DZs from Forsmark stage 2.3 deterministic model in orange and the best fit undulating surfaces in blue and green (Singö).

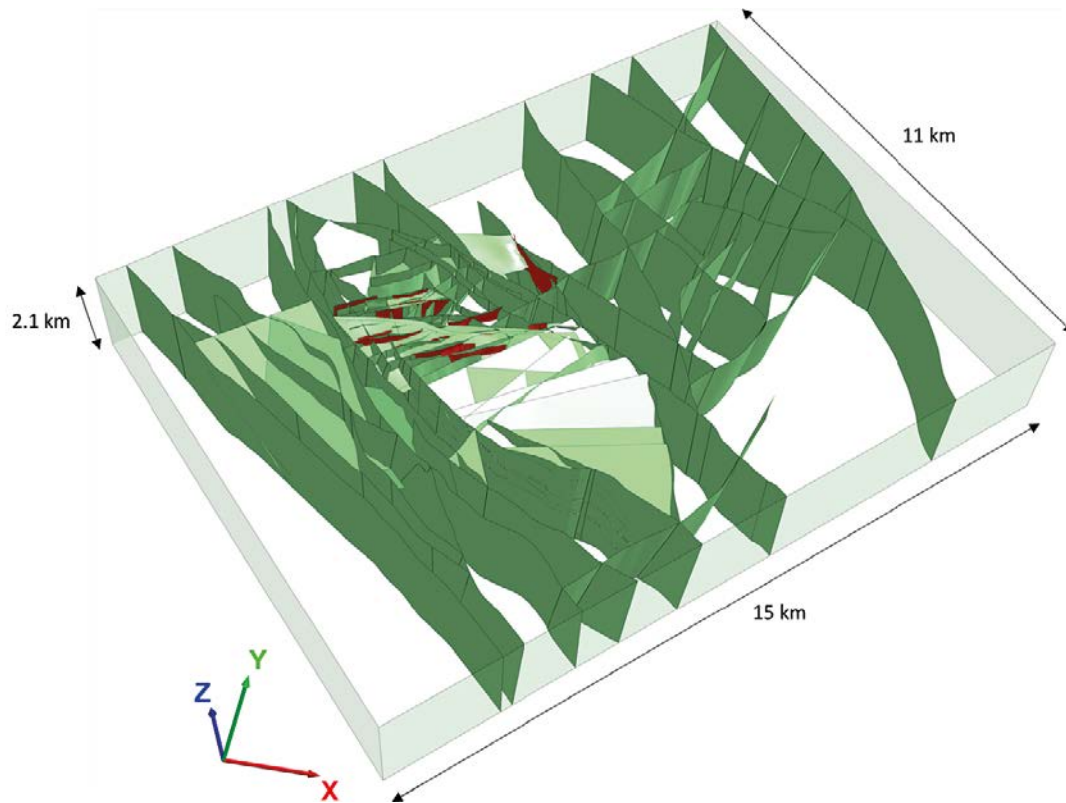


Figure 3-4. Parts of the DZs that have been trimmed (red). Undulating model.

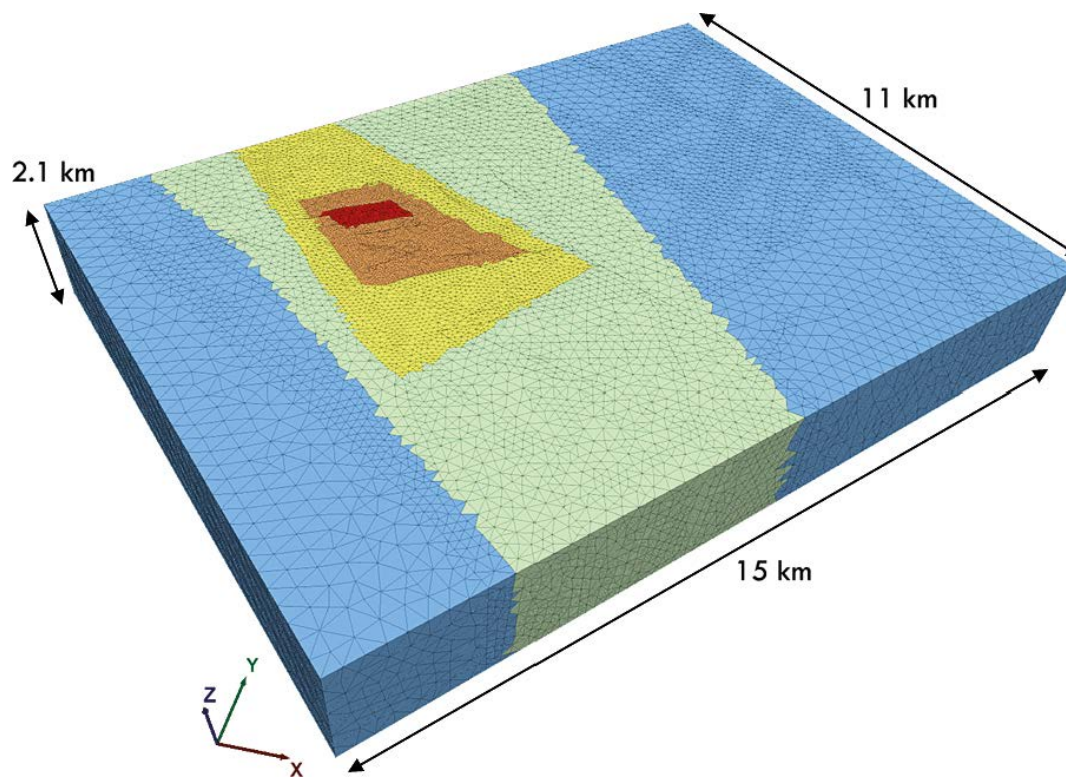


Figure 3-5. Five volumes with various zoning densities. Undulating model.

3.3 Rock mass properties

The rock mass was considered to be isotropic and elastic and was divided into four different geological domains: the main rock mass and three fracture domains surrounding the facilities (FFM01, FFM02, FFM06) (Figure 3-6). The applied elastic parameters consider the fracturing and only the DZs were modelled explicitly. Young's modulus values were estimated based on Modelling stage 2.3 (Glamheden et al. 2008) and Poisson's ratio values were based on empirical analysis of Fracture domains in Glamheden et al. (2007) (Table 3-1). FFM01 and FFM06 were considerably stiffer than FFM02, and the stiffness increased with depth.

Table 3-1. Rock mass elastic parameters after Glamheden et al. (2007) and Glamheden et al. (2008).

Depth range	Above 400 m		Below 400 m	
Elastic parameters	E (GPa)	ν ()	E (GPa)	ν ()
Fracture domain				
Rock mass	65	0.24	65	0.24
FFM01	65	0.24	70	0.24
FFM02	55	0.18	-	-
FFM06	65	0.30	70	0.24

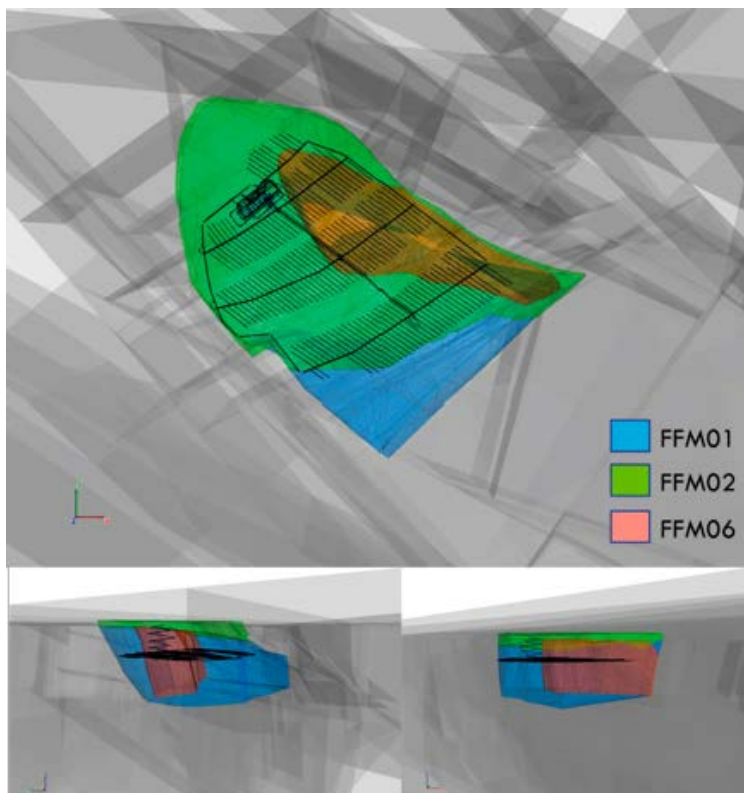


Figure 3-6. Fracture domains surrounding the facilities.

3.4 Deformation zones

All DZs except the Singö DZ were assigned the same basic deformation and strength parameter values (Figure 3-3) based on the Forsmark site descriptive model v2.2 (Glamheden et al. 2007) and its completion at the end of site investigations (SKB 2008) (Table 3-2). The initial values for cohesion and friction were maintained in contacts after failure (perfectly elastoplastic constitutive model). DZ properties varied case by case and the specific sets of case parameters used in Phase 1 and Phase 2 are presented in chapter 3.7.

Table 3-2. Basic stiffness and strength values for DZs. kn: normal stiffness, ks: shear stiffness, coh: cohesion, fric: friction angle, ten: tensile strength.

Parameter	kn (MPa/mm)	ks (MPa/mm)	coh (MPa)	fric (°)	ten (MPa)
Deformation zone					
All, except Singö	80	20	0.7	36	0.001
Singö	0.2	0.01	0.4	31.5	0.001

3.5 In-situ state of stress and ground water

The primary *in-situ* stress state in the models was based on the Martin (2007) interpretation presented in the form of horizontal and vertical stress components (Table 3-3 and Figure 3-7). The interpretation is based on the average mean stresses at depth levels of 0 m (extrapolated), 150 m, 300 m, 400 m and 500 m, with a horizontal stress ratio of 1.7 in addition to a criterion that borehole breakout can initiate at a depth of 1 000 m. The assumption is that σ_1 increases slowly for the first 150 m, then has a higher gradient between 150–400 m and then continues with a lower gradient. For the first 150 m, σ_2 has a similar gradient to σ_1 and after that continues more or less linearly with depth. The vertical component (σ_3) increases linearly with depth, with the same gradient for all depth ranges. The gradients for the deepest depth range are assumed to be valid up to the model bottom at a depth of 2.1 km.

The latest stress state interpretation for the Forsmark area is detailed in Martin (2007). Where the measurements in the Sicada database were studied in Martin (2007), some measurements were ranked as unreliable, but without clear measurement specific basis or listing. The interpretation figure (Figure 3-8 in this report and Figure 7-3 in Martin (2007)) included a greater number of measurements than those listed as acceptable/reliable in the study appendix A in Martin (2007). Some of the magnitudes or depths in the Sicada database (Sicada all in Figure 3-8) also deviate from the values presented in Figure 3-7 in Martin (2007) (orange pentagons in Figure 3-8 in this report). The simulation results of this study were compared with the “Sicada simulation reference” data (see Figure 3-8) which includes the data presented in Appendix A of Martin (2007). This set excludes borehole KFK001 (DBT1 in Martin (2007)) results which have probable thermal issues as well as measurements with major principal stress magnitudes less than 10 MPa, which were also omitted in the Martin (2007) interpretation.

Table 3-3. The primary in-situ stress state based on Martin (2007).

Depth range (m)	σ_h (MPa)	σ_h trend (°)	σ_h (MPa)	σ_h trend (°)	σ_v (MPa)
0–150	19 + 0.008 z	145	11 + 0.006 z	55	0.0265 z
150–400	9.1 + 0.074 z	145	6.8 + 0.034 z	55	0.0265 z
400–600	29.5 + 0.023 z	145	9.2 + 0.028 z	55	0.0265 z

z is depth below rock surface in metres.

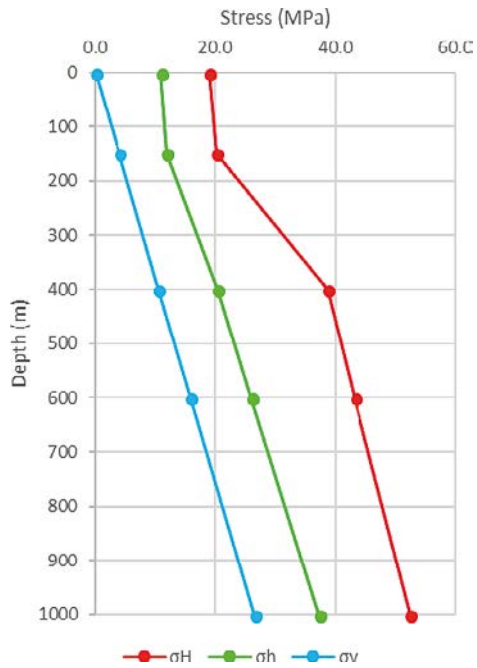


Figure 3-7. The primary in-situ stress state based on Martin (2007).

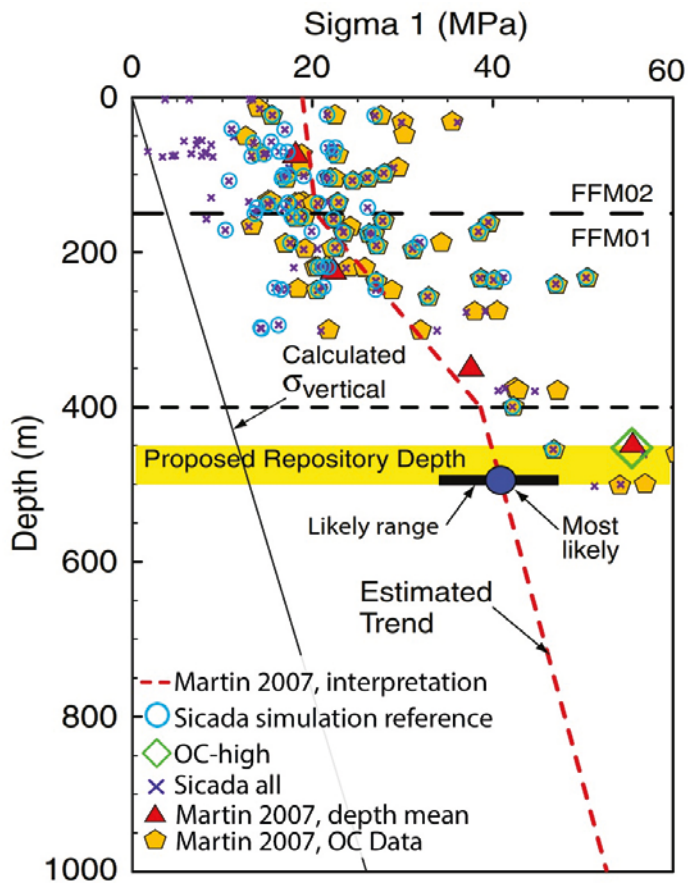


Figure 3-8. The measured major principal stress values versus depth and the Martin (2007) interpretation – the measured values have three data sets, the one used for the Martin (2007) interpretation (orange), SICADA-all and SICADA simulation reference (modified after Martin (2007)).

In Phase 1 simulations the *in-situ* stress state was set directly in the model zones and the bottom boundary was fixed in the normal direction while the sides of the model were fixed in all directions apart from the z-axis. One variation was simulated where σ_2 is set to equal σ_3 . In Phase 2 simulations the stress state was established by applying thrust to opposite vertical model boundaries. “Thrust” in the context of the simulations in this study is the application of a velocity boundary condition to a given surface in the normal direction of the surface that faces into the model. Put simply, the model was “squeezed” from all sides at varying velocities to achieve a target stress state at a given location. The thrust velocity values along the major and minor horizontal stress orientations were different. The first six cases were calculated with depth dependent thrust conditions that directly mimic the primary *in-situ* stress state. The next four cases used more direct and simplified constant thrust boundary conditions with the idea that DZ shear deformation should result in a stress state that corresponds with measurement results. The effect of thrust orientation compared to DZ-geometry was studied by varying the thrust orientation by $\pm 20^\circ$ (Figure 3-9). In all Phase 2 calculations the thrust was macro controlled and stopped when primary *in-situ* conditions were reached in one of the three monitoring spheres at 200 m, 400 m and 600 m levels at the centre of the repository (Figure 3-10). “Macro controlled” refers to the use of a proprietary script written to cycle or solve the model an arbitrary number of cycles (in this case 250) until a set of conditions are fulfilled. The script looped through all of the tetrahedral elements inside each of the three monitoring spheres to obtain the average principal stresses in effect within the individual spheres. If the stresses obtained were equal to or exceeded the target stresses, the script terminated. The target stresses were individually determined for each principal stress and based on the Martin (2007) interpretation, with a target range of $\pm 5\%$. The magnitude of σ_1 near the surface did, however, deviate at maximum $+20\%$. Four additional constant thrust cases were calculated with a higher target stress state (OC-high in Figure 3-8), the results are presented in the appendices but are not discussed further in the report. The different variants of *in-situ* stress states are summarized in Chapter 3.7.2.

Full gravitational water pressure was assumed for all DZs with a water level equal to the rock surface. In Phase 2 simulations, variable excess pore pressure was applied during the glaciation cycle (Chapter 3.6).

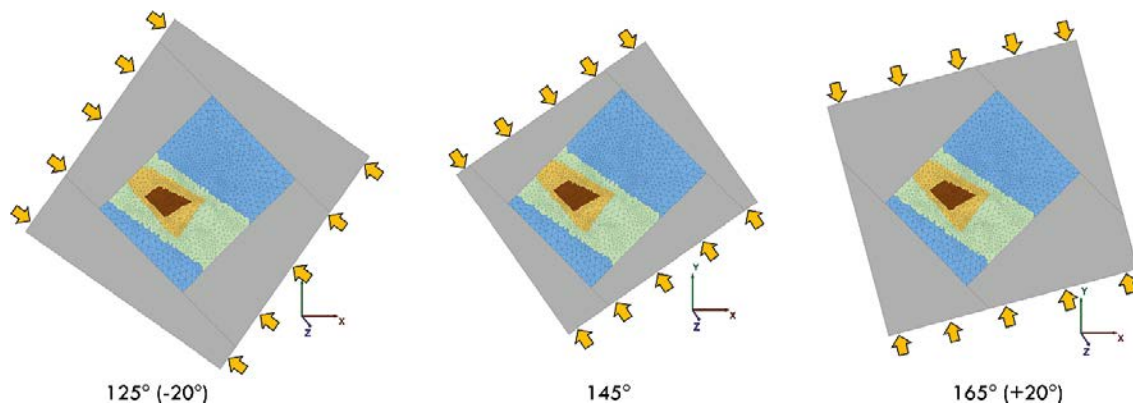


Figure 3-9. The varying major thrust orientations used in the simulations.

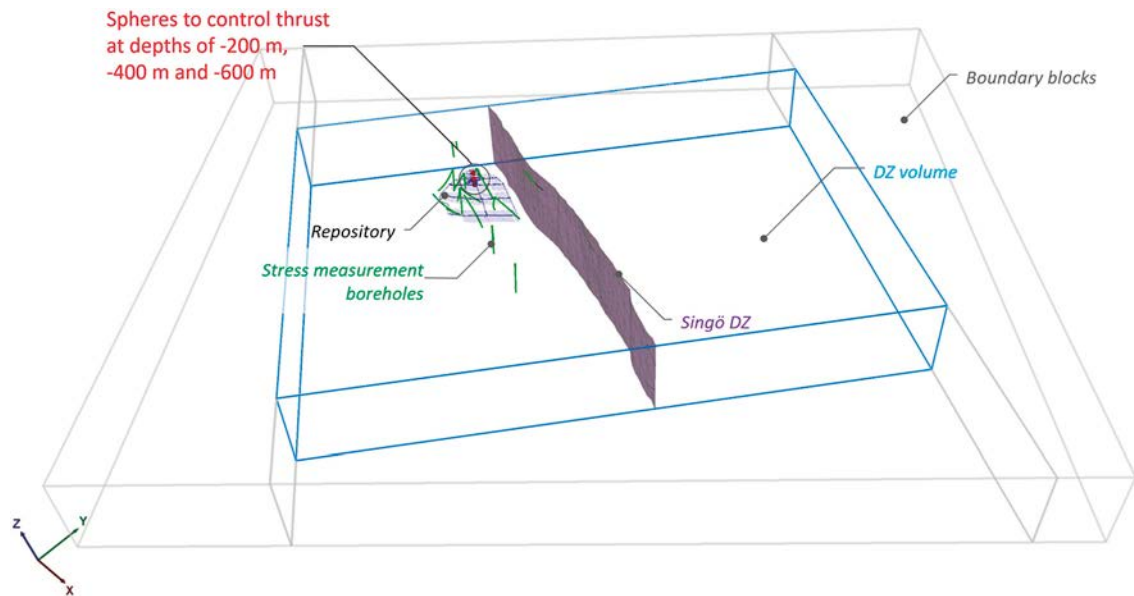


Figure 3-10. Location of the stress calculation spheres to control thrust.

3.6 Glaciation

The models in the simulation Phase 2 included a glaciation cycle. The glaciation scheme was based on analyses performed by Lund et al. (2009) and was the same case as studied in Hökmark et al. (2010). The selected scheme of glaciation consisted of two cycles. For the purposes of this study only the second cycle was considered as it is the most recent one and it produces higher stress changes (Figure 3-11). The simulation cycle for the glaciation consisted of four phases; Forebulge, Glacial maximum, Edge passing and the Removal of glaciation (Table 3-4, Table 3-5). The glacially induced stresses were assumed to be constant with depth and equal to the values calculated for the 500 m level. The maximum error caused by this assumption was about 0.5 MPa. The glacially induced excess pore pressure model was the same as the alternative pore pressure model in Hökmark et al. (2010), equivalent to 98 % of the glacially induced vertical load (Figure 3-12). In this pore pressure model the pressure was constant with depth except in the edge passing phase. Unlike the thrust in the formation of the *in-situ* stress state, the glacially induced stresses and pore pressures corresponding to each simulation phase were set directly in the model zones and DZ surfaces. The glacially induced stress and excess pore pressure drop from the glacial maximum to the edge passing was simulated in three equal phases, to avoid a ‘dynamic’ response when excess vertical stresses are fully removed and the remaining significant portion of the additional horizontal stresses result in increased shear stresses on shallow dipping DZs. An alternative glacial pore pressure model equivalent to 90 % of the glacially induced vertical load was also studied in one simulation. In the removal phase all excess stresses and pore pressures were removed.

Table 3-4. Additional stresses induced by the simulated second glaciation cycle.

	Forebulge			Second maximum			Edge passing		
	Stress [MPa]	dip [deg]	dd [deg]	Stress [MPa]	dip [deg]	dd [deg]	Stress [MPa]	dip [deg]	dd [deg]
σ_1	0	0	3	28.9	0	95	11	0	76
σ_2	-5.4	0	93	24.8	0	185	7.6	0	166
σ_3	0.3	90	0	25.7	90	0	-0.2	90	0

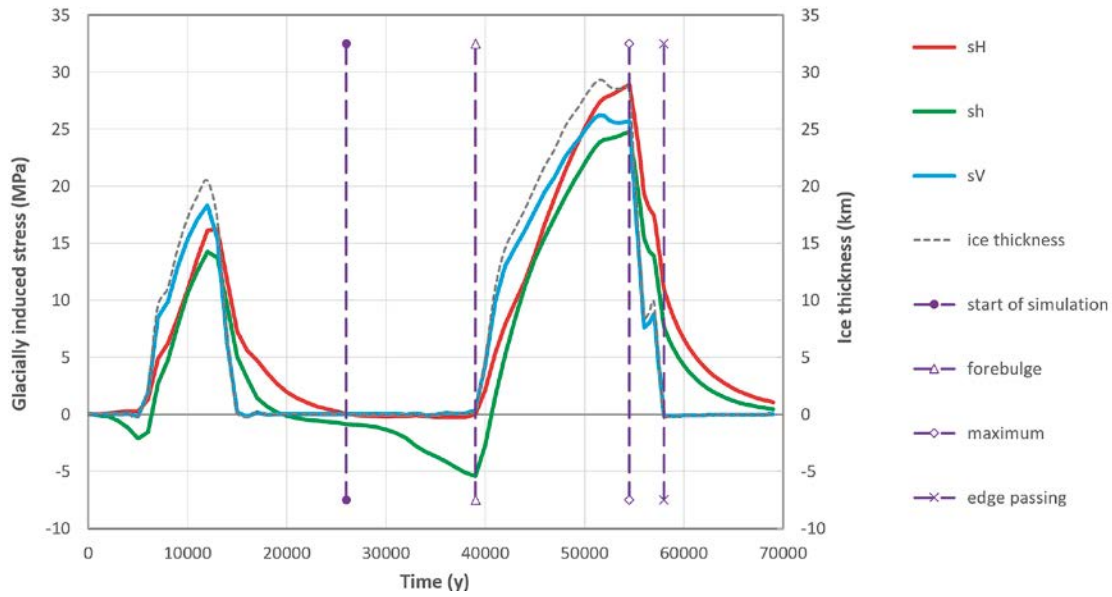


Figure 3-11. Development of glacially induced horizontal and vertical stresses at 500 m depth level and simulated phases modified after Hökmark et al. (2010).

Table 3-5. Total stresses during simulated second glaciation cycle at repository depth (465 m).

	Pre-glaciation			Forebulge			Second maximum			Edge passing		
	Stress [MPa]	dip [deg]	dd [deg]	Stress [MPa]	dip [deg]	dd [deg]	Stress [MPa]	dip [deg]	dd [deg]	Stress [MPa]	dip [deg]	dd [deg]
σ_1	43.5	0	145	41.7	0	152	73.2	0	312	62.0	0	323
σ_2	22.6	0	55	19	0	62	52.0	0	42	39.2	1	53
σ_3	12.3	90	0	12.7	90	0	37.7	90	212	38.2	89	226

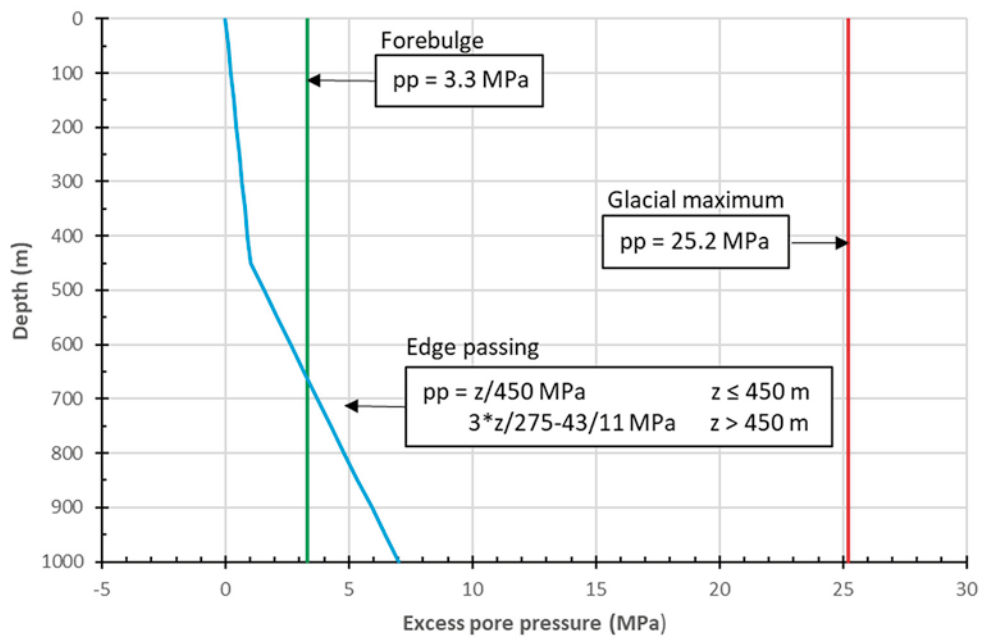


Figure 3-12. Glacially induced excess pore pressure model for Forsmark, after Hökmark et al. (2010).

Table 3-6. Parameter values for Phase 1 simulation cases, differences compared to Case 1-1 are highlighted in orange.

Case	Stress state	Deformation zones and parameter values					Note
		Name	kn (MPa/mm)	ks (MPa/mm)	phi (°)	c (MPa)	
Case 1-1	Martin 2007	All except Singö	80	20	36	0.7	
		Singö (ZFMWNNW0001)	0.2	0.01	31.5	0.4	
Case 1-2	Martin 2007	All except Singö	80	20	20	0.7	
		Singö (ZFMWNNW0001)	0.2	0.01	20	0.4	
Case 1-3	Martin 2007	All except Singö	80	20	20	0.3	
		Singö (ZFMWNNW0001)	0.2	0.01	20	0.3	
Case 1-4	Martin 2007	All except Singö	10	5	20	0.3	
		Singö (ZFMWNNW0001)	0.2	0.01	20	0.3	
Case 1-5	Martin 2007	All except Singö	80	20	10	0.3	
		Singö (ZFMWNNW0001)	0.2	0.01	10	0.3	
Case 1-6	Martin 2007	All except Singö	80	20	20	0.3	1
		Singö (ZFMWNNW0001)	0.2	0.01	20	0.3	
Case 1-7	Martin 2007 $\sigma_2 = \sigma_3$	All except Singö	80	20	20	0.3	
		Singö (ZFMWNNW0001)	0.2	0.01	20	0.3	

1. In Case 1-6 all fracture domains FFM01, FFM02 and FFM06 have the same elastic properties as the Rock mass in Table 3-1.

3.7 Simulation cases

3.7.1 Simulation Phase 1

In simulation Phase 1 seven cases were studied with both planar and undulating models for DZs, resulting in a total of 14 simulations (Table 3-6). The major difference between the cases is the shear strength of DZs. In addition, Case 1-4 had lower DZ stiffnesses, Case 1-6 had uniform elastic properties for all fracture domains and Case 1-7 had a lower minor horizontal stress. Generally, the elastic properties of the rock mass in different fracture domains was according to Table 3-1. In each case the *in-situ* stress state described in Chapter 3.5 was first set directly in the model zones and solved to elastic equilibrium, without allowing any shear deformation in the model. The DZ-surfaces were then allowed to shear based on their strength and stiffness parameters.

3.7.2 Simulation Phase 2

Compared to stress measurement results, Phase 1 models resulted in lower stress values with a narrow variation and therefore:

- The application of the *in-situ* stress state was changed to be established by boundary thrust.
- A glaciation cycle was added.

Phase 2 simulations were performed using the undulating DZ model only. Due to the higher number of simulation phases in each case, the calculation speed was increased by optimizing the discretization of undulating DZ surfaces. This was performed by increasing mesh size outside the repository area and by removing very small blocks that are not critical to the distribution of the stress state. The resulting stress state of this optimized model was verified against Phase 1 results which had a dense discretization.

The target *in-situ* stress state in the models was based on Martin (2007) interpretations (Figure 3-7). To achieve this, either depth dependent (Cases 2-1 to 2-6) or simplified constant (Cases 2-7 to 2-14) normal velocity boundary conditions were applied (Table 3-7). The depth dependency of velocity and the ratio between opposite outer boundaries of the model was first estimated by releasing a set target stress state and further iterated by a set of simulations (Table 3-8). Before the thrust, the model was first run to elastic equilibrium with only the hydrostatic stress gradient according to the rock mass density

of 2650 kg/m³. During the thrust, a macro was used to monitor the stress state between a depth of 400 and 500 m in the repository area and to stop the boundaries when the target stress state was reached (see Section 3.5), with an accuracy of $\pm 5\%$. For Cases 2-7 to 2-10 the target stress was the primary *in-situ* stress model according to Martin (2007) and for Cases 2-11 to 2-14 the mean of all overcoring stress measurement results (OC-high in Figure 3-8), which is approximately 15.4 MPa higher at the 450 m depth level and represents an upper estimate for the *in-situ* stress. The major thrust orientation was equal to a σ_1 trend of 145°, but σ_1 trends of 125° and 165° were also studied. In all cases the rock mass parameters were according to Table 3-1, as in Phase 1 simulations. The basic assumption of DZ parameters were according to Table 3-2, except in four cases where the effect of a lower shear strength was also studied. Glacially induced pore pressure was assumed to be 98 % of the glacially induced vertical load except for one case, in which an equivalent of 90 % of the glacial load was applied. In simulation Phase 2 a total of fourteen case variations were run (Table 3-7), the upper *in-situ* stress estimate Cases 2-11 to 2-14 are presented in the appendices but are not discussed further in this report. Cases 2-11 to 2-14 studied the stress state interaction when the target stress state included the high magnitude overcoring measurements from DBT1. After the glaciation cycle, the minor horizontal stress was over the target in Cases 2-7 to 2-14 and was corrected by pulling the boundaries perpendicular to σ_2 until the principal stresses were within $\pm 5\%$ of the Martin (2007) interpretation. This adjustment was less than 2 MPa. Finally, Case 2-15 was added as a supplementary case after this study was completed, where $\sigma_2 = \sigma_3$. This case is reported in Appendix 9.

Table 3-7. Parameter values and calculation conditions for Phase 2 simulation cases, differences compared to Case 2-1 are highlighted in orange.

Case	Boundary thrust for <i>in-situ</i> stress Target: Martin 2007 @ 400 m level	Deformation parameter values			Excess glacial pore pressure	After glacial stress adjustment
		Name	phi (°)	c (MPa)		
Case 2-1	z-gradient	All except Singö Singö (ZFMWNW0001)	36 31.5	0.7 0.4	98 %	N
Case 2-2	z-gradient	All except Singö Singö (ZFMWNW0001)	36 31.5	0.7 0.4	90 %	N
Case 2-3	z-gradient σ_H, σ_h trends +20°	All except Singö Singö (ZFMWNW0001)	36 31.5	0.7 0.4	98 %	N
Case 2-4	z-gradient σ_H, σ_h trends -20°	All except Singö Singö (ZFMWNW0001)	36 31.5	0.7 0.4	98 %	N
Case 2-5	z-gradient	All except Singö Singö (ZFMWNW0001)	20 20	0.3 0.3	98 %	N
Case 2-6	z-gradient σ_H, σ_h trends -20°	All except Singö Singö (ZFMWNW0001)	20 20	0.3 0.3	98 %	N
Case 2-7	constant	All except Singö Singö (ZFMWNW0001)	36 31.5	0.7 0.4	98 %	Y σ_2 reduced
Case 2-8	constant σ_H, σ_h trends -20°	All except Singö Singö (ZFMWNW0001)	36 31.5	0.7 0.4	98 %	Y σ_2 reduced
Case 2-9	constant	All except Singö Singö (ZFMWNW0001)	20 20	0.3 0.3	98 %	Y σ_2 reduced
Case 2-10	constant σ_H, σ_h trends -20°	All except Singö Singö (ZFMWNW0001)	20 20	0.3 0.3	98 %	Y σ_2 reduced
Case 2-11	constant, OC-high	All except Singö Singö (ZFMWNW0001)	36 31.5	0.7 0.4	98 %	Y σ_2 reduced
Case 2-12	constant, OC-high σ_H, σ_h trends -20°	All except Singö Singö (ZFMWNW0001)	36 31.5	0.7 0.4	98 %	Y σ_2 reduced
Case 2-13	constant, OC-high	All except Singö Singö (ZFMWNW0001)	20 20	0.3 0.3	98 %	Y σ_2 reduced
Case 2-14	constant, OC-high σ_H, σ_h trends -20°	All except Singö Singö (ZFMWNW0001)	20 20	0.3 0.3	98 %	Y σ_2 reduced

* Cases 2-11 to 2-14 have a higher target stress state magnitude, but are otherwise equivalent to Cases 2-7 to 2-10.

Table 3-8. Applied thrust for Phase 2 simulation cases.

Cases	Orientation	Velocity (m/model time step)
2-1 to 2-6	$\sigma_H = \sigma_1$	$2.14 + z \times 2e-3$
	$\sigma_h = \sigma_2$	$0.706 + z \times 9.5805e-4$
2-7 to 2-10	$\sigma_H = \sigma_1$	4.2
	$\sigma_h = \sigma_2$	1.75
2-11 to 2-14	$\sigma_H = \sigma_1$	4.2
	$\sigma_h = \sigma_2$	1.95

z = depth in metres

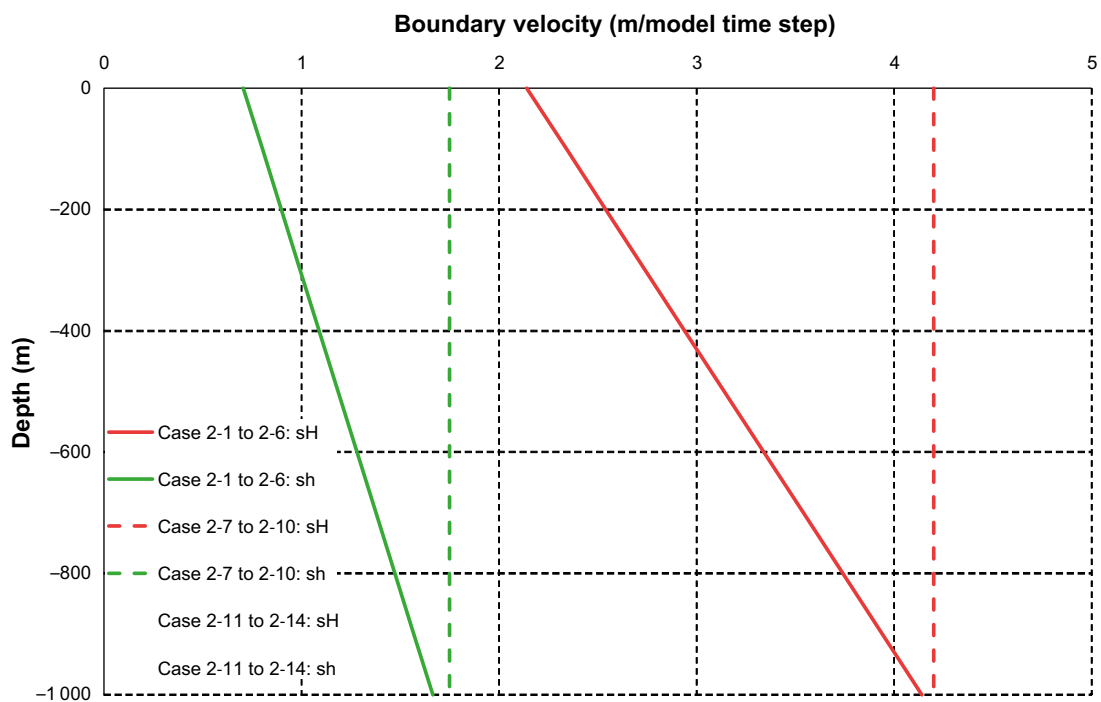


Figure 3-13. Applied thrust for Phase 2 simulation cases.

4 Simulation results

4.1 Presentation of results

The majority of Phase 1 and Phase 2 result figures are presented in the appendices and only the key figures that explain the observed behaviour are included in the main text. The following result figures are presented in the appendices:

- 3D figures of DZ shear displacement contours with maximum values (Appendix 1).
- Lower hemisphere plots of DZ normals, for DZs which have sheared more than 0.1 m (Appendix 2).
- The change of the major principal stress magnitude in a horizontal cross-section at the repository level and the same in two 3D-views (Appendix 3).
- The change of the major principal stress trend in a horizontal cross-section at the repository level and the same in two 3D-views (Appendix 4).
- The major principal stress magnitude, trend and σ_1/σ_2 ratio with mean and 90 % variation limits for each hundred meter depth interval in a 2400 m wide vertical cylinder covering the majority of the repository area (Figure 4-1) (Appendix 5).
- The major principal stress magnitude and trend distributions over a rectangular area (2400 m x 2800 m x 90 m) encompassing the repository area (Figure 4-2) (Appendix 6).
- The correlation between measured and simulated σ_1 and σ_2 magnitudes and depth dependency of σ_1 and σ_2 with confidence and prediction bands. The measured values used for this analysis (Sicada simulation reference in Figure 3-8) include the overcoring results used in Martin's (2007) stress field interpretation (see Appendix A in Martin (2007)). The linear trend of correlation in the figure is forced through the origin while the linear fit for measured values versus depth is forced to have a zero depth intersection equal to the Martin (2007) stress interpretation (Table 3-3). Phase 2 simulation results also include σ_3 versus depth figures. Simulation results are obtained from a spherical volume closest to respective stress measurement locations (Figure 4-3) (Appendix 7).
- The distribution of measured and simulated major principal stress trends (Appendix 8).

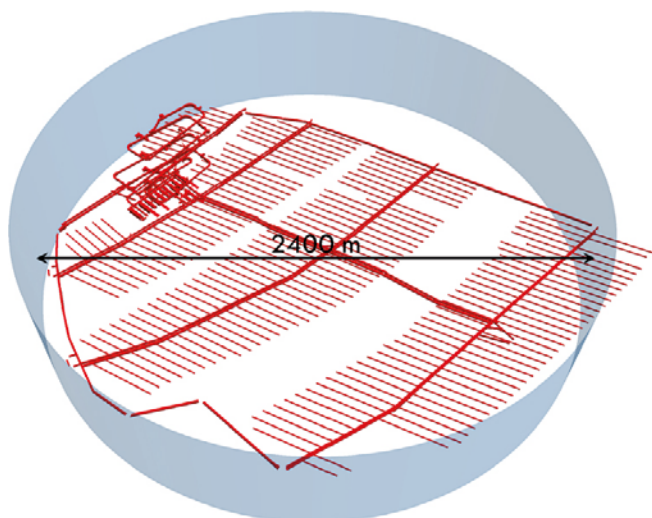


Figure 4-1. Cylindrical data acquisition volume for average stress magnitude and trend values.

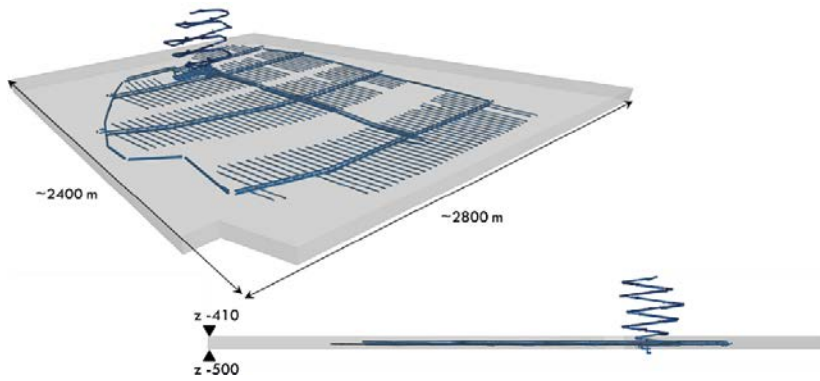


Figure 4-2. The data acquisition volume for frequency analysis of the distributions of the magnitude and trend of σ_1 at repository depth.

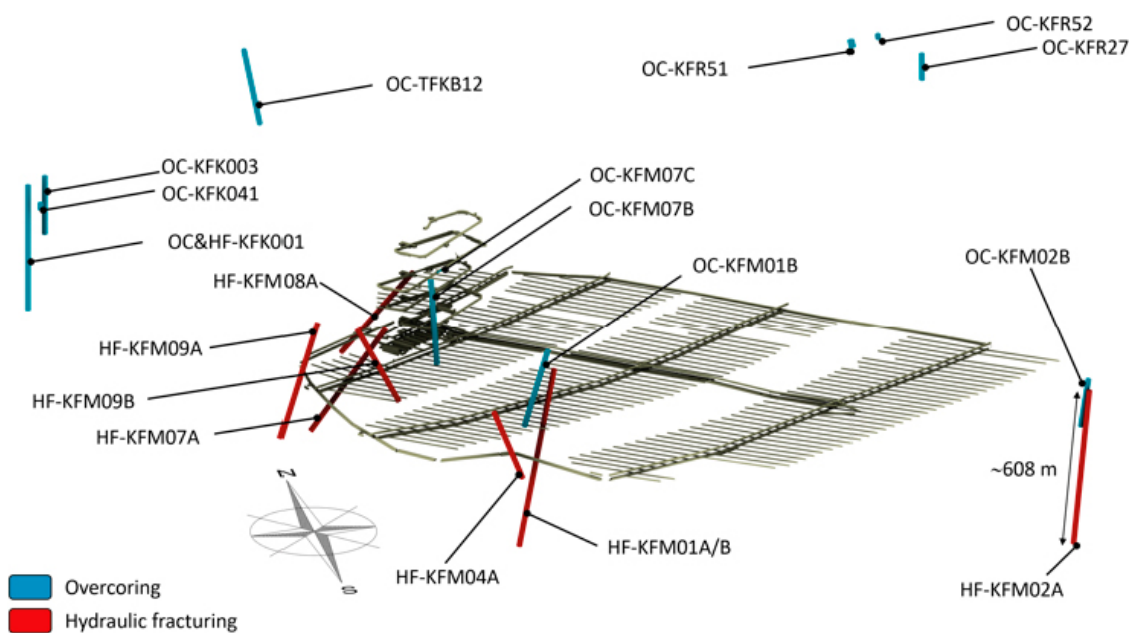


Figure 4-3. Stress measurement locations used for extracting data from the simulation results for correlation comparisons.

4.2 First simulation phase

Phase 1 simulations were performed with both planar and undulating DZ geometries and a pre-set *in-situ* stress field. The following is focused on Cases 1-1 and 1-3 and the parameters from these cases were further used in the Phase 2 simulations. Case 1-1 was the reference case with initial DZ parameter values and in Case 1-3 both DZ friction and cohesion have been reduced from 36° and 0.7 MPa to 20° and 0.3 MPa, respectively. The Singö zone parameters were also reduced but from 31.5° and 0.4 MPa to 20° and 0.3 MPa, respectively.

At large scale, the shear behaviour of planar and undulating models was similar (Figure 4-5), but summarizing the number of sheared contacts and the accumulated shear for the model indicates that undulating DZs shear more and shear extends to a greater depth (Figure 4-6). Further comparison of the vertical Singö and the sub-horizontal ZFMK1 DZs indicated that especially the sub-horizontal undulating DZs slip more (Figure 4-7 to Figure 4-10), slip referring to both “slipping now” and “slipped (past)”. Shear of planar vertical DZs was more widely spread in Case 1-5 which had the lowest shear strength parameters and Case 1-7 where the minor horizontal stress was equal to the vertical stress.

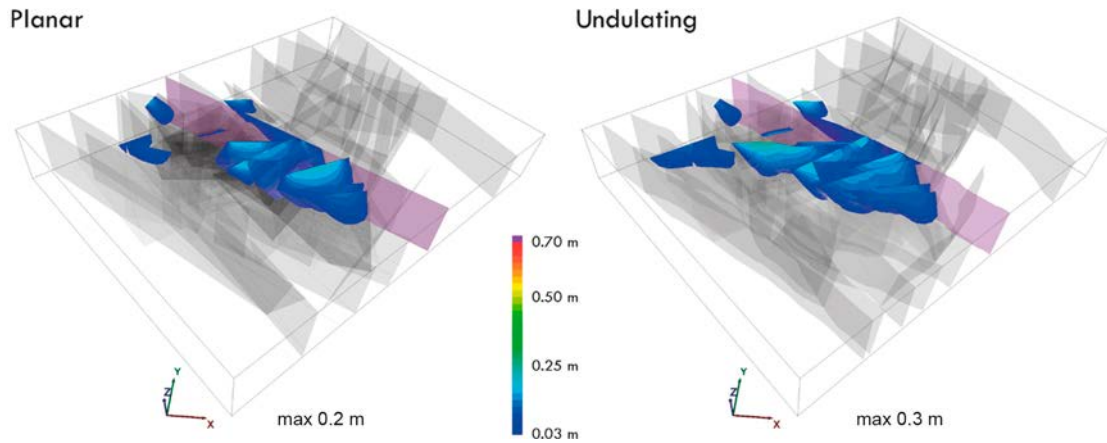


Figure 4-4. DZ total shear displacements in Cases 1-1.

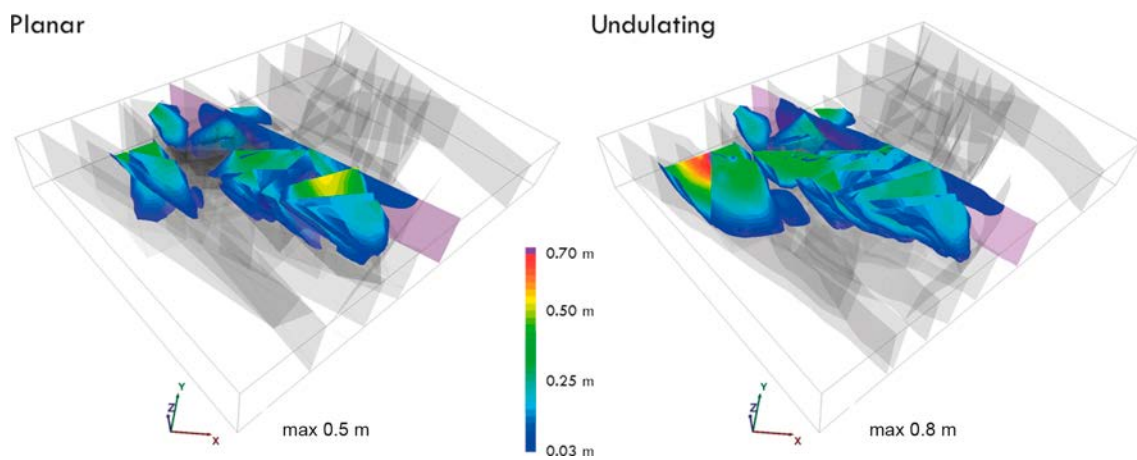


Figure 4-5. DZ total shear displacements in Cases 1-3.

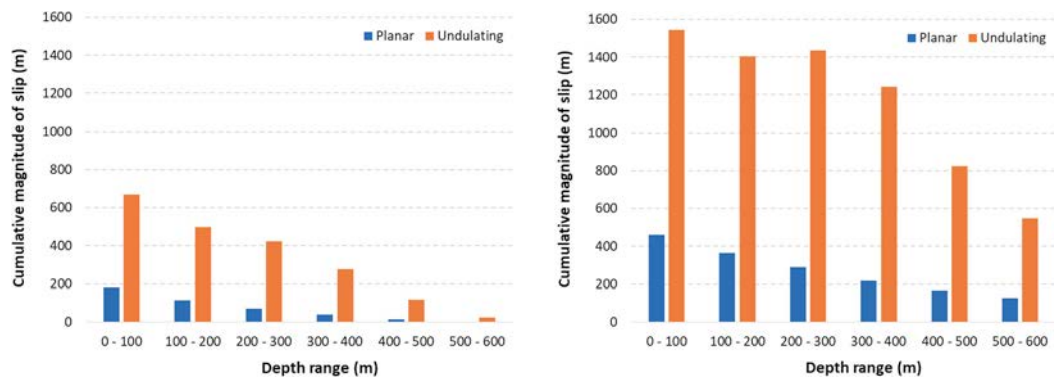


Figure 4-6. Cumulative magnitude of sheared contacts in Case 1-1 (left) and Case 1-3 (right).

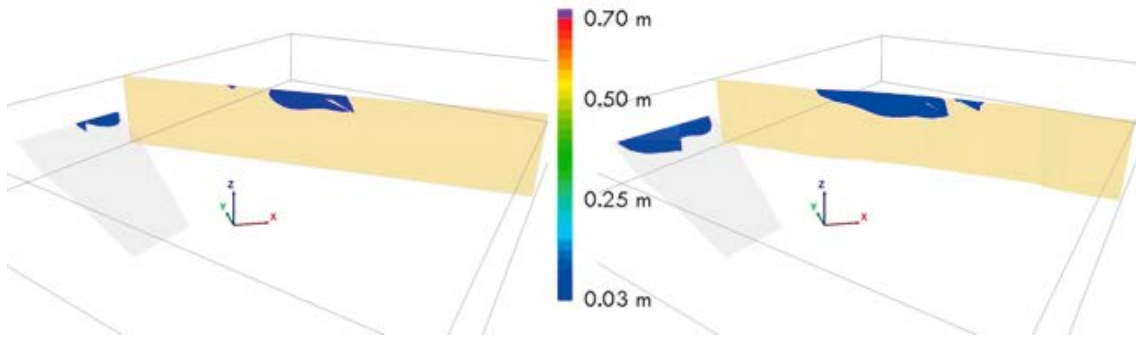


Figure 4-7. DZ total shear displacements for the Singö and ZFMK1 DZs in Case 1-1, left: planar, right: undulating.

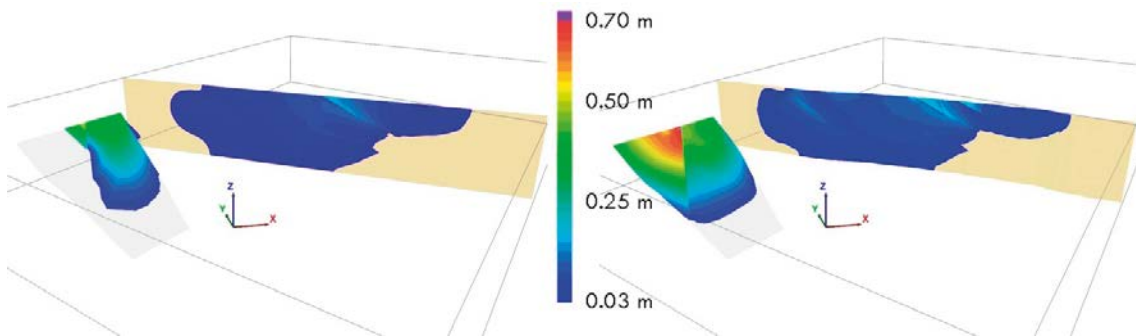


Figure 4-8. DZ total shear displacements for the Singö and ZFMK1 DZs in Case 1-3, left: planar, right: undulating.

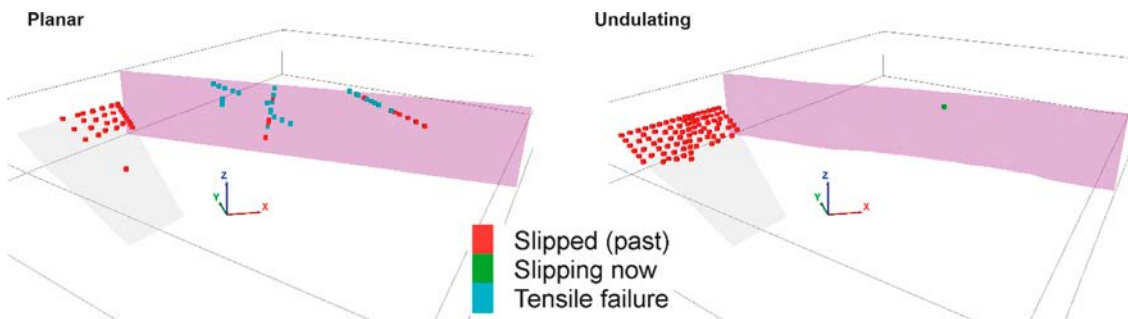


Figure 4-9. DZ state for the Singö and ZFMK1 DZ in Case 1-1.

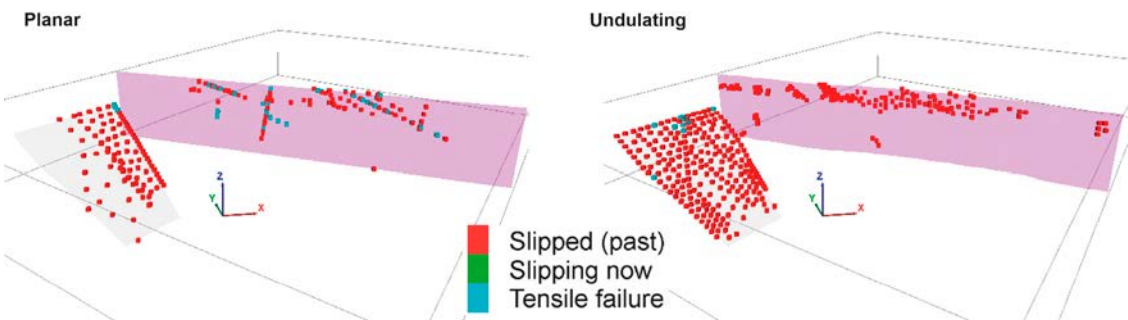


Figure 4-10. DZ state for the Singö and ZFMK1 DZ in Case 1-3.

The difference between the two simulation approaches was somewhat more apparent when considering the influence on the stress state. The undulating models exhibited a larger variation in σ_1 magnitude and trend, especially at shallow depths (Figure 4-11 to Figure 4-16). The volume of influence was also significantly larger in the undulating models. In Case 1-1 the variation of σ_1 magnitude and trend at repository level was generally less than ± 5 MPa and $\pm 20^\circ$. Due to the greater cumulative magnitude and larger area of shear of shallow dipping DZs in Case 1-3 (Figure 4-5), the variation of σ_1 magnitude was influenced generally by ± 10 MPa on the NE side of the repository and locally up to ± 20 MPa related to two DZs. At the repository level, the trend changes of major compression remained below $\pm 20^\circ$.

In the full repository volume the major principal stress decreased in all cases with respect to Martin's (2007) stress model, used as input, which is a logical consequence of fixed boundaries and DZ shear (Figure 4-15). The mean orientation of compression and the ratio between the horizontal stresses was fairly insensitive at repository depth. At shallow depths the orientation of the maximum compression can change over 75° when the applied stress state is released by slipping shallow DZs in the SE. Only the ultimate cases, 1-5 and 1-7, resulted in a clearly lower stress magnitude also at the repository depth. The mean σ_1 trend was fairly insensitive in all of the studied cases, although the variation increased significantly closer to the surface.

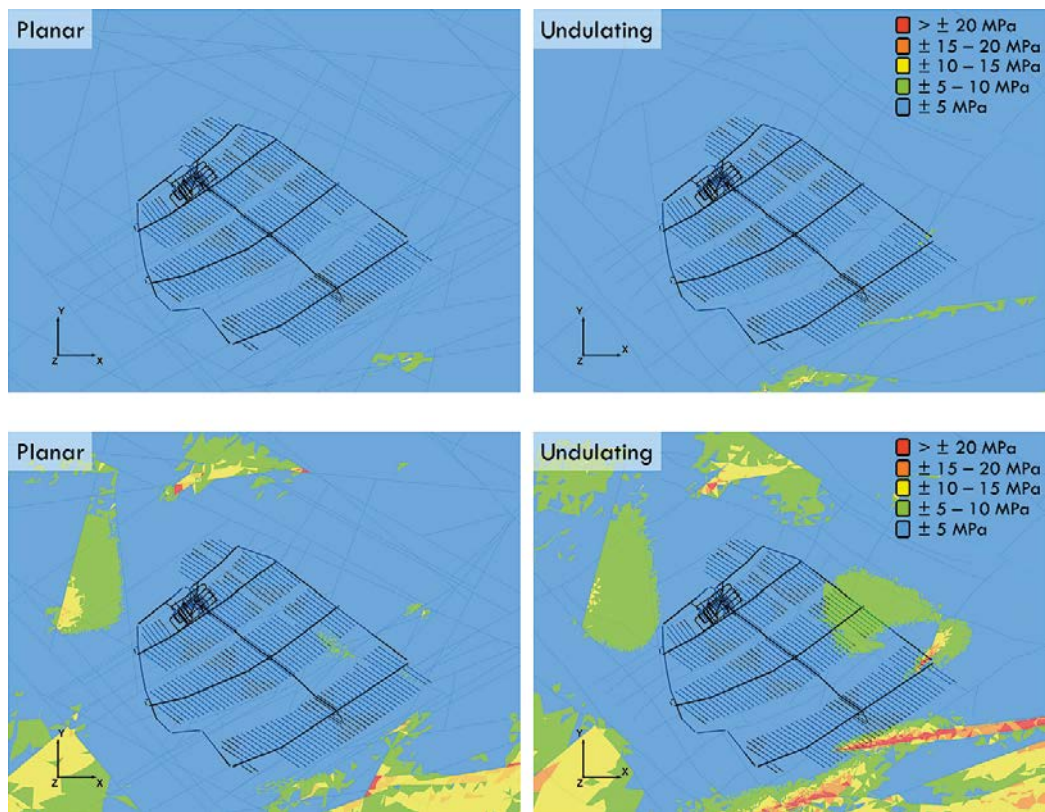


Figure 4-11. Change in σ_1 magnitude, horizontal section from repository level, Case 1-1 (above) and Case 1-3 (below).

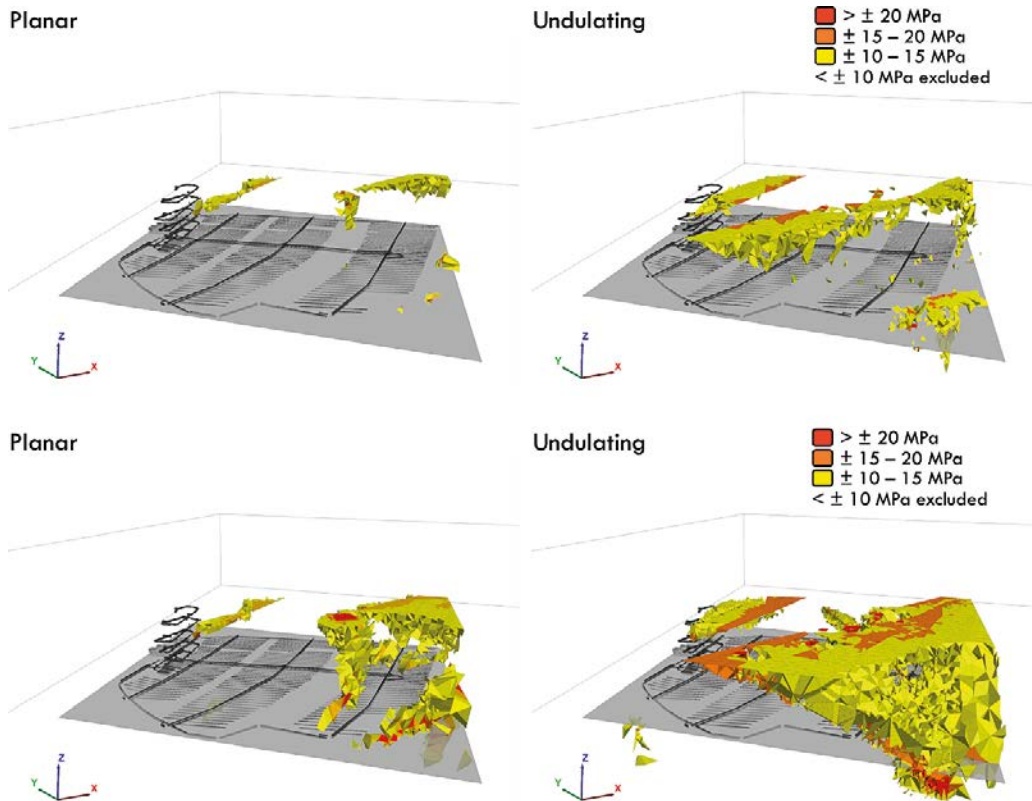


Figure 4-12. Change in σ_1 magnitude, 3D-view with repository, Case 1-1 (above) and Case 1-3 (below).

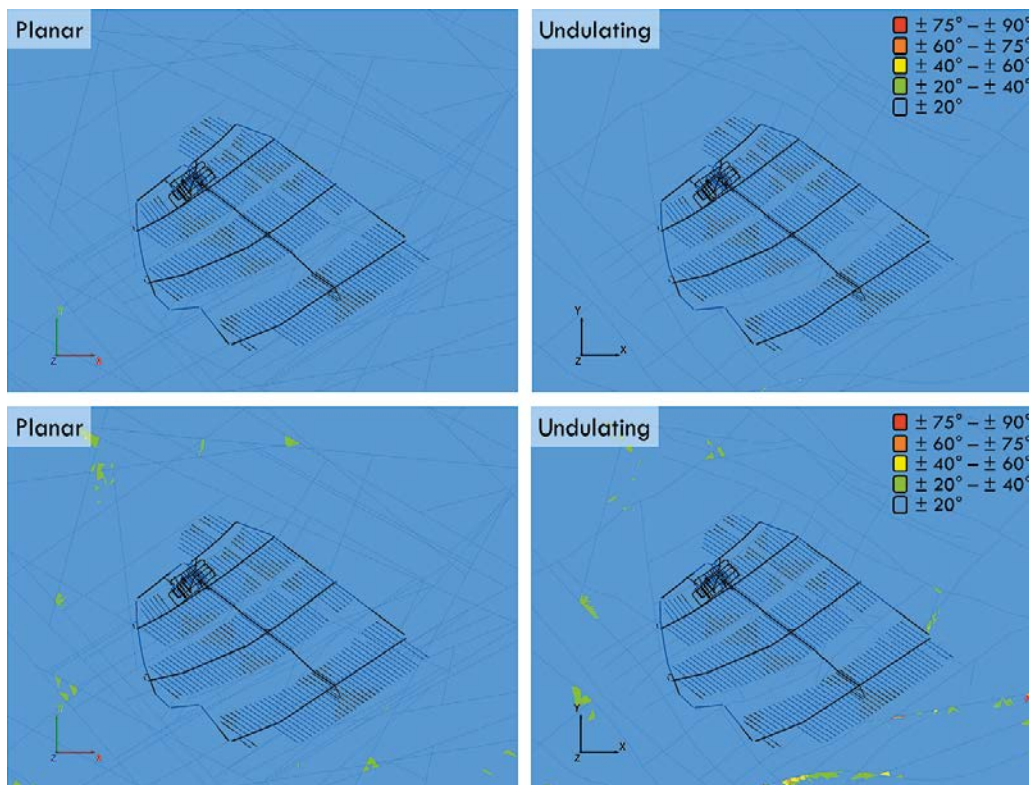


Figure 4-13. Change in σ_1 trend, horizontal section from repository level, Case 1-1 (above) and Case 1-3 (below).

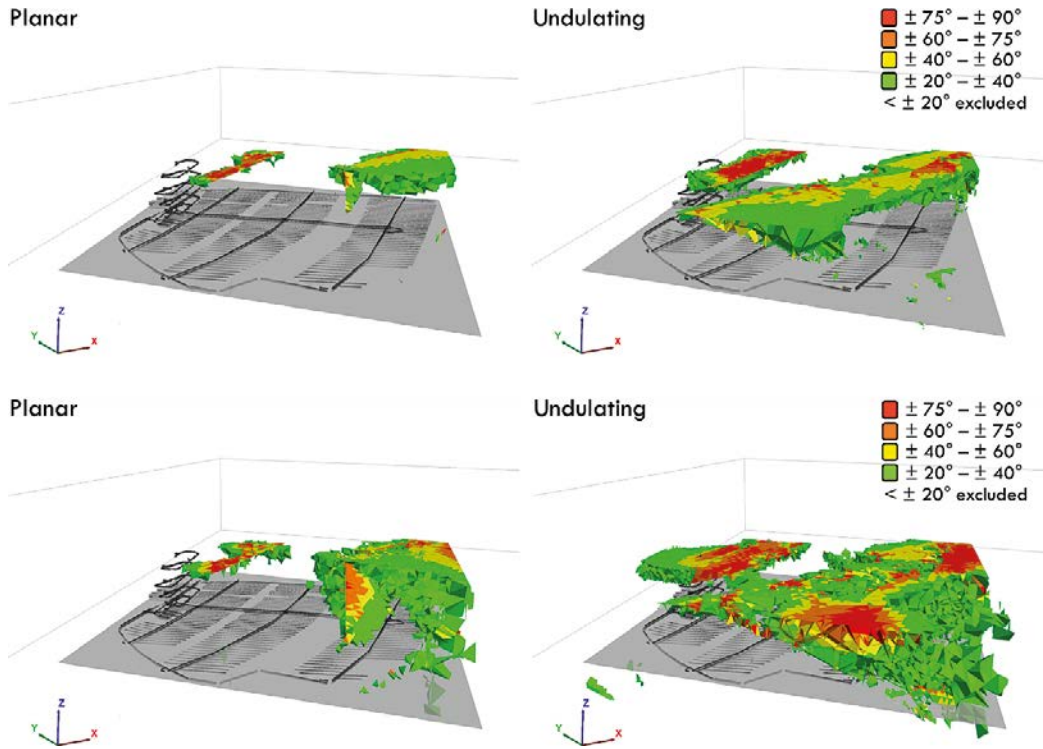


Figure 4-14. Change in σ_1 trend, 3D-view with repository, Case 1-1 (above) and Case 1-3 (below).

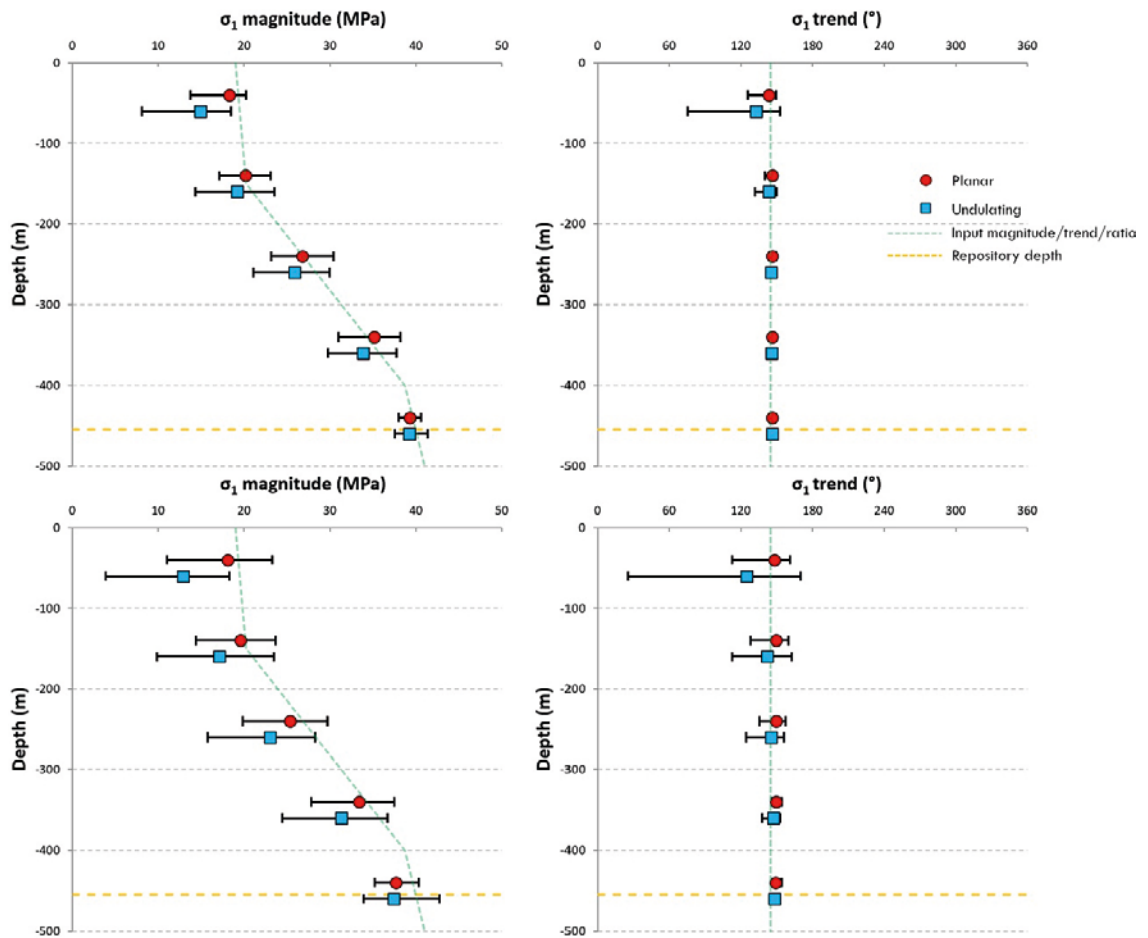


Figure 4-15. Mean and 90 % variation interval of σ_1 magnitude and trend for hundred meter intervals, Case 1-1 (above) and Case 1-3 (below).

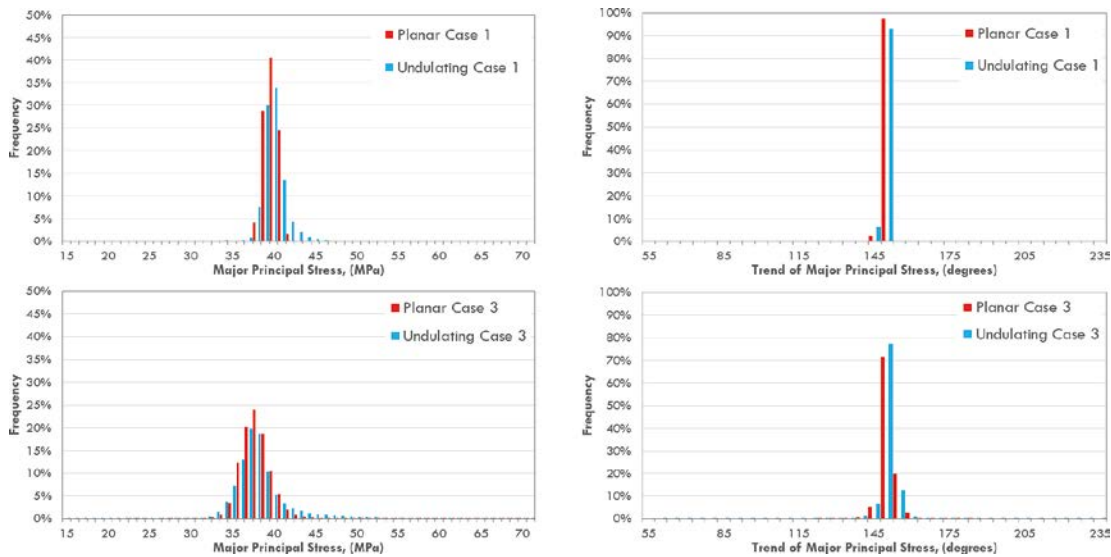


Figure 4-16. Distributions of σ_1 magnitude and trend at repository depth, Case 1-1 above and Case 1-3 below.

Due to the applied modelling approach and observed shear, all the simulated cases exhibited a moderate to poor correlation with *in-situ* stress measurements if compared using the closest elements to actual measurement locations (Figure 4-17 and Figure 4-18). The coefficient of determination (COD) was between 0.89 and 0.94 indicating that the assumed linear correlation is good but the slope of the fit varied from 0.82 to 0.61 for planar DZ model cases and from 0.81 to 0.65 for undulating DZ model cases, with a COD of 1.0 indicating perfect correlation. The slope values confirmed that the simulated stresses are generally 20 % to 40 % lower than measured stresses. The σ_1 -depth figures also indicated that the variation of simulated stresses was much narrower than measured scatter.

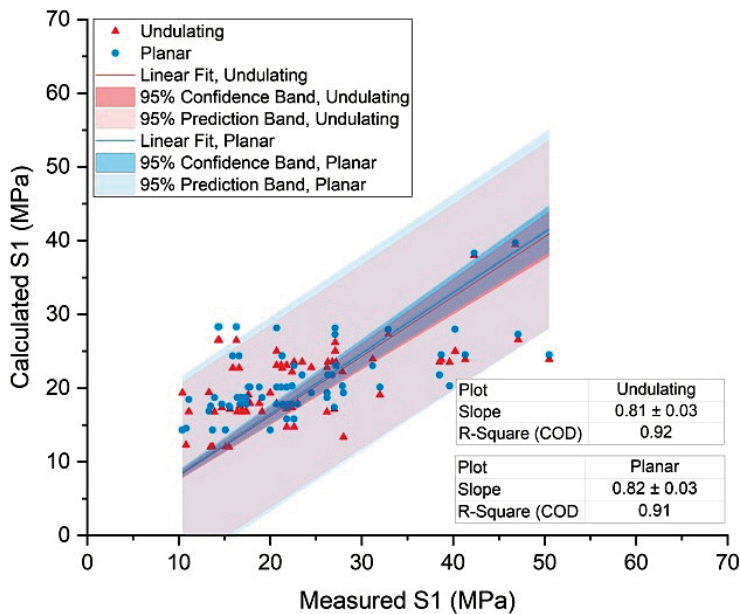


Figure 4-17a. Case 1-1: Correlation between measured and simulated major principal stress σ_1 magnitudes.

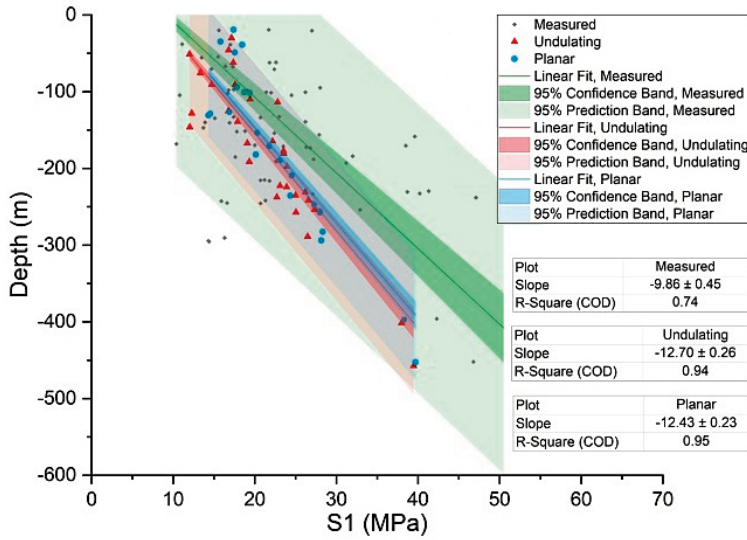


Figure 4-17b. Case 1-1: Correlation between measured and simulated major principal stress σ_1 versus depth.

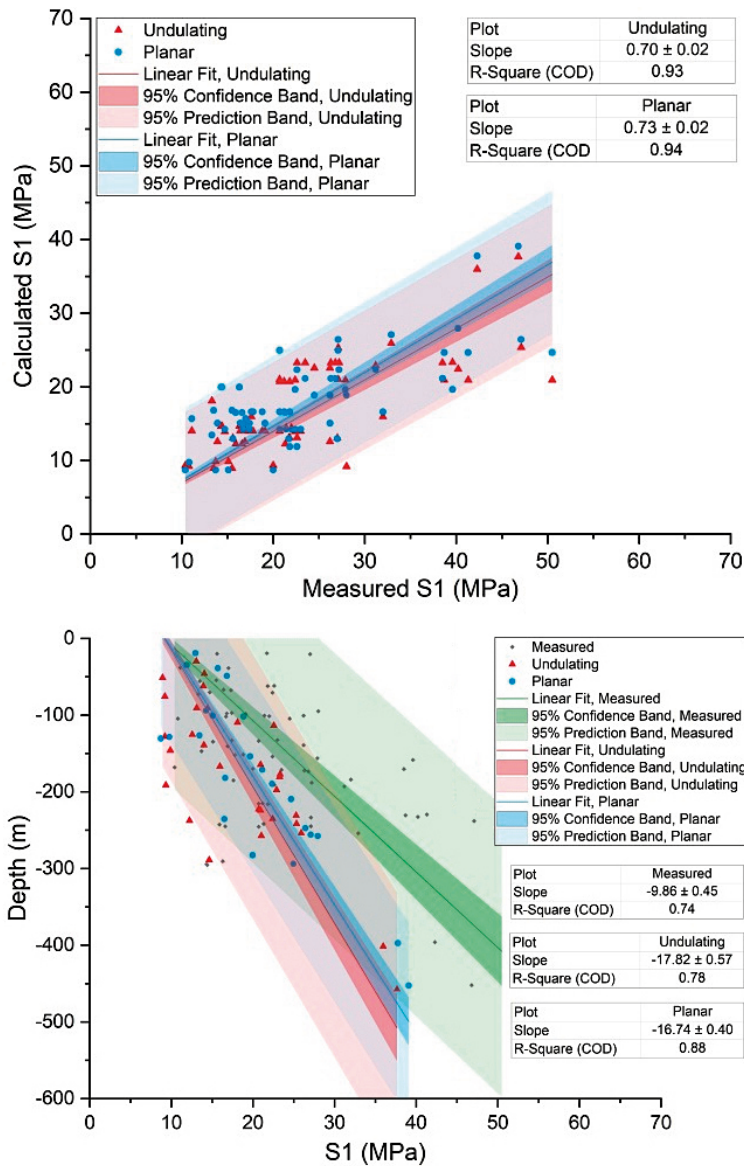


Figure 4-18. Case 1-3: Correlation between measured and simulated major principal stress σ_1 magnitudes (upper) and σ_1 versus depth (lower).

A summary of the studied cases indicates that with both the planar and undulating DZ geometry the amount and depth of shear was primarily defined by the friction angle and the normal stress i.e., higher values for both decreased shear deformation and area of shear. Additionally, the undulating DZ geometry exhibited more total shear deformation and area of shear than planar geometry. Reducing DZ stiffnesses to approximately 1/10 of the original value increased shear displacements only slightly (Case 1-4 vs Case 1-3). The studied $\pm 10\%$ change in rock mass modulus did not indicate any notable response in DZ shear (Case 1-6 vs Case 1-3). A lower minor horizontal stress decreased the normal stress on vertical DZs, increasing shear displacement (Case 1-7 vs Case 1-3). Increasing shear decreased the major principal stress while also increasing the variation of stress magnitudes and orientations. Apart from the ultimate and most unrealistic Cases 1-5 and 1-7, the repository level stress state was only slightly affected by the DZ shear.

The applied modelling approach, where the *in-situ* stress was set directly, is poorly suited to study the magnitudes of overcoring stress measurements because the given *in-situ* stress state pre-orders the resulting stress state and is released by shear. The best correlation between measured and simulated major principal stress values was achieved with Case 1-1 parameters, although the planar model, which was practically the same as the undulating model, provided a slightly better fit. For this reason, the method of introducing the stress state to the model was changed in the second simulation phase in which the stress state was instead driven by boundary conditions, simulating the tectonic ridge push.

4.3 Second simulation phase

Simulation Phase 2 was performed with undulating DZ geometry only and it was primarily aimed at increasing the variation of both stress magnitudes and orientations while maintaining the mean values as close to the Martin (2007) target stress state as possible. The second objective was to achieve a better correlation with measured stresses. To obtain this, the *in-situ* stress state was established by boundary thrust conditions followed by one glaciation cycle. After removing the glacial loads, the mean stress at the repository level was checked and brought back to pre-glacial levels if necessary. The studied cases with different thrust orientations and DZ shear strength parameters are summarized in Table 3-7. The following sections focus on the major differences between Phase 2 and Phase 1 results, highlighting major differences between the simulated cases while comparing the simulated stress state with overcoring stress measurement results.

Building the in-situ stress state – differences between Phase 1 and Phase 2

Although the Phase 1 and Phase 2 simulations resulted in a very similar stress state, shallow dipping DZs and part of the NE or SW dipping sub-vertical DZs sheared more significantly and to greater depths in Phase 2 (Figure 4-19 and Figure 4-20). Shallow dipping DZs sheared up to a depth of 700 m in Phase 2, compared to 300 m in Phase 1. The Singö DZ experienced notable shear and shear extended throughout the model, as it had the lowest shear resistance. The most notable difference compared to Phase 1 simulations was the higher variation of the resulting stresses and their orientations (Figure 4-21). It was already higher than in Phase 1 simulations after primary thrust and was further increased during the glacial cycle. The glaciation cycle did, however, decrease the major principal stress magnitudes above the 300 m level, but the difference was less than 5 MPa. The magnitude variation originated by thrust extended below the 1 000 m level compared to Phase-1 simulations, where it was already minimal at the repository level. The variation of the major principal stress trend extended to greater depths but was minor below the 300 m level.

With the same parameter values, undulating DZ geometries and gradient thrust conditions targeting equivalent stresses between cases at the 450-level, Cases 1-1 and 2-1, the thrust model resulted in an approximately 5 MPa lower major principal stress at depths above 100 m when compared to Martin's (2007) interpretation. Between depths of 100 m and 350 m, the major principal stress was 5 MPa higher while magnitudes were approximately equal to Martin's (2007) interpretation between depths of 350 m and 500 m (Figure 4-21).

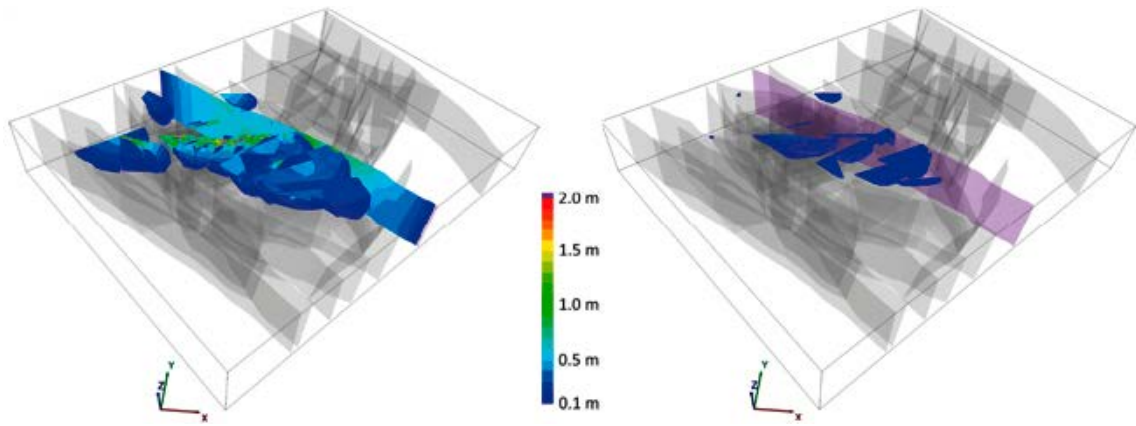


Figure 4-19. DZ total shear displacement contours for Case 2-1 (left) and Case 1-1 (right).

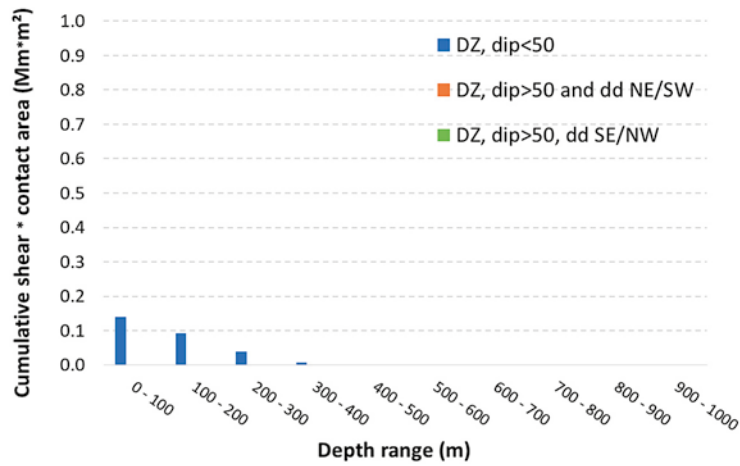
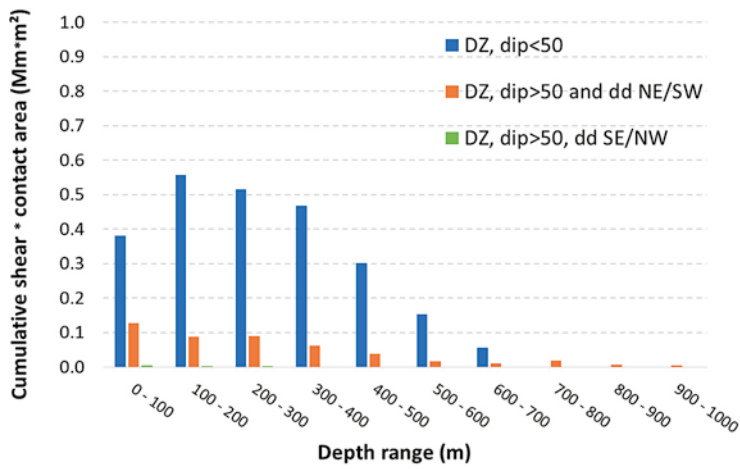


Figure 4-20. Cumulative shear displacement multiplied by associated area versus depth for major orientations sets of DZ, Case 2-1 above and Case 1-1 below.

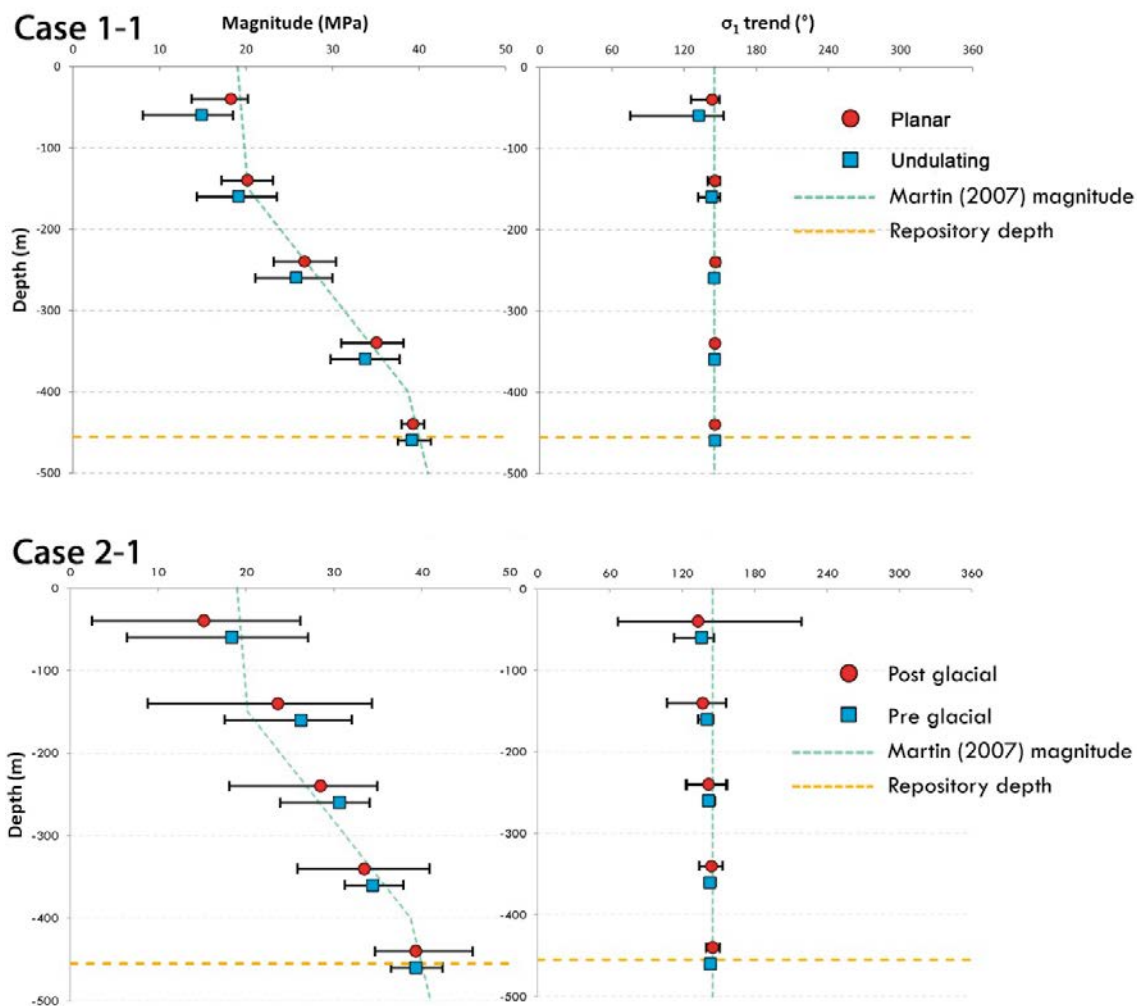


Figure 4-21. The mean and 90 % variation interval of σ_1 magnitude and trend for hundred meter intervals for Cases 1-1 (above) and 2-1 (below).

Key results and differences between simulated cases

The major differences between Phase 2 simulation cases were the type of the applied boundary thrust, the orientation of thrust compared to the DZ geometry and the shear resistance of the DZs. When the model stress state was established by thrust until a pre-set target stress state at the repository level was reached, the general model response was very similar between Phase 2 models, but the following differences could be observed (Appendix 1b and Appendix 5b):

- Applying the thrust using constant boundary velocities instead of gradient thrust boundary conditions did not have any notable effect on the resulting stress states. The results for otherwise identical case pairs 2-7/2-1, 2-8/2-4, 2-9/2-5 and 2-10/2-6 were practically the same. The reason for this was that the gradient of the thrust displacement equalized to a mean value within a relatively short distance from the model boundary in a model geometry that is thin, wide and plate-shaped.
- The reduction of excess glacial pore pressure from 98 % to 90 % had no notable effect on the resulting stress state or shear magnitudes (Cases 2-2 versus Case 2-1).
- Rotating the thrust orientation $+20^\circ$ to DZ geometry increased shear of the vertical Singö DZ but had very little effect on shallow DZ behaviour. No notable effect could be seen in σ_1 magnitudes but the σ_1/σ_2 ratio was decreased by 10 % to 20 % above the 200 m level. Rotating thrust orientation with -20° did, however, reduce shear mainly of the Singö DZ but also slightly of the shallow dipping DZs. The σ_1/σ_2 ratio was increased by 10 % to 20 % above the 200 m level (Cases 2-3 and 2-4 versus Case 2-1).

- Reduction of DZ shear resistance increased shear magnitudes and extended the depth to which shear occurs in shallow dipping DZs from 700 m to well below 1 000 m (Figure 4-22) (Case 2-5 versus Case 2-1). Additionally, other vertical DZs than Singö also sheared. As a result of increased shear, the variation of the major principal stress magnitude and trend also increased. In both cases, variation was higher down to the 550 m level and was more or less constant at greater depths (Figure 4-23). The variation of the trend of σ_1 also increased above the 300 m level but below this level remained fairly narrow (Figure 4-24).
- The rotation of thrust with reduced DZ shear strength mainly reduced shear of vertical DZs similar to Case 2-4. Variation of the major principal stress magnitude and trend were regardless considerably higher than in the base Case 2-1, but approximately the same as in the unrotated case (Case 2-6 versus Cases 2-5 and 2-1) (Figure 4-23 and Figure 4-24).
- The results of the simulations after the full glaciation cycle had been applied showed a decrease in the major principal stress and σ_1/σ_2 ratio while the variation of magnitudes and orientations was also considerably increased (Figure 4-23, Figure 4-24 and Appendix 5).
- Based on the simulated cases, the expected variation of the major principal stress magnitude in the designed repository area is generally less than 5 MPa, but in very narrow volumes close to DZs changes up to 20 MPa are possible (Cases 2-1 to 2-4)(Figure 4-25). With reduced DZ shear strength, variation could be up to 10 MPa in a wider area (Cases 2-5 and 2-6). The variation of the major principal stress trend in the planned repository area remained below ± 20 degrees (Figure 4-26). ± 20 degrees is commonly used as a limiting value for good reliability in stress measurement interpretation (Heidbach et al. 2016).

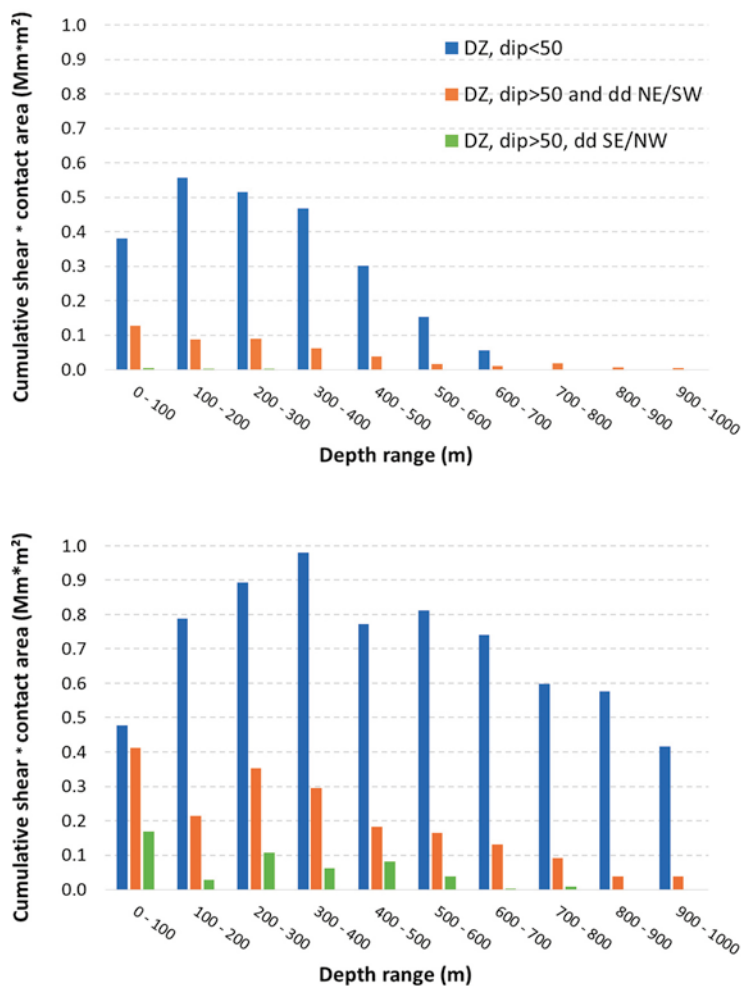
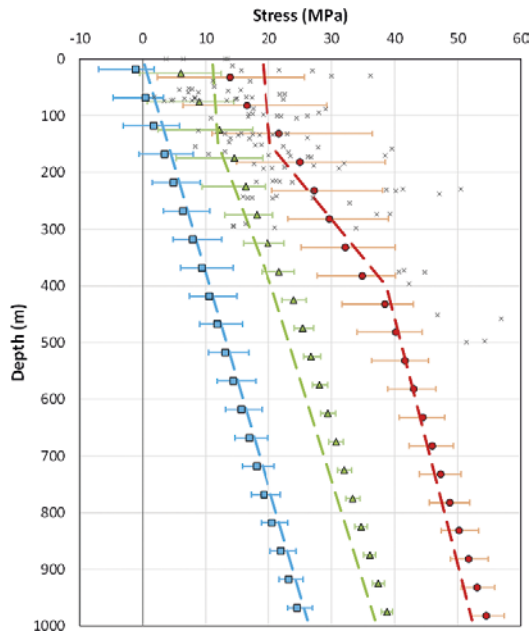
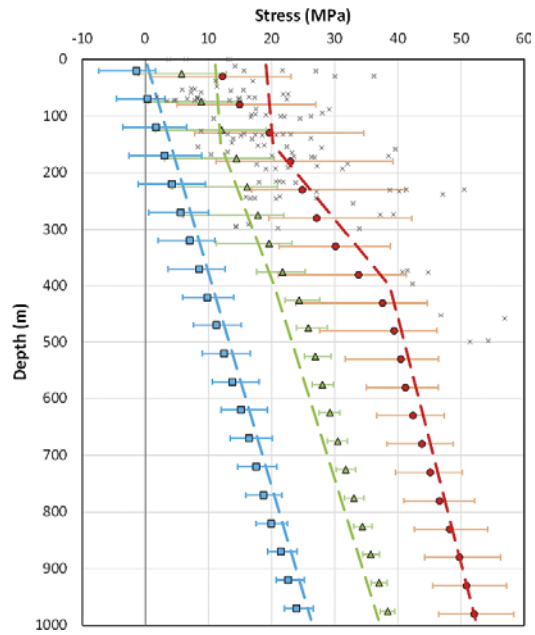


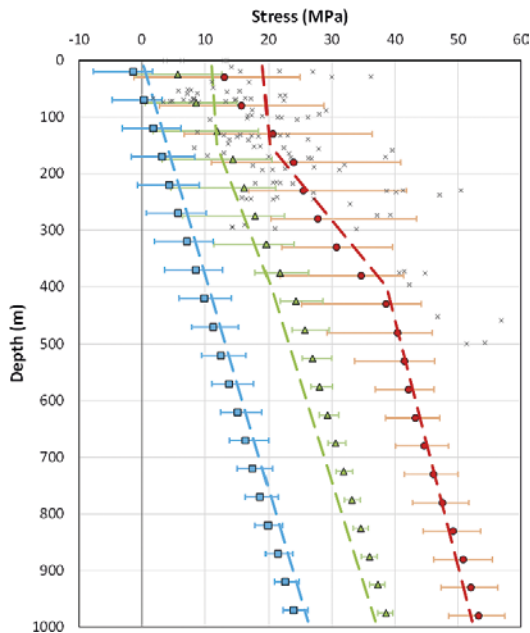
Figure 4-22. The cumulative shear displacement multiplied by the associated area versus depth for major orientations sets of DZ, Case 2-1 above and Case 2-5 below.



Case 2-1



Case 2-5



Case 2-6

- Phase-2, σ_1
- ▲ Phase-2, σ_2
- Phase-2, σ_3
- Martin 2007, σ_H
- Martin 2007, σ_h
- Martin 2007, σ_{vert}
- × SICADA All, σ_1

Figure 4-23. The resulting mean principal stress with 90 % variation limits for Cases 2-1, 2-5 and 2-6 with the Martin (2007) stress model and all major principal stress results measured using the overcoring method (Sicada all in Figure 3-8).

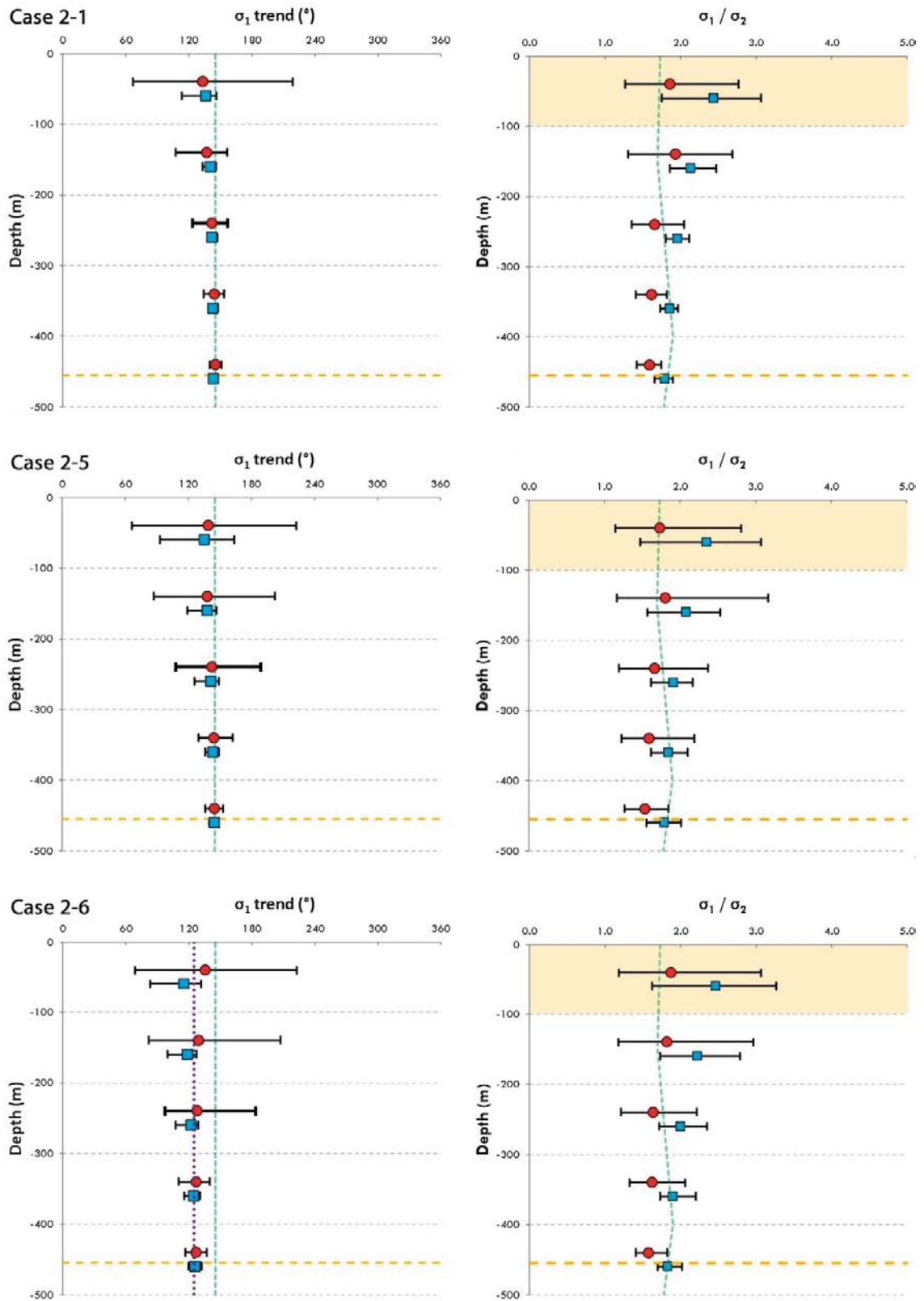


Figure 4-24. The trend and 90 % variation interval of the major principal stress and σ_1/σ_2 ratio before and after the glaciation cycle for Cases 2-1, 2-5 and 2-6.

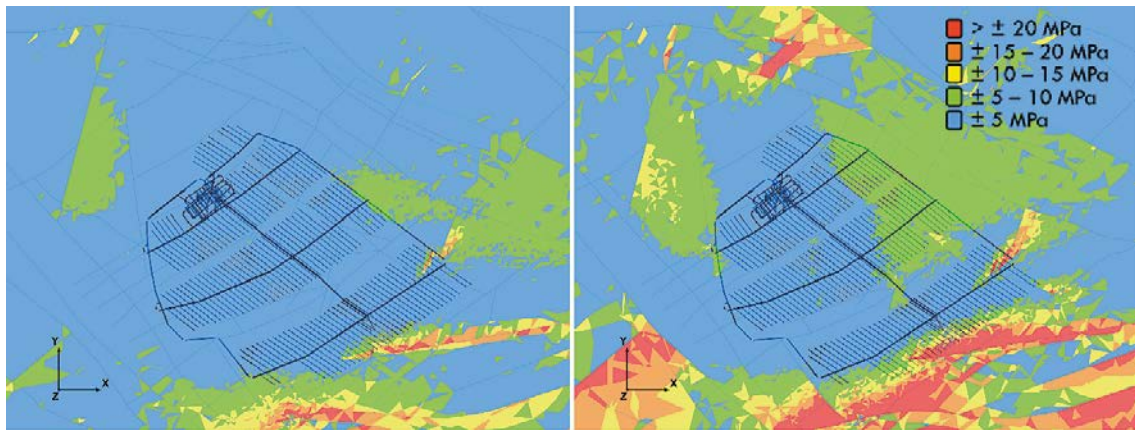


Figure 4-25. The variation of the major principal stress magnitude at the repository level in Cases 2-1 (left) and 2-3 (right).

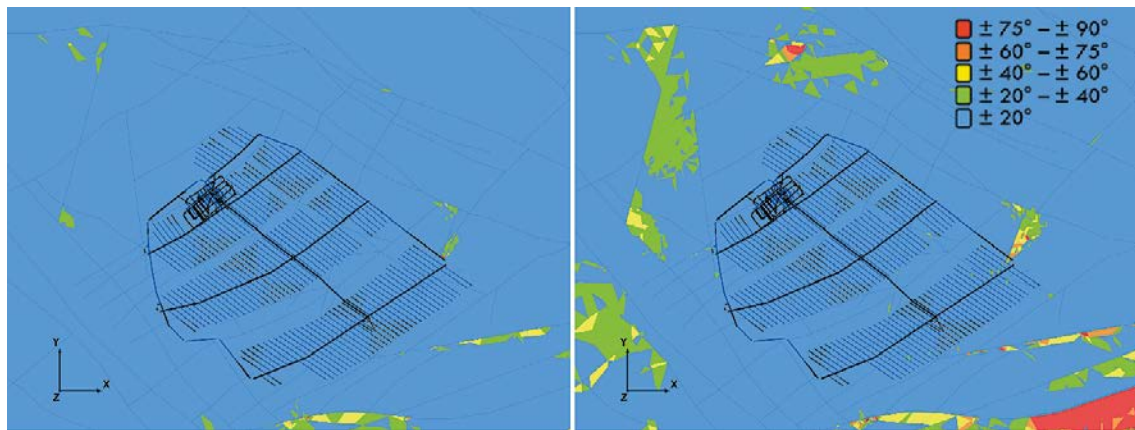


Figure 4-26. The variation of the major principal stress trend at the repository level in Cases 2-1 (left) and 2-3 (right).

Correlation of simulated stresses with most reliable measured overcoring results

A comparison of the simulated principal stresses with the Martin (2007) interpretation indicated that all of the studied Cases, 2-1 to 2-10, provide a fairly good correlation except for a depth range of 0 to 150 m (Figure 4-23). In addition, a direct comparison and ranking was performed between measured principal stress components with simulated equivalents obtained from one zone/model element closest to the measurement point location. Ranking was performed using the slope of a linear fit between the measured and simulated stress magnitudes which should be close to one for a good fit together with the coefficient of determination (COD) value which is one, indicating that the fitted line explains all the variability of the response data around its mean (Figure 4-27 and Figure 4-28). Additionally, linear fit slopes for magnitude-depth values and widths of 95 % prediction bands were compared (Figure 4-27). The linear fit for the measured magnitude-depth was forced through the Martin (2007) zero depth intercept value for compatibility between resulting linear regressions, which is 19 MPa for σ_H and 11 MPa for σ_h . The goodness of fit of the magnitude-depth dependency was ranked based on the difference between the slopes of measured and simulation cases and the difference of the COD-values. The minor principal stress σ_3 values were not used for ranking (Figure 4-29).

Figure 4-27 to Figure 4-29 present the principal stresses at measurement points before and after the glaciation cycle, while the values before glaciation are omitted from Appendices 7a and 7b. Generally, as in Case 2-1, the mean major principal stresses fit the measured values better before glaciation but were approximately 10 % lower after glaciation. The technical modelling issue related to this is discussed in Chapter 5. The match of the intermediate principal stress σ_2 was normally worst because

the major principal stress was used to control thrust and also due to the previously mentioned technical issue. The variation (COD) between measured and calculated values does not change remarkably after the glaciation cycle, but with regards to the magnitude-depth relation it increased significantly and resulted in a better match to the variation of the measured values.

Based on the applied ranking system, the goodness of fit of Cases 2-1 to 2-6 was practically the same (Table 4-1 and Table 4-2), but Case 2-3 with basic material parameter values and +20 degrees rotated thrust resulted in the best score. The intermediate principal stress generally had worse goodness of fit values due to the applied thrust control method. Cases 2-7 to 2-10 had a lower goodness of fit ranking which was not because of the applied constant thrust but due to the applied thrust stop control value, which was a compromise between σ_1 and σ_2 values at the repository location, which resulted in a slightly lower target σ_1 .

Table 4-1. Goodness of fit ranking values for simulation Phase 2 cases, values are coloured from best (green) to worst (red).

Case	σ_1				σ_2			
	Measured versus simulated		Magnitude versus depth		Measured versus simulated		Magnitude versus depth	
	Δ slope	1-COD	Δ slope	Δ COD	Δ slope	1-COD	Δ slope	Δ COD
Case 2-1	0.07	0.09	0.05	0.02	0.13	0.20	0.21	0.36
Case 2-2	0.08	0.09	0.05	0.04	0.11	0.21	0.16	0.34
Case 2-3	0.03	0.09	0.02	0.01	0.10	0.18	0.16	0.28
Case 2-4	0.08	0.09	0.06	0.02	0.12	0.23	0.12	0.27
Case 2-5	0.10	0.09	0.06	0.07	0.11	0.19	0.12	0.21
Case 2-6	0.12	0.09	0.15	0.06	0.03	0.22	0.08	0.21
Case 2-7	0.11	0.09	0.09	0.06	0.24	0.21	0.58	0.29
Case 2-8	0.12	0.09	0.13	0.03	0.25	0.23	0.52	0.22
Case 2-9	0.13	0.08	0.14	0.09	0.20	0.18	0.42	0.19
Case 2-10	0.19	0.10	0.25	0.11	0.17	0.23	0.23	0.19

Table 4-2. Sum of goodness of fit ranking values for simulation Phase 2 cases, values are coloured from best (green) to worst (red).

Case	Sum of ranking values for;		
	$\sigma_1 + \sigma_2$	σ_1	σ_2
Case 2-1	1.1	0.2	0.9
Case 2-2	1.1	0.3	0.8
Case 2-3	0.9	0.1	0.7
Case 2-4	1.0	0.2	0.7
Case 2-5	1.0	0.3	0.6
Case 2-6	1.0	0.4	0.5
Case 2-7	1.7	0.3	1.3
Case 2-8	1.6	0.4	1.2
Case 2-9	1.4	0.4	1.0
Case 2-10	1.5	0.7	0.8

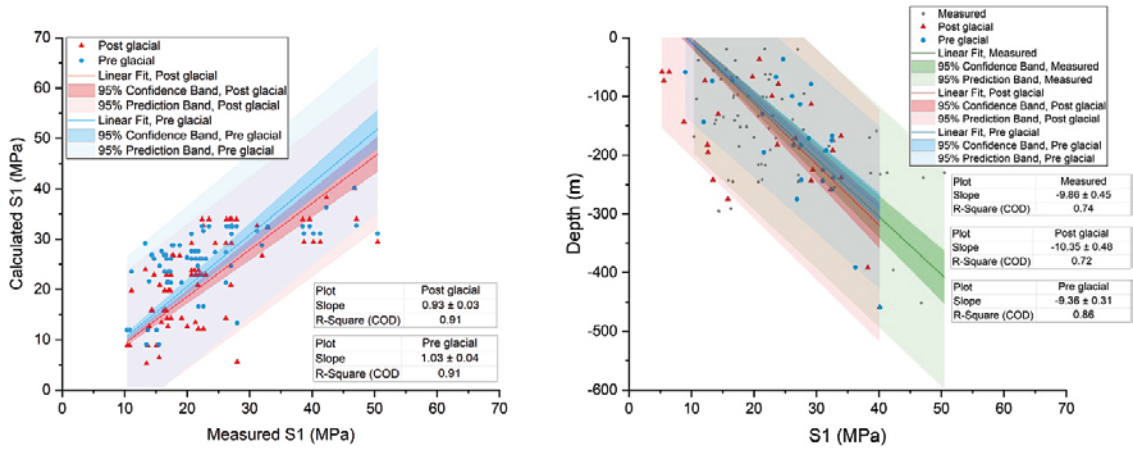


Figure 4-27. Case 2-1, σ_1 magnitude correlation with OC stress measurements.

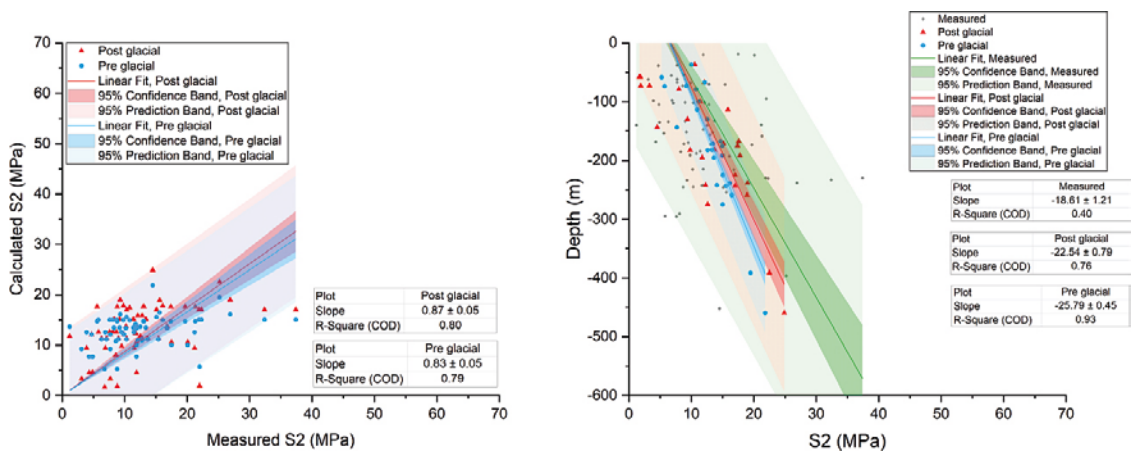


Figure 4-28. Case 2-1, σ_2 magnitude correlation with OC stress measurements.

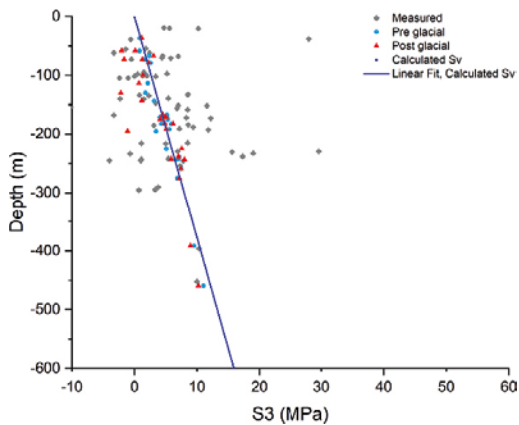


Figure 4-29. Case 2-1, σ_3 magnitude correlation with OC stress measurements.

5 Discussion and conclusions

This study demonstrated that it is possible to build and run a 3DEC model with very complicated, non-planar, DZ geometry requiring reasonable computation times. The total number of modelled surfaces was 110 and many of them were almost parallel and intersected each other. Low angle surface intersections caused some technical challenges due to code functionality and required care from the user to assign the contact properties correctly.

The Phase-1 and Phase-2 simulations indicated that the simulation of realistic variation of *in-situ* stress measurements required that the stress state was established by boundary thrust conditions and included disturbances caused by the latest major glaciation cycle. The use of undulating DZ surface geometry alone was found to result in more realistic scatter in the stress state magnitudes and orientations. Boundary thrust further increased the scatter in stress magnitudes and orientations, which resulted in scatter closer to observed measurements. The effect of boundary thrust conditions alone was not analysed, as a model with planar DZ geometry and boundary thrust conditions was not included in the study. Additionally, a similarly realistic match with the measurement results was obtained with simple constant thrust and more complicated thrust boundary conditions. The effect of more complicated thrust conditions appeared to be negligible especially in thin and wide plate-shaped model geometries.

When the stress state was established by thrust, the resulting mean stresses were fairly insensitive to the studied DZ parameter values. If DZ parameters were in a realistic range, the lower shear strength mainly increased the resulting variation of stress magnitudes and orientations as thrust was continued until the target stress state was achieved at the control location. Based on the above, the rock mass and DZ parameter values presented in Rock Mechanics Forsmark v2.2 and v2.3 can be considered appropriate.

All of the simulated thrust cases with a target stress level at the repository level equivalent to Martin's (2007) interpretation, Cases 2-1 to 2-6 (2-10), resulted in a fairly good correlation with Martin's (2007) interpretation overall, but Case 2-3 (σ_1 trend $+20^\circ$) resulted in the best correlation with the most reliably ranked overcoring stress measurements. This correlation is, however, only statistically the best match as very large differences exist in point to point comparison. This is nonetheless very understandable if the uncertainties related to the true nature of the DZ surfaces and the resolution of the applied simulation model are considered. Fracturing at stress-measurement scale also affects measurement results but could not be included at the scale of this study.

The simulated magnitudes of the major and intermediate principal stresses were generally about 10 % lower than measured magnitudes up to a depth of 150 meters from the surface, which were at least partly caused by modelling artefacts.

A thrust model with the modelled DZs cannot easily result in the mean stress magnitude-depth relation introduced in Martin's (2007) interpretation at depths above 150 m, where almost constant major and intermediate principal stress magnitudes are apparent. This is largely a result of maximum DZ shear, which is the primary factor that affects stress magnitudes, occurring close to the surface where the normal stress is low thereby resulting in lower stress magnitudes. Stress magnitudes were therefore always lower at the surface in comparison to Martin's (2007) interpreted trend above 150 m.

The thrust model supports the high variation of stress measurement result magnitudes and orientations observed above 300 m level fairly well. Very low magnitudes were, however, common in the simulation results indicating that the low stress measurement results could, in fact, be possible and not due to faulty or biased measurements, and these data should not be discarded per se. Conversely, simulation result variation also indicated higher magnitudes, but not to the level of extremely high measurement results which probably have suffered from thermal issues as reported in Martin (2007).

Although it was originally planned, the effects of *a*) a non-linear, normal-stress stiffening, DZ contact stiffness model and *b*) spatial shear strength variation were not studied. Based on the results, the factors above could affect the variation of stress magnitudes and their orientation, but no major changes are expected as the studied range of shear strength values is already broad.

The following recommendations apply to any future simulations:

- All of the reliably ranked stress measurement values and locations should be used for thrust control. During thrust, the absolute difference between the measured and simulated magnitudes at each point should be calculated, summed and monitored. Optimum thrust can be defined as the minimum of the summed monitored value. An additional criterion should be that the slope of the linear fit between the measured and simulated stresses should be between 0.95 and 1.05.
- Simple constant velocity thrust conditions should be applied.
- The macro-controlled normal velocity boundary conditions could be optimised to obtain a more accurate horizontal stress ratio.
- The bounding blocks around the DZ area should be equal in width and not wedge shaped as in this study. The varying thickness in the thrust direction introduces a minor inaccuracy in the applied thrust.

During this study it was noted that the reliability ranking of existing overcoring stress measurement results is not well documented or it is at least challenging to discern from a single document. Additionally, part of the measurements were excluded from Martin's (2007) interpretation without the omitted measurements being clearly identified in the report.

References

SKB's (Svensk Kärnbränslehantering AB) publications can be found at www.skb.com/publications.

Glamheden R, Fredriksson A, Röshoff K, Karlsson J, Hakami H, Christansson R, 2007.

Rock mechanics Forsmark. Site descriptive modelling, Forsmark stage 2.2. SKB R-07-31, Svensk Kärnbränslehantering AB.

Glamheden R, Lanaro F, Karlsson J, Lindberg U, Wrafter J, Hakami H, Johansson M, 2008.

Rock mechanics Forsmark. Modelling stage 2.3. Complementary analysis and verification of the rock mechanics model. SKB R-08-66, Svensk Kärnbränslehantering AB.

Hakami H, 2006. Numerical studies on spatial variation of the in-situ stress field at

Forsmark – a further step. Site descriptive modelling Forsmark – stage 2.1. SKB R-06-124, Svensk Kärnbränslehantering AB.

Hakami H, Min K-B, 2009. Modelling of the state of stress. Preliminary site description Laxemar subarea – version 1.2. SKB R-06-17, Svensk Kärnbränslehantering AB.

Heidbach O, Rajabi M, Reiter K, Ziegler M, 2016. World Stress Map Database Release 2016. GFZ Data Services. doi:10.5880/WSM.2016.001

Hökmark H, Lönnqvist M, Fälth B, 2010. THM-issues in repository rock. Thermal, mechanical, thermo-mechanical and hydro-mechanical evolution of the rock at the Forsmark and Laxemar sites. SKB TR-10-23, Svensk Kärnbränslehantering AB.

Itasca, 2019. 3DEC, version 5.2: Distinct element modeling of jointed and blocky material in 3D. Minneapolis, MN: Itasca Consulting Group, Inc. Available at: <https://www.itascacg.com/software/3dec> [30 April 2019].

Lund B, Schmidt P, Hieronymus C, 2009. Stress evolution and fault stability during the Weichselian glacial cycle. SKB TR-09-15, Svensk Kärnbränslehantering AB.

Martin C D, 2007. Quantifying in-situ stress magnitudes and orientations for Forsmark. Forsmark stage 2.2. SKB R-07-26, Svensk Kärnbränslehantering AB.

SKB, 2008. Site description of Forsmark at completion of the site investigation phase. SDM-Site Forsmark. SKB TR-08-05, Svensk Kärnbränslehantering AB.

Stephansson O, Ljunggren C, Jing L, 1991. Stress measurements and tectonic implications for Fennoscandia. *Tectonophysics* 189, 317–322.

Stephens M B, Simeonov A, 2015. Description of deformation zone model version 2.3, Forsmark. SKB R-14-28, Svensk Kärnbränslehantering AB.

Tonon F, Amadei B, Pan E, Frangopol D M, 2001. Bayesian estimation of rock mass boundary conditions with applications to the AECL underground research laboratory. *International Journal of Rock Mechanics and Mining Sciences* 38, 995–1027.

Tonon F, Amadei B, 2003. Stresses in anisotropic rock masses: an engineering perspective building on geological knowledge. *International Journal of Rock Mechanics and Mining Sciences* 40, 1099–1120.

Valli J, Kuula H, Hakala M, 2011. Modelling of the *in-situ* stress state at the Olkiluoto site, Western Finland. Posiva Working Report 2011-34, Posiva Oy, Finland.

Valli J, Hakala M, Siren T, 2016. Stress-Geology Interaction Modelling at Olkiluoto. In Proceedings of the 7th International Symposium on In-Situ Rock Stress, Tampere, Finland, 10–12 May 2016. International Society for Rock Mechanics and Rock Engineering, 352–361.

Simulation Phase 1 – DZ total shear displacements

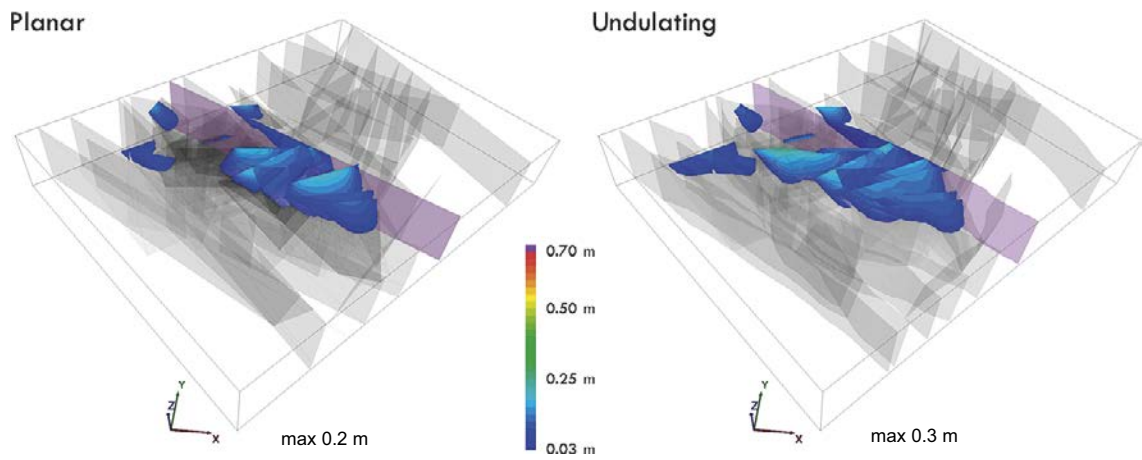


Figure A1a-1. Case 1-1, DZ total shear displacements.

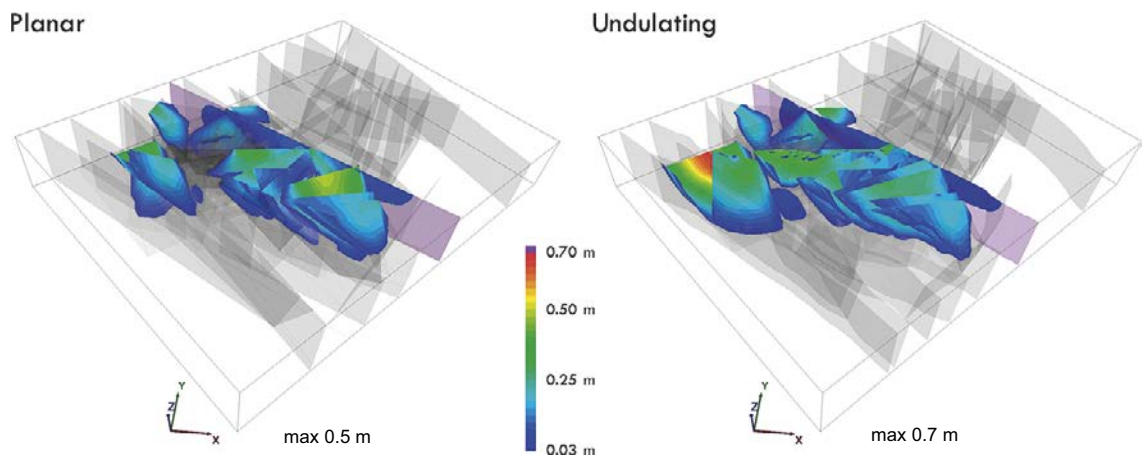


Figure A1a-2. Case 1-2, DZ total shear displacements.

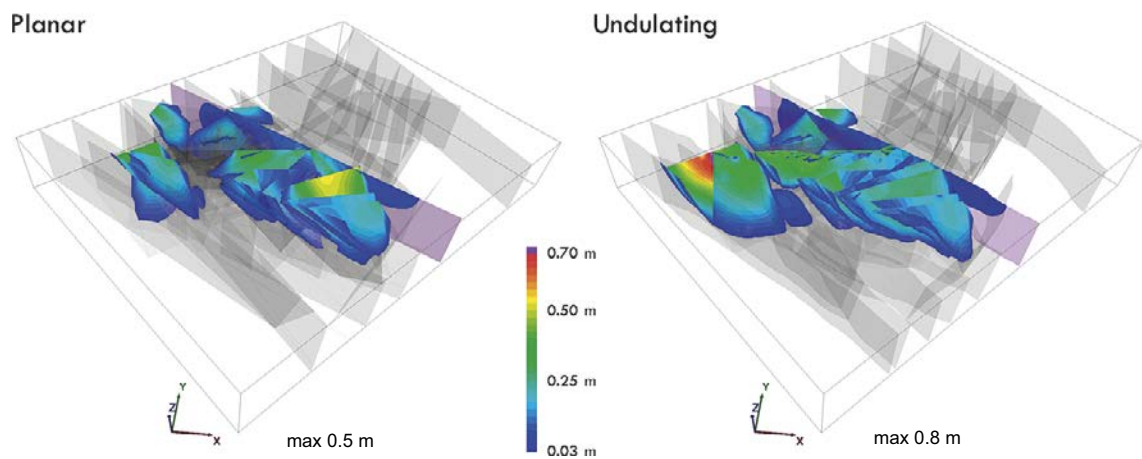


Figure A1a-3. Case 1-3, DZ total shear displacements.

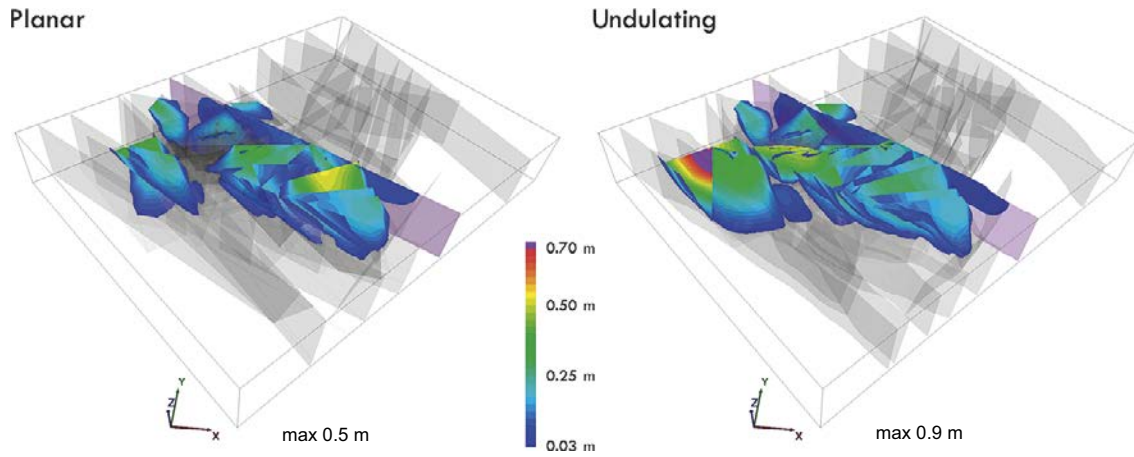


Figure A1a-4. Case 1-4, DZ total shear displacements.

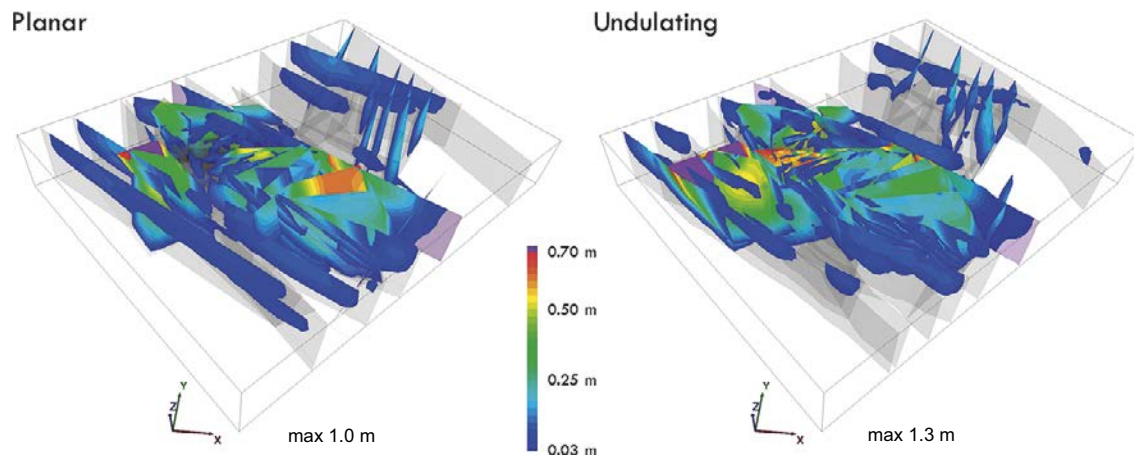


Figure A1a-5. Case 1-5, DZ total shear displacements.

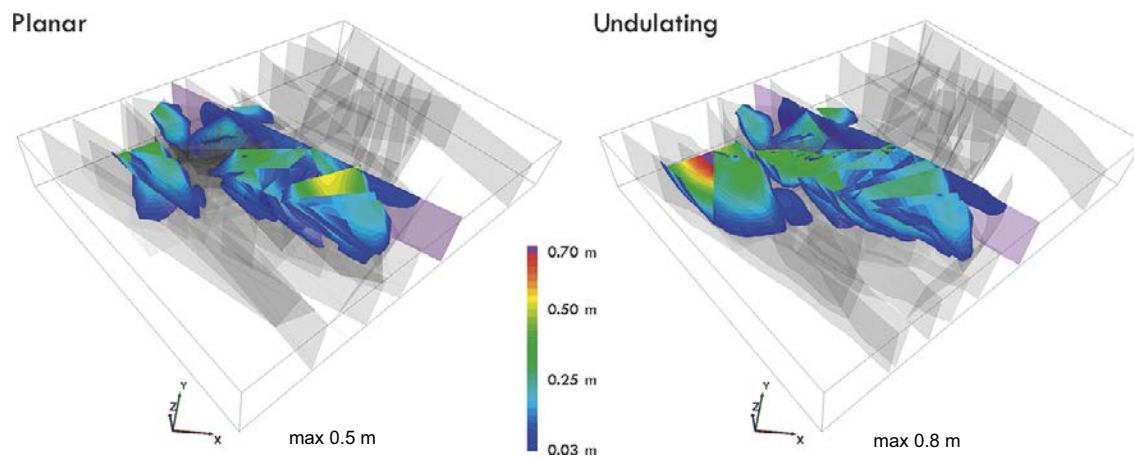


Figure A1a-6. Case 1-6, DZ total shear displacements.

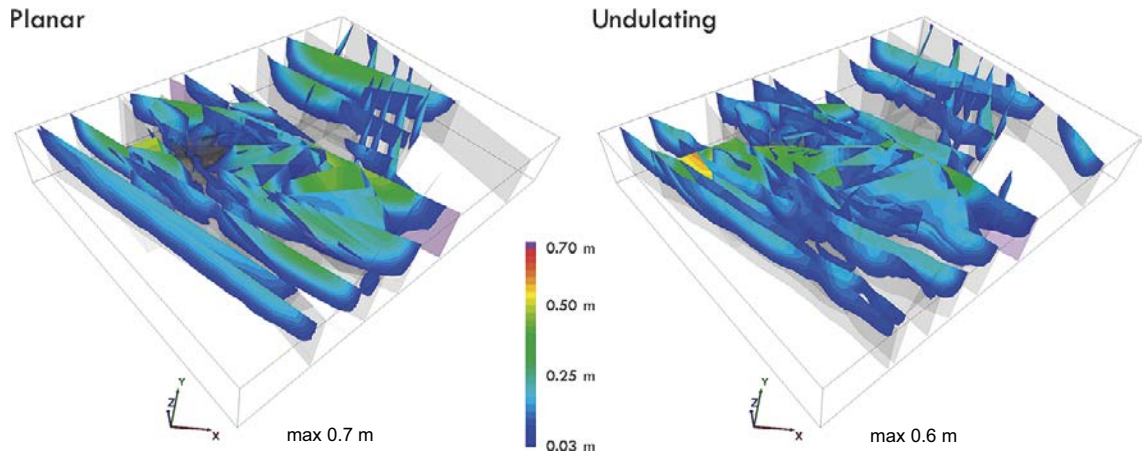


Figure A1a-7. Case 1-7, DZ total shear displacements.

Simulation Phase 2 – DZ total shear displacements

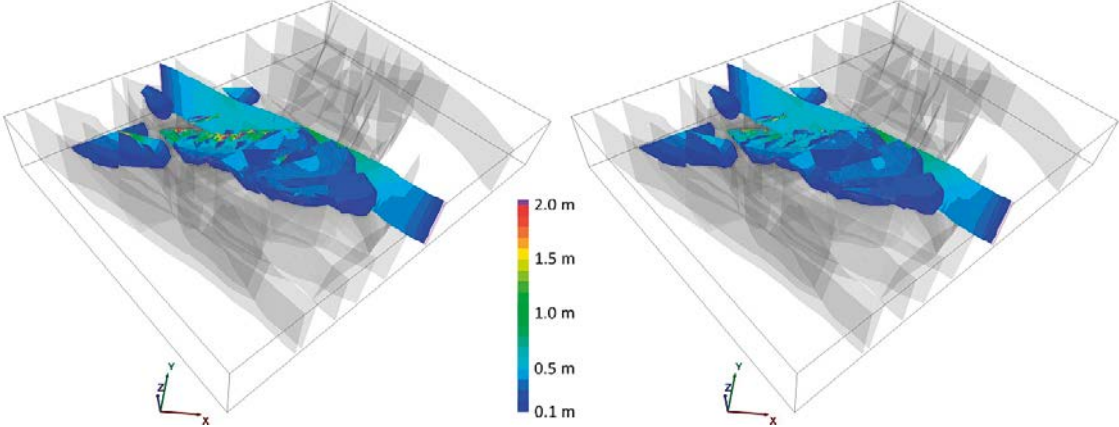


Figure A1b-1. Case 2-1 (left) and Case 2-2 (right), DZ total shear displacements.

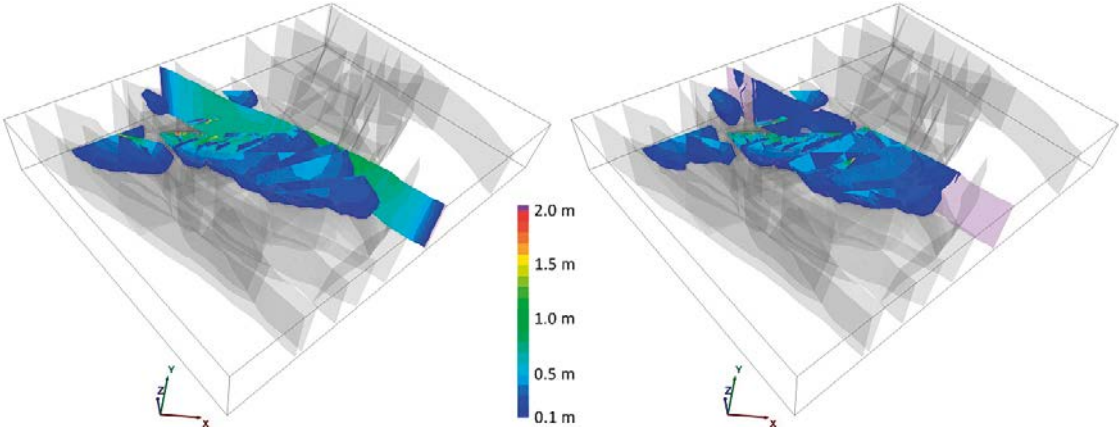


Figure A1b-2. Case 2-3 (left) and Case 2-4 (right), DZ total shear displacements.

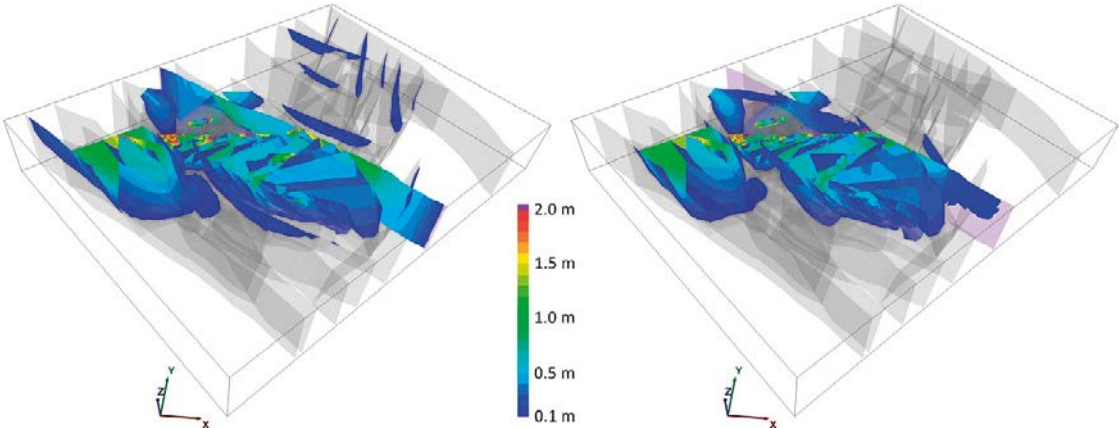


Figure A1b-3. Case 2-5 (left) and Case 2-6 (right), DZ total shear displacements.

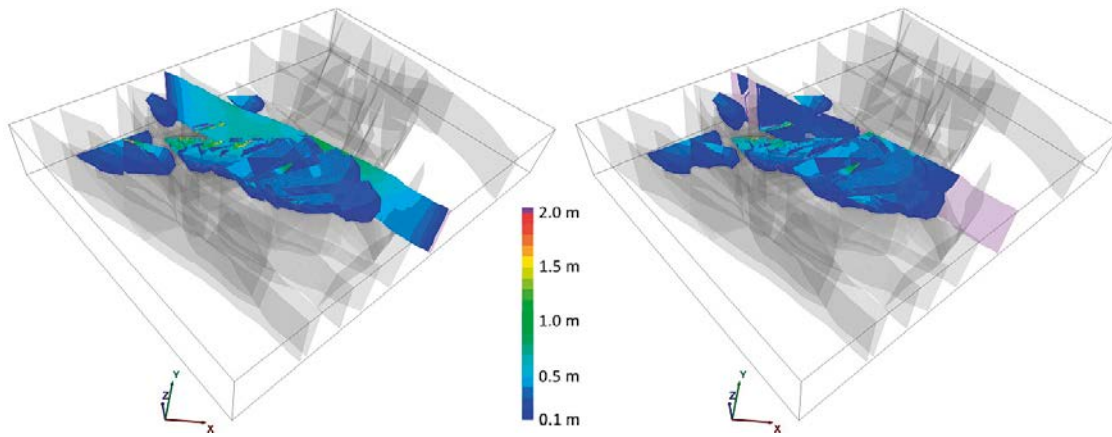


Figure A1b-4. Case 2-7 (left) and Case 2-8 (right), DZ total shear displacements.

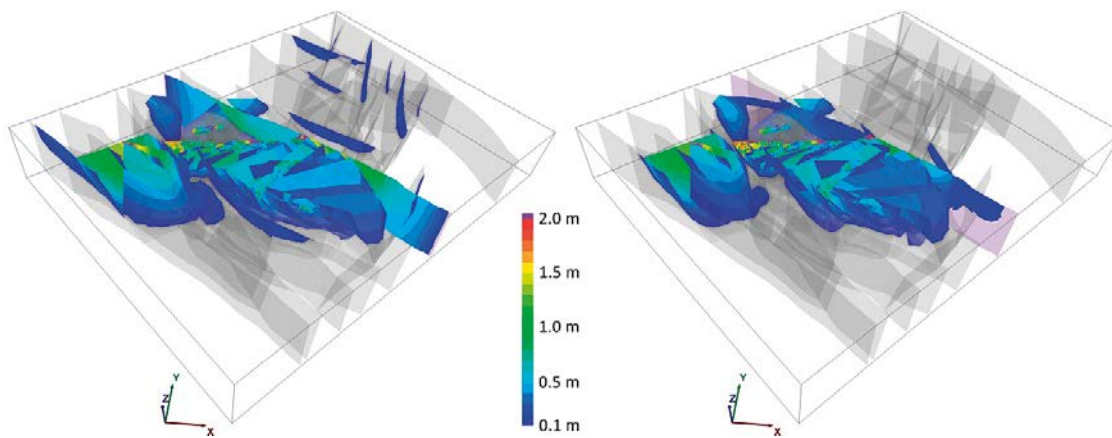


Figure A1b-5. Case 2-9 (left) and Case 2-10 (right), DZ total shear displacements.

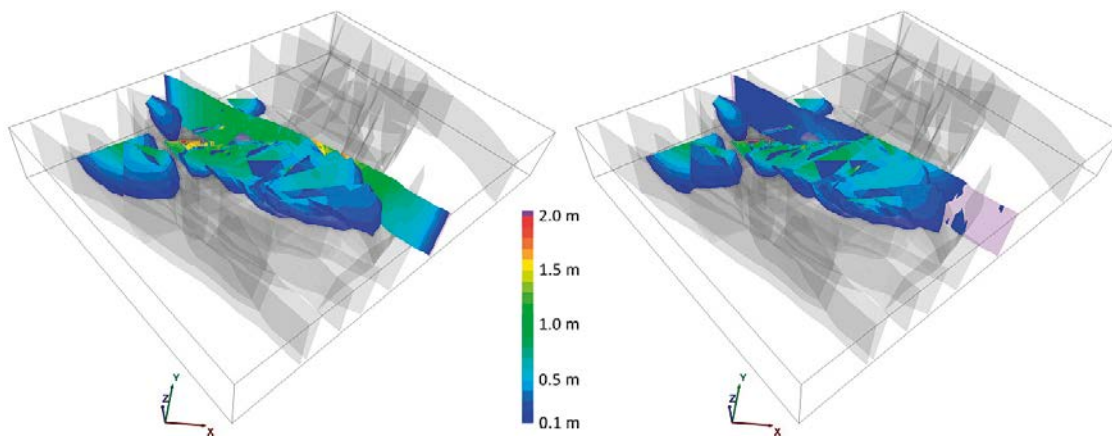


Figure A1b-6. Case 2-11 (left) and Case 2-12 (right), DZ total shear displacements.

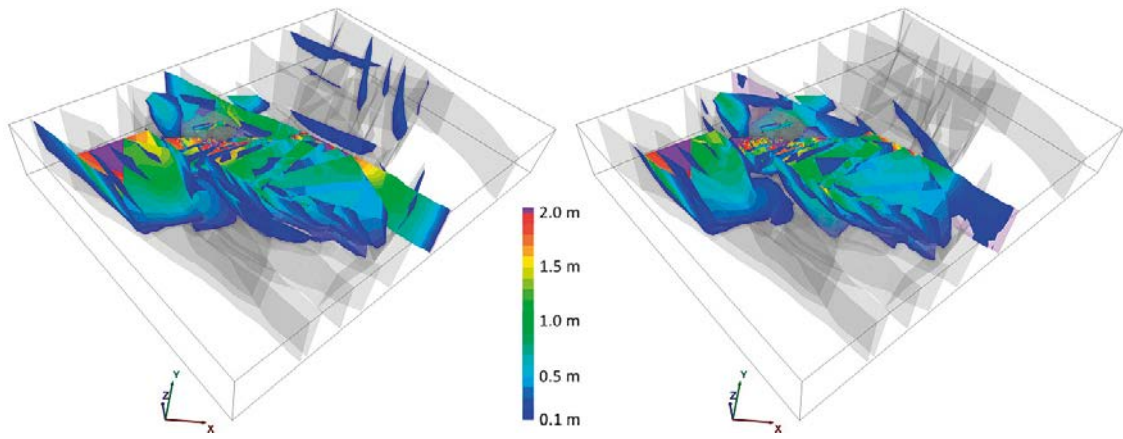


Figure A1b-7. Case 2-13 (left) and Case 2-14 (right), DZ total shear displacements.

Simulation Phase 1 – lower hemisphere equal angle projections of sheared zones

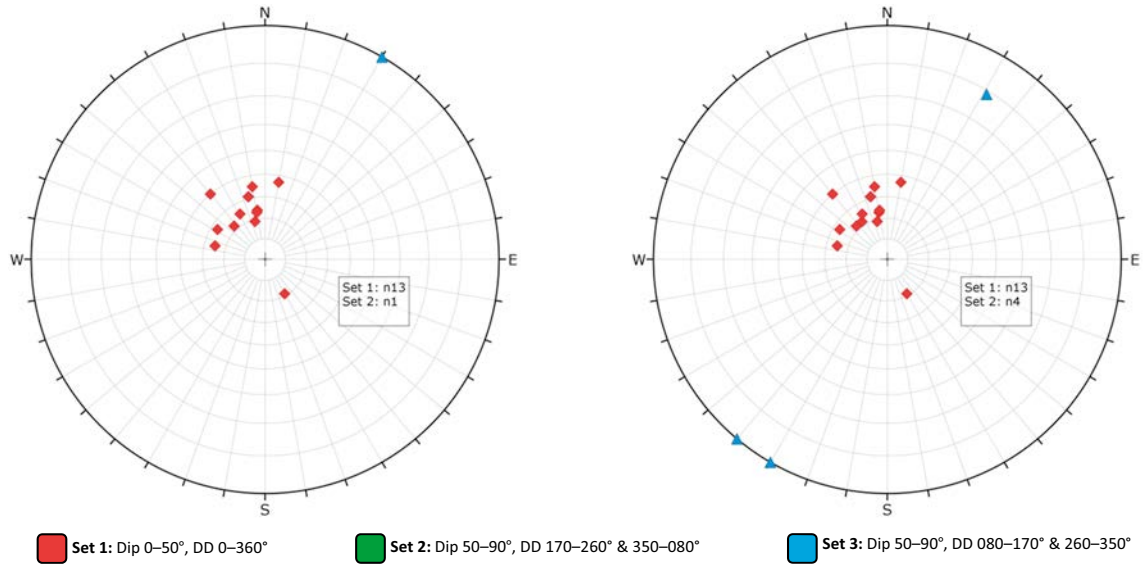


Figure A2a-1. Planar Case 1-1 (left) and Undulating Case 1-1 (right). Lower hemisphere equal angle projections of sheared zones.

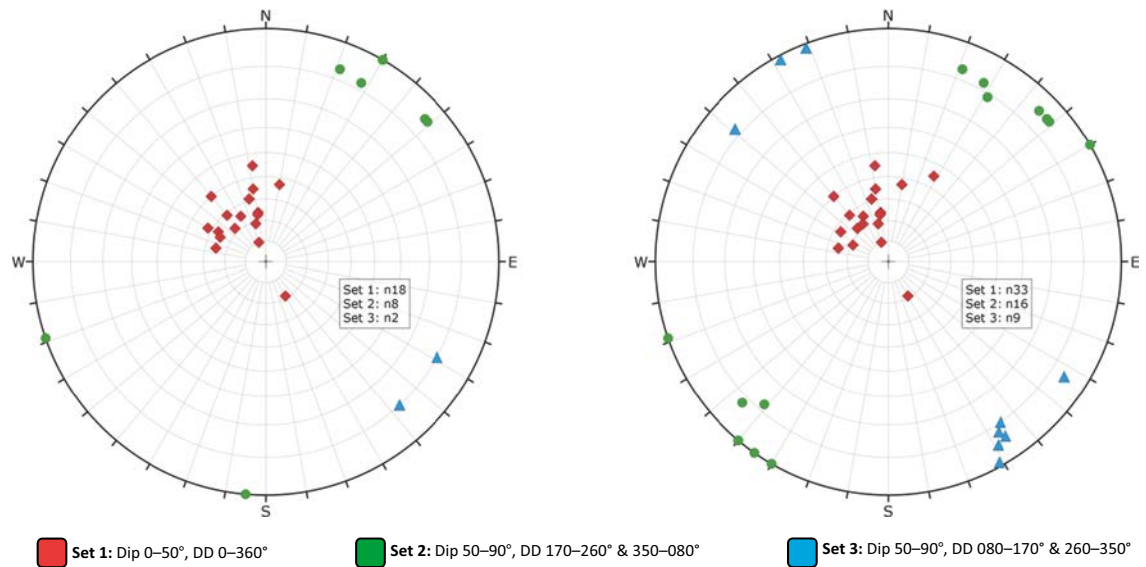


Figure A2a-2. Planar Case 1-2 (left) and Undulating Case 1-2 (right). Lower hemisphere equal angle projections of sheared zones.

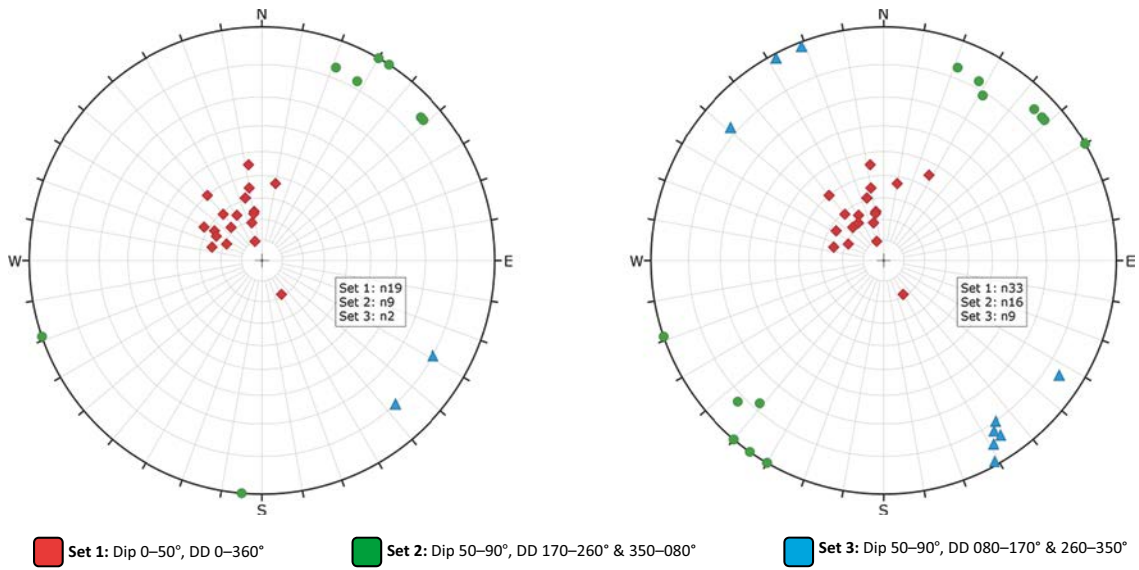


Figure A2a-3. Planar Case 1-3 (left) and Undulating Case 1-3 (right). Lower hemisphere equal angle projections of sheared zones.

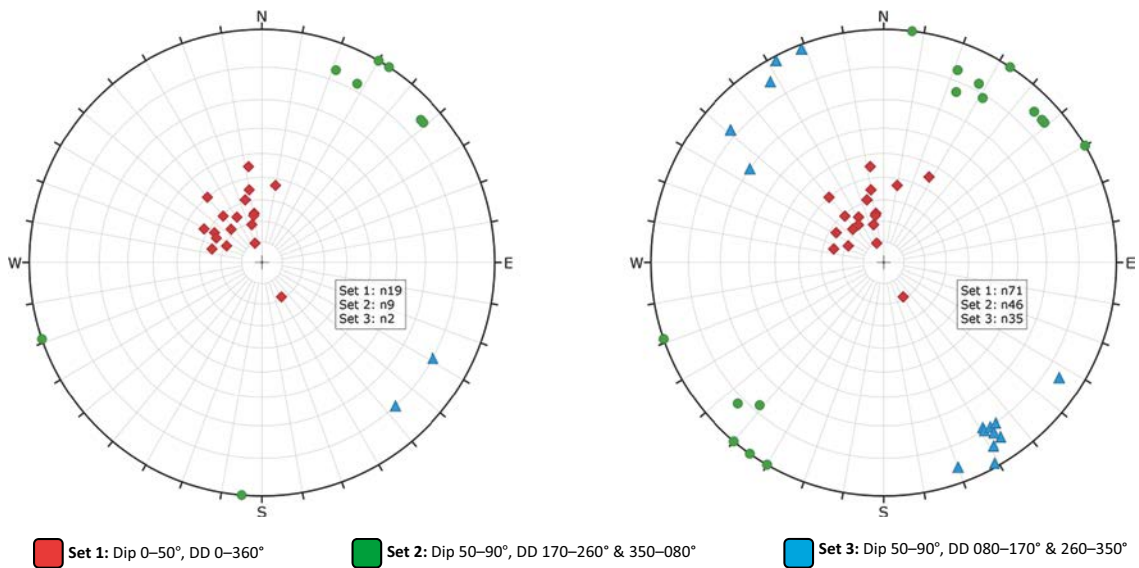


Figure A2a-4. Planar Case 1-4 (left) and Undulating Case 1-4 (right). Lower hemisphere equal angle projections of sheared zones.

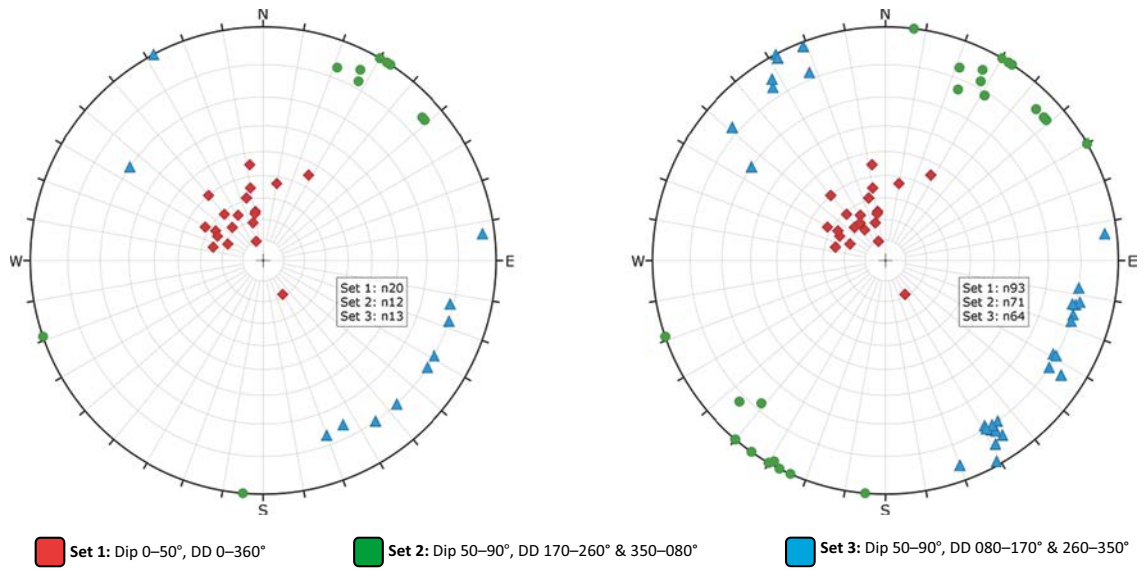


Figure A2a-5. Planar Case 1-5 (left) and Undulating Case 1-5 (right). Lower hemisphere equal angle projections of sheared zones.

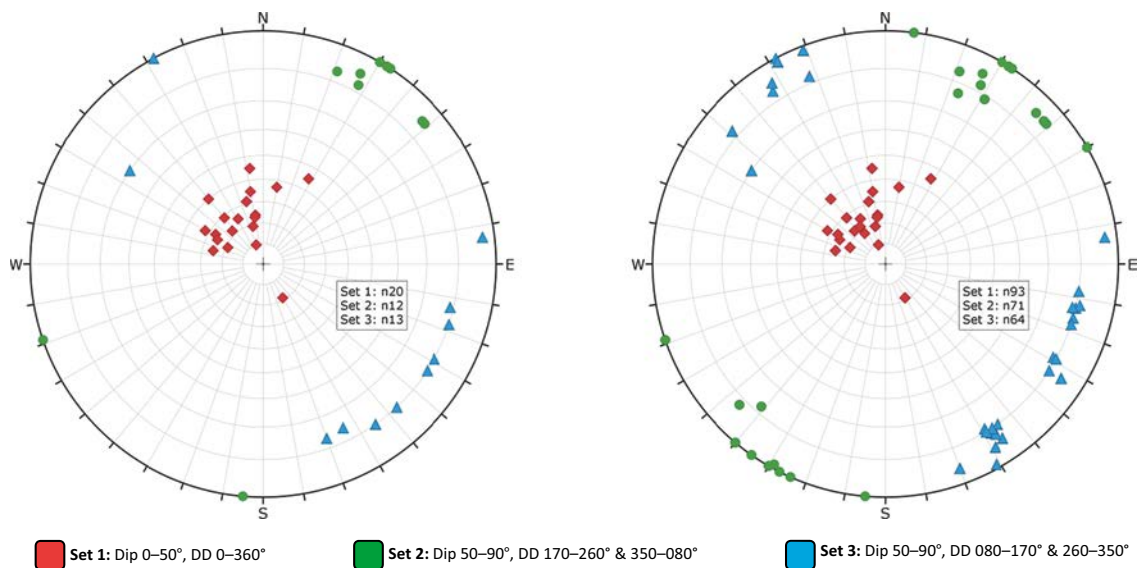


Figure A2a-6. Planar Case 1-6 (left) and Undulating Case 1-6 (right). Lower hemisphere equal angle projections of sheared zones.

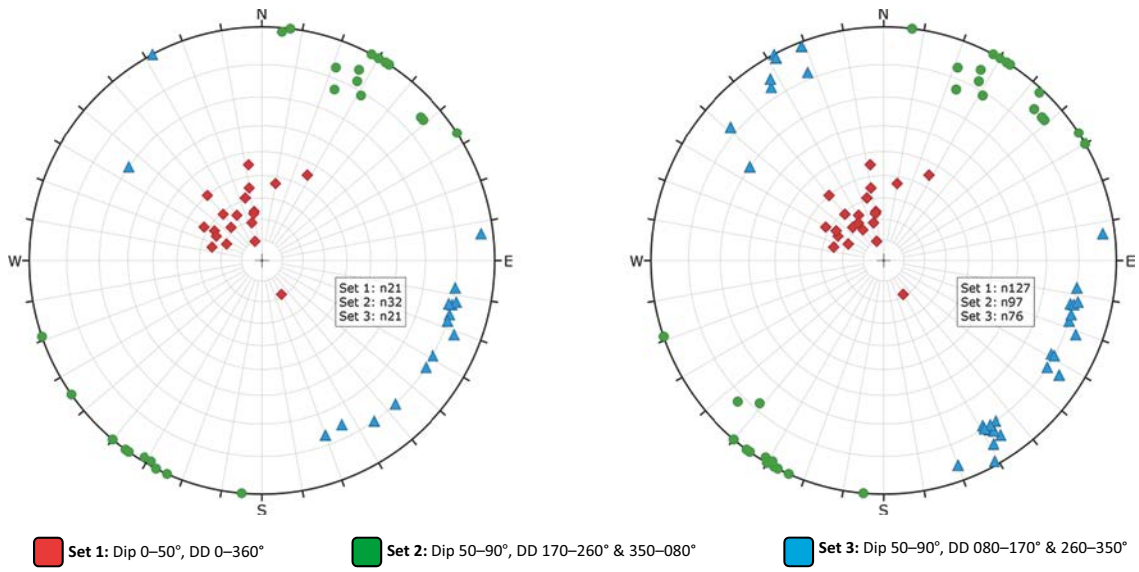


Figure A2a-7. Planar Case 1-7 (left) and Undulating Case 1-7 (right). Lower hemisphere equal angle projections of sheared zones.

Simulation Phase 2 – lower hemisphere equal angle projections of sheared zones

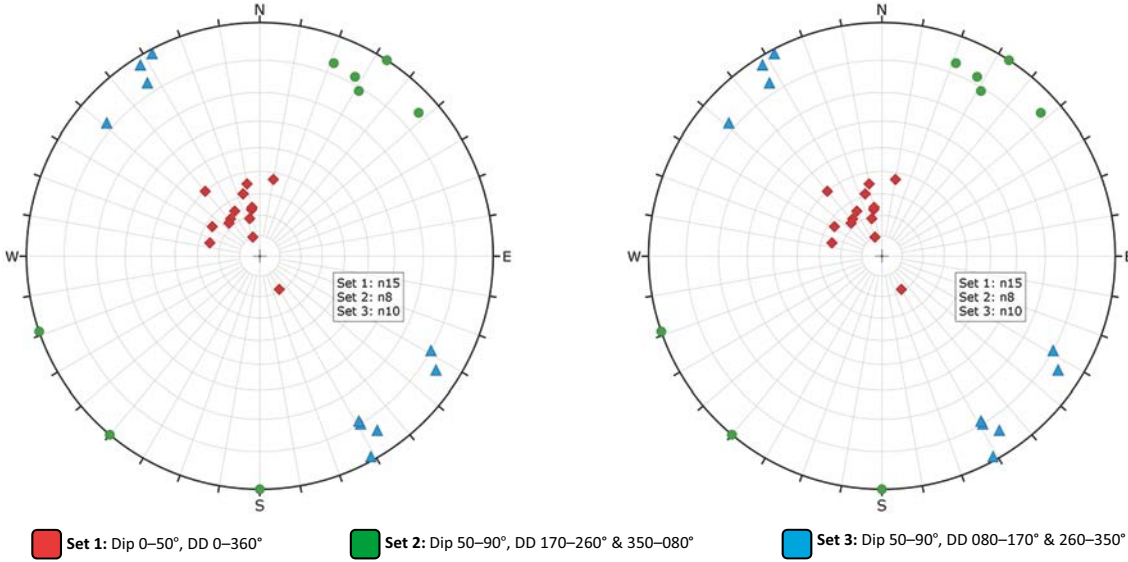


Figure A2b-1. Case 2-1 (left) and Case 2-2 (right). Lower hemisphere equal angle projections of sheared zones.

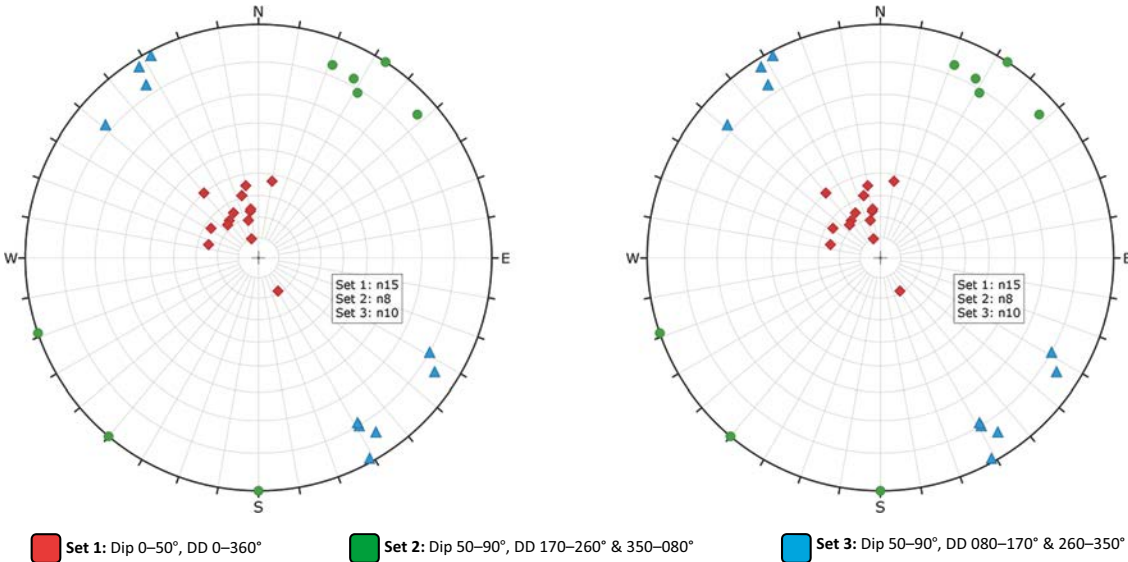


Figure A2b-2. Case 2-3 (left) and Case 2-4 (right). Lower hemisphere equal angle projections of sheared zones.

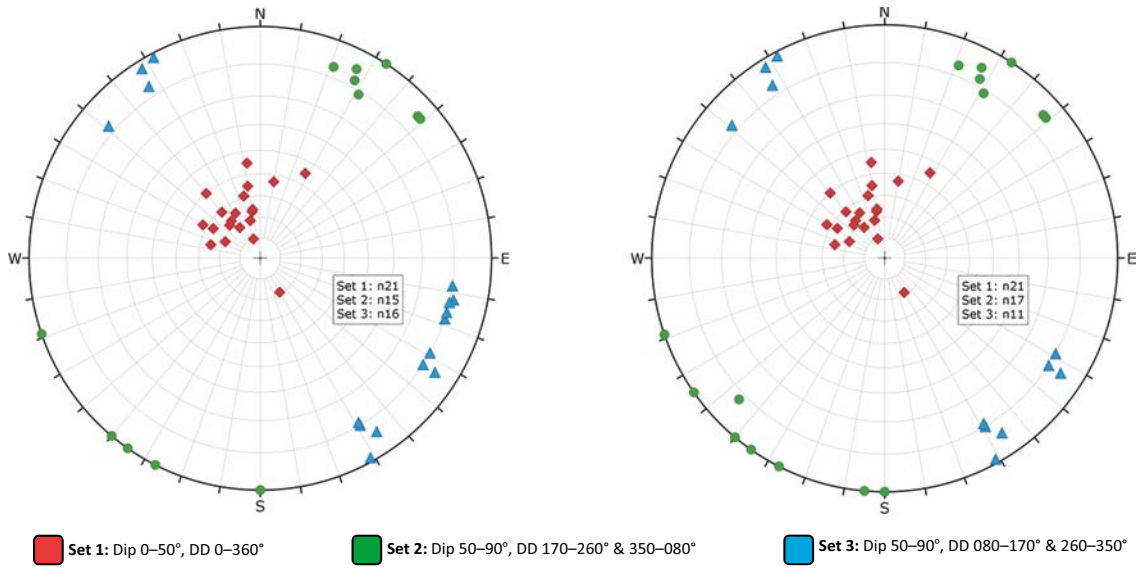


Figure A2b-3. Case 2-5 (left) and Case 2-6 (right). Lower hemisphere equal angle projections of sheared zones.

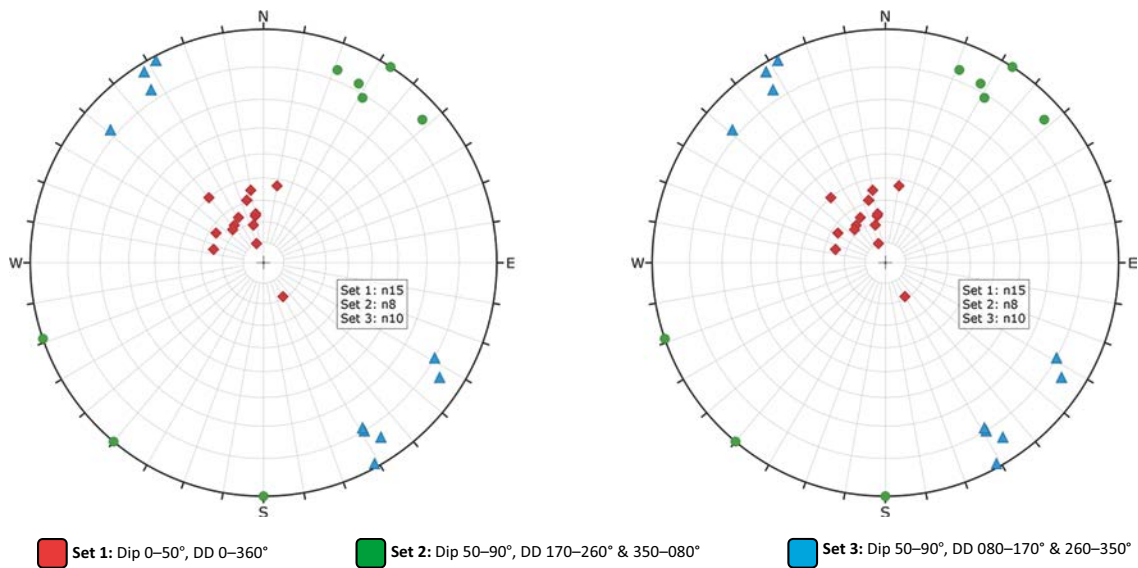


Figure A2b-4. Case 2-7 (left) and Case 2-8 (right). Lower hemisphere equal angle projections of sheared zones.

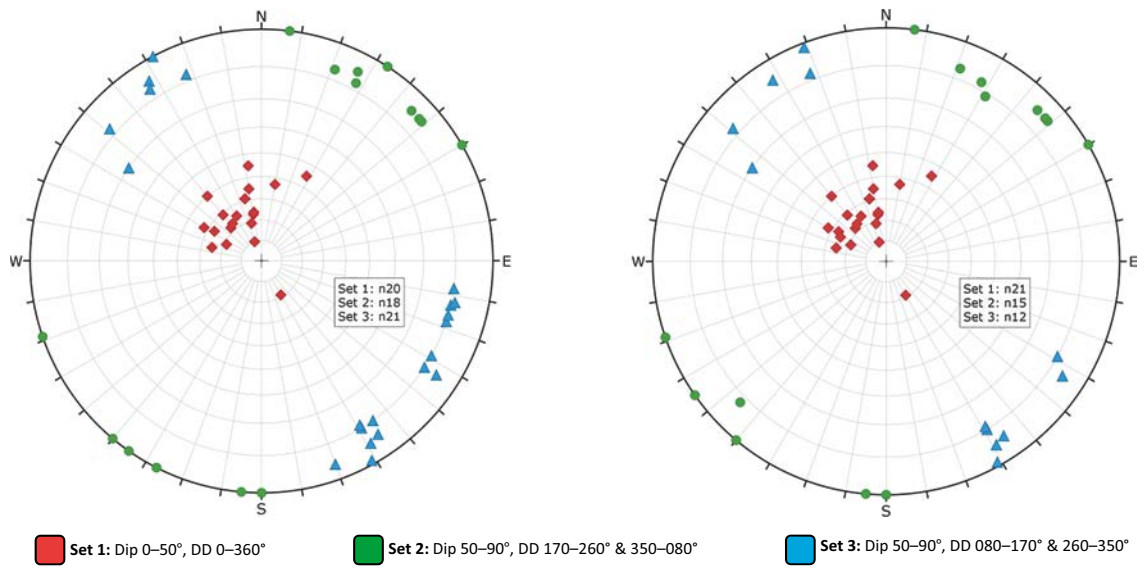


Figure A2b-5. Case 2-9 (left) and Case 2-10 (right). Lower hemisphere equal angle projections of sheared zones.

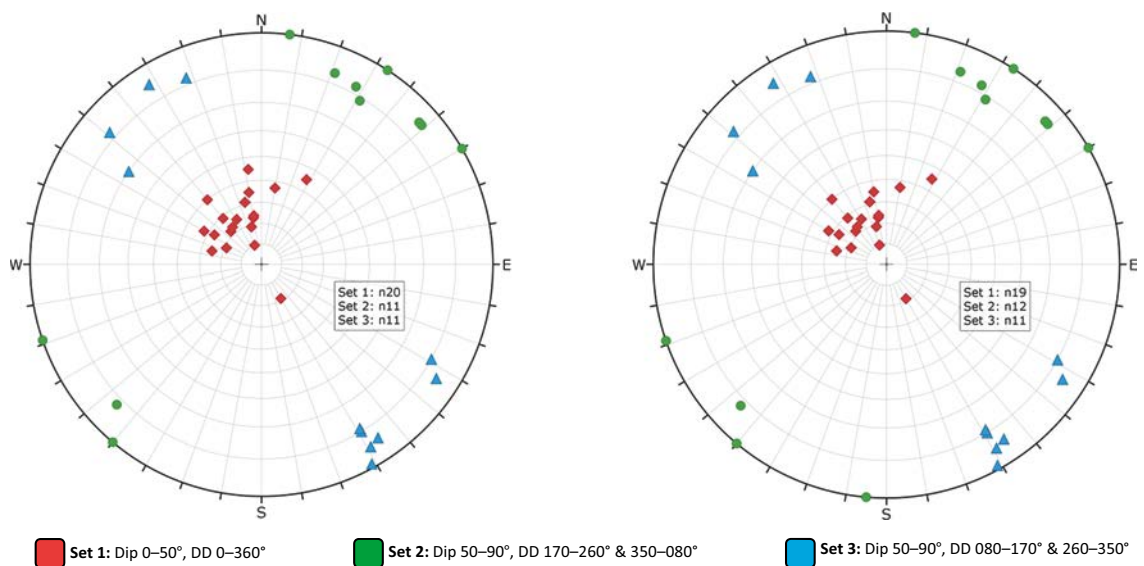


Figure A2b-6. Case 2-11 (left) and Case 2-12 (right). Lower hemisphere equal angle projections of sheared zones.

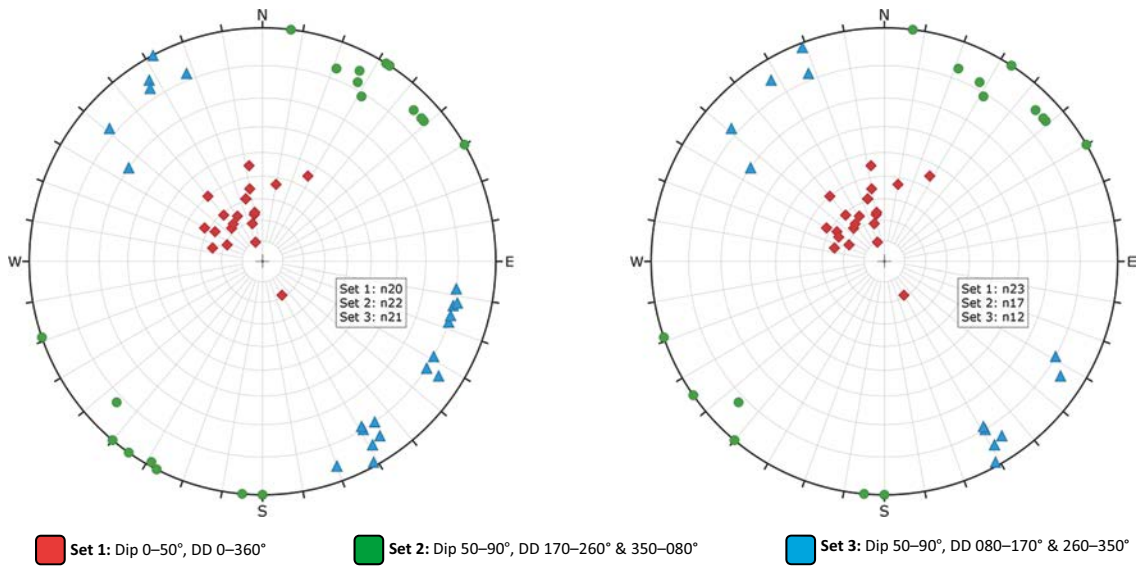


Figure A2b-7. Case 2-13 (left) and Case 2-14 (right). Lower hemisphere equal angle projections of sheared zones.

Simulation Phase 1 – change in σ_1 magnitude

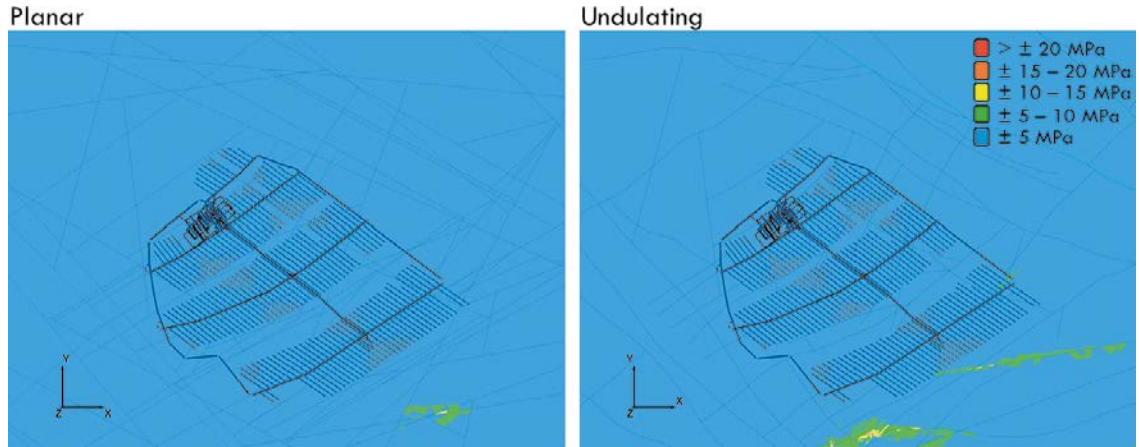


Figure A3a-1. Case 1-1, Change in σ_1 magnitude, horizontal section from repository level.

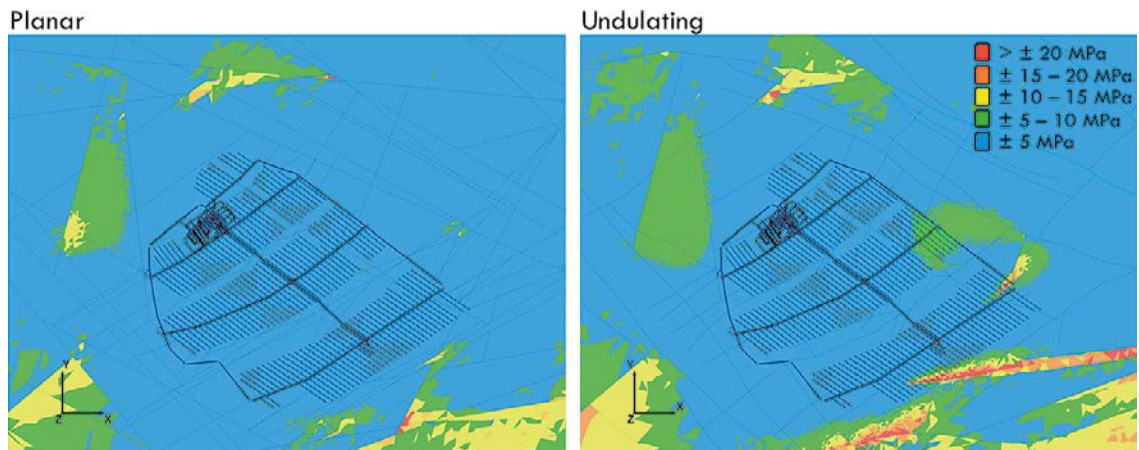


Figure A3a-2. Case 1-2, Change in σ_1 magnitude, horizontal section from repository level.

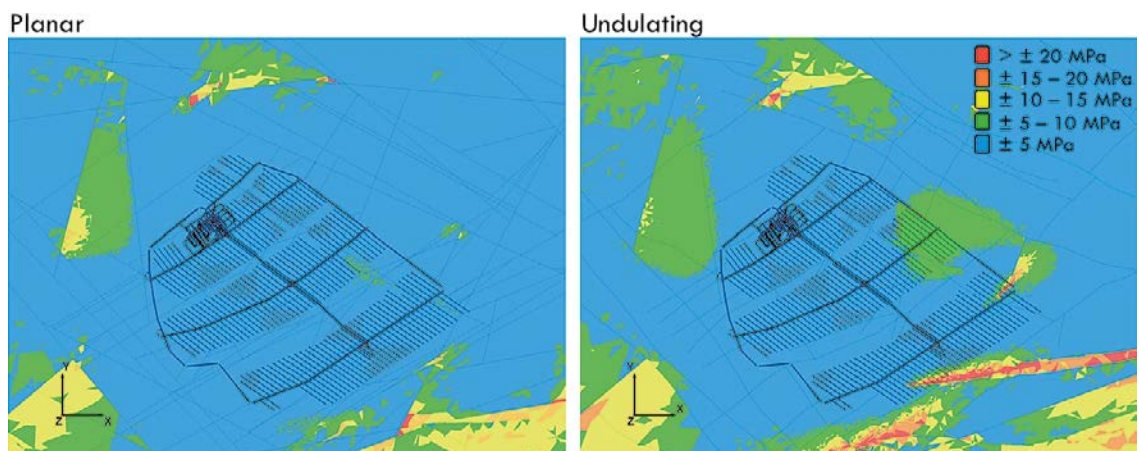


Figure A3a-3. Case 1-3, Change in σ_1 magnitude, horizontal section from repository level.

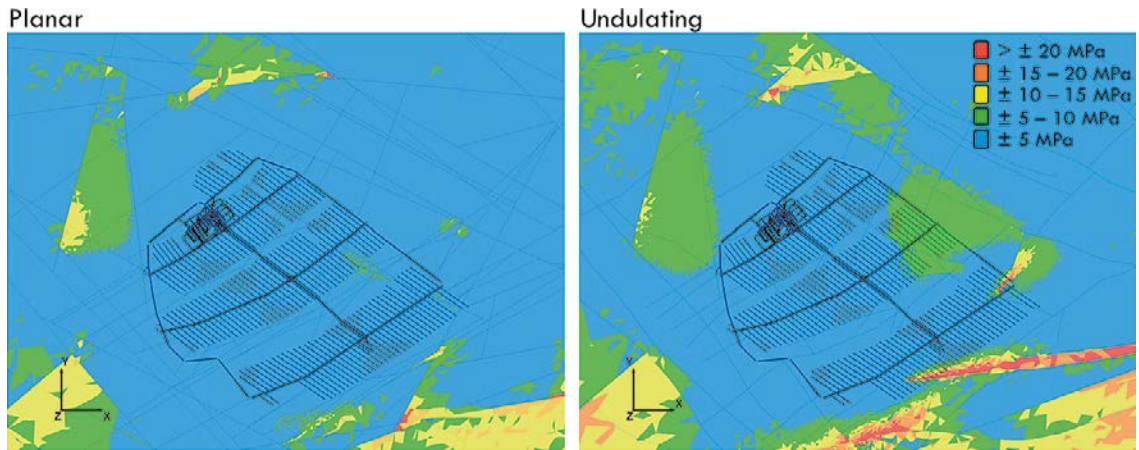


Figure A3a-4. Case 1-4, Change in σ_1 magnitude, horizontal section from repository level.

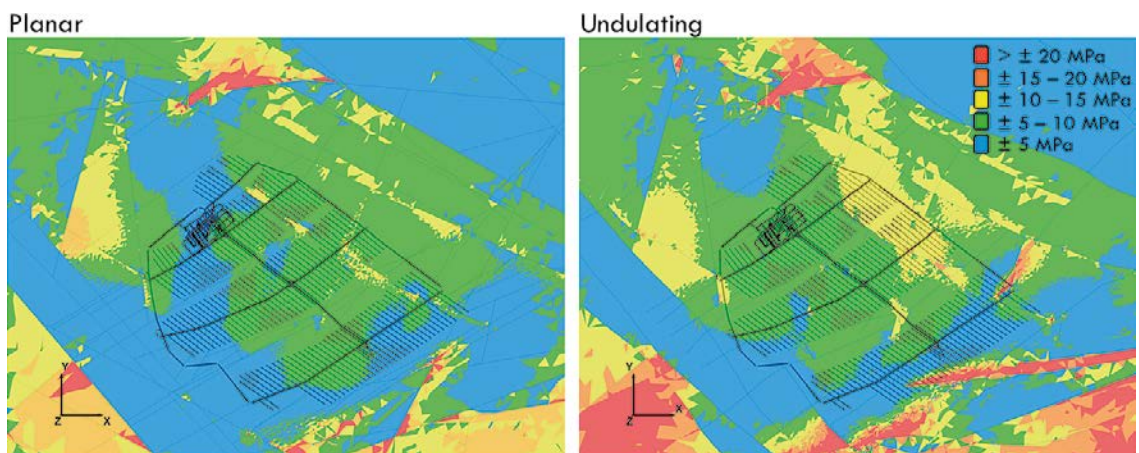


Figure A3a-5. Case 1-5, Change in σ_1 magnitude, horizontal section from repository level.

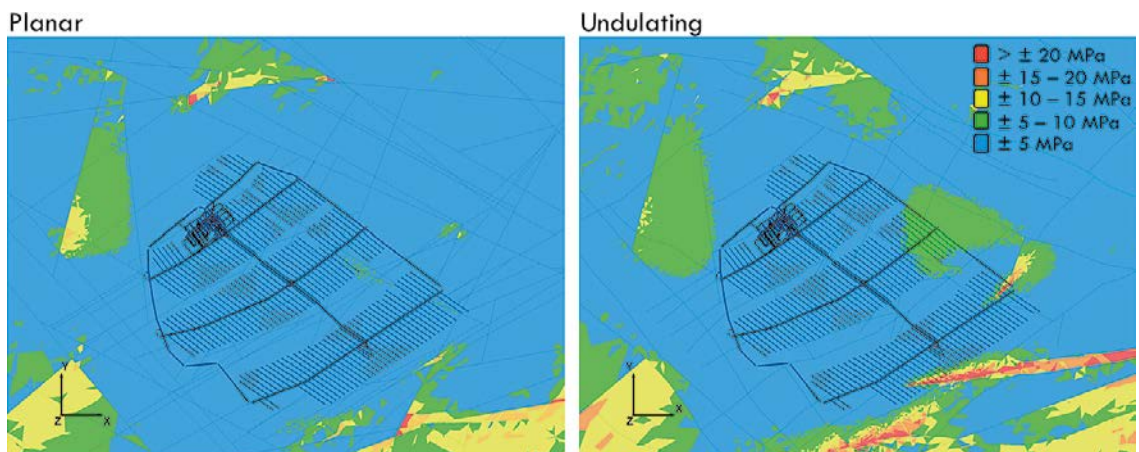


Figure A3a-6. Case 1-6, Change in σ_1 magnitude, horizontal section from repository level.

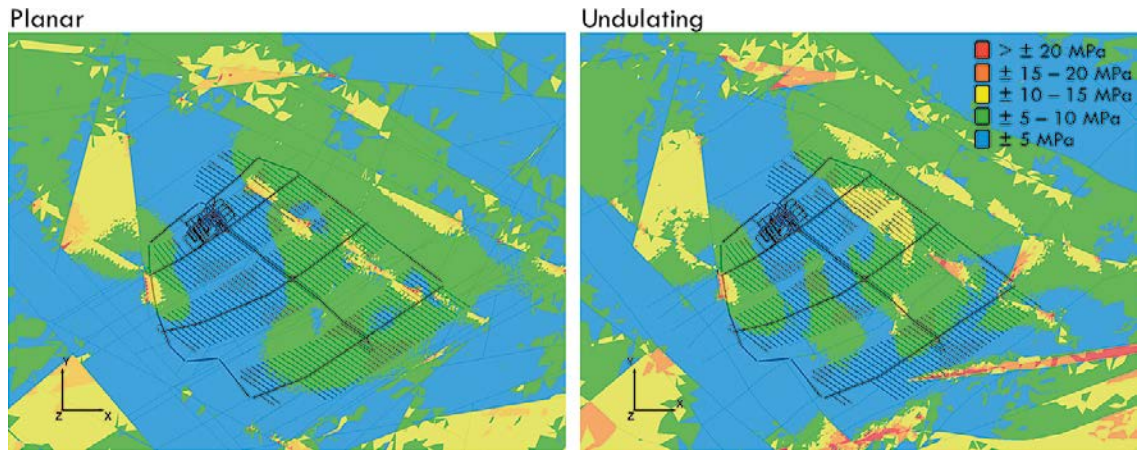


Figure A3a-7. Case 1-7, change in σ_1 magnitude, horizontal section from repository level.

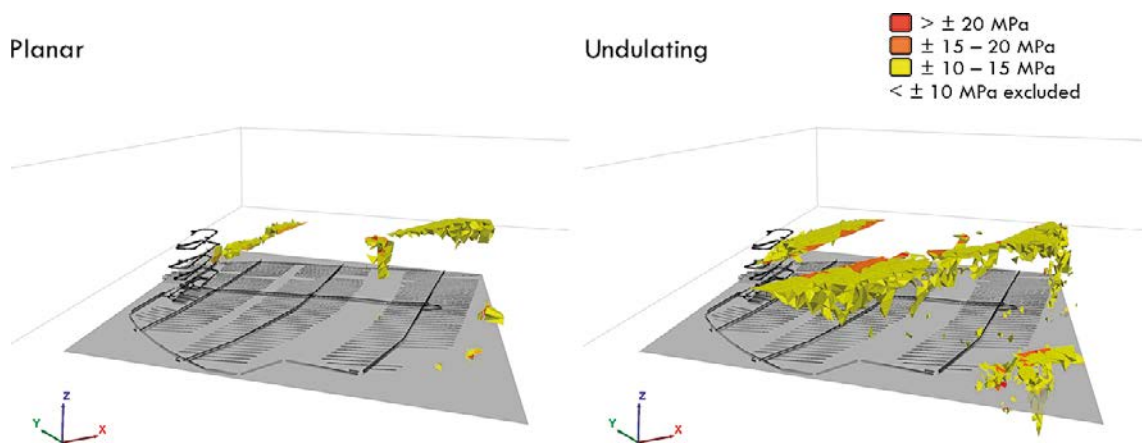


Figure A3a-8. Change in σ_1 magnitude, isometric view, Case 1-1.

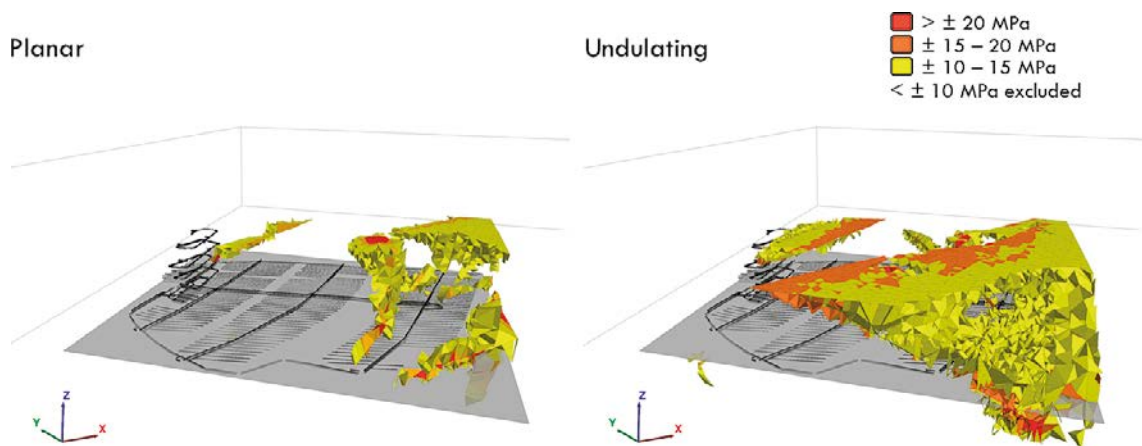
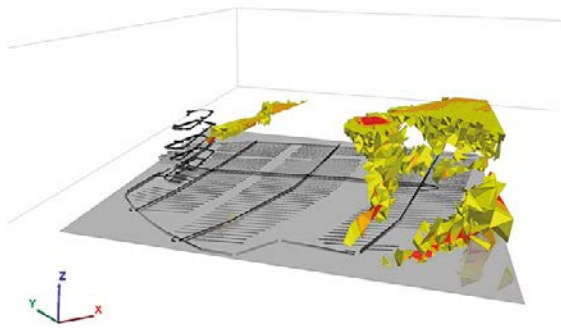


Figure A3a-9. Change in σ_1 magnitude, isometric view, Case 1-2.

Planar



Undulating

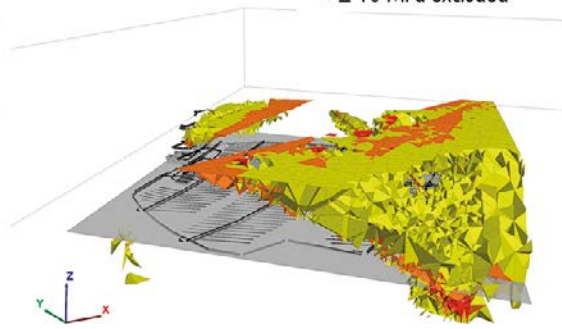
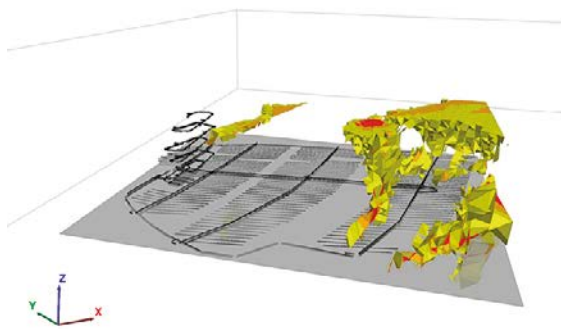


Figure A3a-10. Change in σ_1 magnitude, isometric view, Case 1-3.

Planar



Undulating

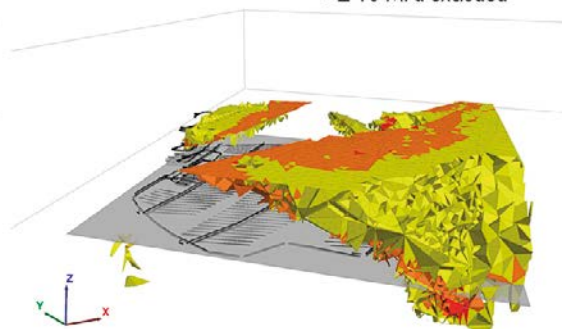
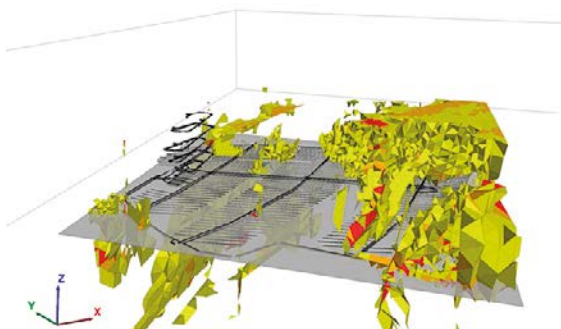


Figure A3a-11. Change in σ_1 magnitude, isometric view, Case 1-4.

Planar



Undulating

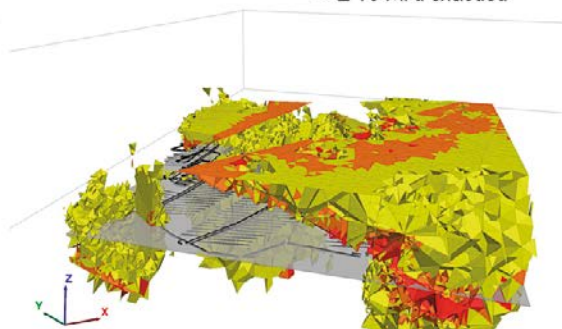


Figure A3a-12. Change in σ_1 magnitude, isometric view, Case 1-5.

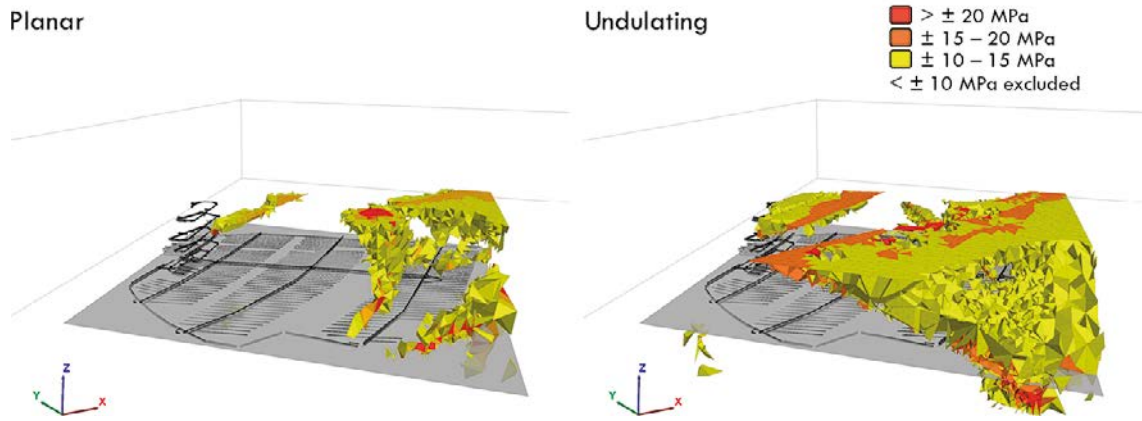


Figure A3a-13. Change in σ_1 magnitude, isometric view, Case 1-6.

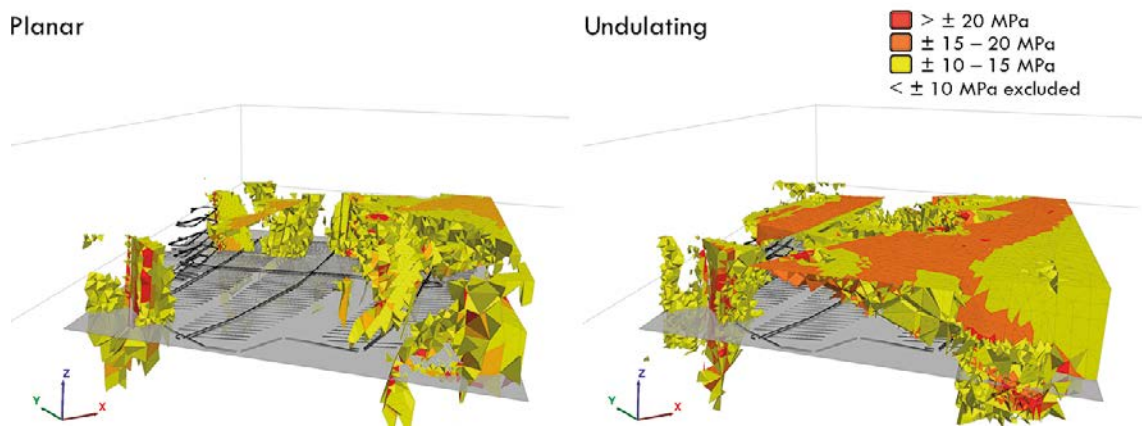


Figure A3a-14. Change in σ_1 magnitude, isometric view, Case 1-7.

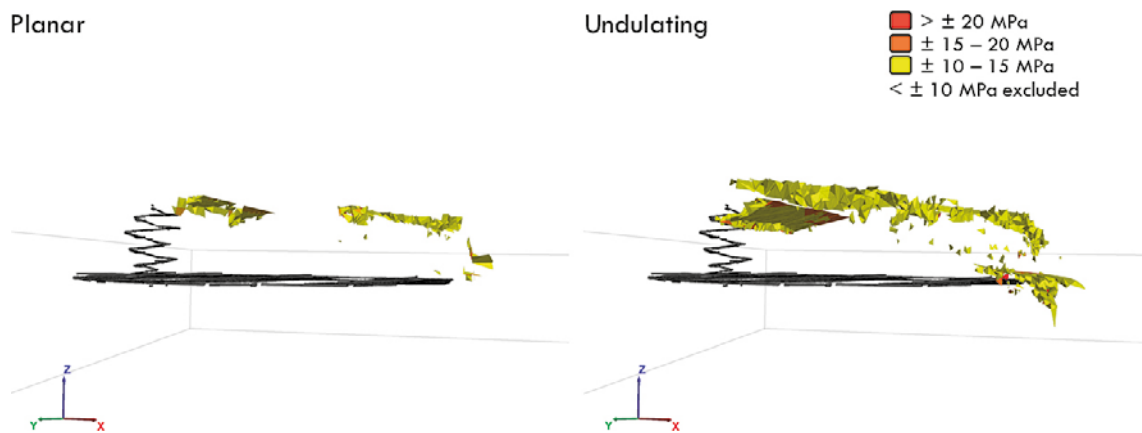
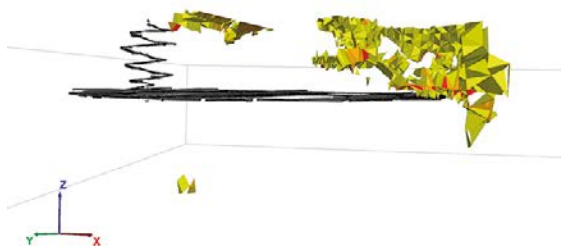


Figure A3a-15. Change in σ_1 magnitude, view from repository level, Case 1-1.

Planar



Undulating

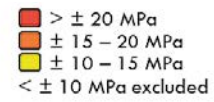
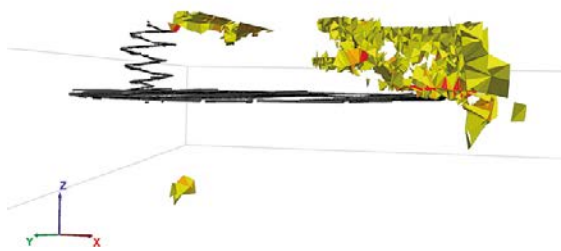


Figure A3a-16. Change in σ_1 magnitude, view from repository level, Case 1-2.

Planar



Undulating

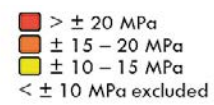
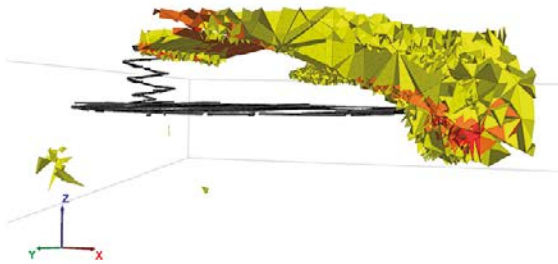
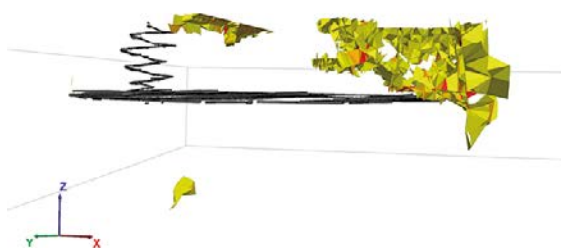


Figure A3a-17. Change in σ_1 magnitude, view from repository level, Case 1-3.

Planar



Undulating

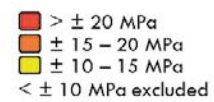
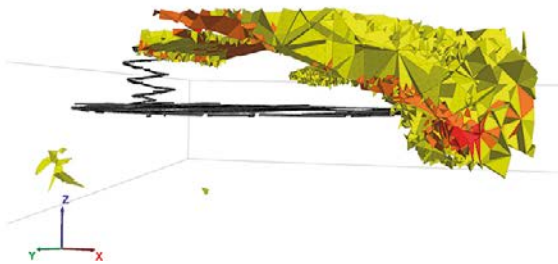


Figure A3a-18. Change in σ_1 magnitude, view from repository level, Case 1-4.

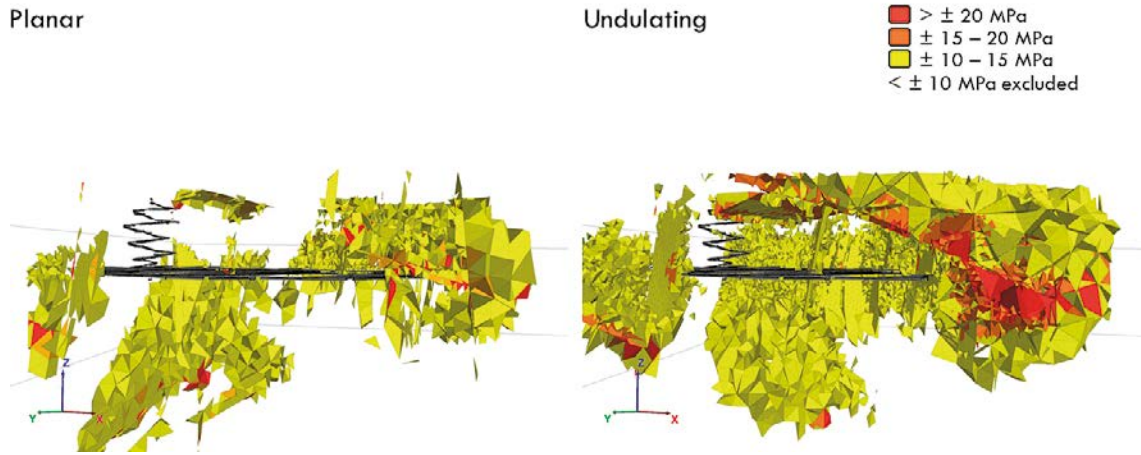


Figure A3a-19. Change in σ_1 magnitude, view from repository level, Case 1-5.

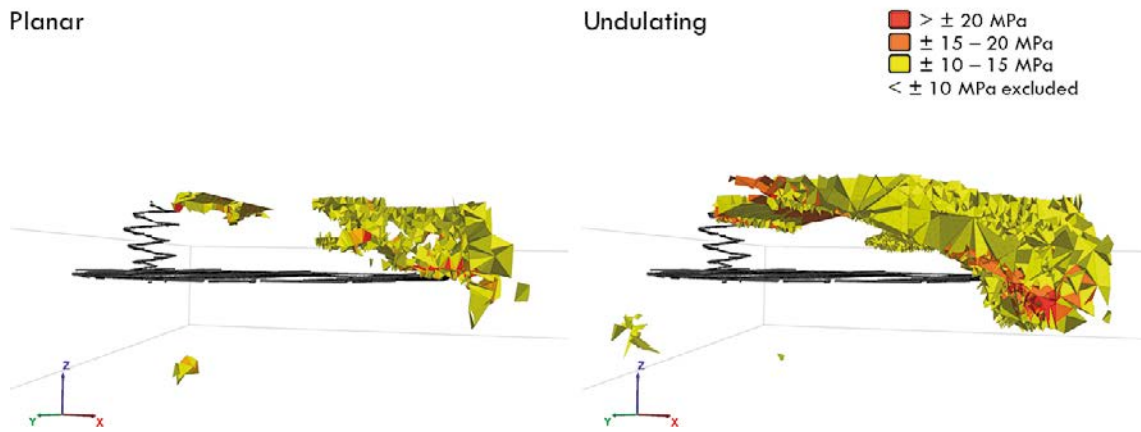


Figure A3a-20. Change in σ_1 magnitude, view from repository level, Case 1-6.

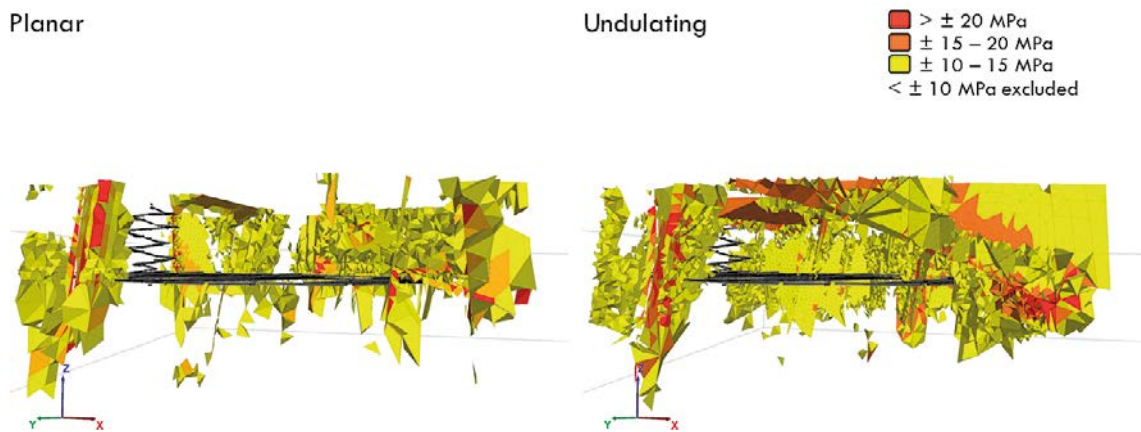


Figure A3a-21. Change in σ_1 magnitude, view from repository level, Case 1-7.

Simulation Phase 2 – change in σ_1 magnitude

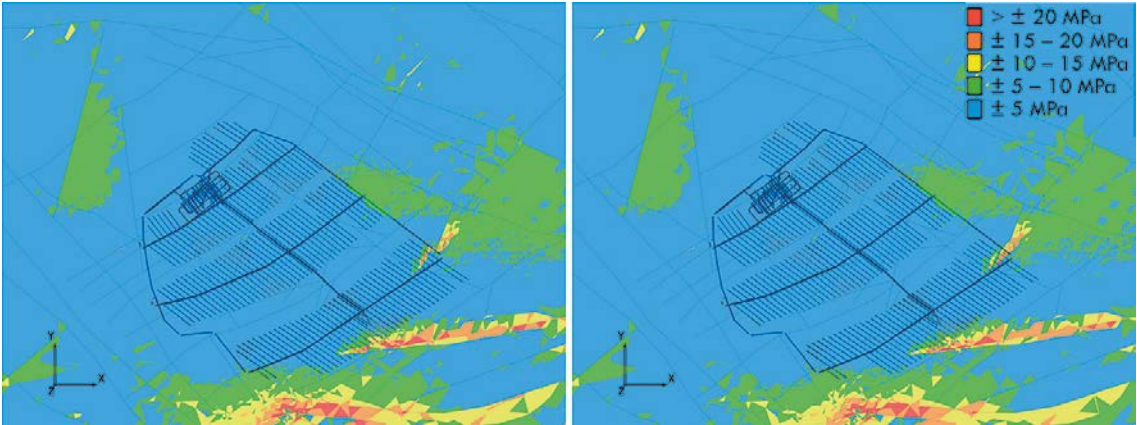


Figure A3b-1. Case 2-1 (left) and Case 2-2 (right). Change in σ_1 magnitude, horizontal section from repository level.

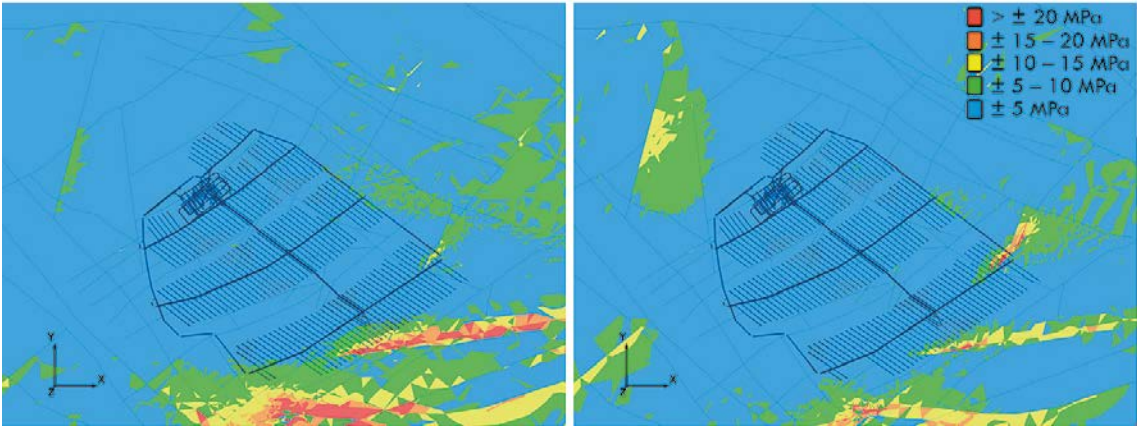


Figure A3b-2. Case 2-3 (left) and Case 2-4 (right). Change in σ_1 magnitude, horizontal section from repository level.

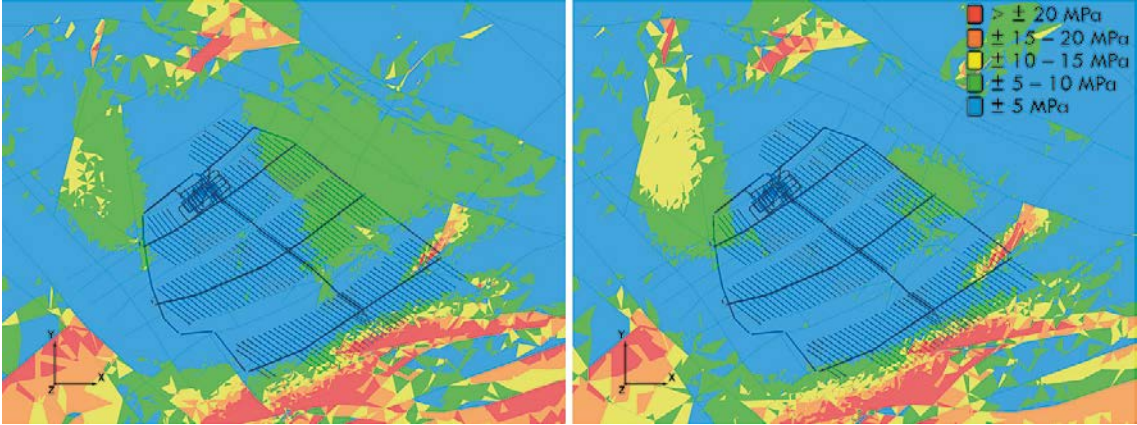


Figure A3b-3. Case 2-5 (left) and Case 2-6 (right). Change in σ_1 magnitude, horizontal section from repository level.

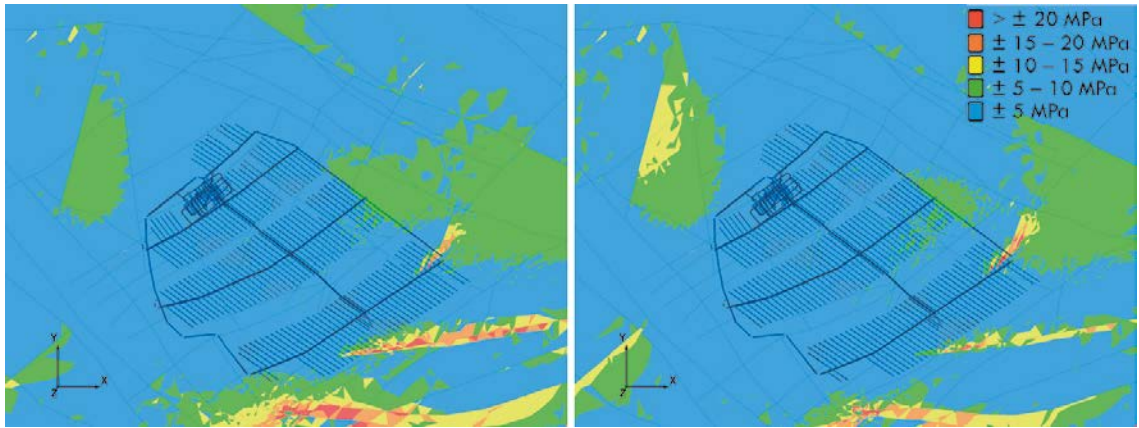


Figure A3b-4. Case 2-7 (left) and Case 2-8 (right). Change in σ_1 magnitude, horizontal section from repository level.

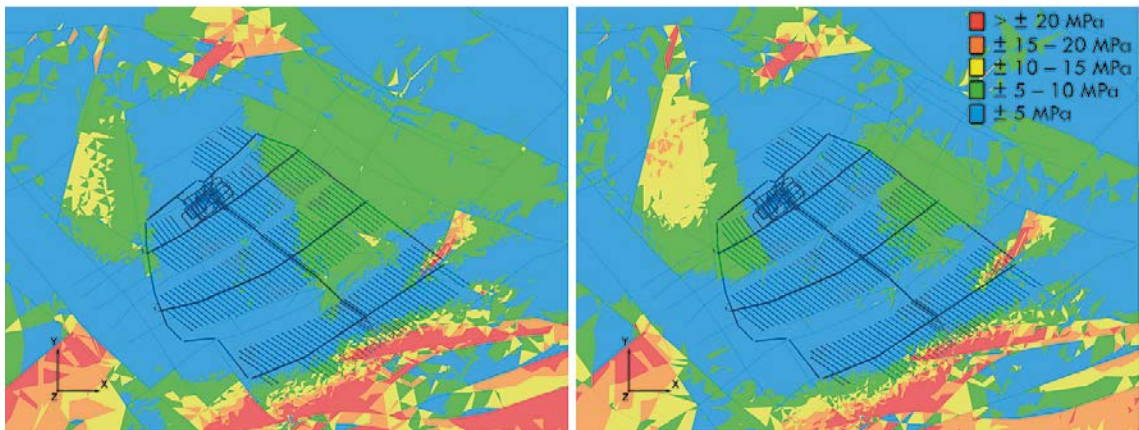


Figure A3b-5. Case 2-9 (left) and Case 2-10 (right). Change in σ_1 magnitude, horizontal section from repository level.

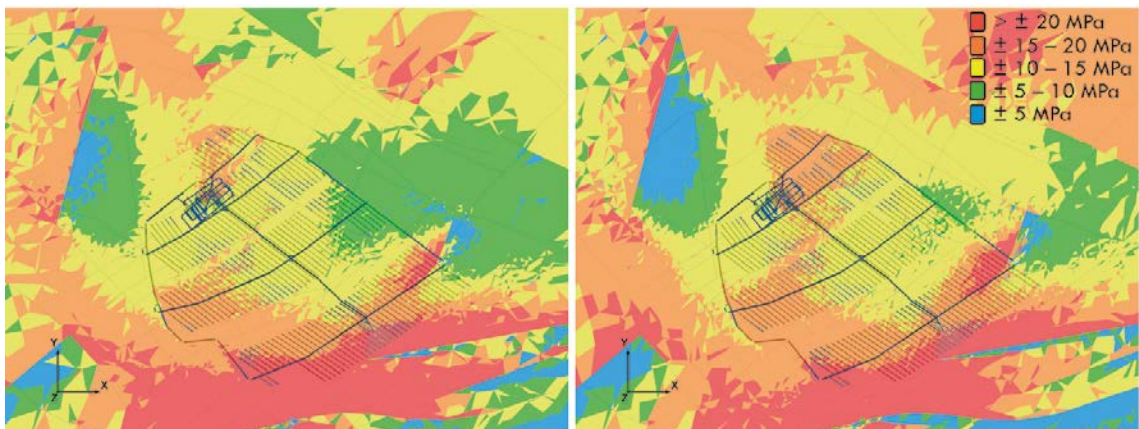


Figure A3b-6. Case 2-11 (left) and Case 2-12 (right). Change in σ_1 magnitude, horizontal section from repository level.

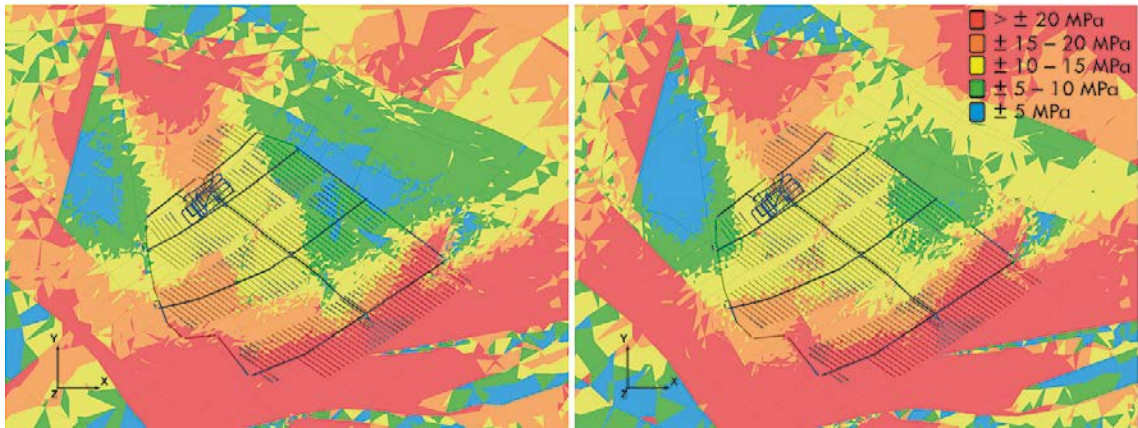


Figure A3b-7. Case 2-13 (left) and Case 2-14 (right). Change in σ_1 magnitude, horizontal section from repository level.

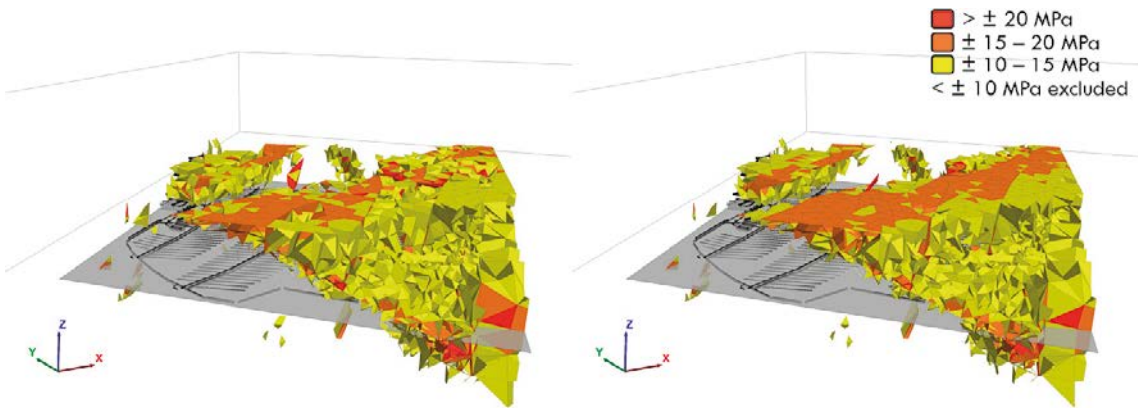


Figure A3b-8. Case 2-1 (left) and Case 2-2 (right). Change in σ_1 magnitude, isometric view.

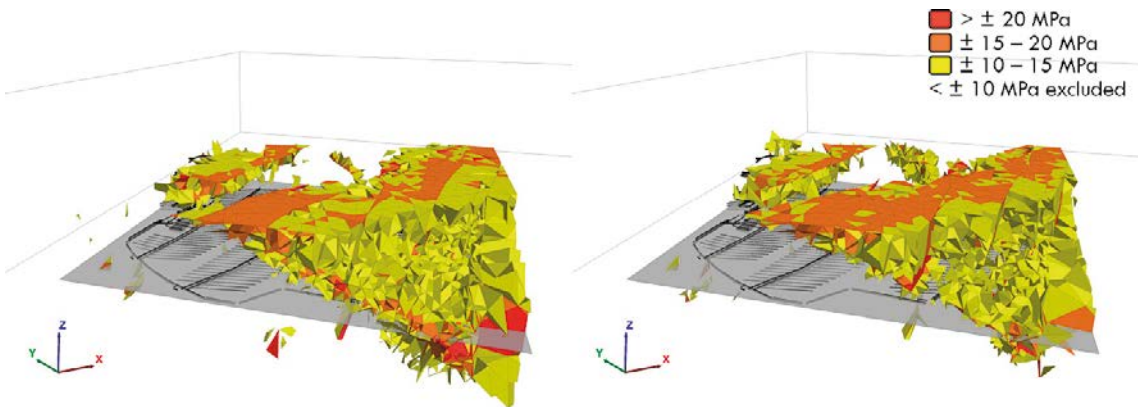


Figure A3b-9. Case 2-3 (left) and Case 2-4 (right). Change in σ_1 magnitude, isometric view.

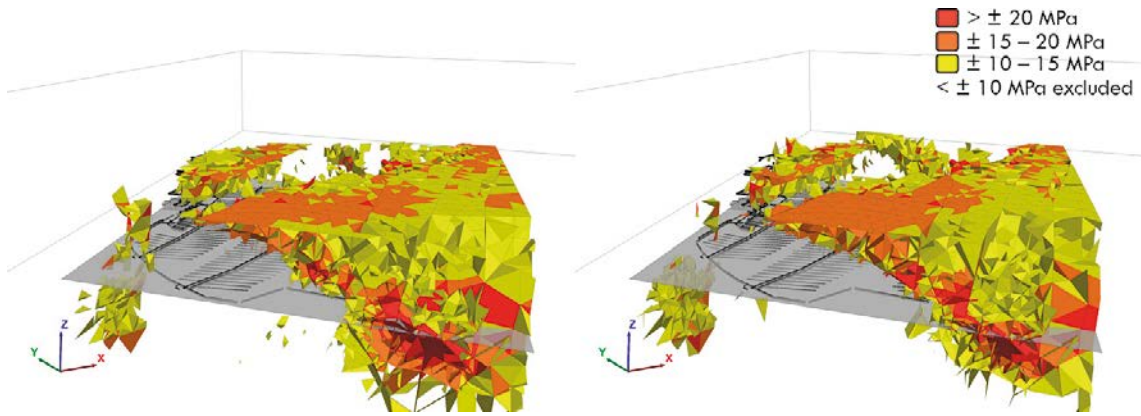


Figure A3b-10. Case 2-5 (left) and Case 2-6 (right). Change in σ_1 magnitude, isometric view.

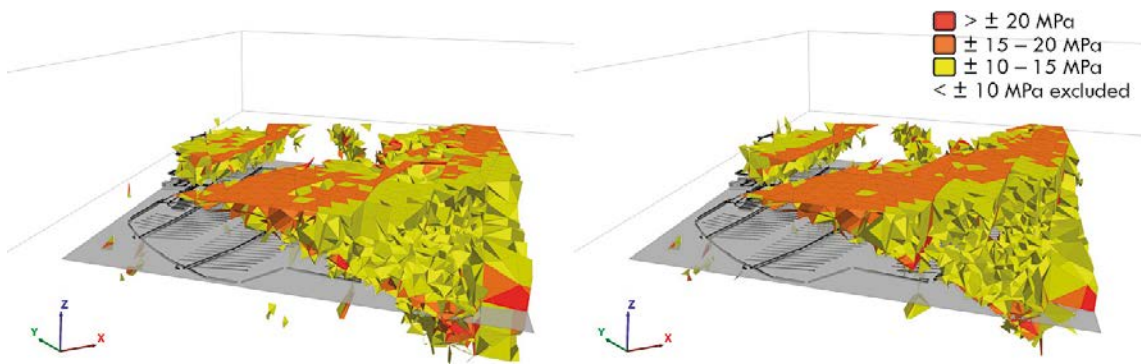


Figure A3b-11. Case 2-7 (left) and Case 2-8 (right). Change in σ_1 magnitude, isometric view.

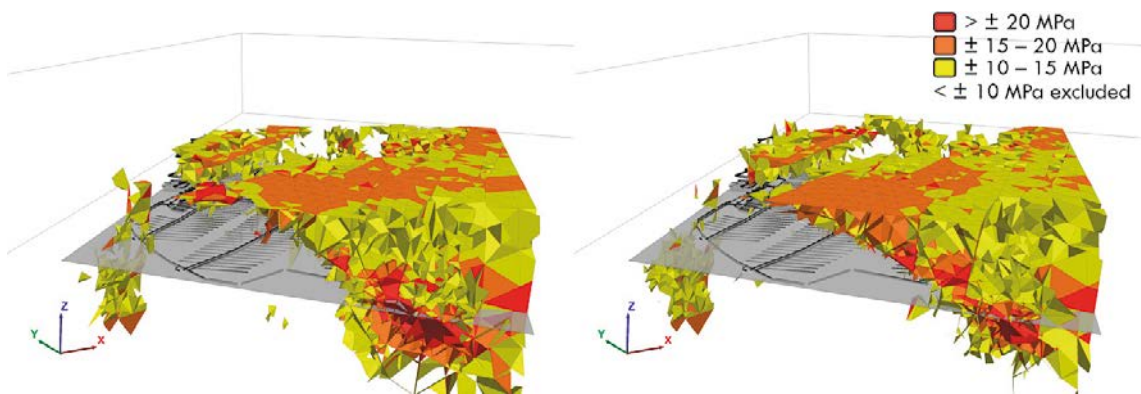


Figure A3b-12. Case 2-9(left) and Case 2-10 (right). Change in σ_1 magnitude, isometric view.

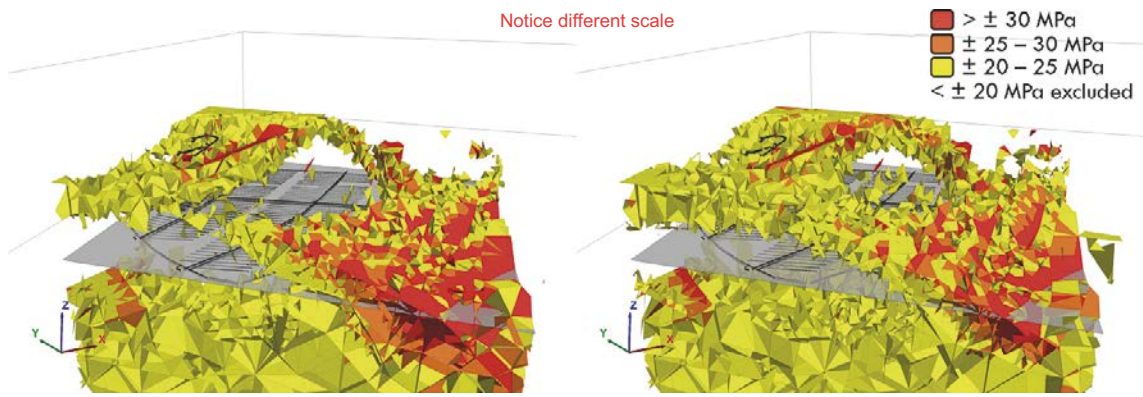


Figure A3b-13. Case 2-11 (left) and Case 2-12 (right). Change in σ_1 magnitude, isometric view.

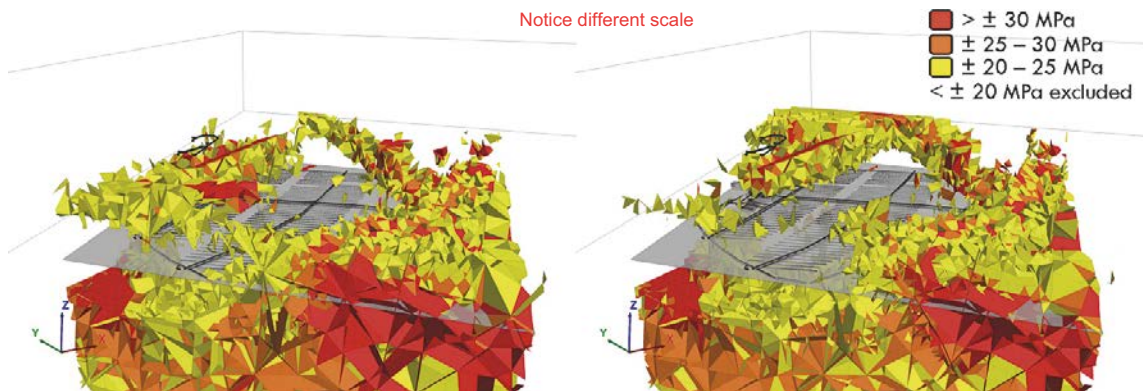


Figure A3b-14. Case 2-13 (left) and Case 2-14 (right). Change in σ_1 magnitude, isometric view.

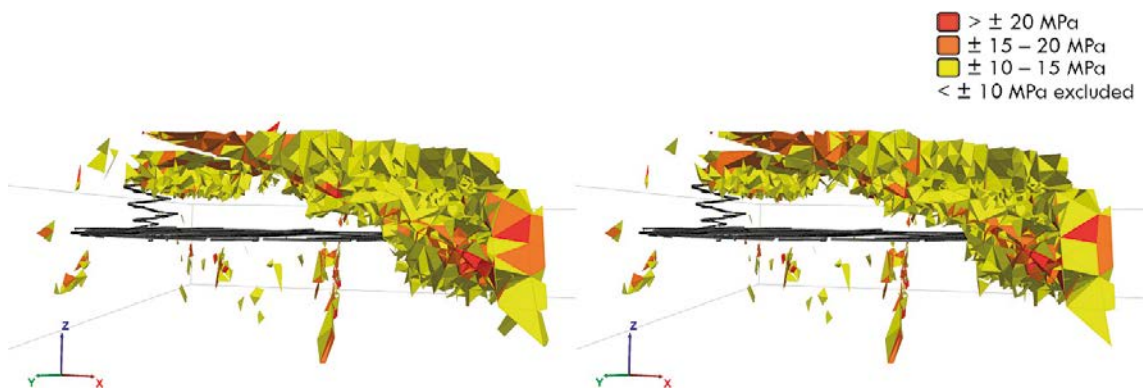


Figure A3b-15. Case 2-1 (left) and Case 2-2 (right). Change in σ_1 magnitude, view from repository level.

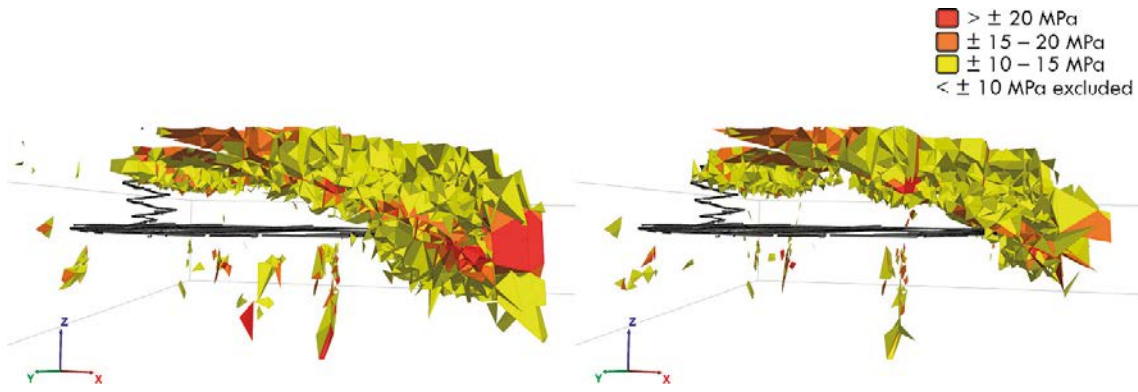


Figure A3b-16. Case 2-3 (left) and Case 2-4 (right). Change in σ_1 magnitude, view from repository level.

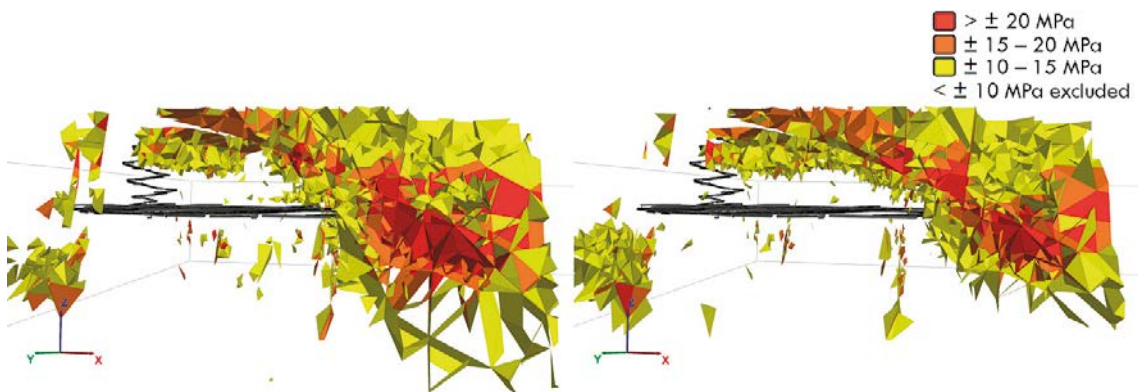


Figure A3b-17. Case 2-5 (left) and Case 2-6 (right). Change in σ_1 magnitude, view from repository level.

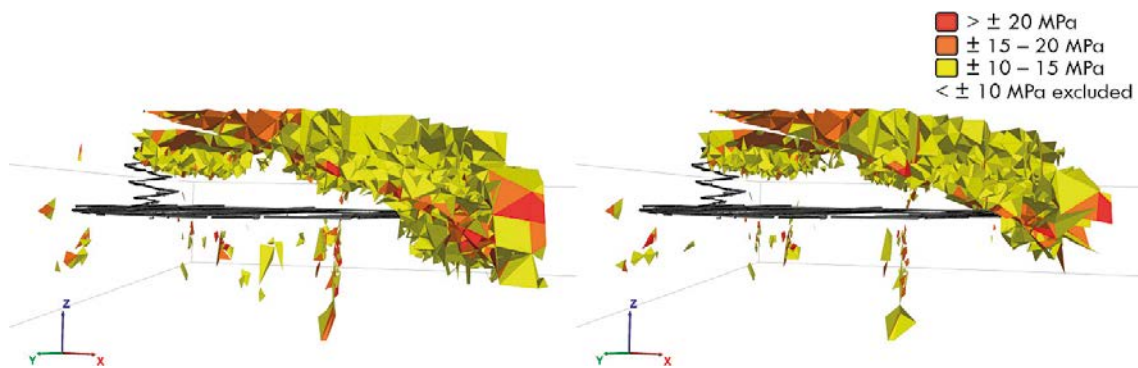


Figure A3b-18. Case 2-7(left) and Case 2-8 (right). Change in σ_1 magnitude, view from repository level.

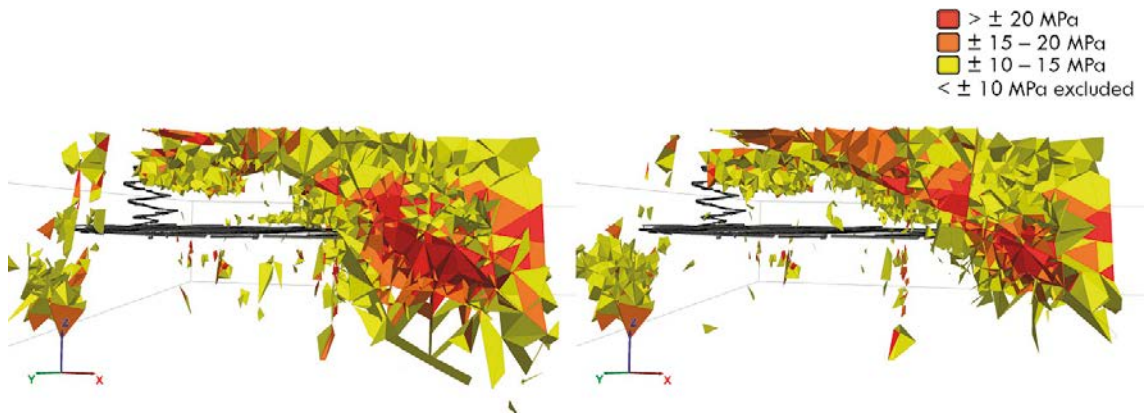


Figure A3b-19. Case 2-9 (left) and Case 2-10 (right). Change in σ_1 magnitude, view from repository level.

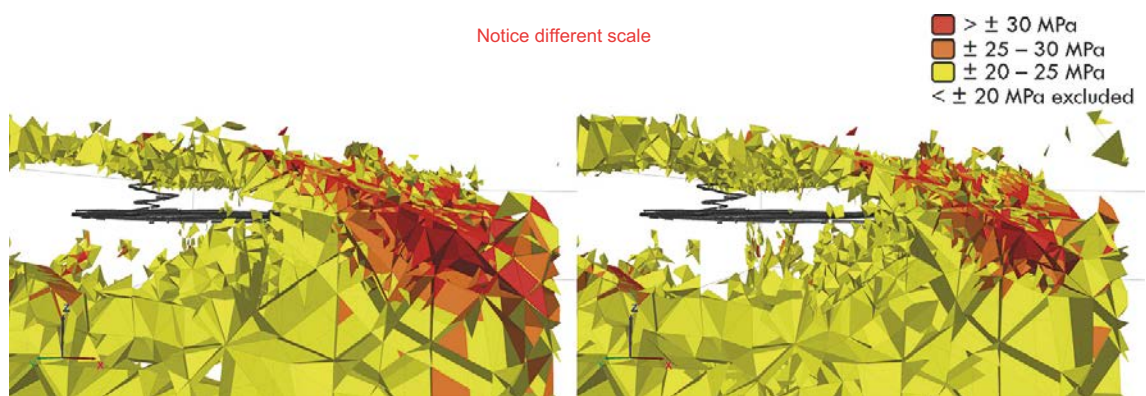


Figure A3b-20. Case 2-11 (left) and Case 2-12 (right). Change in σ_1 magnitude, view from repository level.

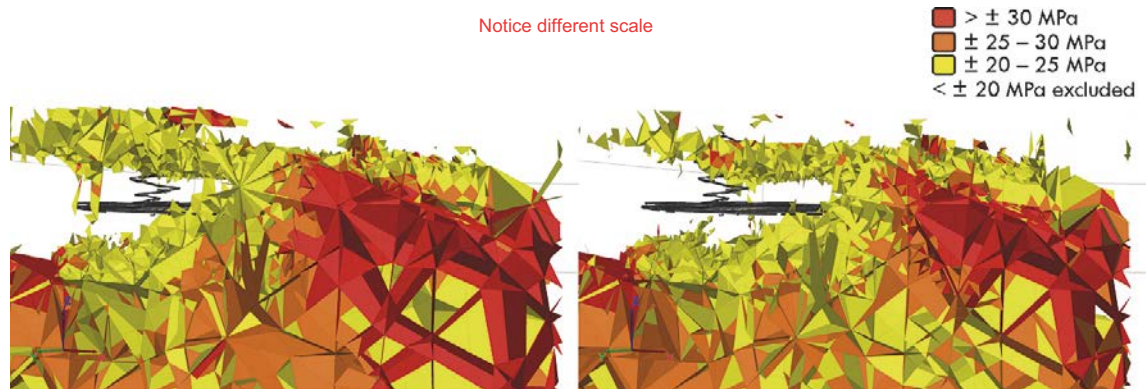


Figure A3b-21. Case 2-13 (left) and Case 2-14 (right). Change in σ_1 magnitude, view from repository level.

Simulation Phase 1 – change in σ_1 trend

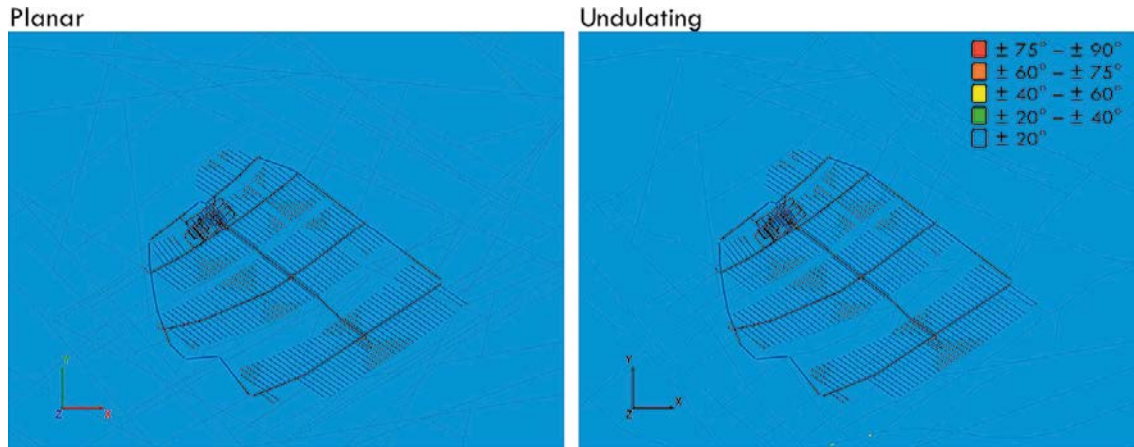


Figure A4a-1. Change in σ_1 trend, horizontal section from repository level, Case 1.

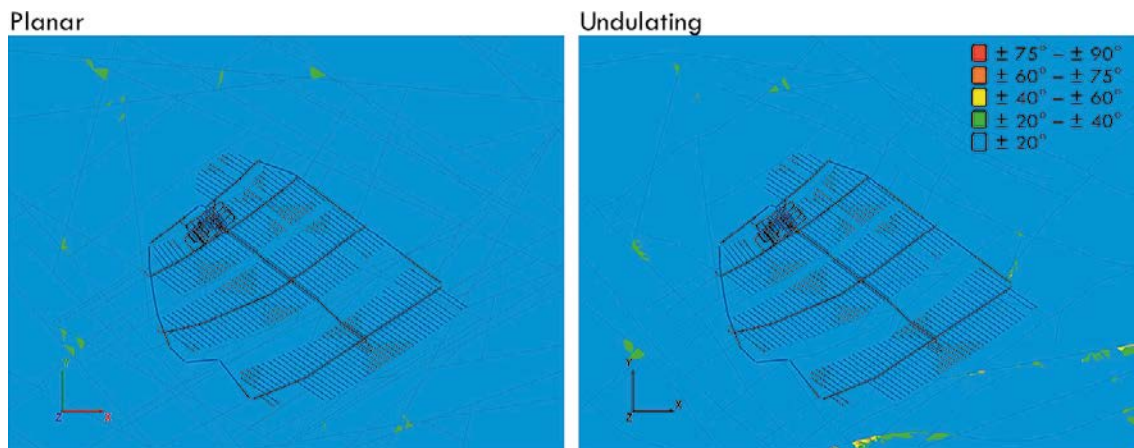


Figure A4a-2. Change in σ_1 trend, horizontal section from repository level, Case 2.

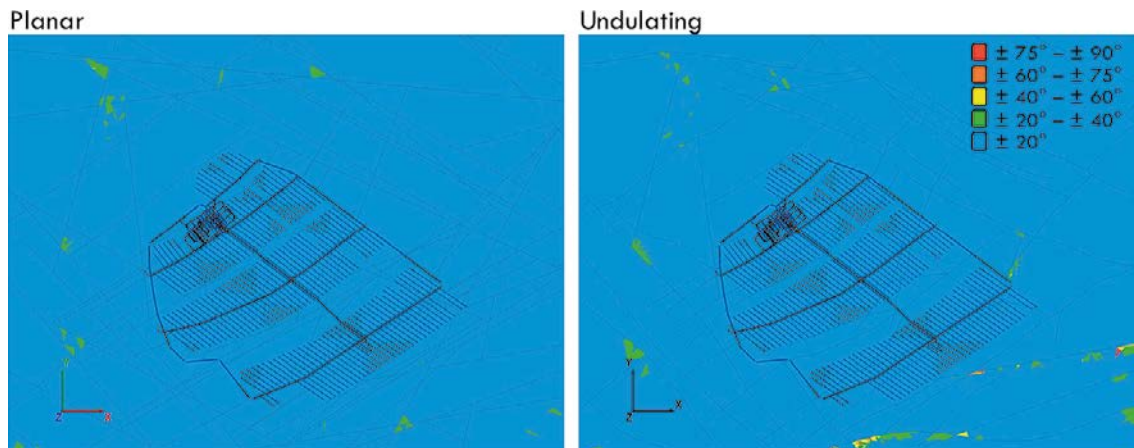


Figure A4a-3. Change in σ_1 trend, horizontal section from repository level, Case 3.

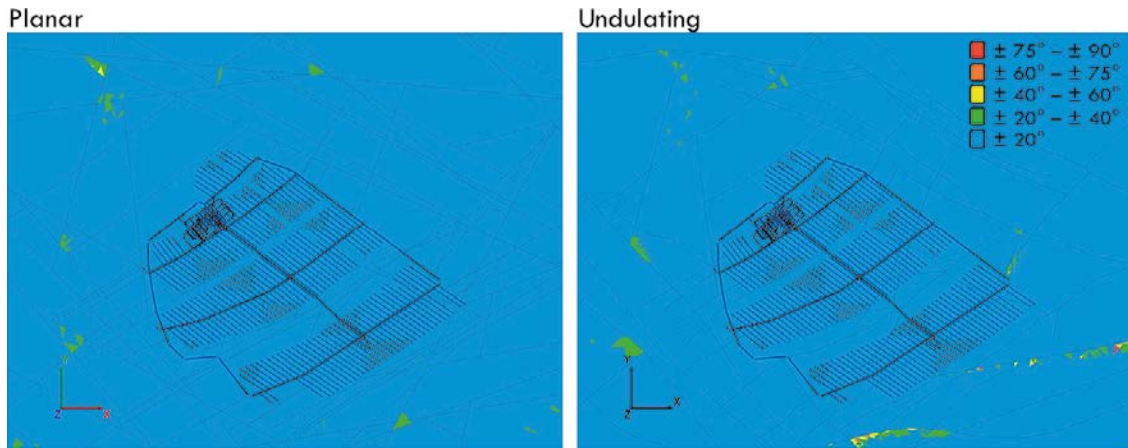


Figure A4a-4. Change in σ_1 trend, horizontal section from repository level, Case 4.

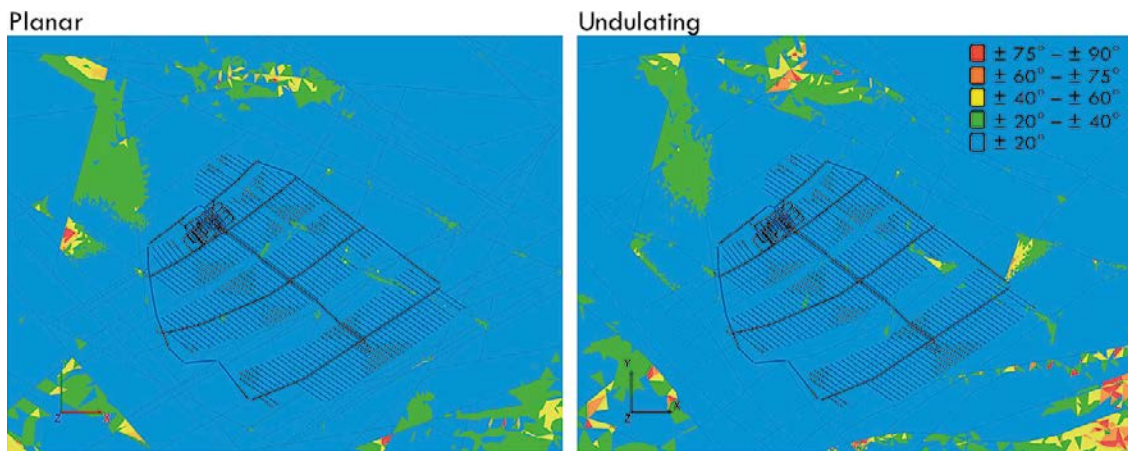


Figure A4a-5. Change in σ_1 trend, horizontal section from repository level, Case 5.

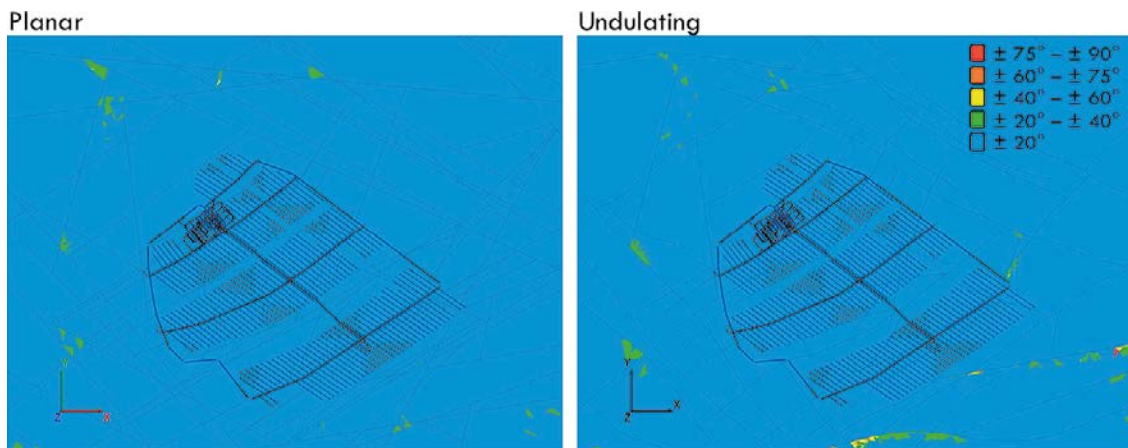


Figure A4a-6. Change in σ_1 trend, horizontal section from repository level, Case 6.

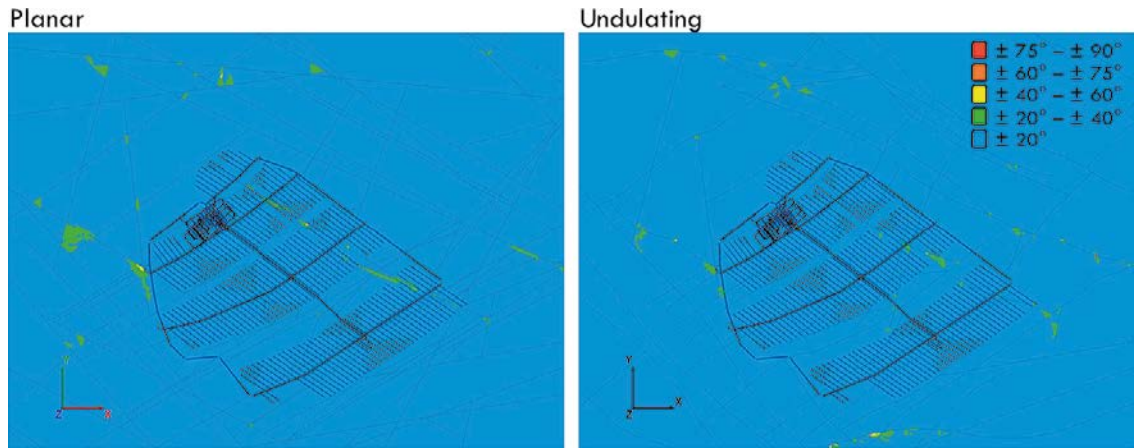


Figure A4a-7. Change in σ_1 trend, horizontal section from repository level, Case 7.

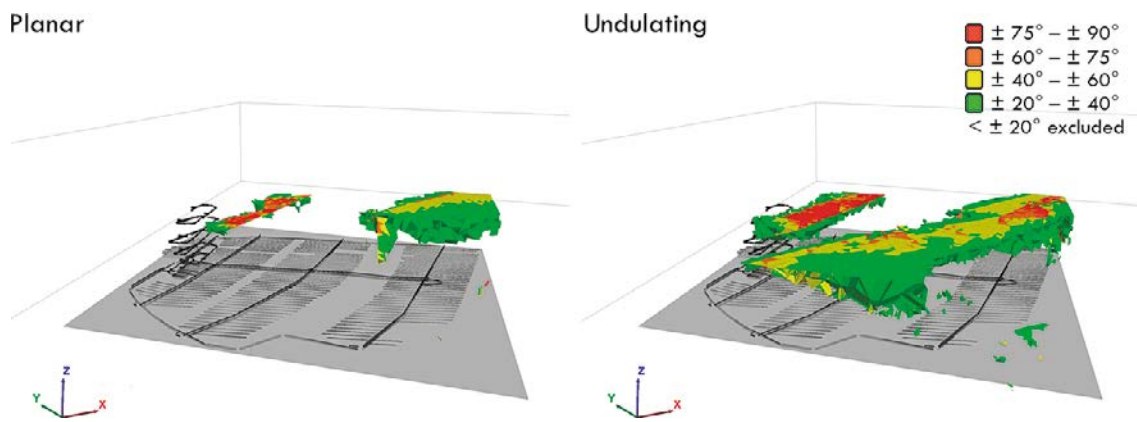


Figure A4a-8. Change in σ_1 trend, isometric view, Case 1.

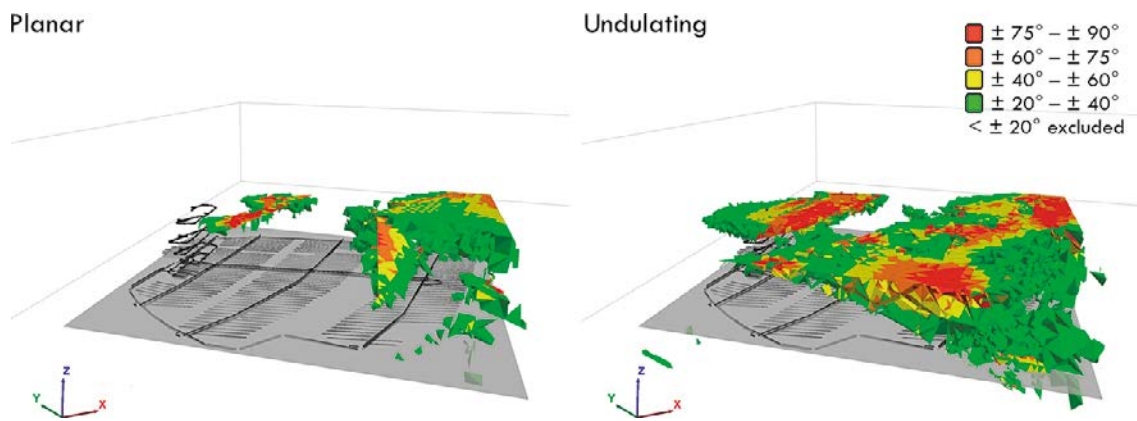
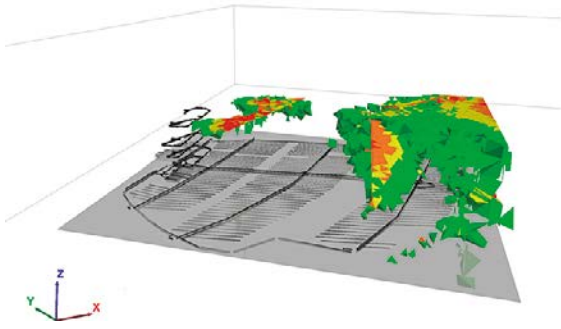


Figure A4a-9. Change in σ_1 trend, isometric view, Case 2.

Planar



Undulating

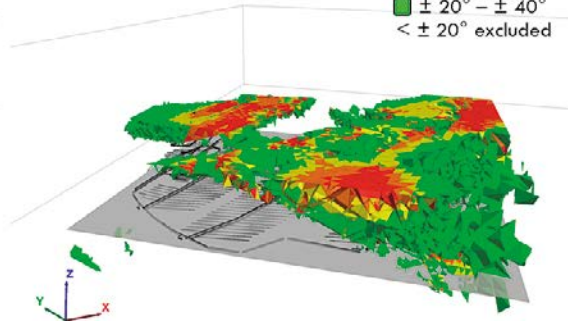
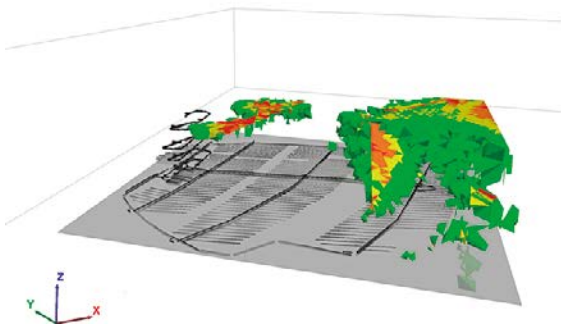


Figure A4a-10. Change in σ_1 trend, isometric view, Case 3.

Planar



Undulating

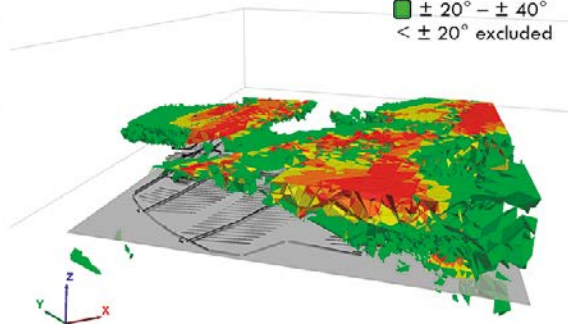
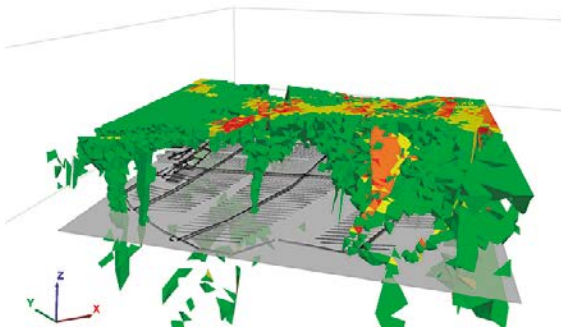


Figure A4a-11. Change in σ_1 trend, isometric view, Case 4.

Planar



Undulating

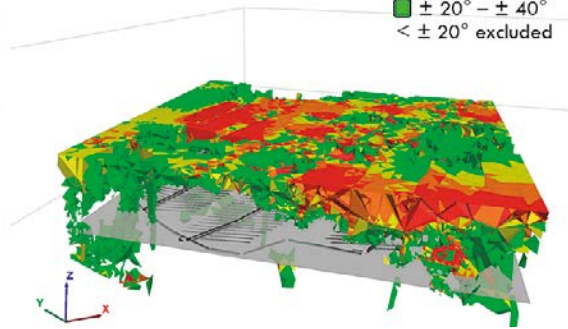


Figure A4a-12. Change in σ_1 trend, isometric view, Case 5.

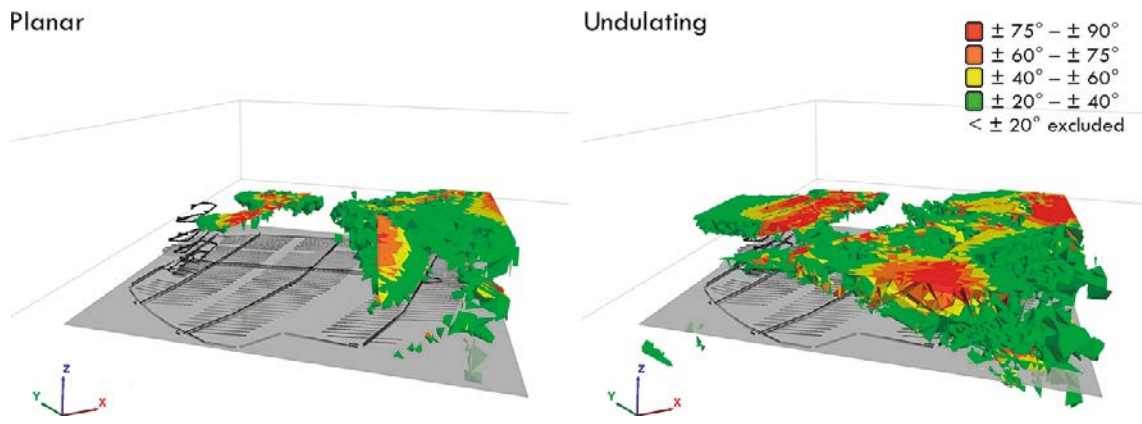


Figure A4a-13. Change in σ_1 trend, isometric view, Case 6.

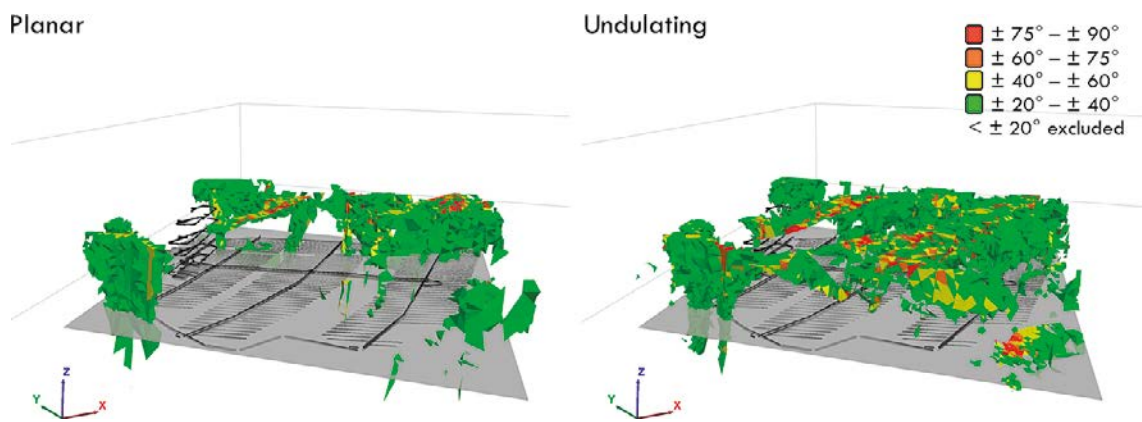


Figure A4a-14. Change in σ_1 trend, isometric view, Case 7.

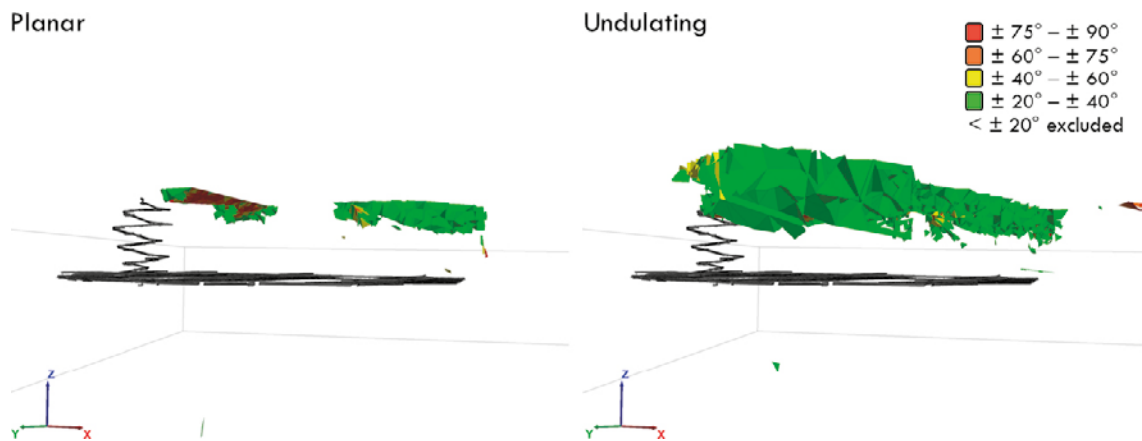


Figure A4a-15. Change in σ_1 trend, view from repository level, Case 1.

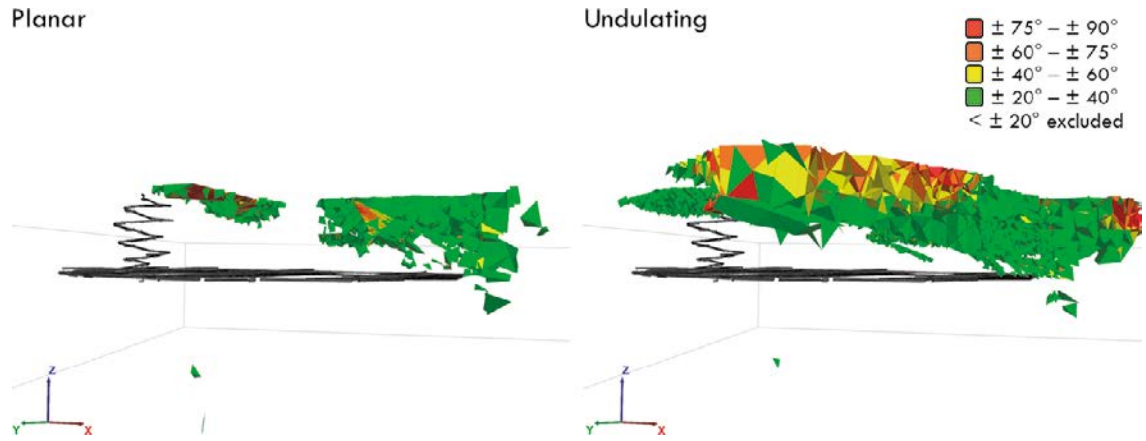


Figure A4a-16. Change in σ_1 trend, view from repository level, Case 2.

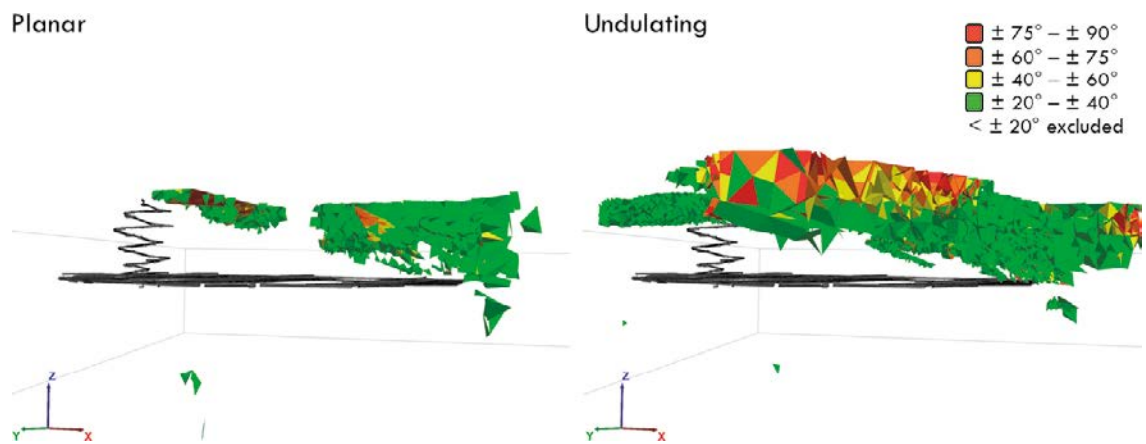


Figure A4a-17. Change in σ_1 trend, view from repository level, Case 3.

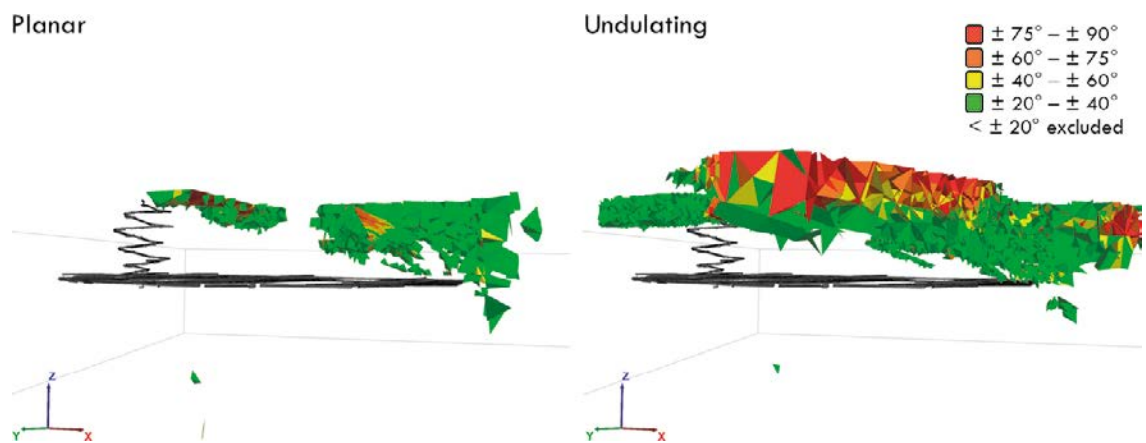


Figure A4a-18. Change in σ_1 trend, view from repository level, Case 4.

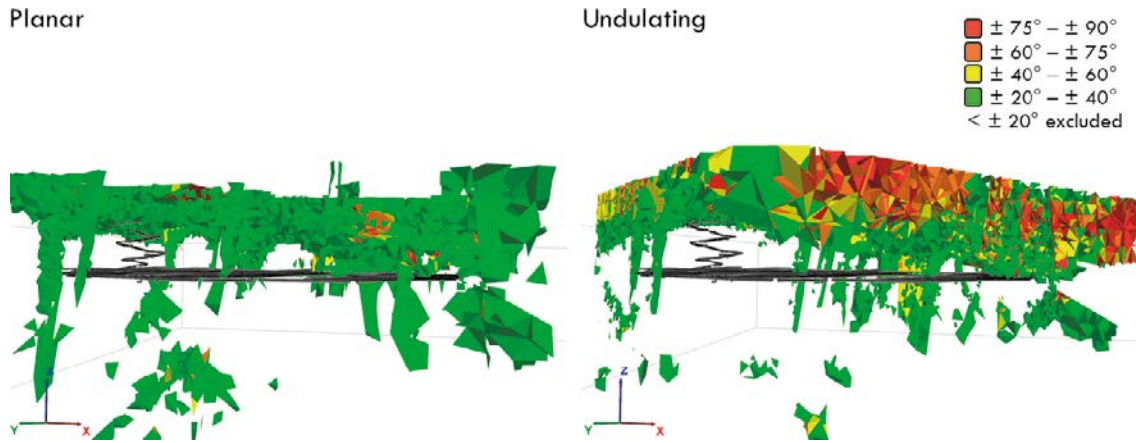


Figure A4a-19. Change in σ_1 trend, view from repository level, Case 5.

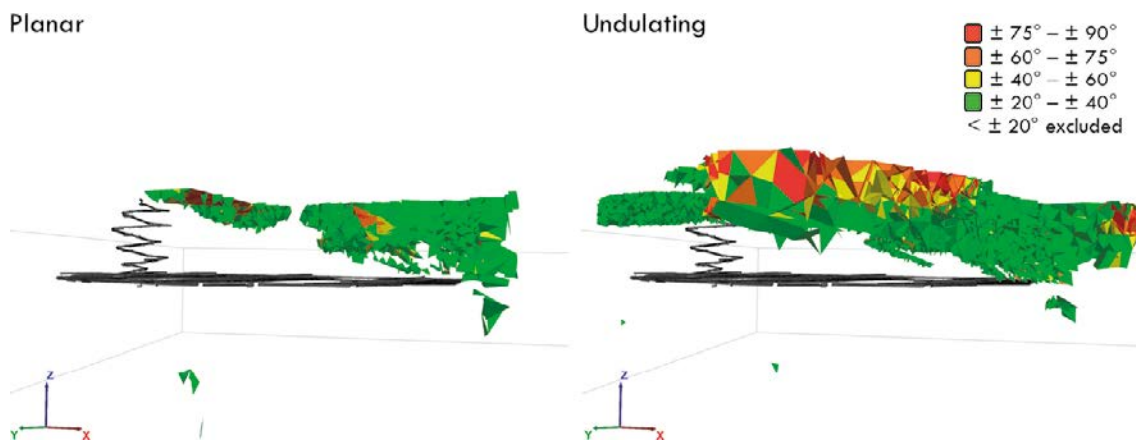


Figure A4a-20. Change in σ_1 trend, view from repository level, Case 6.

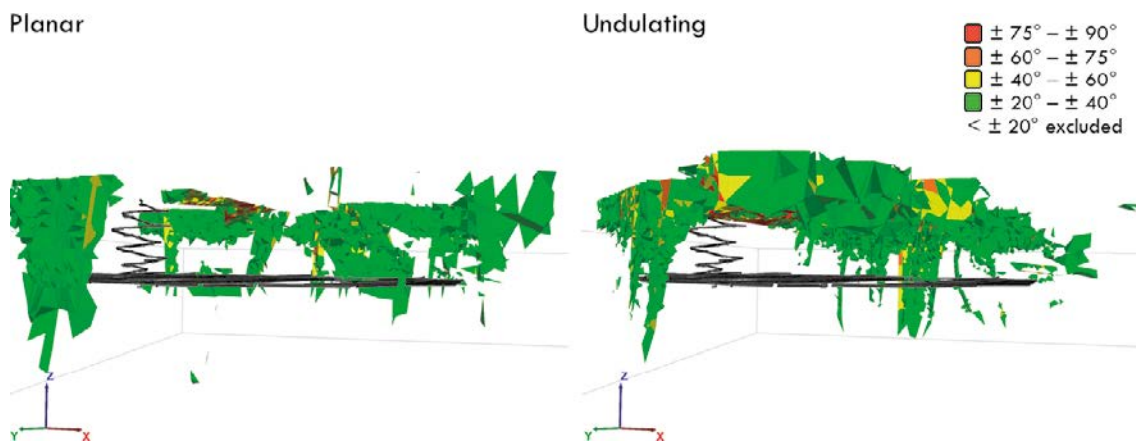


Figure A4a-21. Change in σ_1 trend, view from repository level, Case 7.

Simulation Phase 2 – change in σ_1 trend

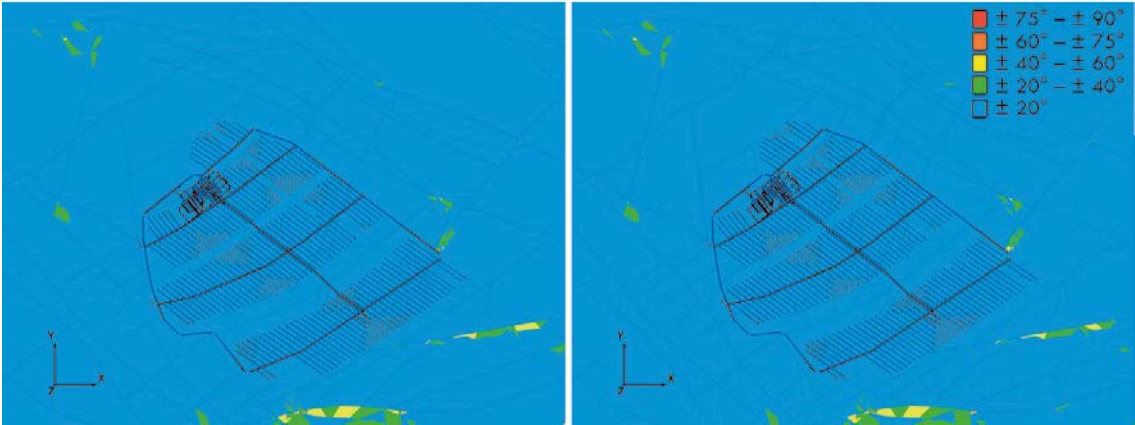


Figure A4b-1. Case 2-1 (left) and Case 2-2 (right). Change in σ_1 trend, horizontal section from repository level.

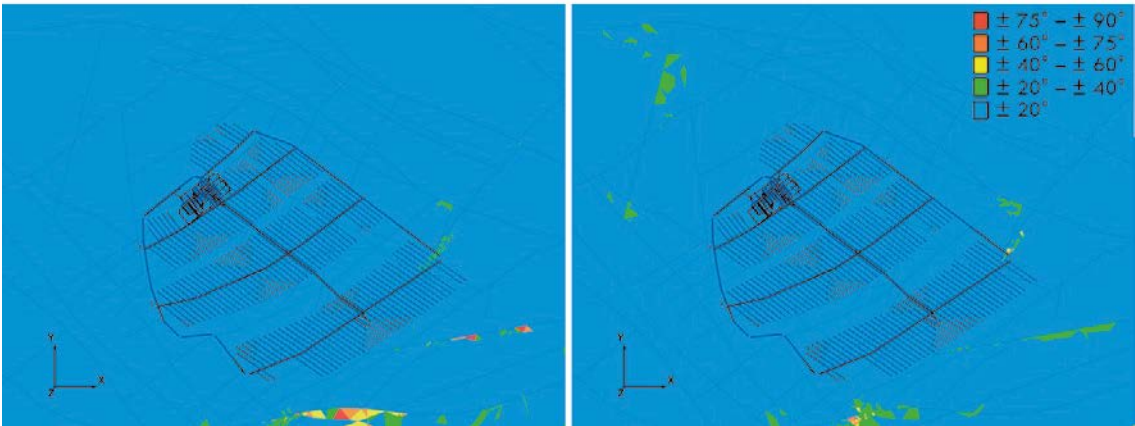


Figure A4b-2. Case 2-3 (left) and Case 2-4 (right). Change in σ_1 trend, horizontal section from repository level.

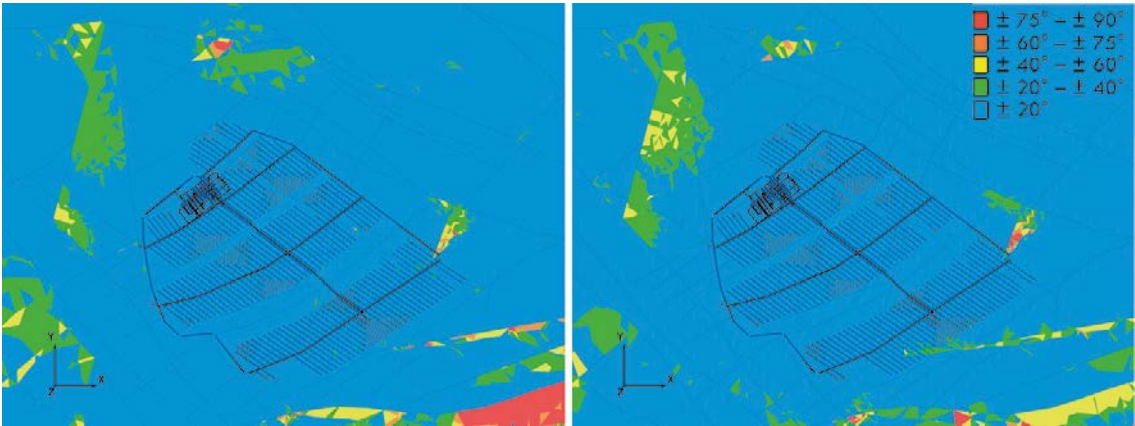


Figure A4b-3. Case 2-5 (left) and Case 2-6 (right). Change in σ_1 trend, horizontal section from repository level.

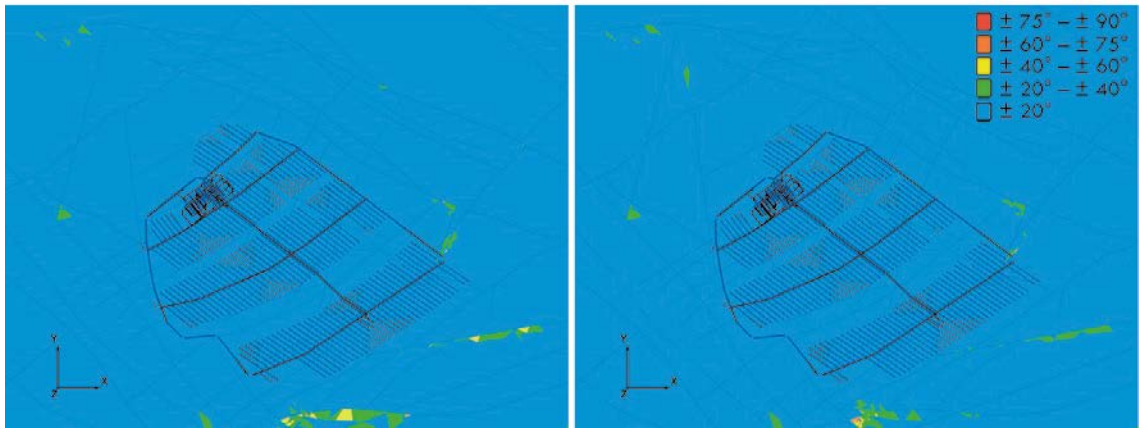


Figure A4b-4. Case 2-7 (left) and Case 2-8 (right). Change in σ_1 trend, horizontal section from repository level.

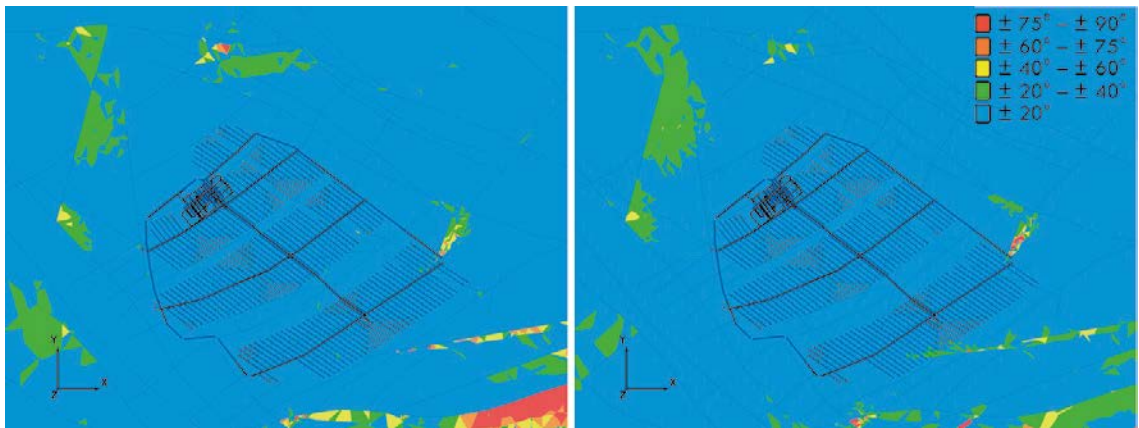


Figure A4b-5. Case 2-9 (left) and Case 2-10 (right). Change in σ_1 trend, horizontal section from repository level.

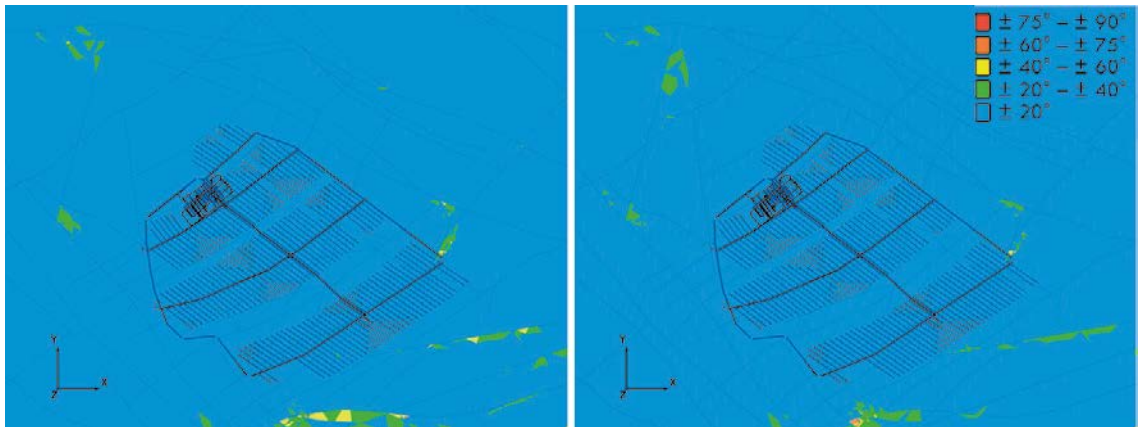


Figure A4b-6. Case 2-11 (left) and Case 2-12 (right). Change in σ_1 trend, horizontal section from repository level.

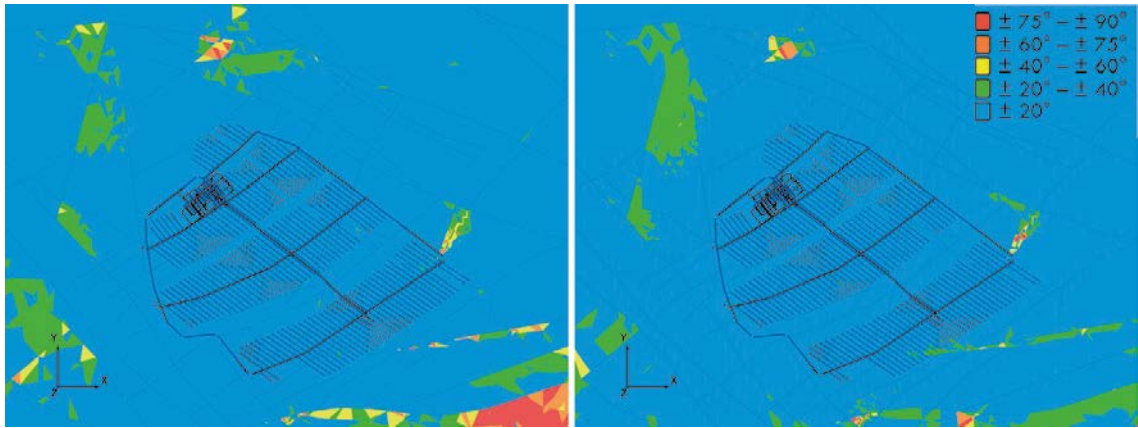


Figure A4b-7. Case 2-13 (left) and Case 2-14 (right). Change in σ_1 trend, horizontal section from repository level.

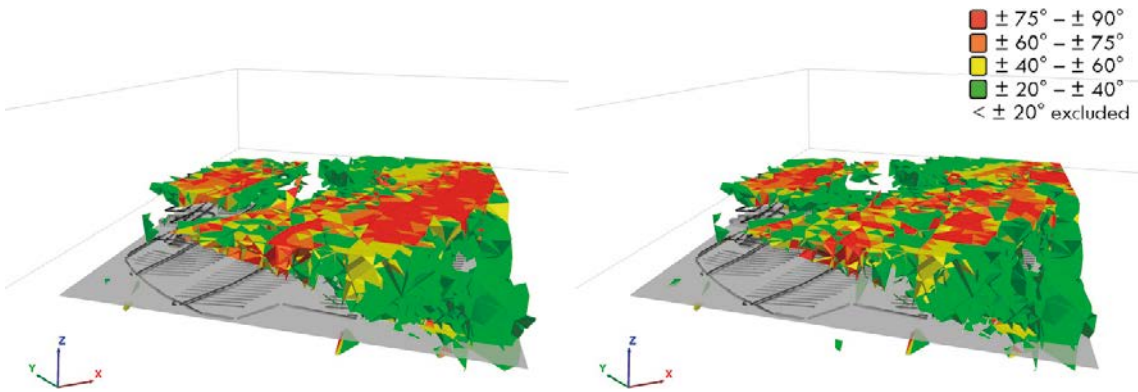


Figure A4b-8. Case 2-1 (left) and Case 2-2 (right). Change in σ_1 trend, isometric view.

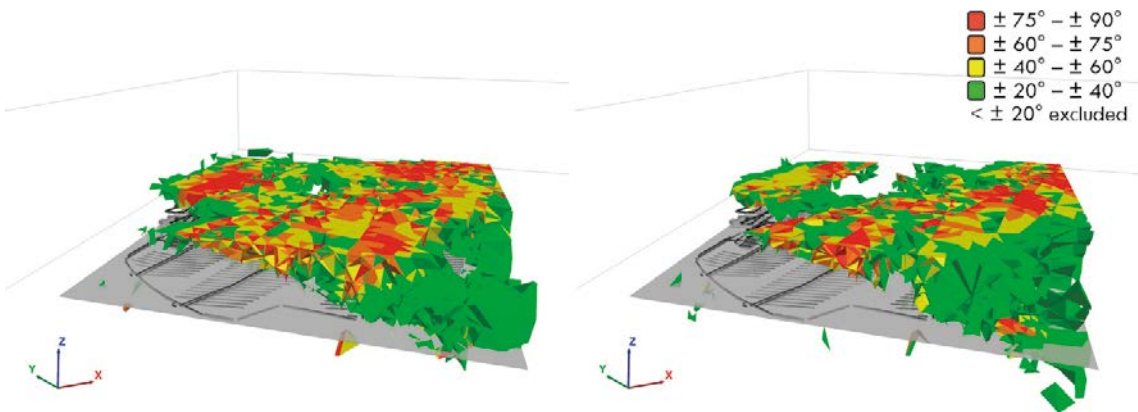


Figure A4b-9. Case 2-3 (left) and Case 2-4 (right). Change in σ_1 trend, isometric view.

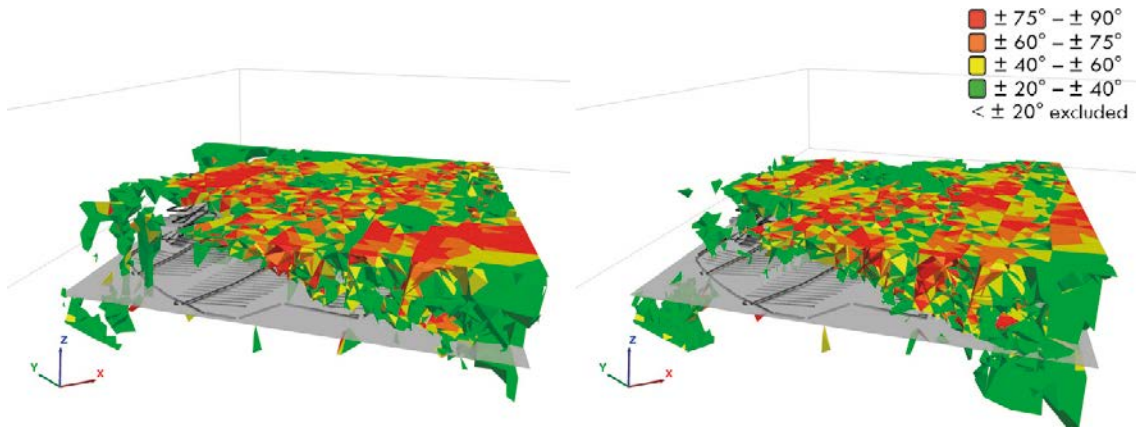


Figure A4b-10. Case 2-5 (left) and Case 2-6 (right). Change in σ_1 trend, isometric view.

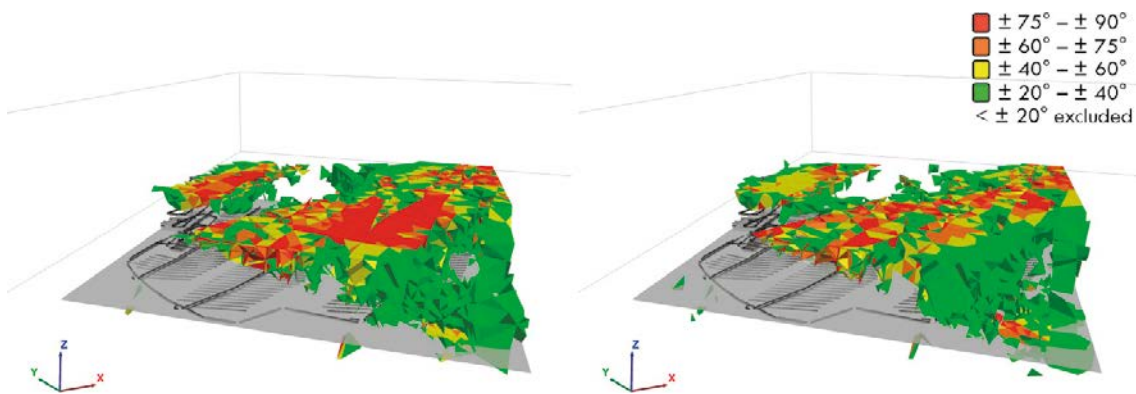


Figure A4b-11. Case 2-7 (left) and Case 2-8 (right). Change in σ_1 trend, isometric view.

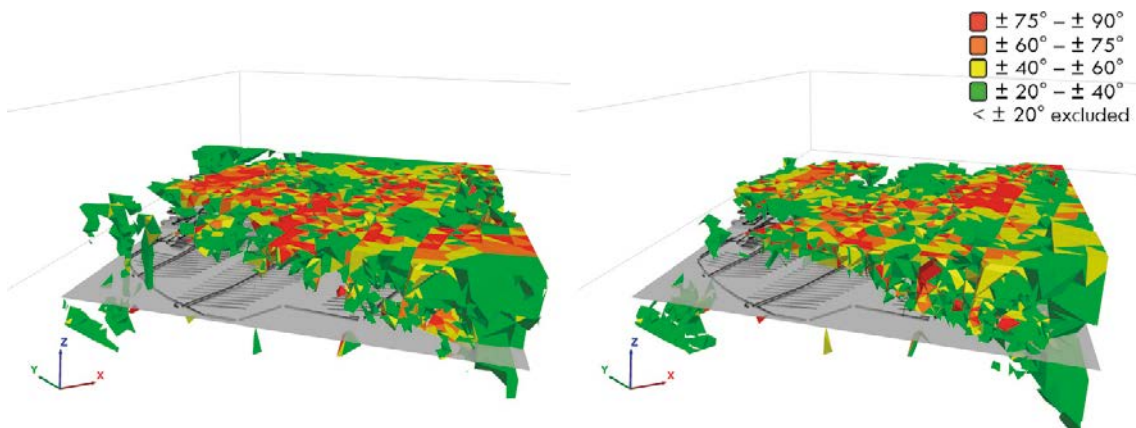


Figure A4b-12. Case 2-9 (left) and Case 2-10 (right). Change in σ_1 trend, isometric view.

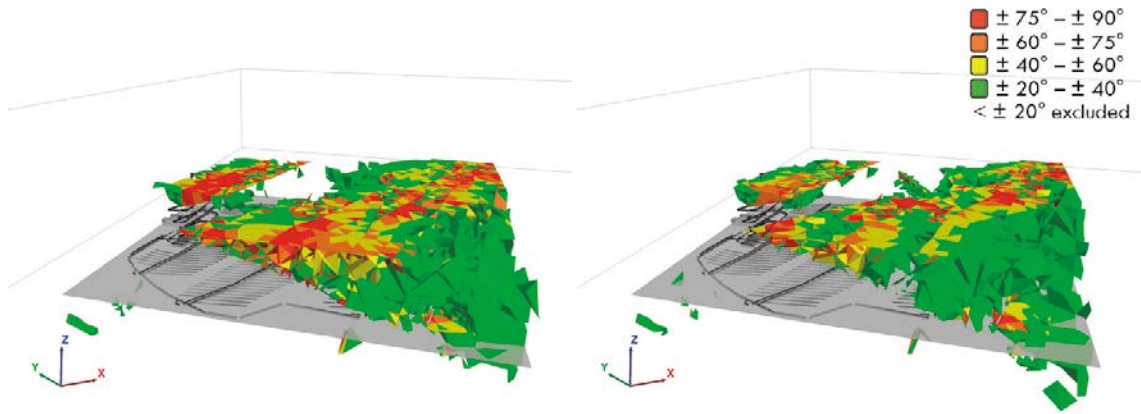


Figure A4b-13. Case 2-11 (left) and Case 2-12 (right). Change in σ_1 trend, isometric view.

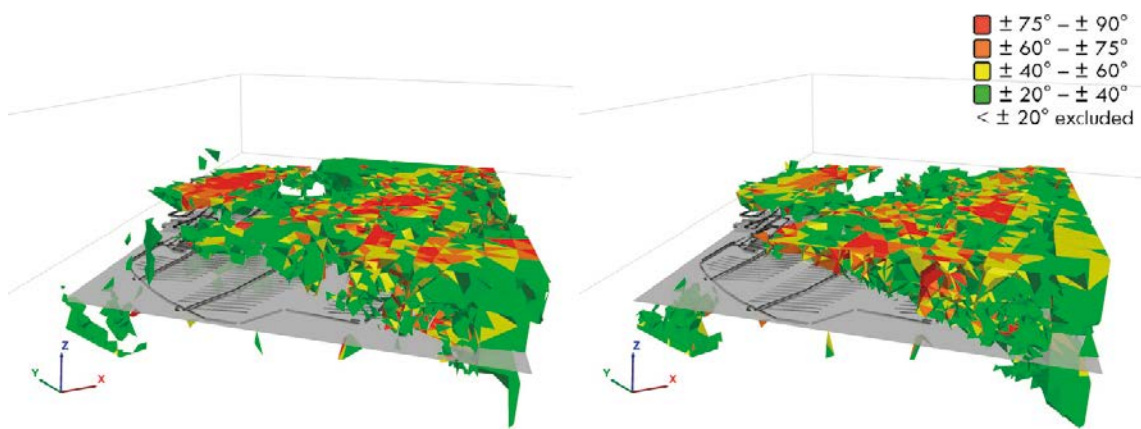


Figure A4b-14. Case 2-13 (left) and Case 2-14 (right). Change in σ_1 trend, isometric view.

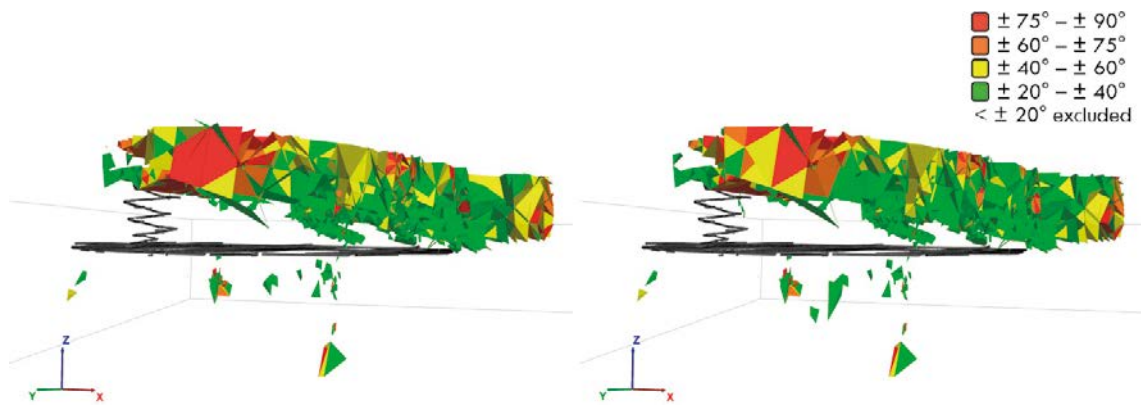


Figure A4b-15. Case 2-1 (left) and Case 2-2 (right). Change in σ_1 trend, view from repository level.

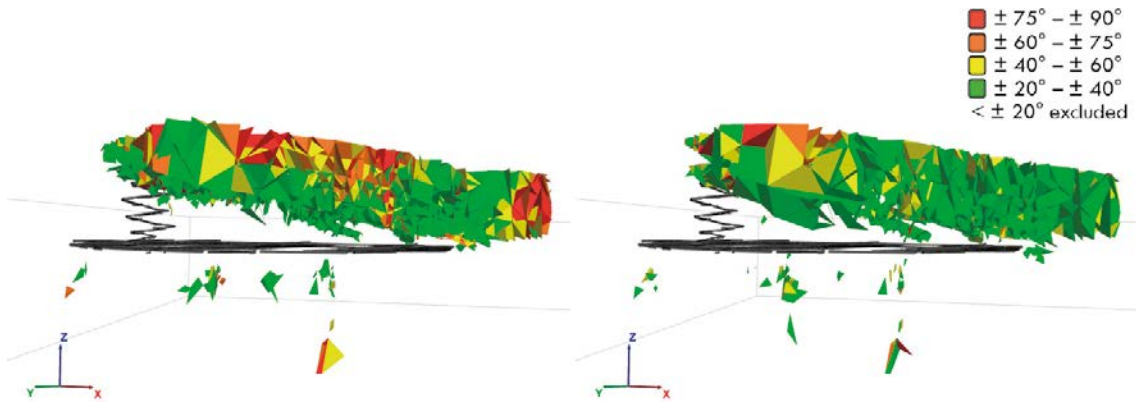


Figure A4b-16. Case 2-3 (left) and Case 2-4 (right). Change in σ_1 trend, view from repository level.

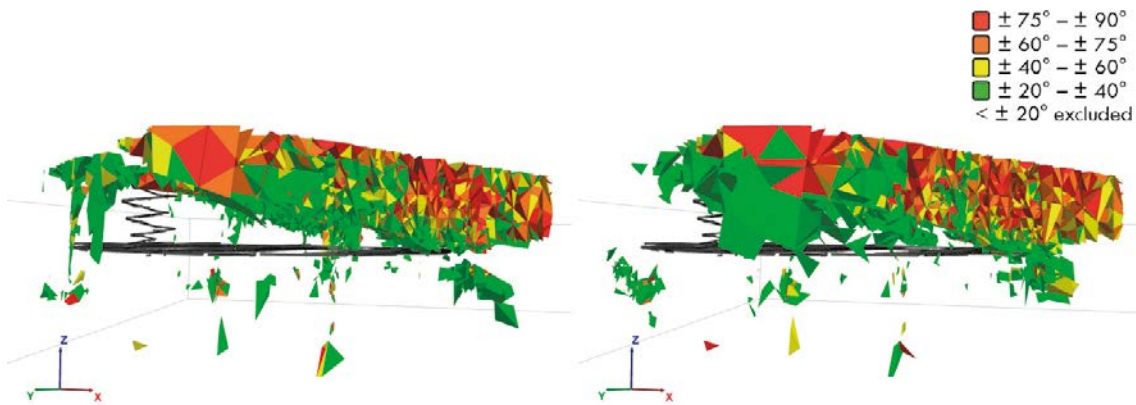


Figure A4b-17. Case 2-5 (left) and Case 2-6 (right). Change in σ_1 trend, view from repository level.

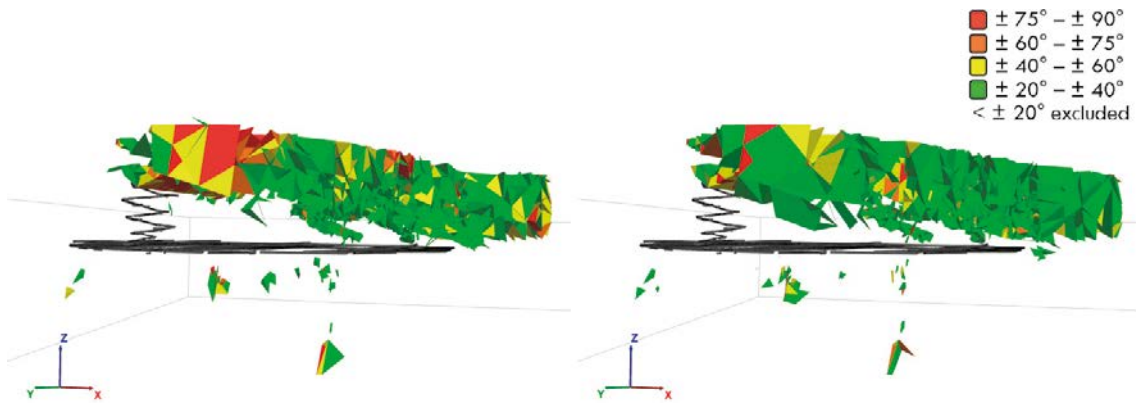


Figure A4b-18. Case 2-7 (left) and Case 2-8 (right). Change in σ_1 trend, view from repository level.

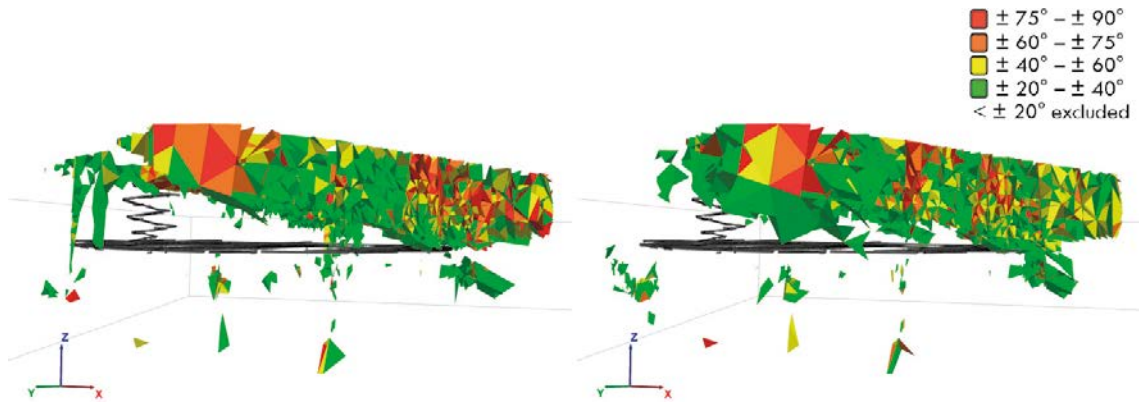


Figure A4b-19. Case 2-9 (left) and Case 2-10 (right). Change in σ_1 trend, view from repository level.

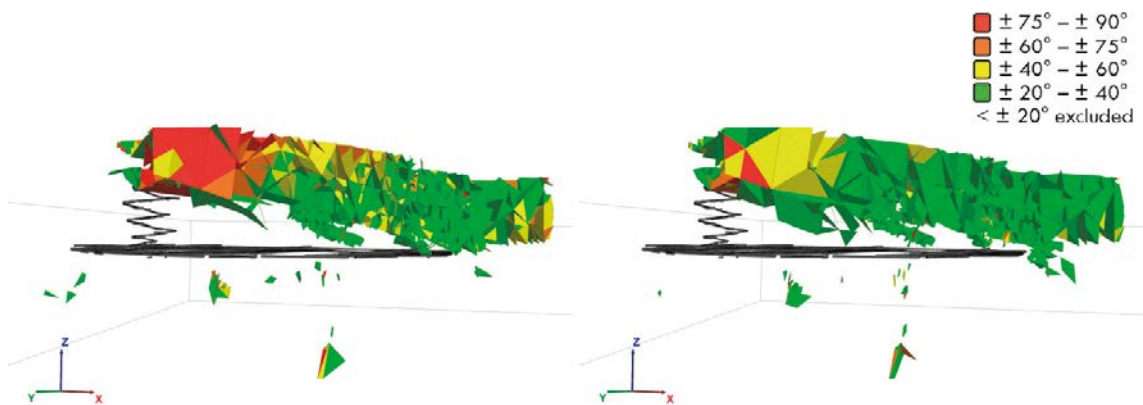


Figure A4b-20. Case 2-11 (left) and Case 2-12 (right). Change in σ_1 trend, view from repository level.

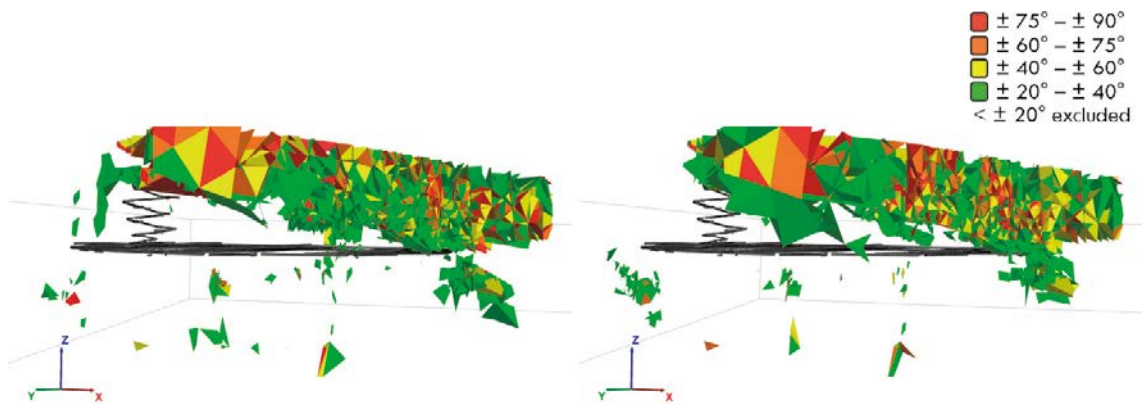


Figure A4b-21. Case 2-13 (left) and Case 2-14 (right). Change in σ_1 trend, view from repository level.

Simulation Phase 1 – mean and variation of σ_1 magnitude, trend and σ_1/σ_2 ratio for hundred meter intervals (90 % variation interval)

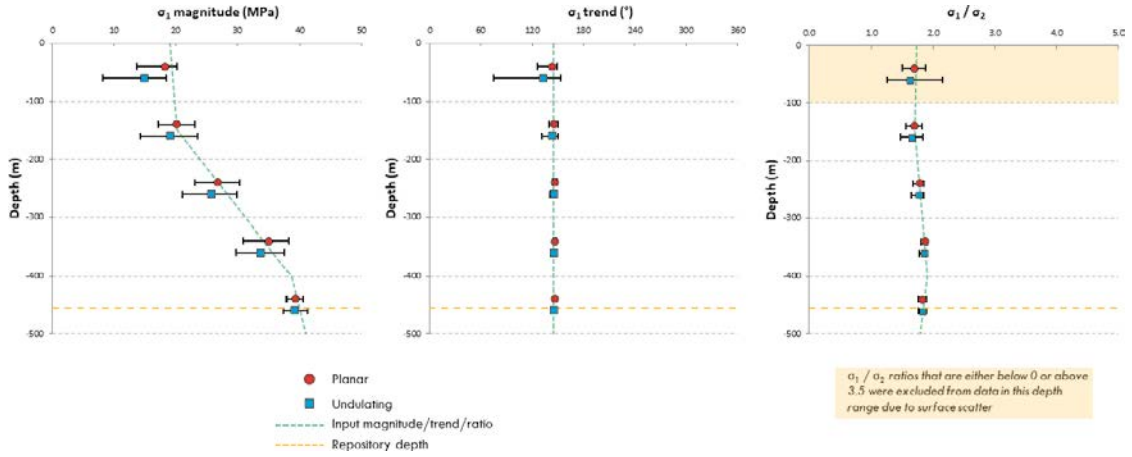


Figure A5a-1. Mean and variation of σ_1 magnitude, trend and σ_1/σ_2 ratio for hundred meter intervals, Case 1-1.

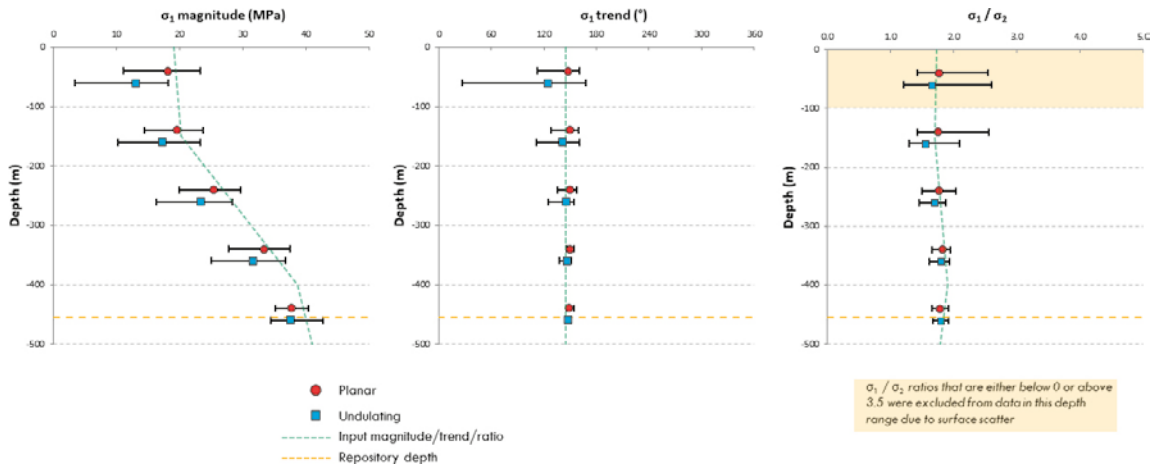


Figure A5a-2. Mean and variation of σ_1 magnitude, trend and σ_1/σ_2 ratio for hundred meter intervals, Case 1-2.

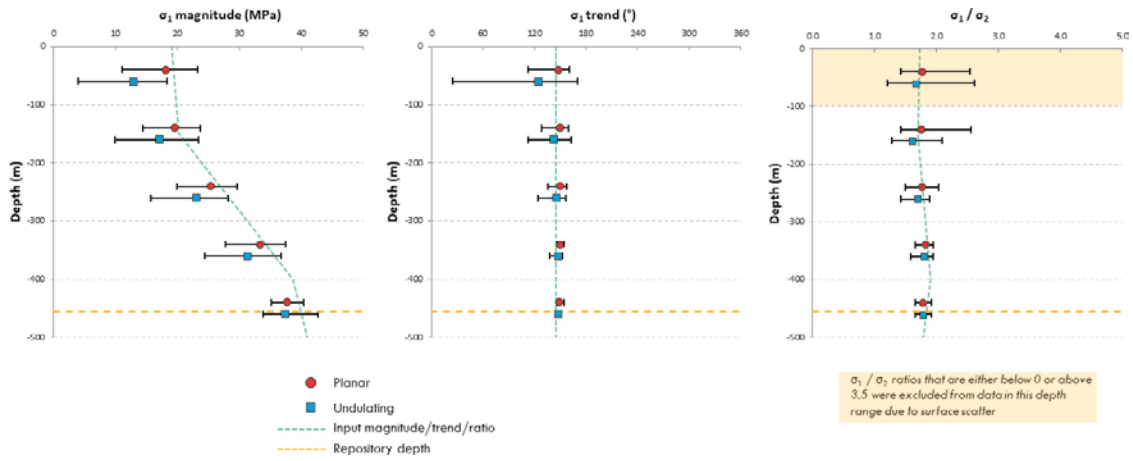


Figure A5a-3. σ_1 trend/magnitude and σ_1/σ_2 averages, Case 1-3.

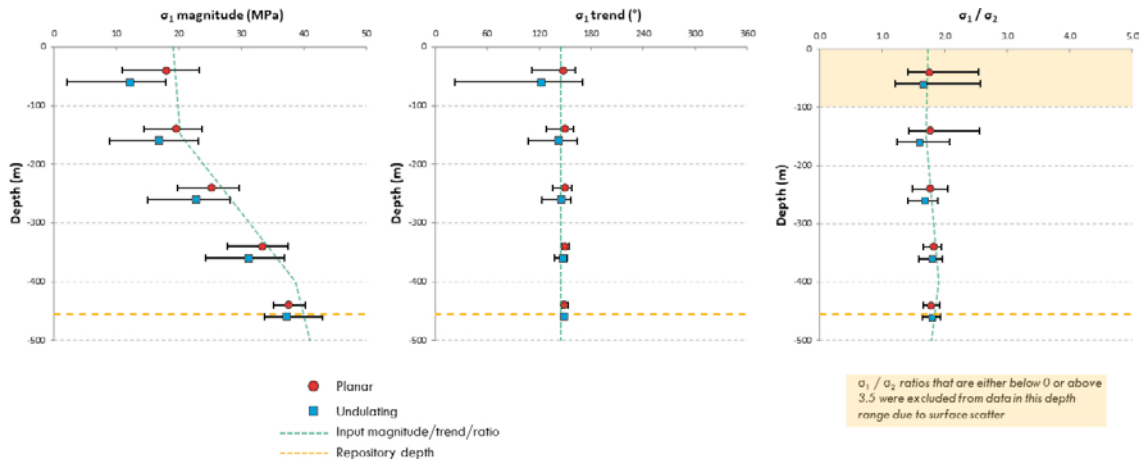


Figure A5a-4. Mean and variation of σ_1 magnitude, trend and σ_1/σ_2 ratio for hundred meter intervals, Case 1-4.

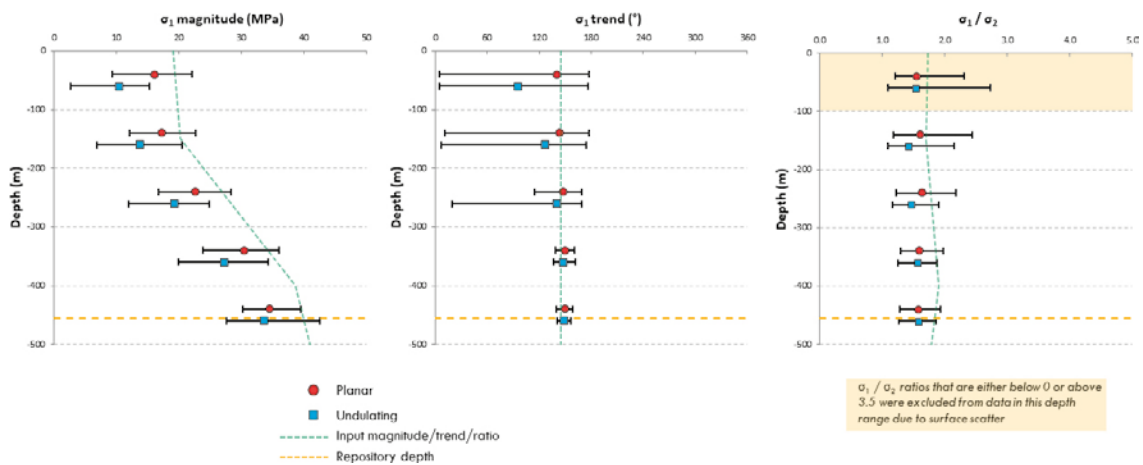


Figure A5a-5. Mean and variation of σ_1 magnitude, trend and σ_1/σ_2 ratio for hundred meter intervals, Case 1-5.

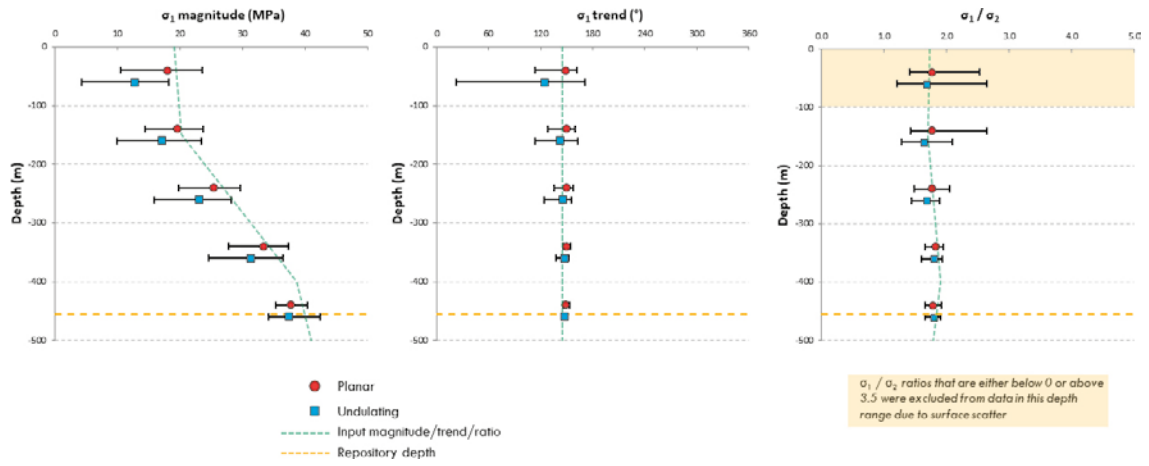


Figure A5a-6. Mean and variation of σ_1 magnitude, trend and σ_1/σ_2 ratio for hundred meter intervals, Case 1-6.

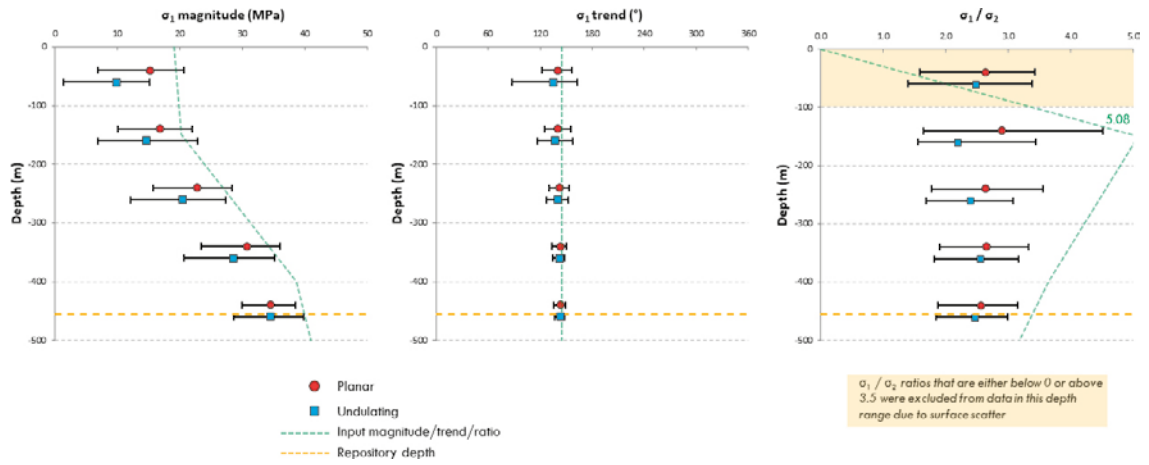


Figure A5a-7. Mean and variation of σ_1 magnitude, trend and σ_1/σ_2 ratio for hundred meter intervals, Case 1-7.

Simulation Phase 2
– pre/post glacial mean and variation of σ_1 magnitude, trend and σ_1/σ_2 ratio for hundred meter intervals (90 % variation interval)

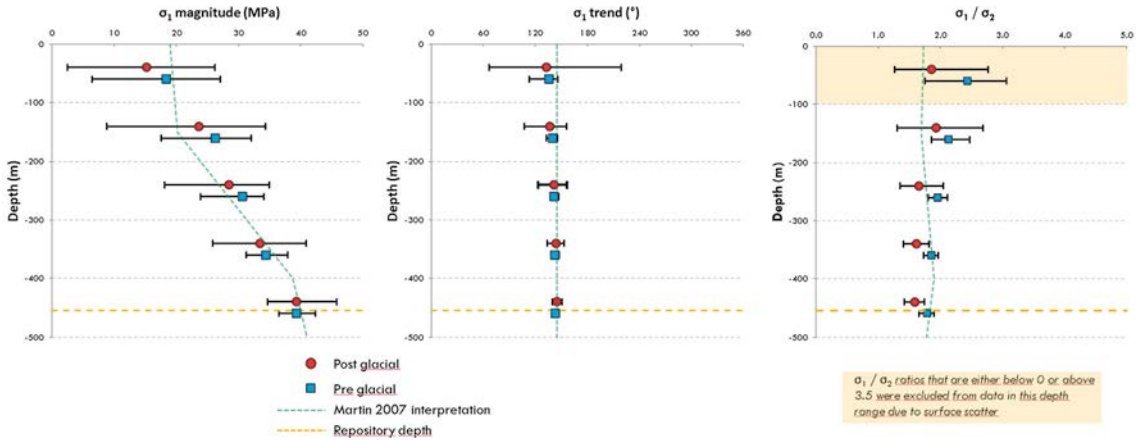


Figure A5b-1. Pre/post glacial mean and variation of σ_1 magnitude, trend and σ_1/σ_2 ratio for hundred meter intervals, Case 2-1.

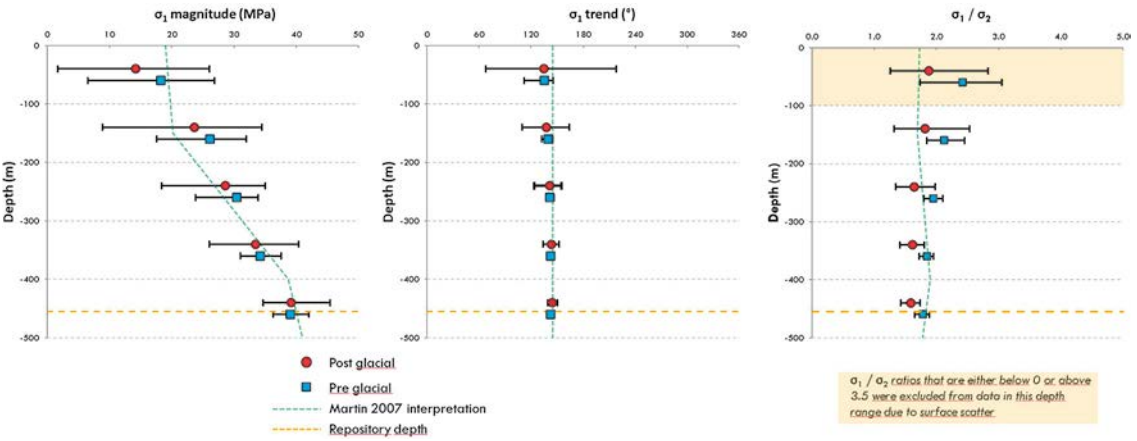


Figure A5b-2. Pre/post glacial mean and variation of σ_1 magnitude, trend and σ_1/σ_2 ratio for hundred meter intervals, Case 2-2.

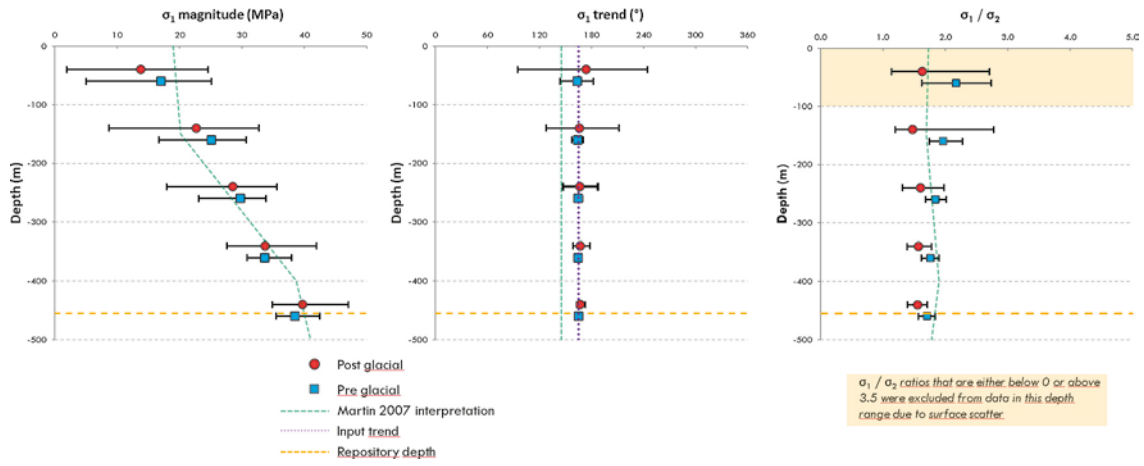


Figure A5b-3. Pre/post glacial mean and variation of σ_1 magnitude, trend and σ_1/σ_2 ratio for hundred meter intervals, Case 2-3.

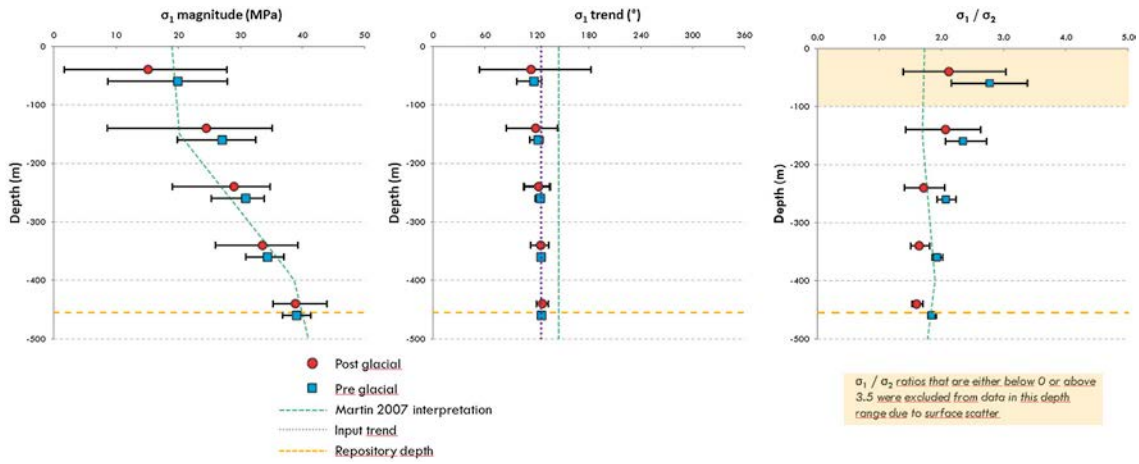


Figure A5b-4. Pre/post glacial mean and variation of σ_1 magnitude, trend and σ_1/σ_2 ratio for hundred meter intervals, Case 2-4.

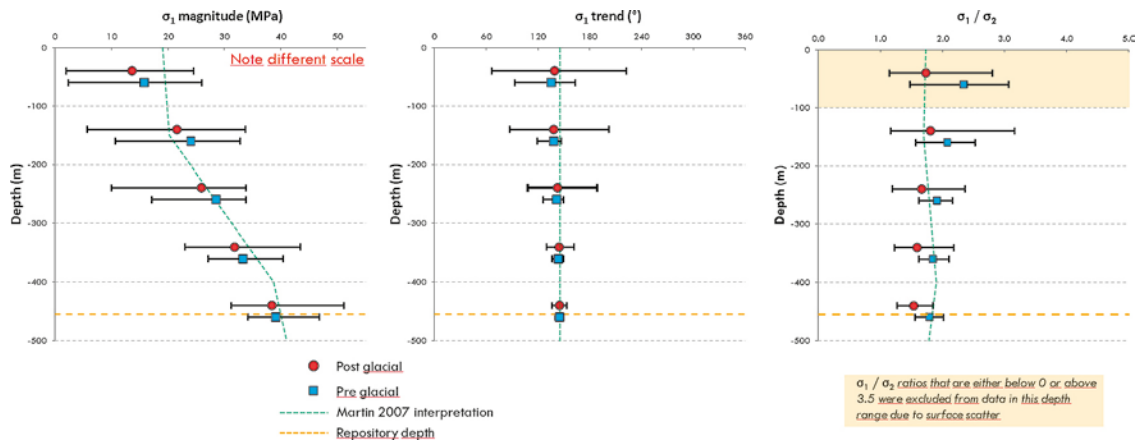


Figure A5b-5. Pre/post glacial mean and variation of σ_1 magnitude, trend and σ_1/σ_2 ratio for hundred meter intervals, Case 2-5.

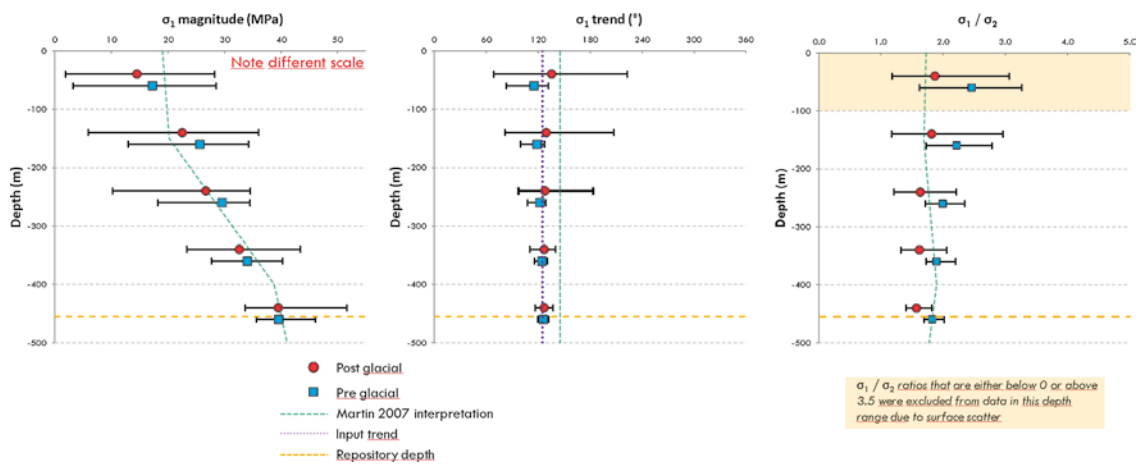


Figure A5b-6. Pre/post glacial mean and variation of σ_1 magnitude, trend and σ_1/σ_2 ratio for hundred meter intervals, Case 2-6.

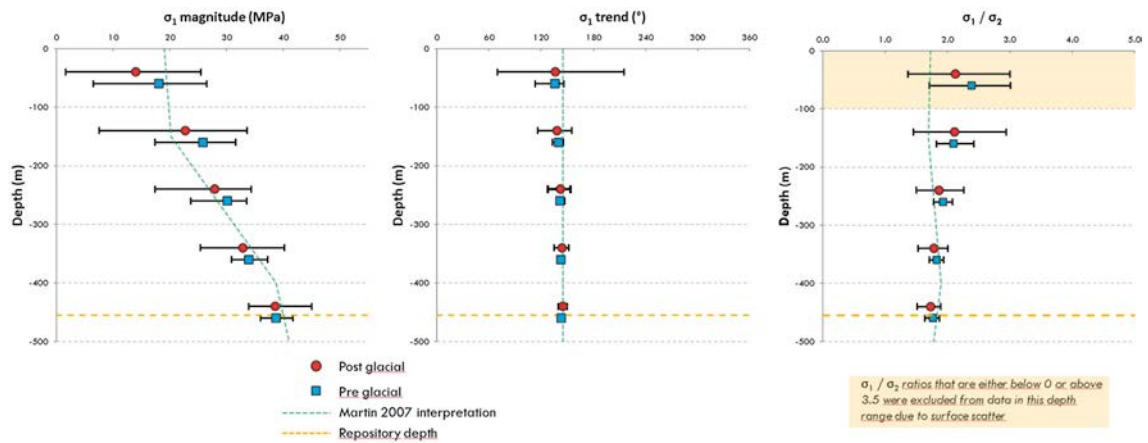


Figure A5b-7. Pre/post glacial mean and variation of σ_1 magnitude, trend and σ_1/σ_2 ratio for hundred meter intervals, Case 2-7.

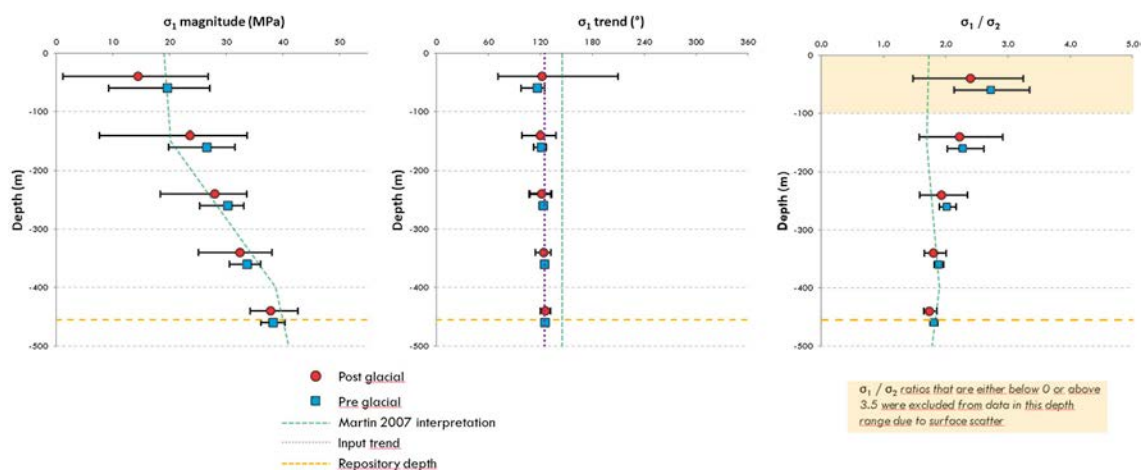


Figure A5b-8. Pre/post glacial mean and variation of σ_1 magnitude, trend and σ_1/σ_2 ratio for hundred meter intervals, Case 2-8.

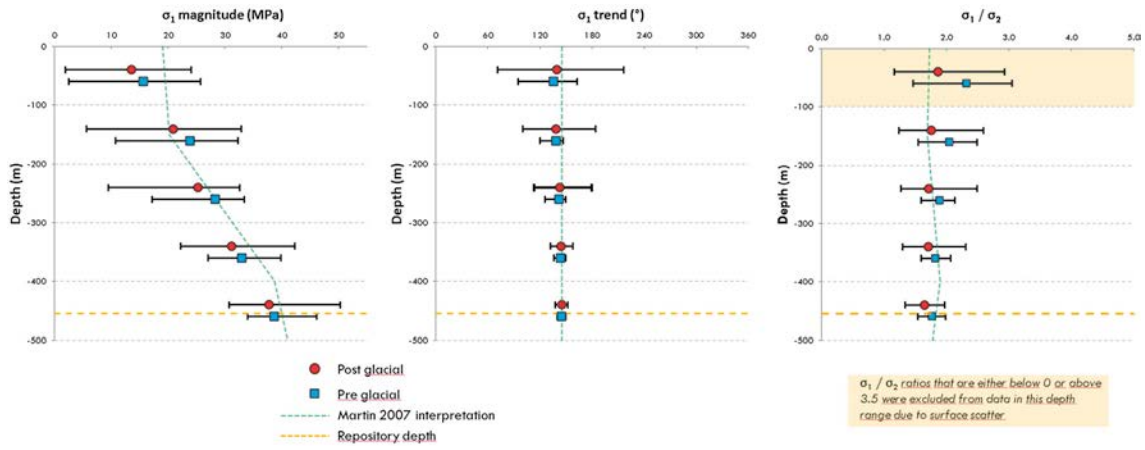


Figure A5b-9. Pre/post glacial mean and variation of σ_1 magnitude, trend and σ_1/σ_2 ratio for hundred meter intervals, Case 2-9.

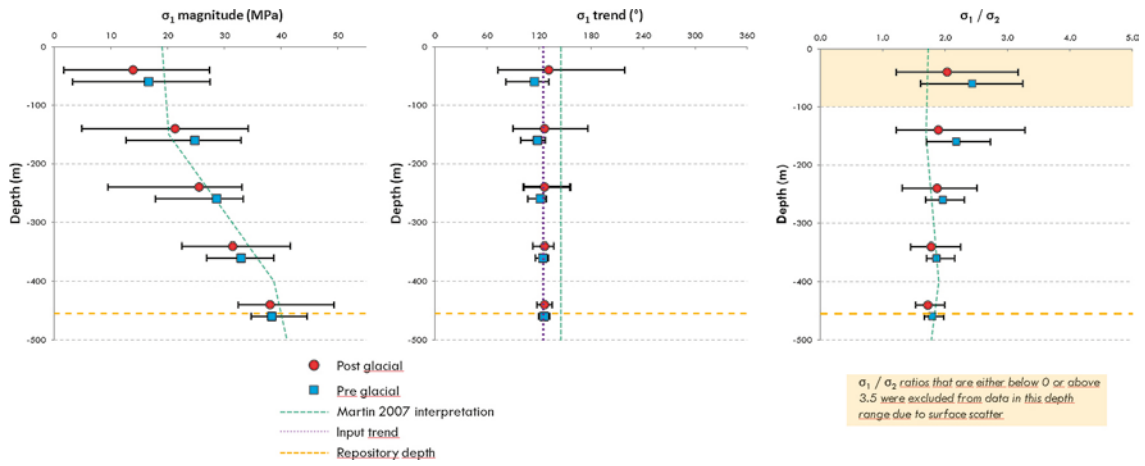


Figure A5b-10. Pre/post glacial mean and variation of σ_1 magnitude, trend and σ_1/σ_2 ratio for hundred meter intervals, Case 2-10.

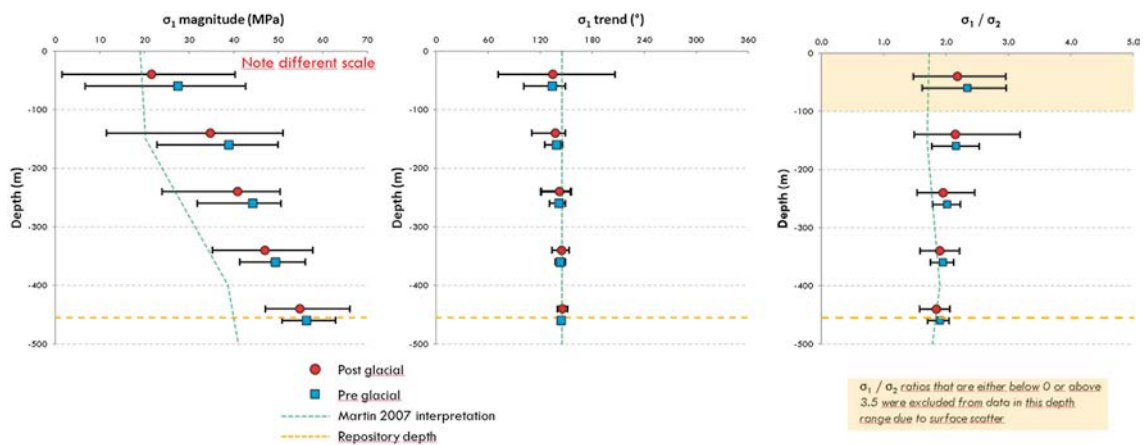


Figure A5b-11. Pre/post glacial mean and variation of σ_1 magnitude, trend and σ_1/σ_2 ratio for hundred meter intervals, Case 2-11.

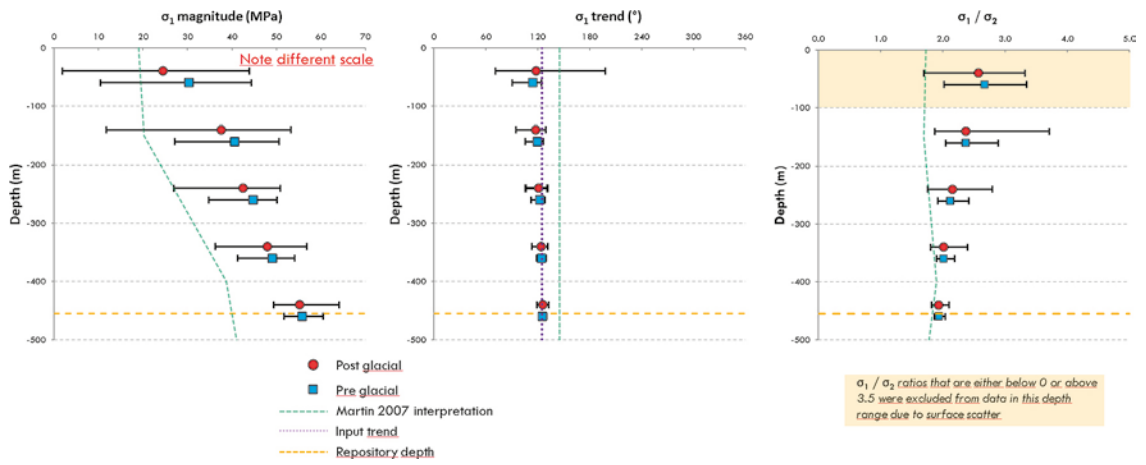


Figure A5b-12. Pre/post glacial mean and variation of σ_1 magnitude, trend and σ_1/σ_2 ratio for hundred meter intervals, Case 2-12.

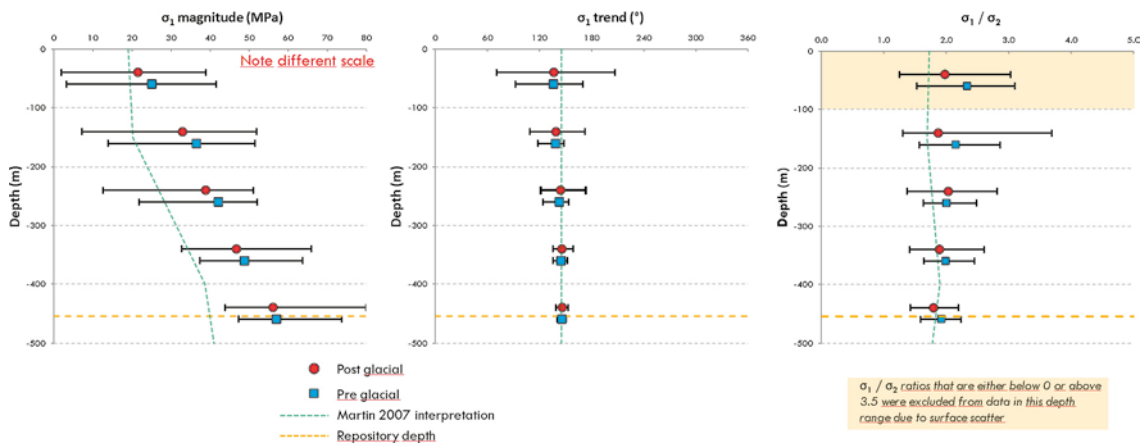


Figure A5b-13. Pre/post glacial mean and variation of σ_1 magnitude, trend and σ_1/σ_2 ratio for hundred meter intervals, Case 2-13.

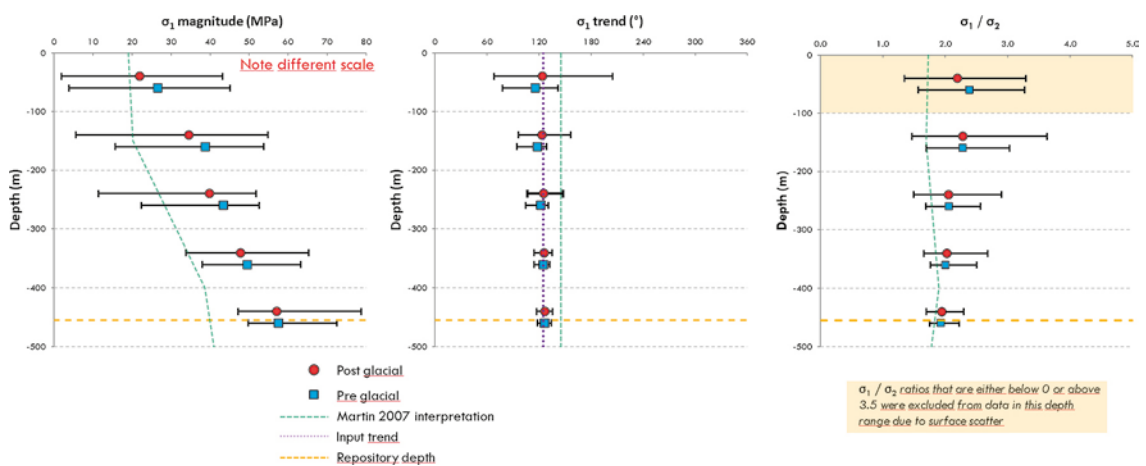


Figure A5b-14. Pre/post glacial mean and variation of σ_1 magnitude, trend and σ_1/σ_2 ratio for hundred meter intervals, Case 2-14.

Simulation Phase 1 – frequency of σ_1 trend and magnitude variation at repository depth

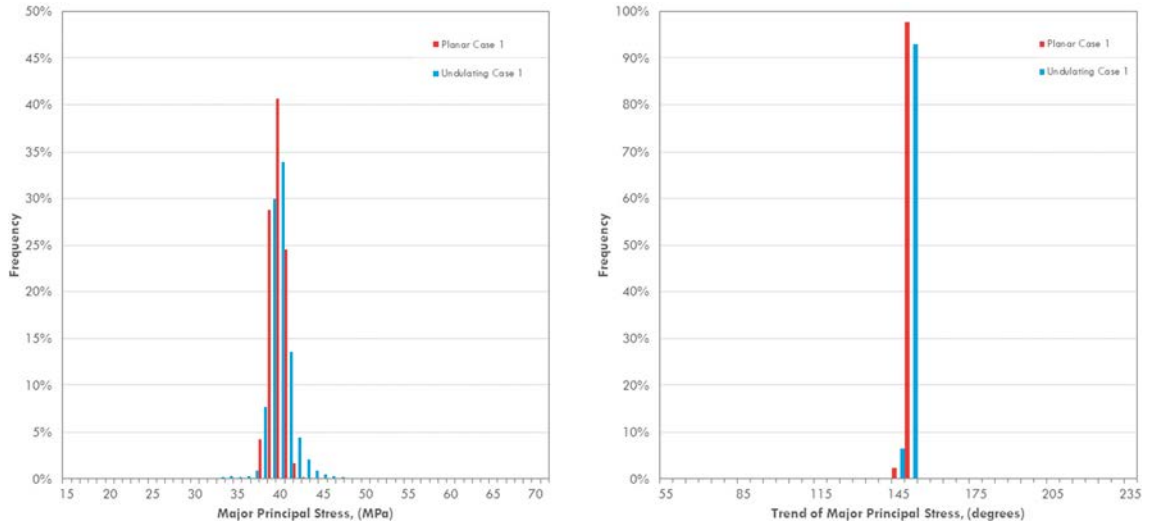


Figure A6a-1. Distributions of σ_1 magnitude and trend at repository depth, Case 1-1.

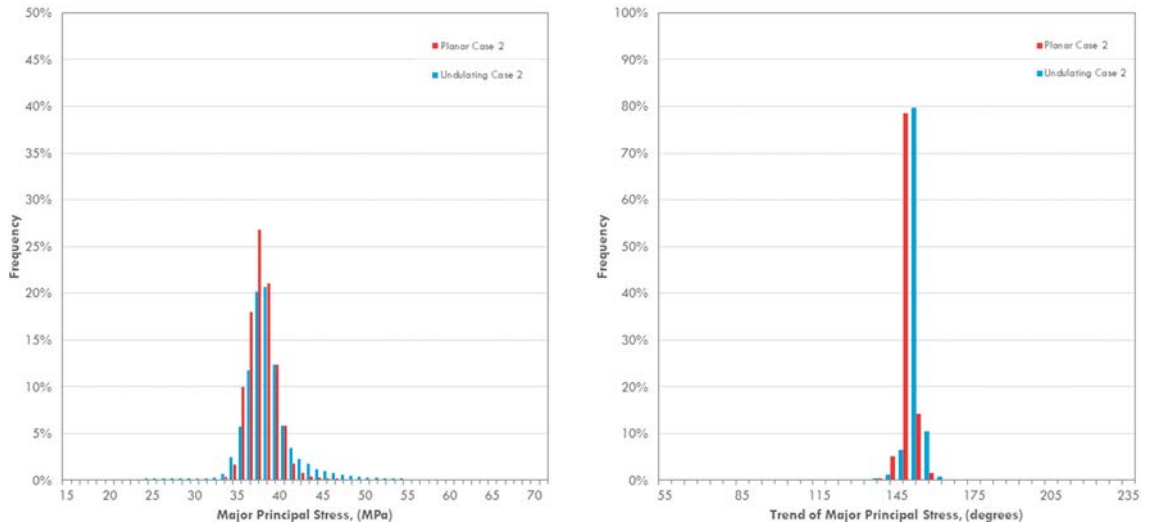


Figure A6a-2. Distributions of σ_1 magnitude and trend at repository depth, Case 1-2.

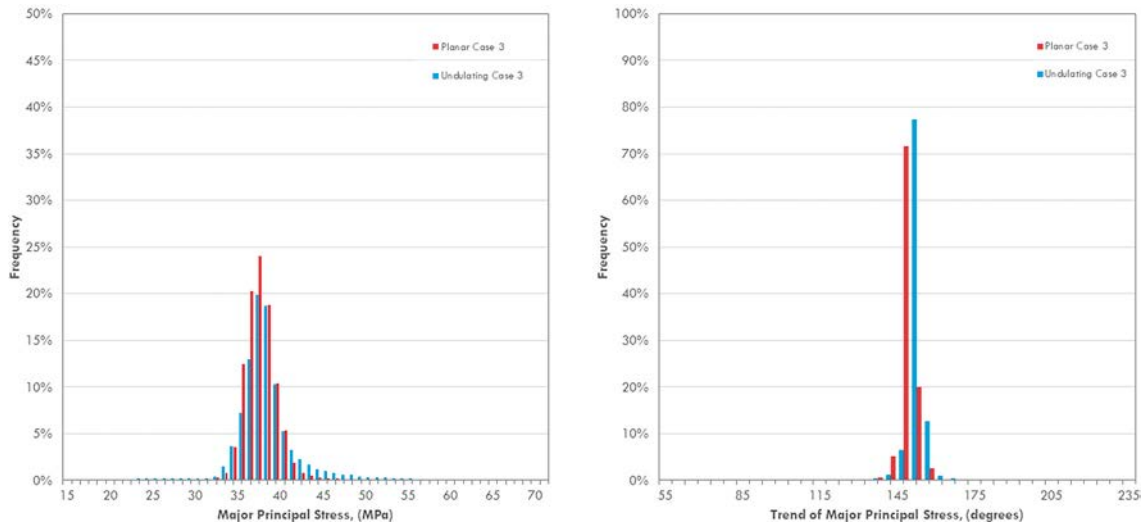


Figure A6a-3. Distributions of σ_1 magnitude and trend at repository depth, Case 1-3.

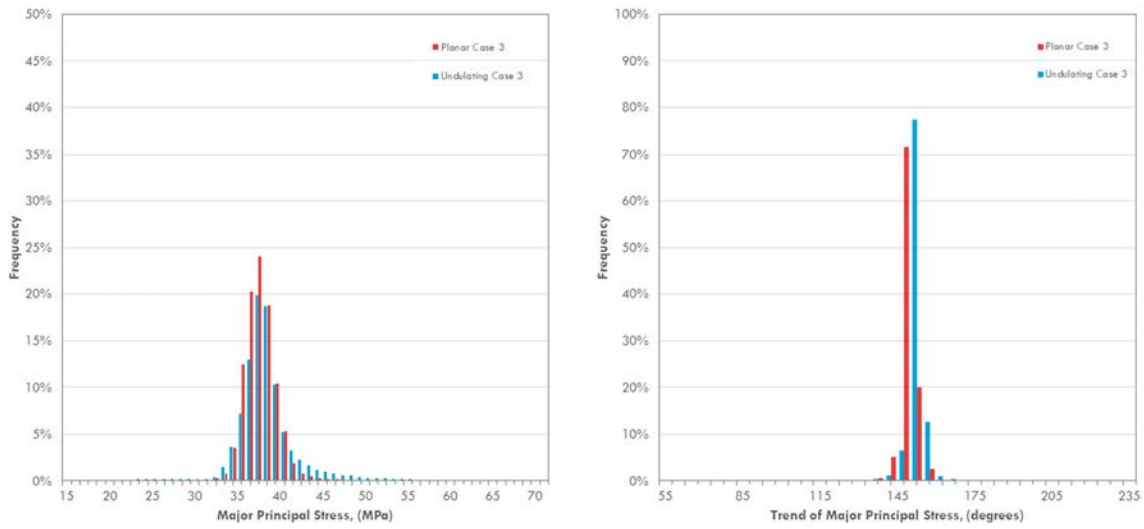


Figure A6a-4. Distributions of σ_1 magnitude and trend at repository depth, Case 1-4.

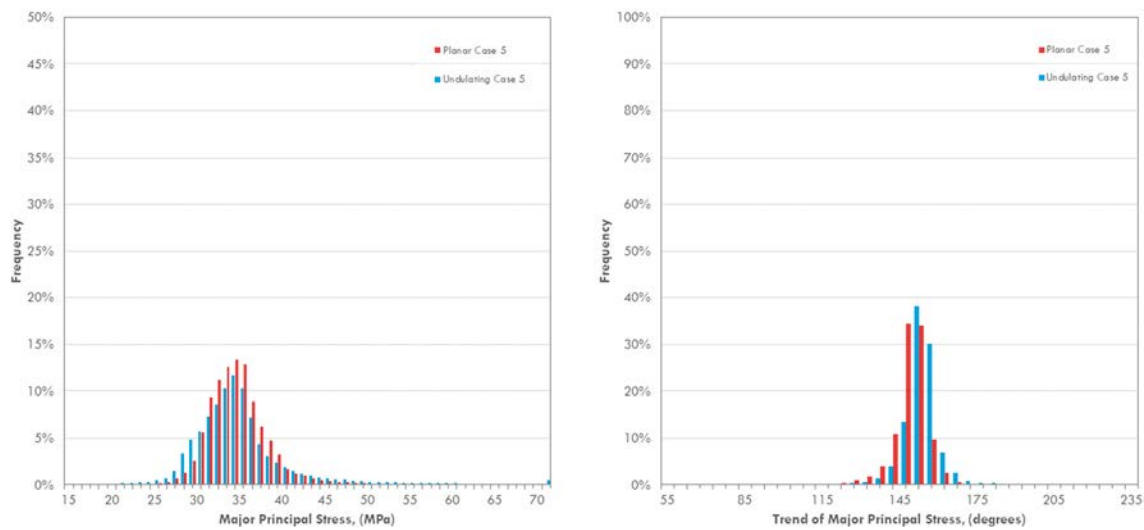


Figure A6a-5. Distributions of σ_1 magnitude and trend at repository depth, Case 1-5.

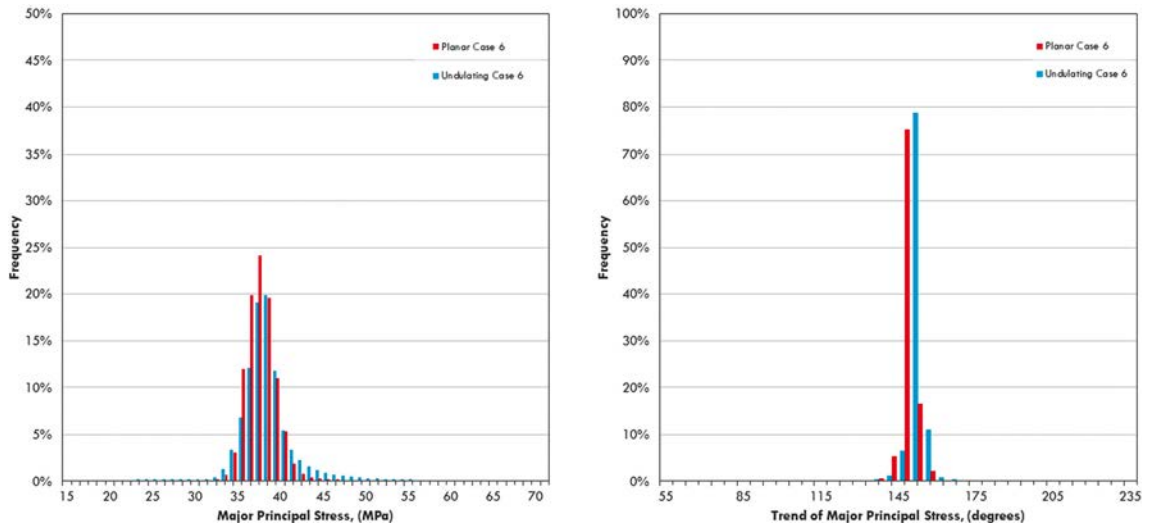


Figure A6a-6. Distributions of σ_1 magnitude and trend at repository depth, Case 1-6.

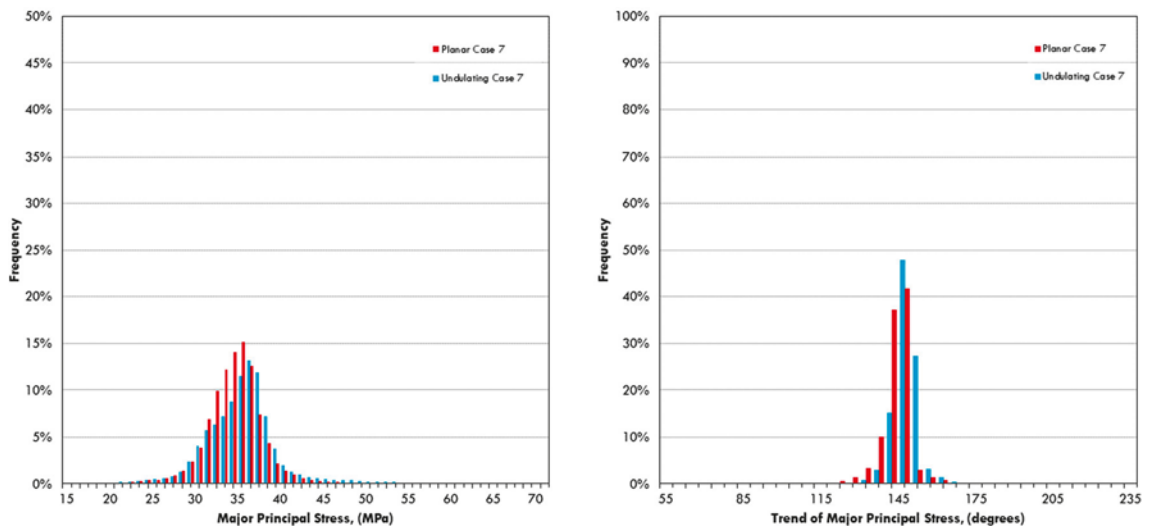


Figure A6a-7. Distributions of σ_1 magnitude and trend at repository depth, Case 1-7.

Simulation Phase 2 – pre/post glacial frequency of σ_1 trend and magnitude variation at repository depth

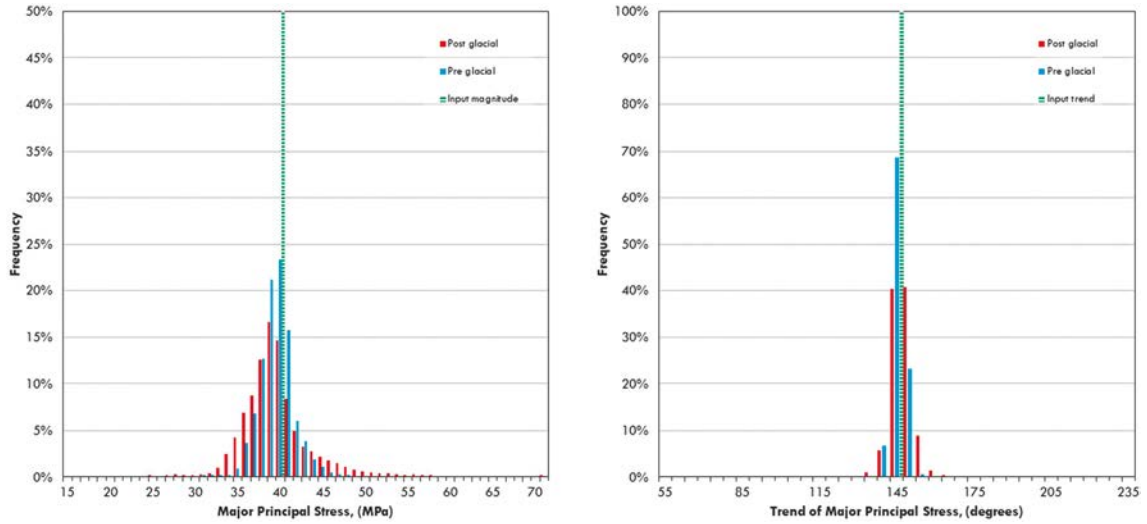


Figure A6b-1. Pre/post glacial distributions of σ_1 magnitude and trend at repository depth, Case 2-1.

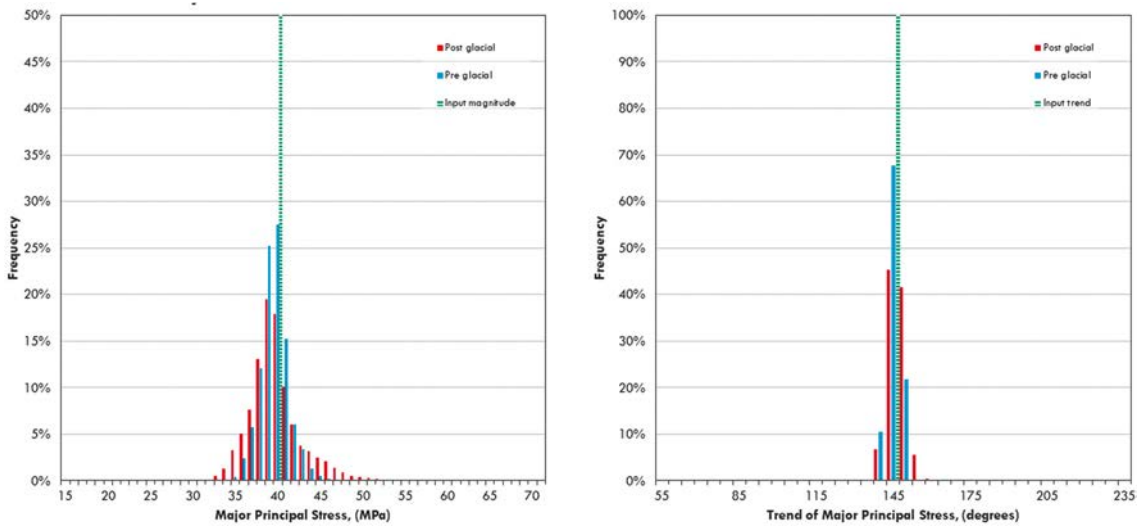


Figure A6b-2. Pre/post glacial distributions of σ_1 magnitude and trend at repository depth, Case 2-2.

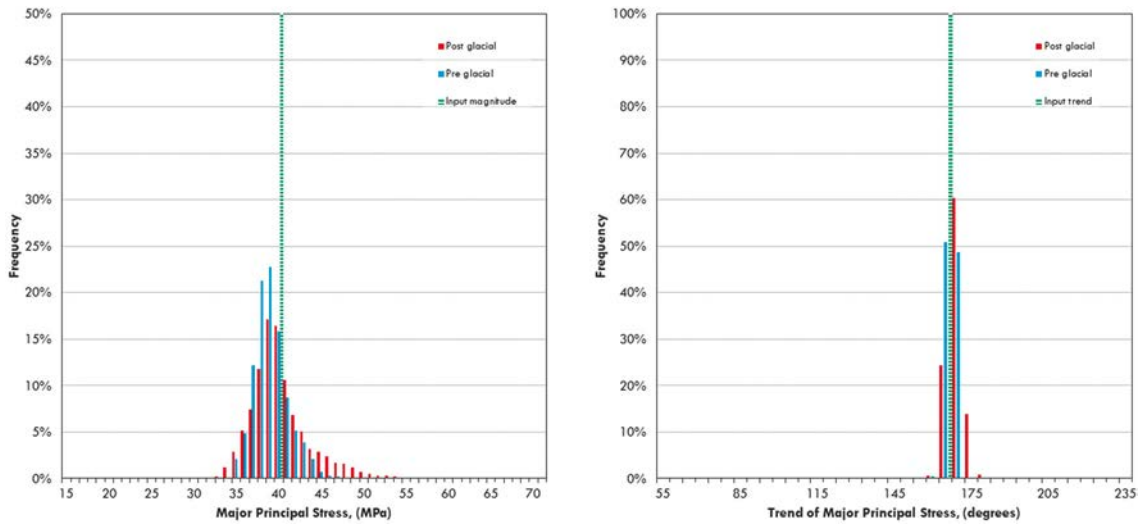


Figure A6b-3. Pre/post glacial distributions of σ_1 magnitude and trend at repository depth, Case 2-3.

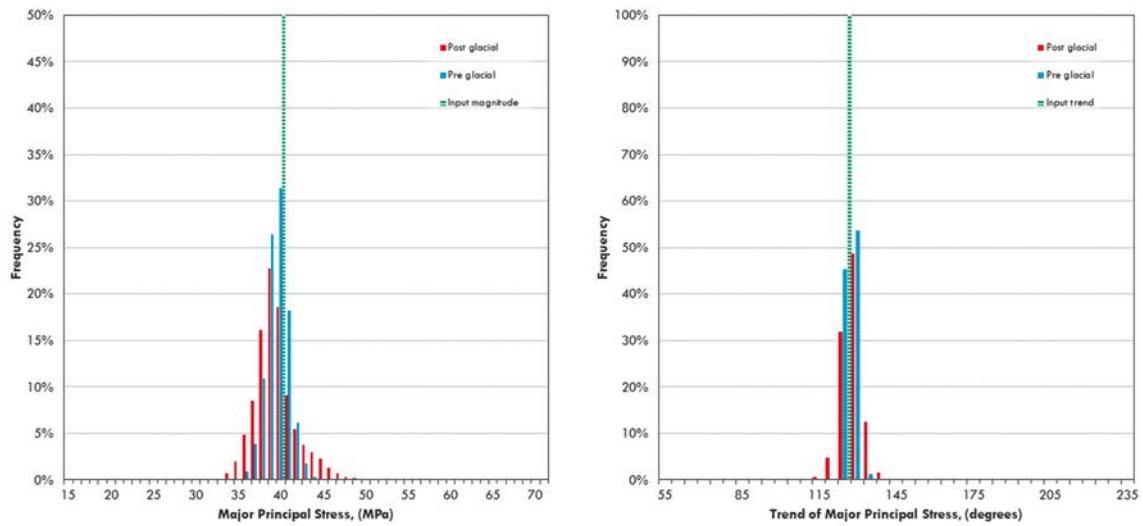


Figure A6b-4. Pre/post glacial distributions of σ_1 magnitude and trend at repository depth, Case 2-4.

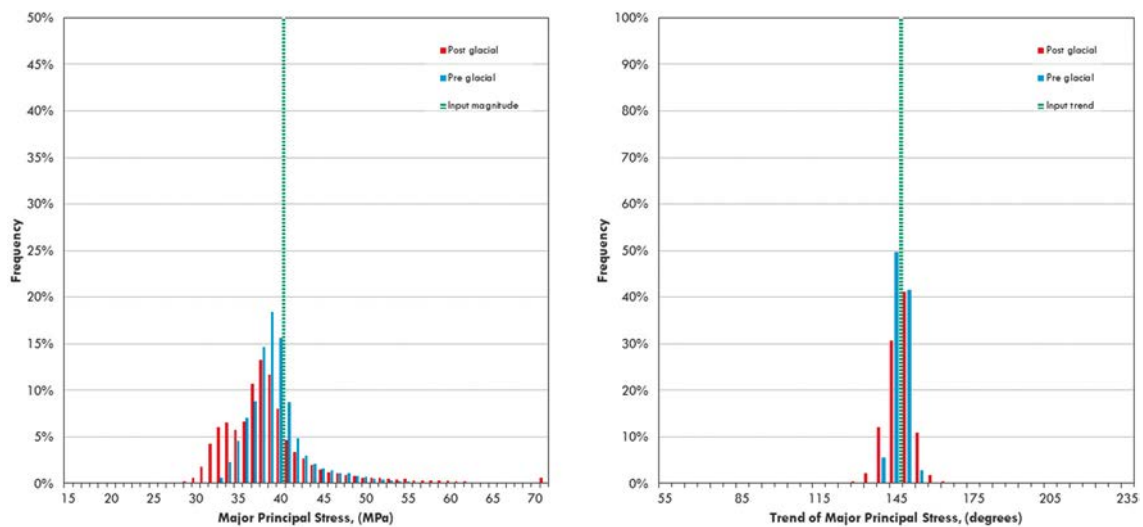


Figure A6b-5. Pre/post glacial distributions of σ_1 magnitude and trend at repository depth, Case 2-5.

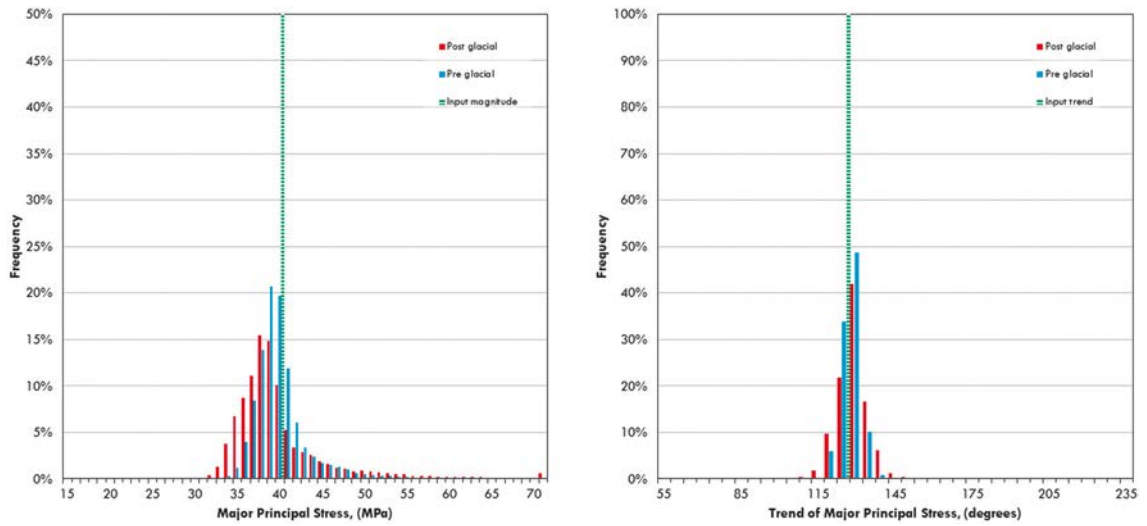


Figure A6b-6. Pre/post glacial distributions of σ_1 magnitude and trend at repository depth, Case 2-6.

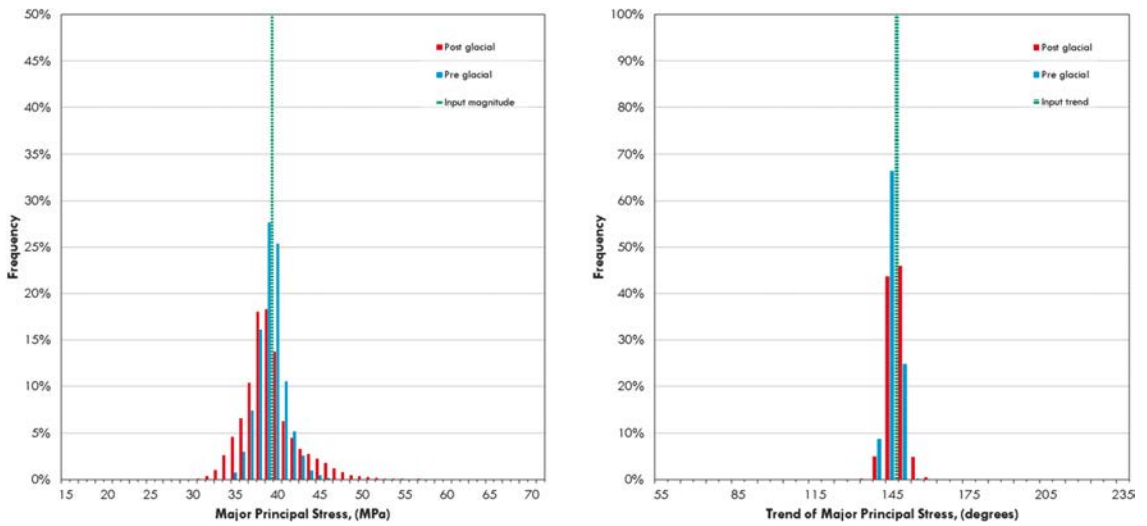


Figure A6b-7. Pre/post glacial distributions of σ_1 magnitude and trend at repository depth, Case 2-7.

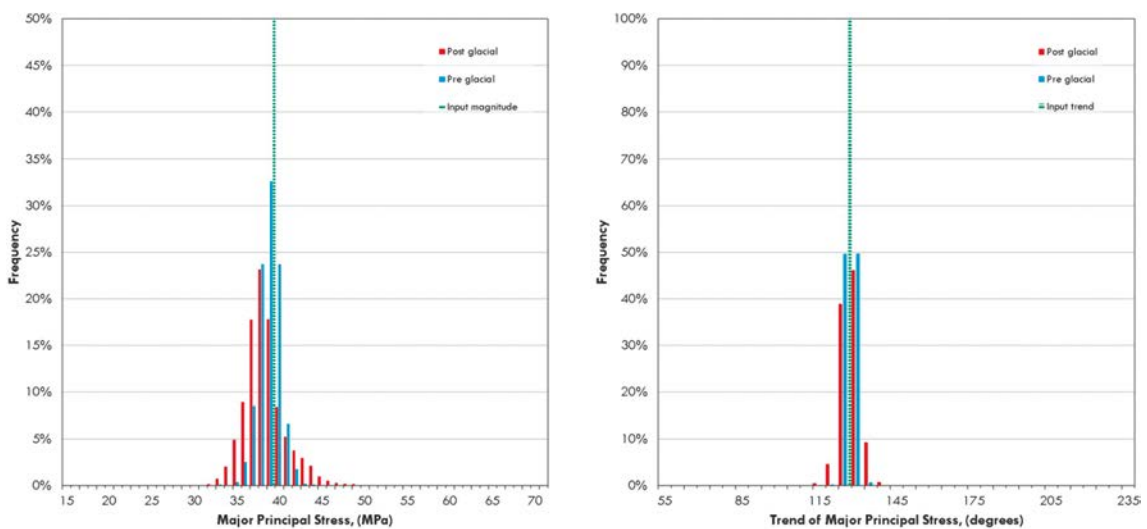


Figure A6b-8. Pre/post glacial distributions of σ_1 magnitude and trend at repository depth, Case 2-8.

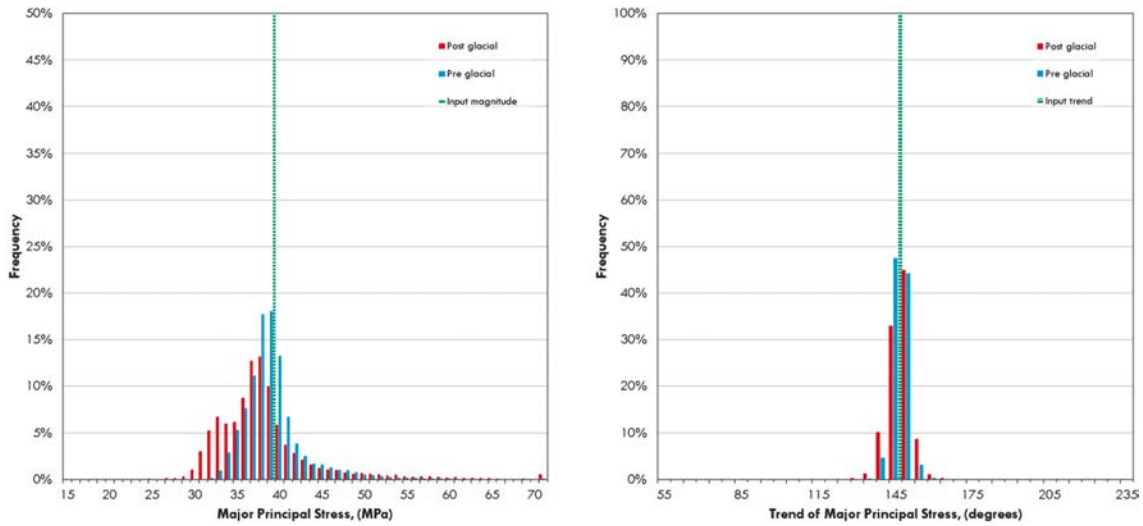


Figure A6b-9. Pre/post glacial distributions of σ_1 magnitude and trend at repository depth, Case 2-9.

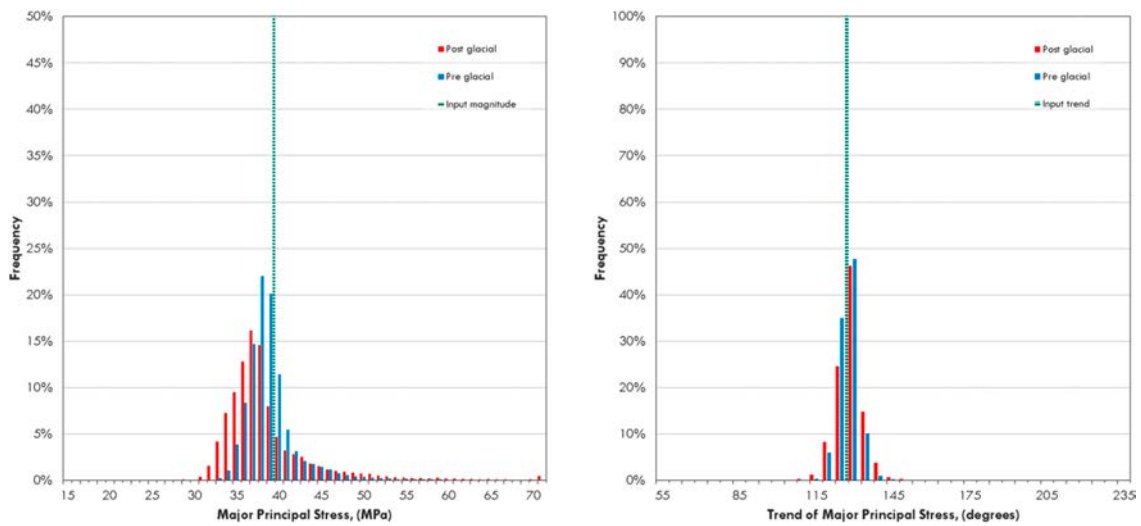


Figure A6b-10. Pre/post glacial distributions of σ_1 magnitude and trend at repository depth, Case 2-10.

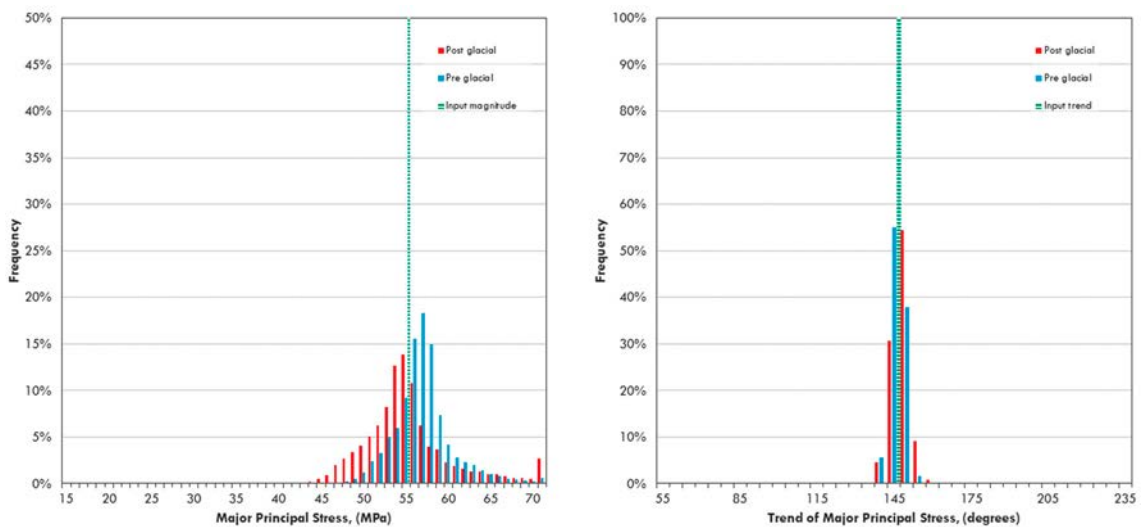


Figure A6b-11. Pre/post glacial distributions of σ_1 magnitude and trend at repository depth, Case 2-11.

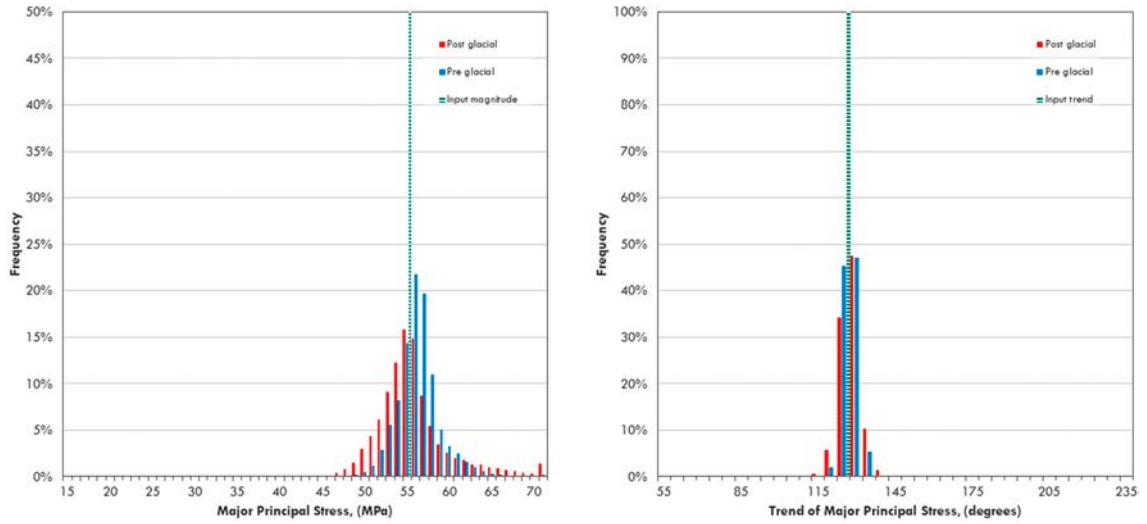


Figure A6b-12. Pre/post glacial distributions of σ_1 magnitude and trend at repository depth, Case 2-12.

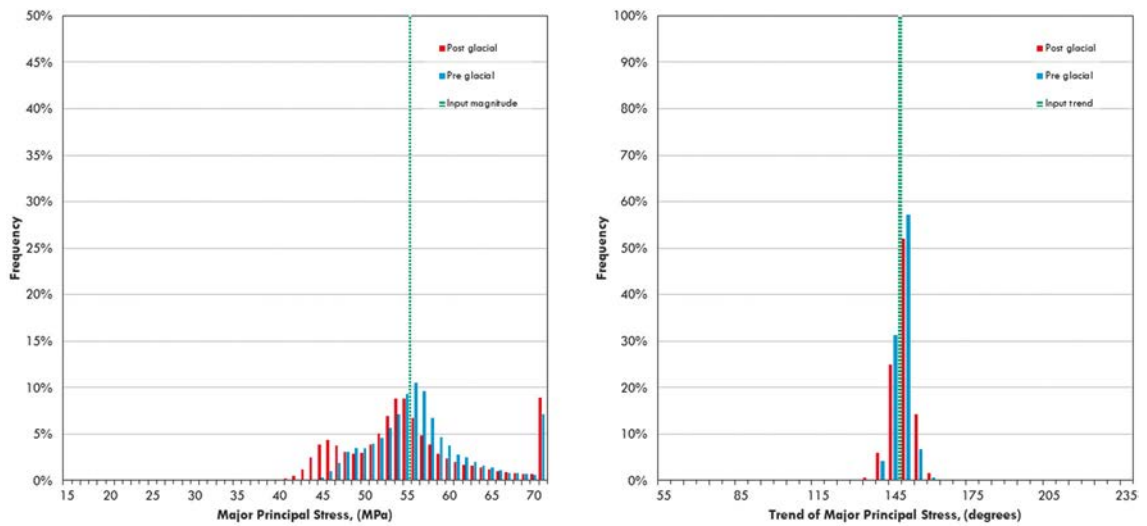


Figure A6b-13. Pre/post glacial distributions of σ_1 magnitude and trend at repository depth, Case 2-13.

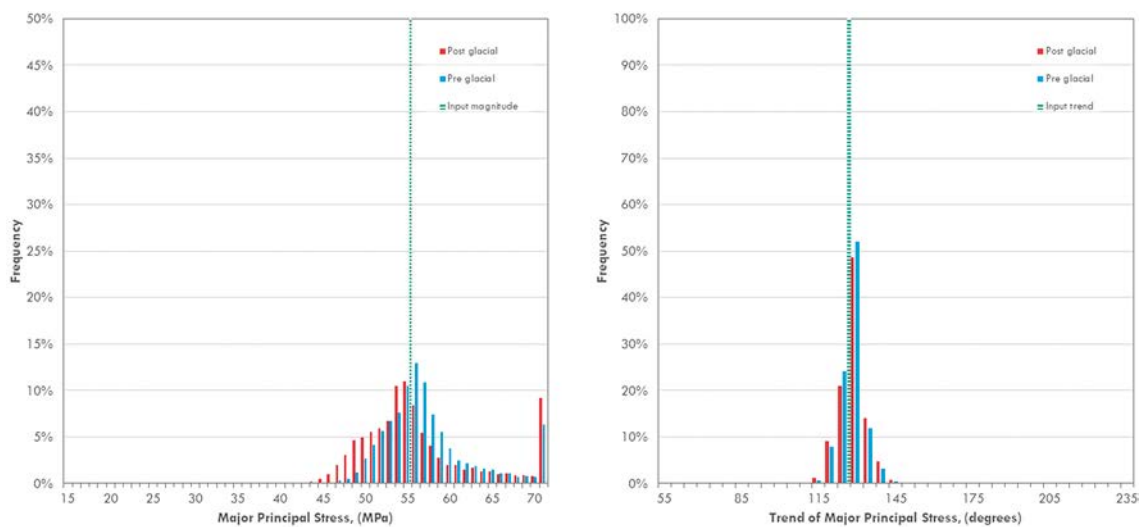


Figure A6b-14. Pre/post glacial distributions of σ_1 magnitude and trend at repository depth, Case 2-14.

Simulation Phase 1 – σ_1 magnitude and trend correlation with stress measurements

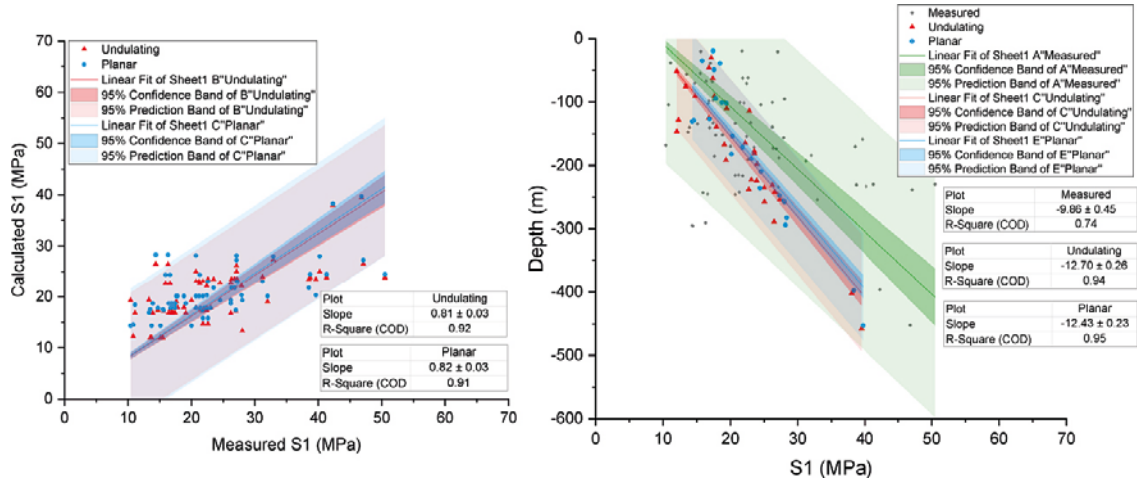


Figure A7a-1. Case 1-1, σ_1 magnitude correlation with OC stress measurements.

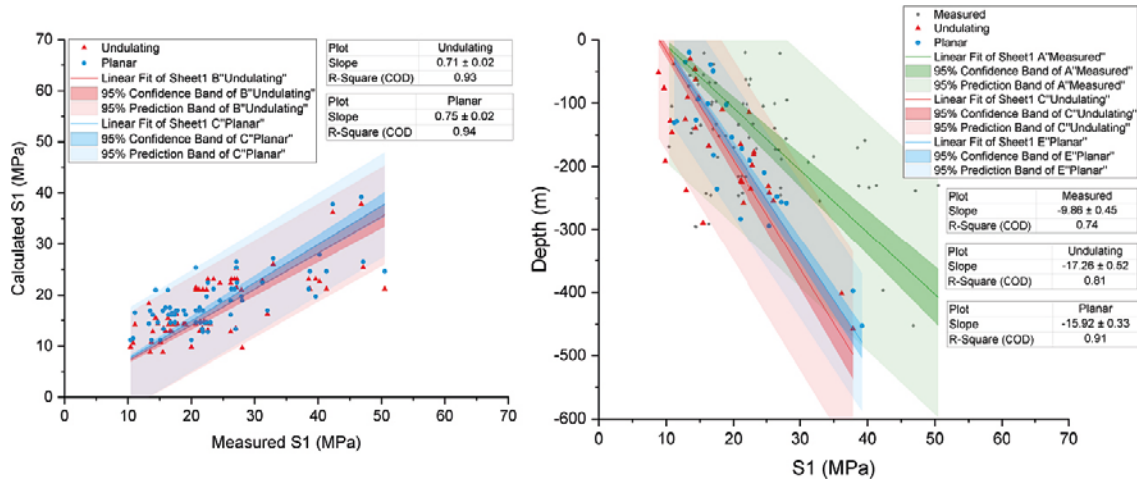


Figure A7a-2. Case 1-2, σ_2 magnitude correlation with OC stress measurements.

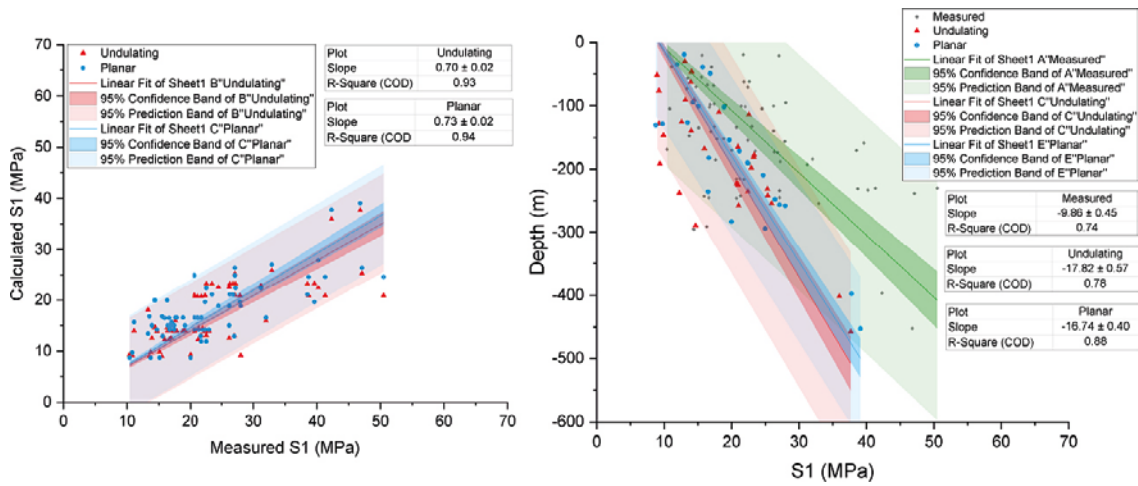


Figure A7a-3. Case 1-3, σ_1 magnitude correlation with OC stress measurements.

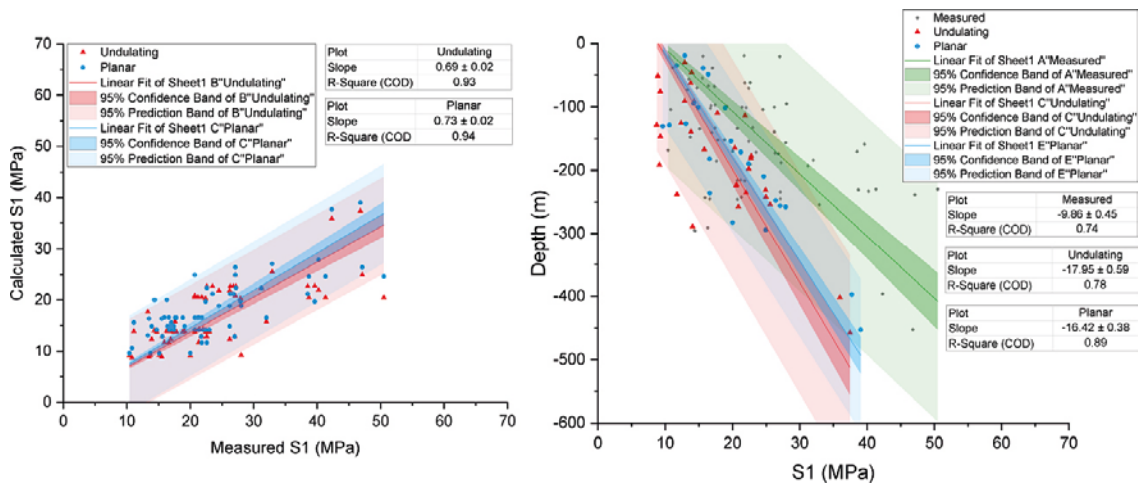


Figure A7a-4. Case 1-4, σ_2 magnitude correlation with OC stress measurements.

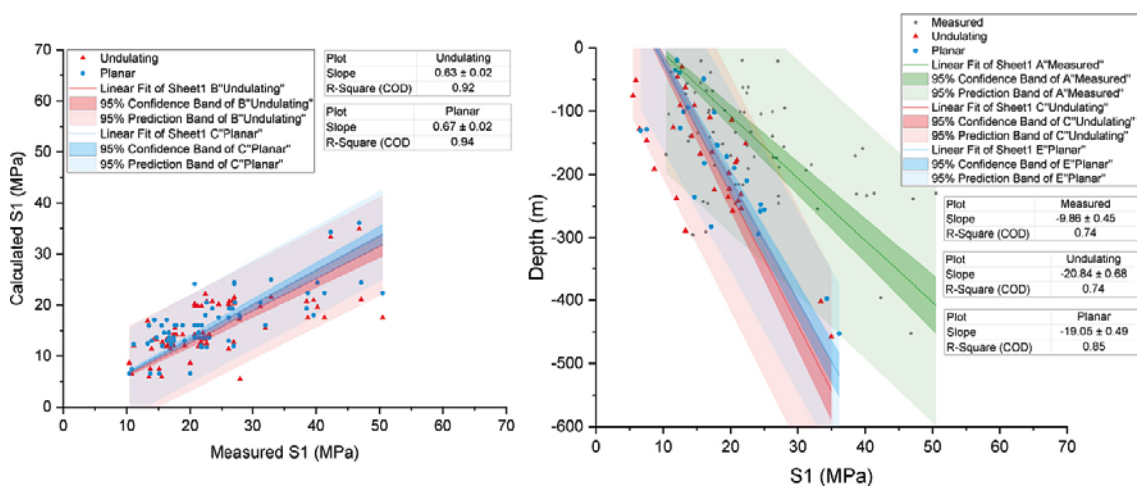


Figure A7a-5. Case 1-5, σ_1 magnitude correlation with OC stress measurements.

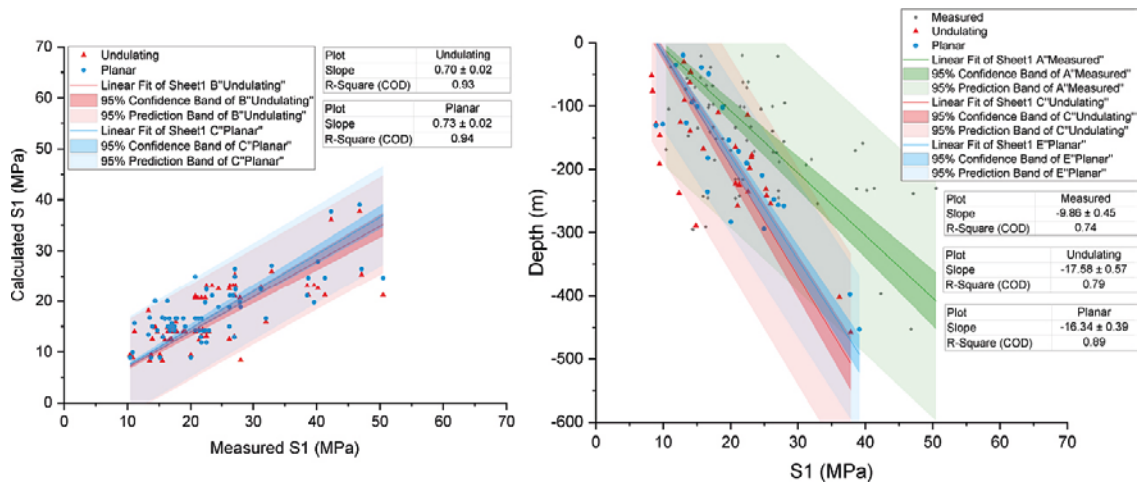


Figure A7a-6. Case I-6, σ_1 magnitude correlation with OC stress measurements.

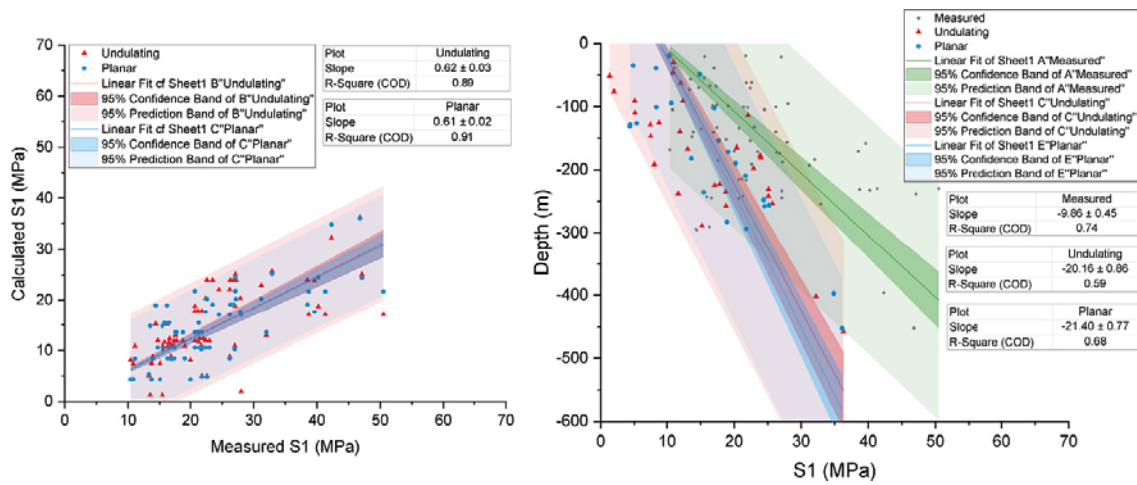


Figure A7a-7. Case I-7, σ_2 magnitude correlation with OC stress measurements.

Simulation Phase 2 – post glacial σ_1 and σ_2 and σ_3 magnitude correlation with stress measurements

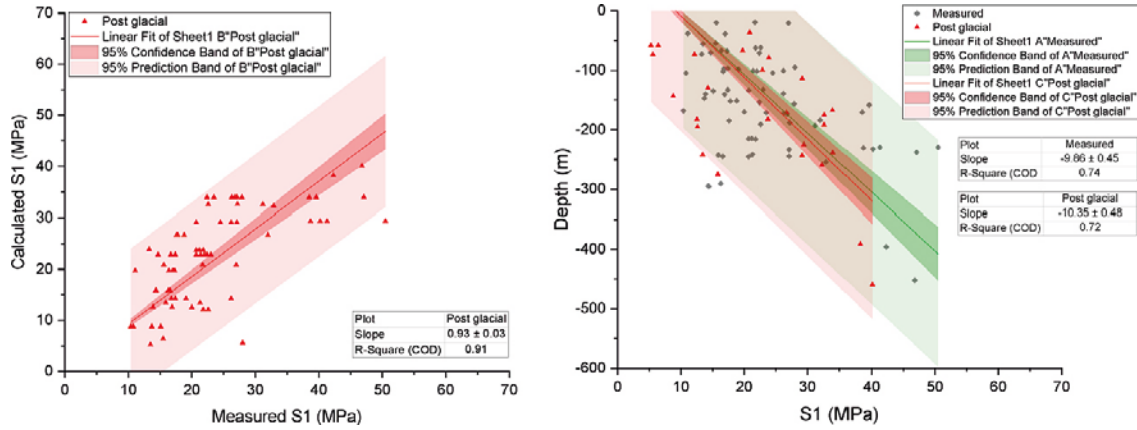


Figure A7b-1. Case 2-1, σ_1 magnitude correlation with OC stress measurements.

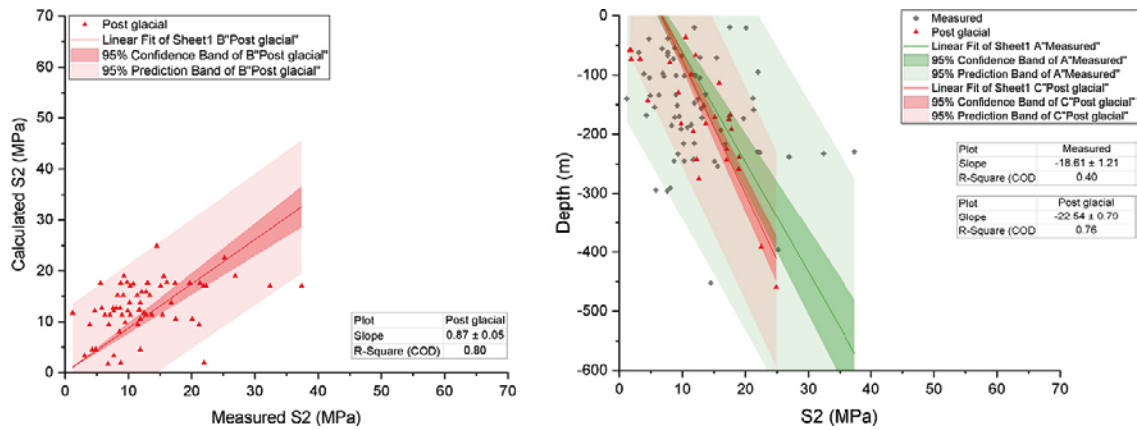


Figure A7b-2. Case 2-1, σ_2 magnitude correlation with OC stress measurements.

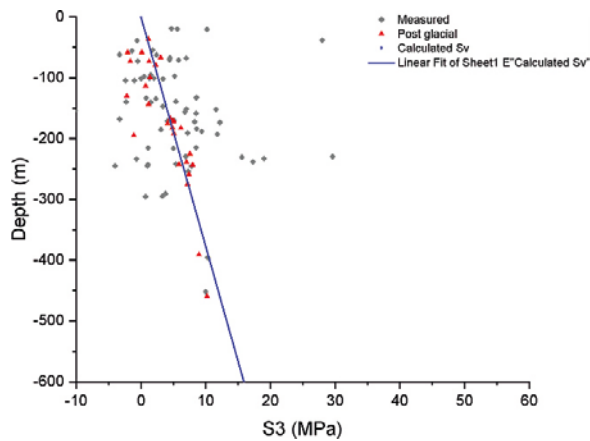


Figure A7b-3. Case 2-1, σ_3 magnitude correlation with OC stress measurements.

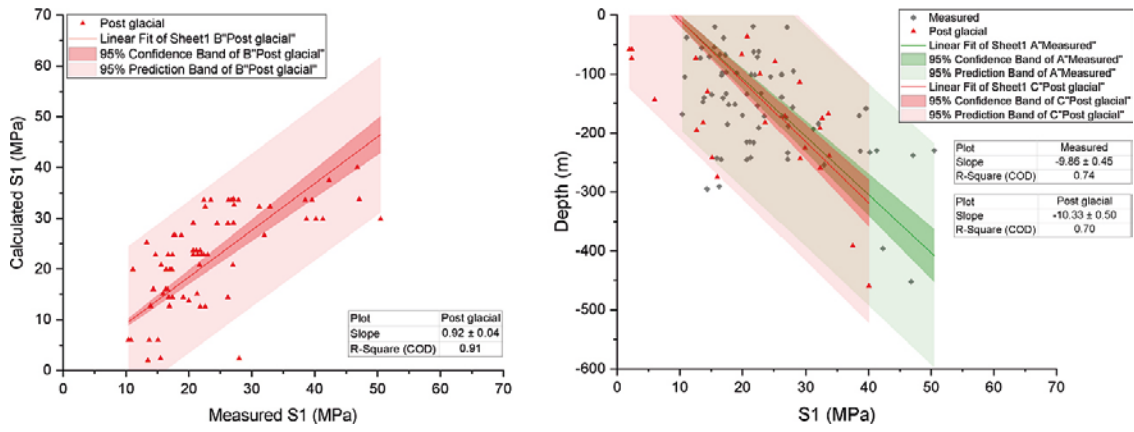


Figure A7b-4. Case 2-2, σ_1 magnitude correlation with OC stress measurements.

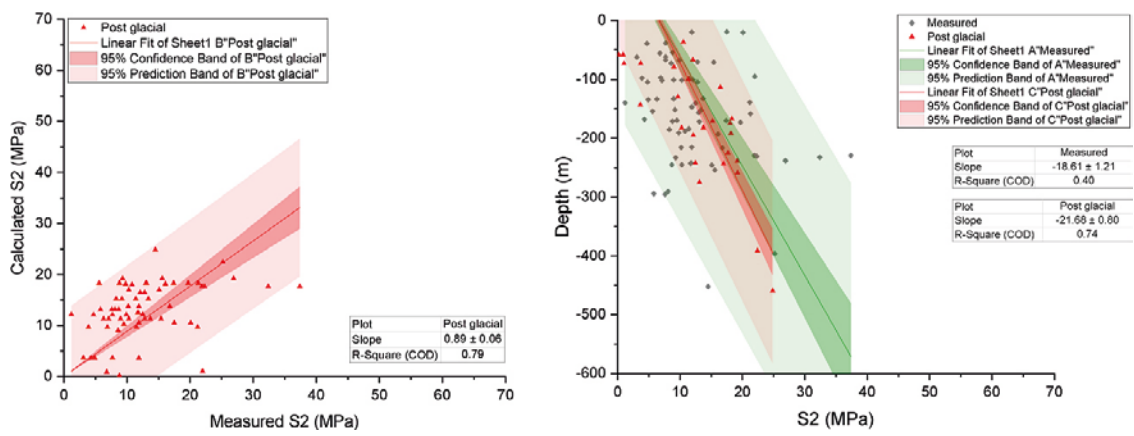


Figure A7b-5. Case 2-2, σ_2 magnitude correlation with OC stress measurements.

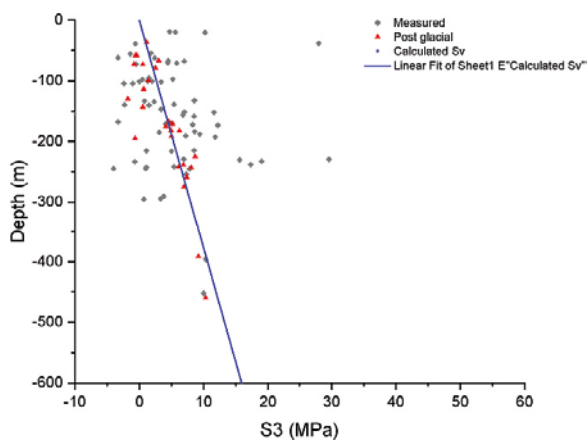


Figure A7b-6. Case 2-2, σ_3 magnitude correlation with OC stress measurements.

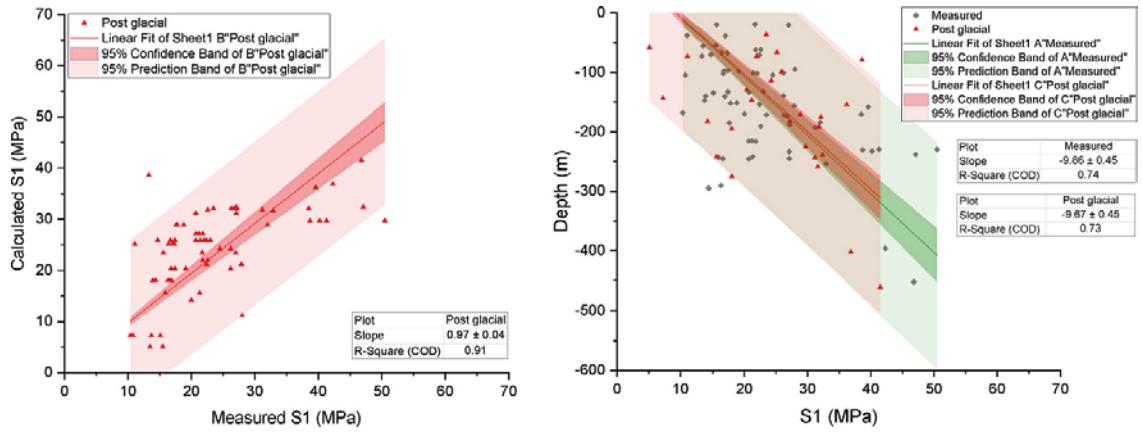


Figure A7b-7. Case 2-3, σ_1 magnitude correlation with OC stress measurements.

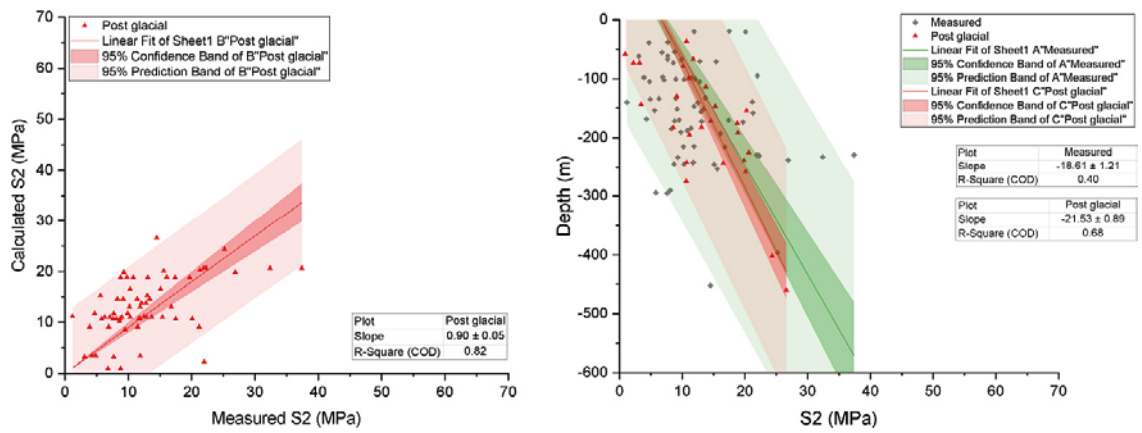


Figure A7b-8. Case 2-3, σ_2 magnitude correlation with OC stress measurements.

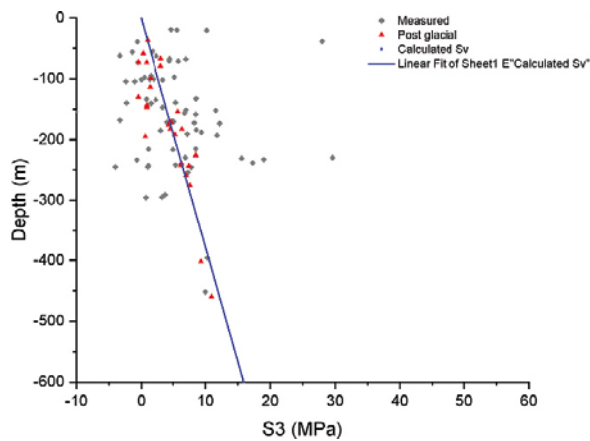


Figure A7b-9. Case 2-3, σ_3 magnitude correlation with OC stress measurements.

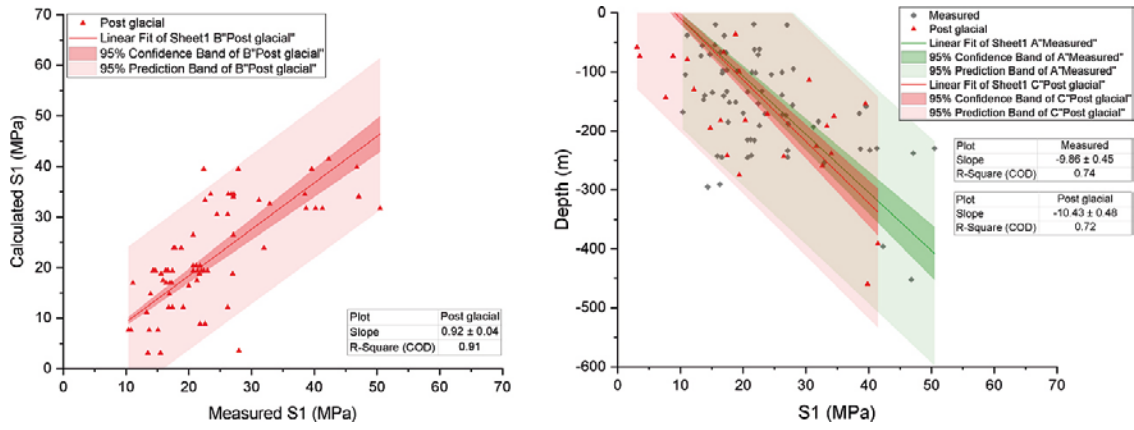


Figure A7b-10. Case 2-4, σ_1 magnitude correlation with OC stress measurements.

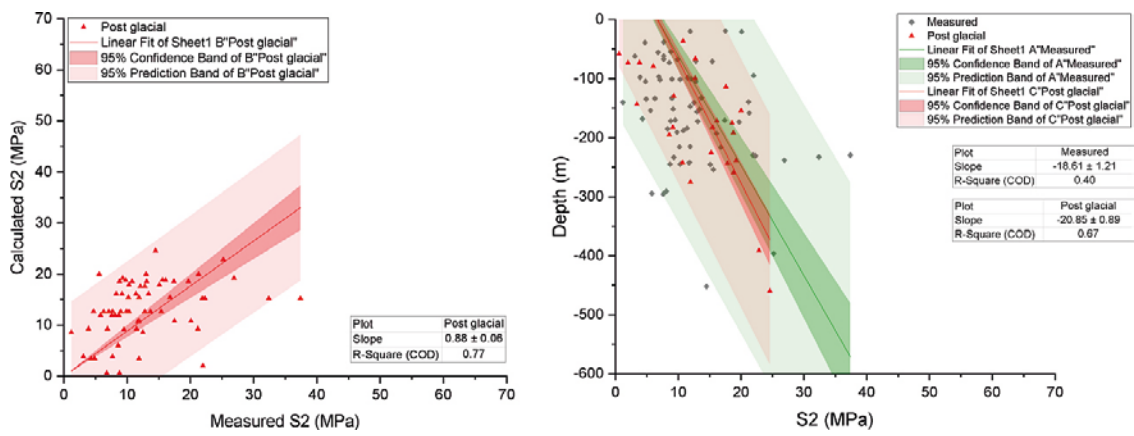


Figure A7b-11. Case 2-4, σ_2 magnitude correlation with OC stress measurements.

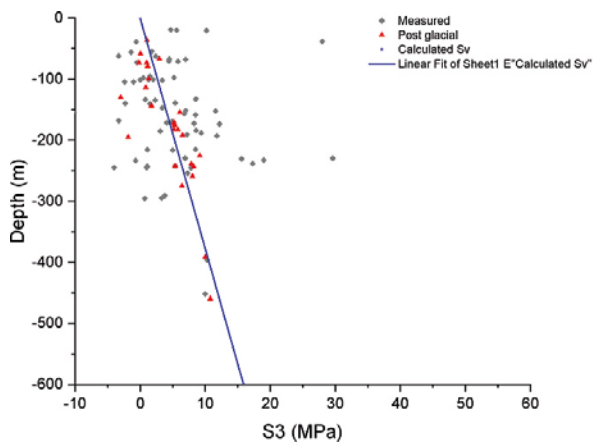


Figure A7b-12. Case 2-4, σ_3 magnitude correlation with OC stress measurements.

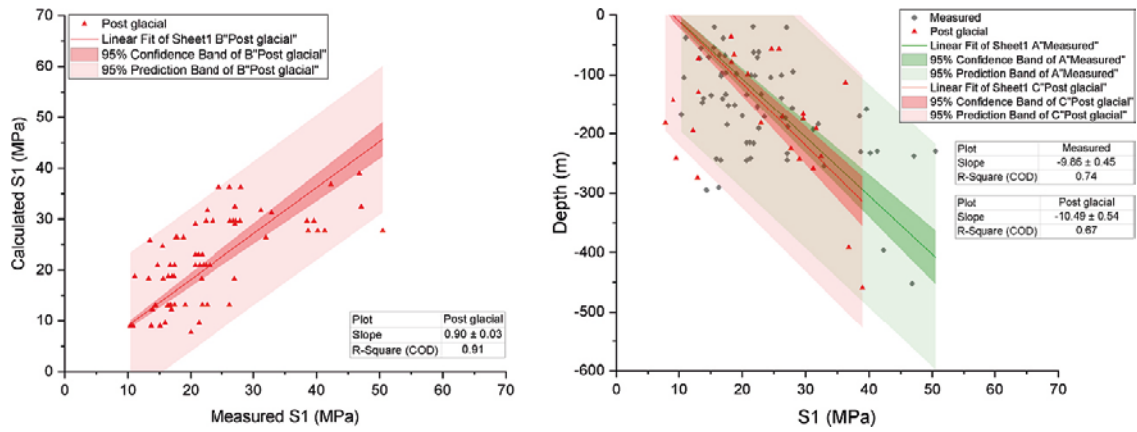


Figure A7b-13. Case 2-5, σ_1 magnitude correlation with OC stress measurements.

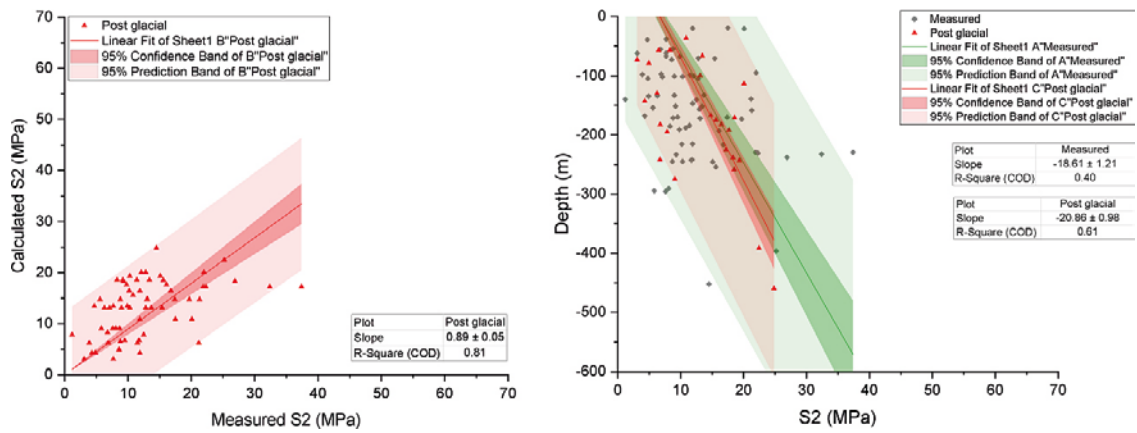


Figure A7b-14. Case 2-5, σ_2 magnitude correlation with OC stress measurements.

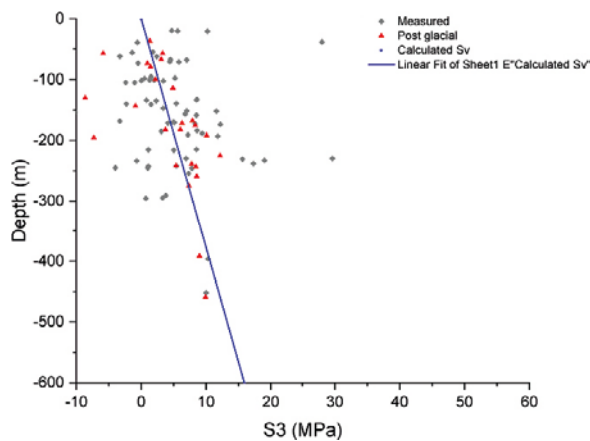


Figure A7b-15. Case 2-5, σ_3 magnitude correlation with OC stress measurements.

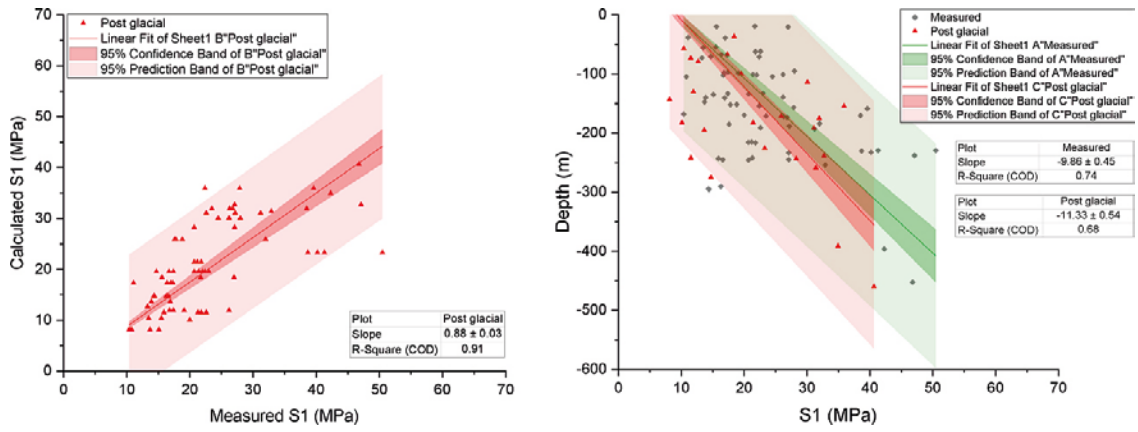


Figure A7b-16. Case 2-6, σ_1 magnitude correlation with OC stress measurements.

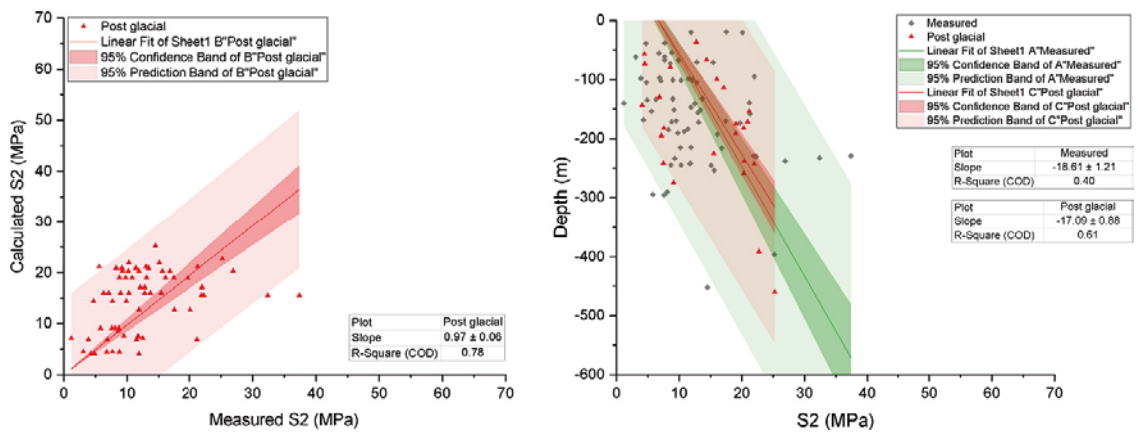


Figure A7b-17. Case 2-6, σ_2 magnitude correlation with OC stress measurements.

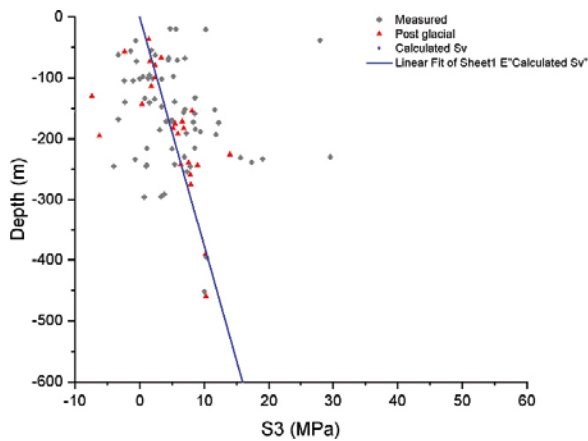


Figure A7b-18. Case 2-6, σ_3 magnitude correlation with OC stress measurements.

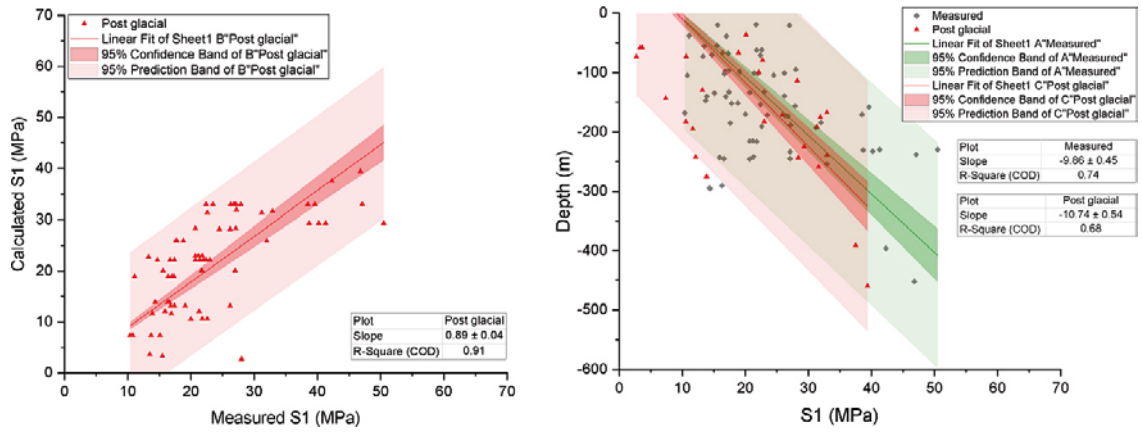


Figure A7b-19. Case 2-7, σ_1 magnitude correlation with OC stress measurements.

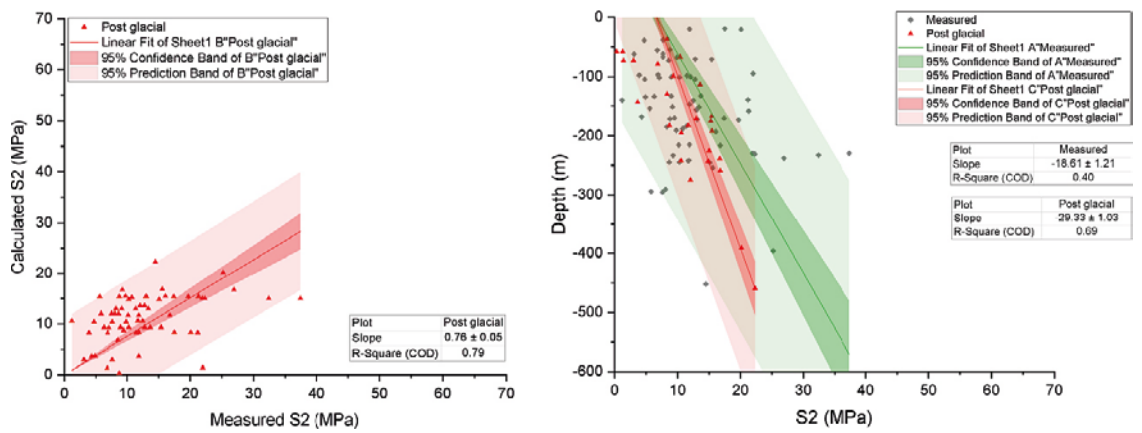


Figure A7b-20. Case 2-7, σ_2 magnitude correlation with OC stress measurements.

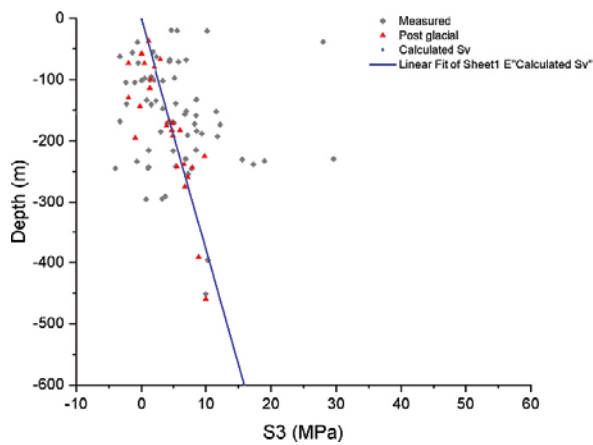


Figure A7b-21. Case 2-7, σ_3 magnitude correlation with OC stress measurements.

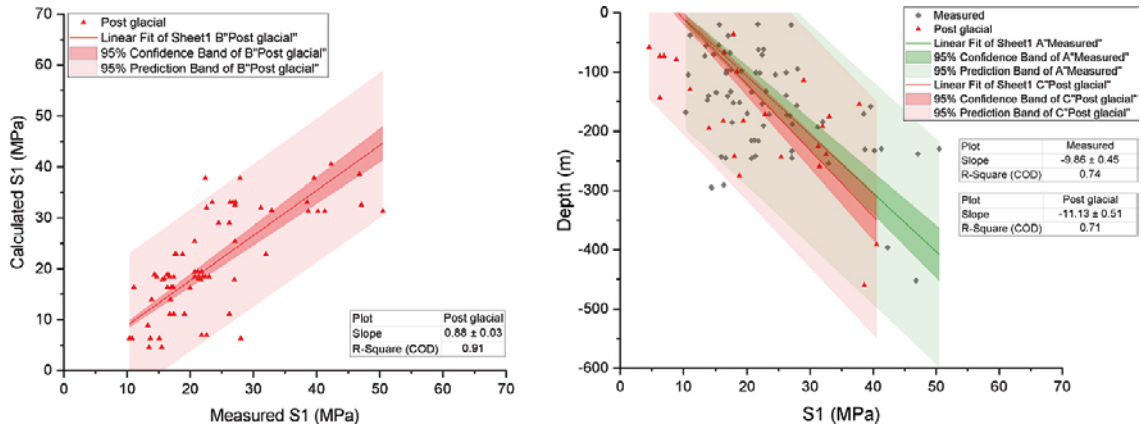


Figure A7b-22. Case 2-8, σ_1 magnitude correlation with OC stress measurements.

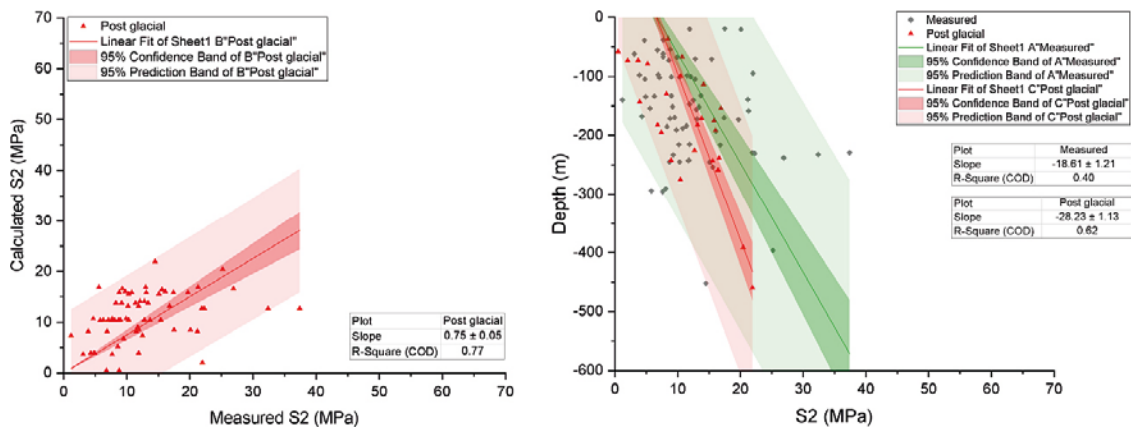


Figure A7b-23. Case 2-8, σ_2 magnitude correlation with OC stress measurements.

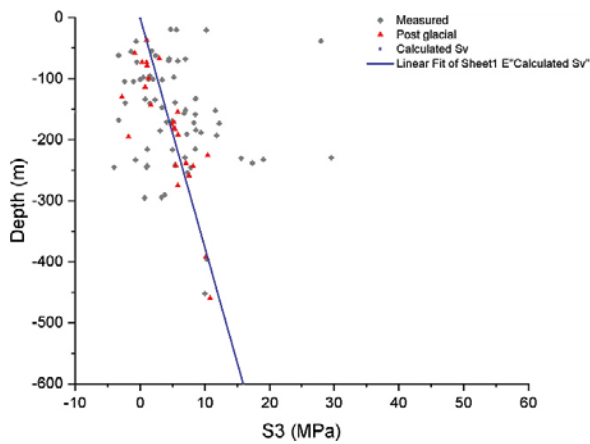


Figure A7b-24. Case 2-8, σ_3 magnitude correlation with OC stress measurements.

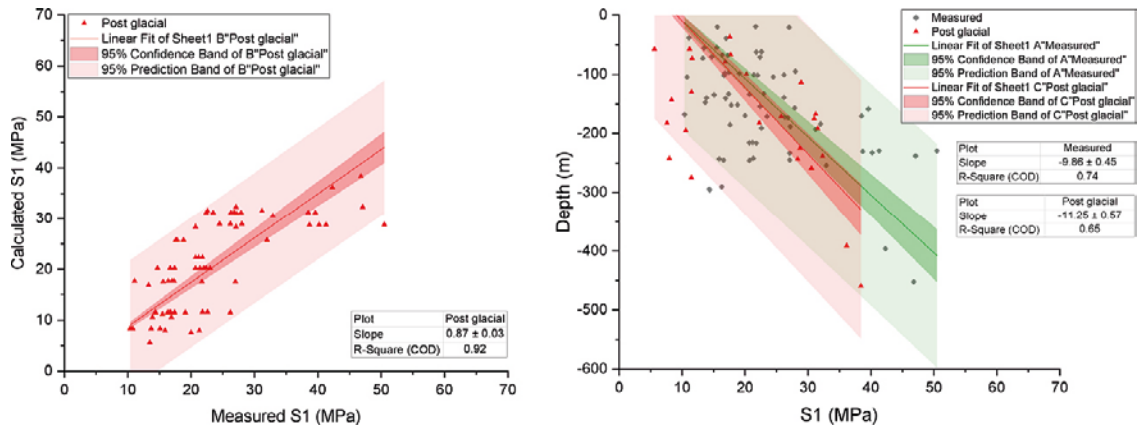


Figure A7b-25. Case 2-9, σ_1 magnitude correlation with OC stress measurements.

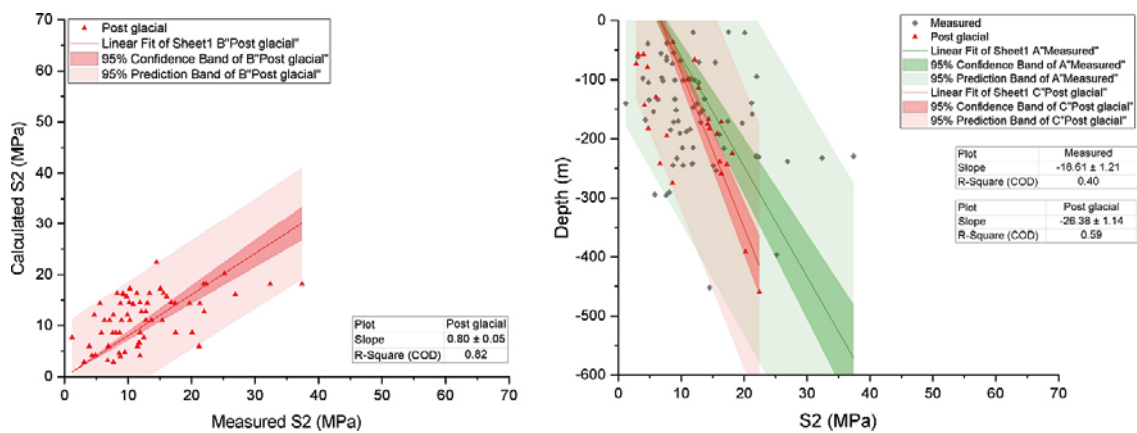


Figure A7b-26. Case 2-9, σ_2 magnitude correlation with OC stress measurements.

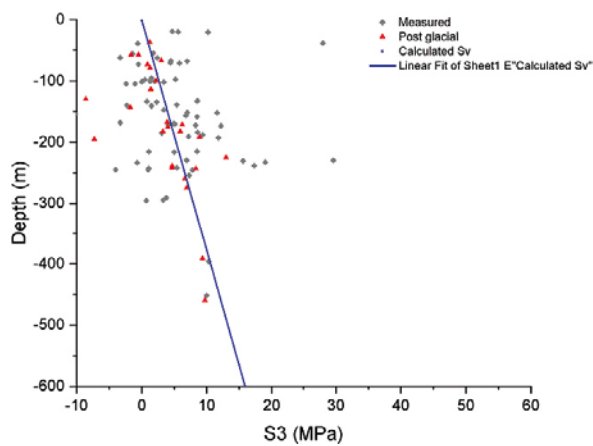


Figure A7b-27. Case 2-9, σ_3 magnitude correlation with OC stress measurements.

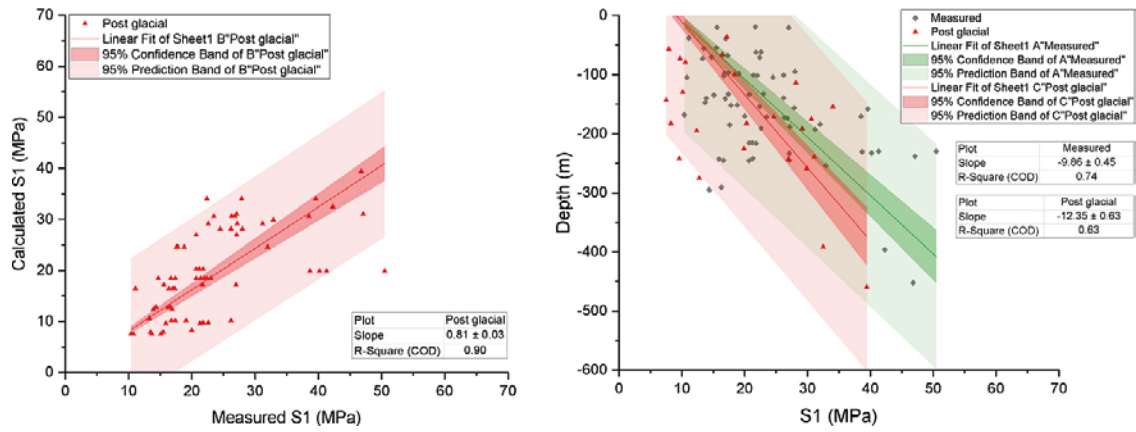


Figure A7b-28. Case 2-10, σ_1 magnitude correlation with OC stress measurements.

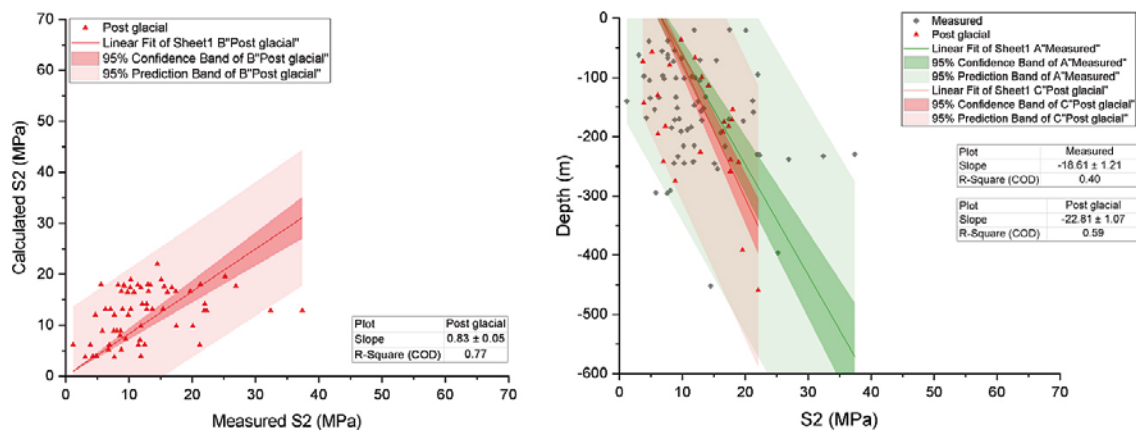


Figure A7b-29. Case 2-10, σ_2 magnitude correlation with OC stress measurements.

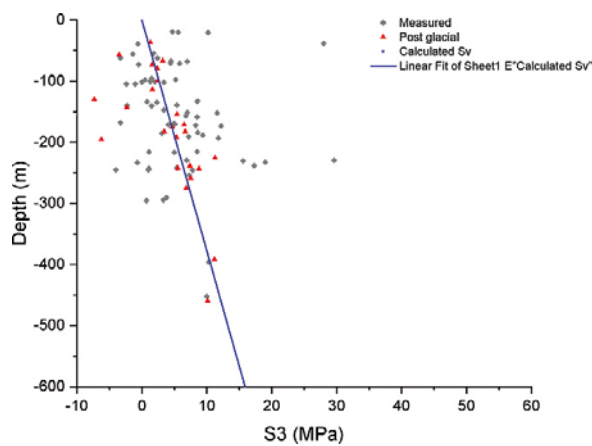


Figure A7b-30. Case 2-10, σ_3 magnitude correlation with OC stress measurements.

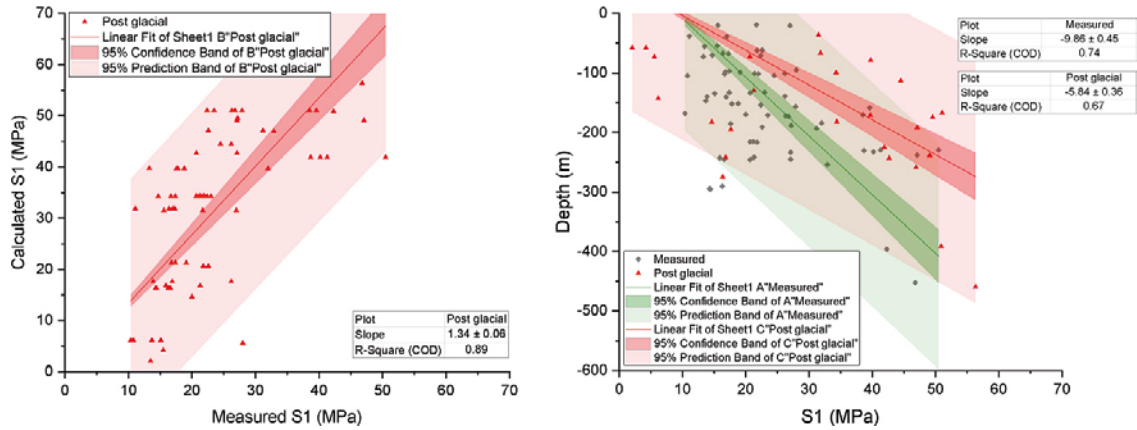


Figure A7b-31. Case 2-11, σ_1 magnitude correlation with OC stress measurements.

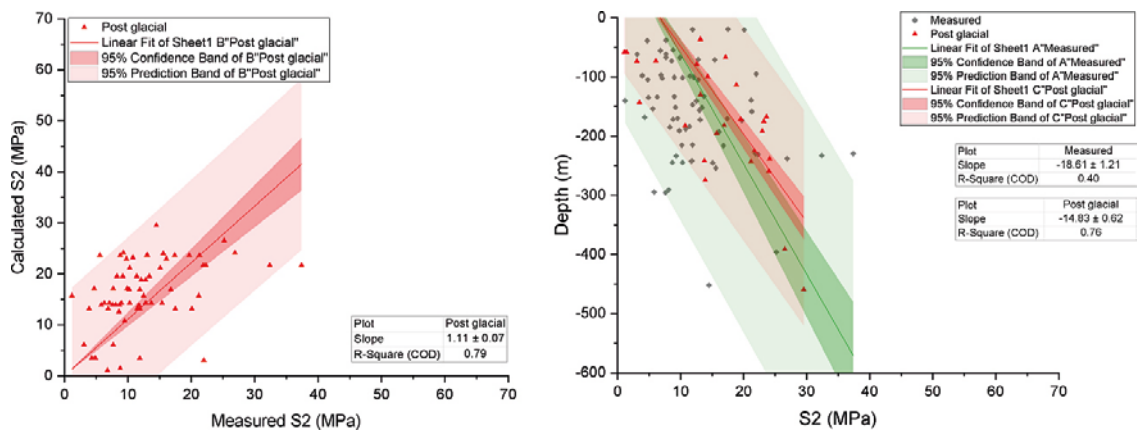


Figure A7b-32. Case 2-11, σ_2 magnitude correlation with OC stress measurements.

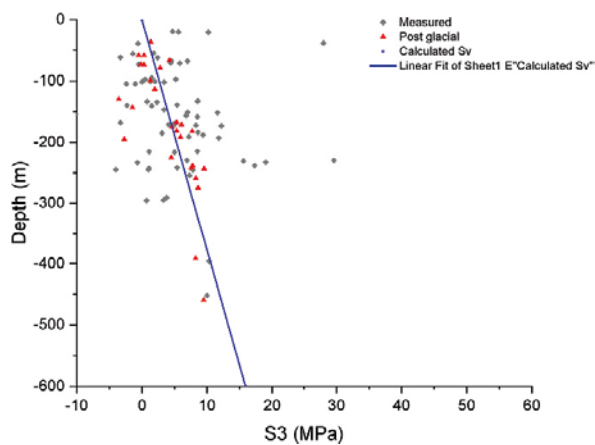


Figure A7b-33. Case 2-11, σ_3 magnitude correlation with OC stress measurements.

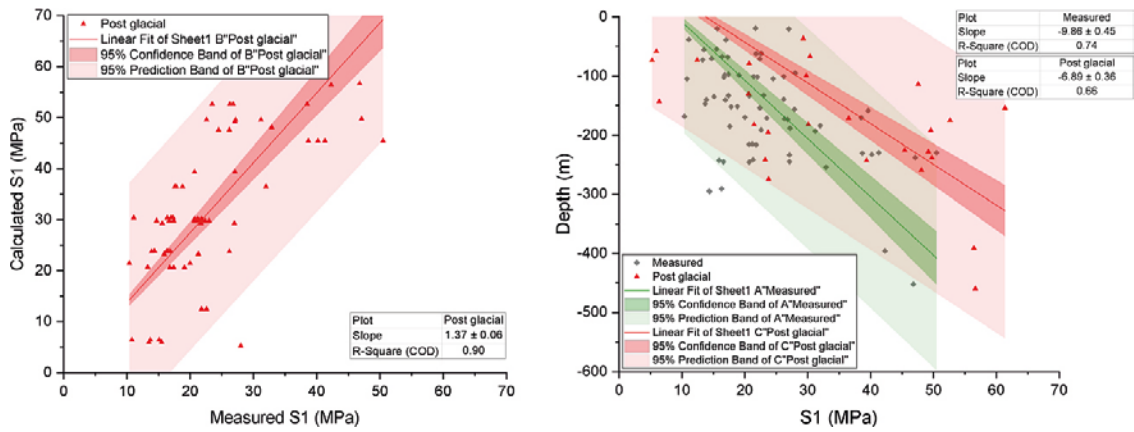


Figure A7b-34. Case 2-12, σ_1 magnitude correlation with OC stress measurements.

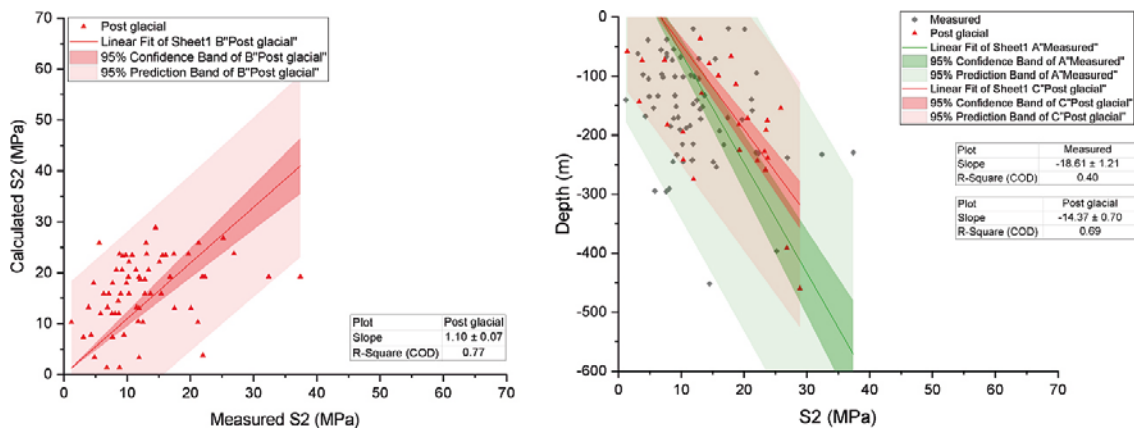


Figure A7b-35. Case 2-12, σ_2 magnitude correlation with OC stress measurements.

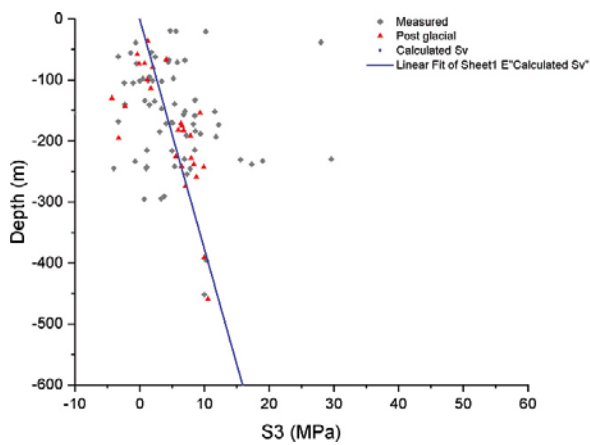


Figure A7b-36. Case 2-12, σ_3 magnitude correlation with OC stress measurements.

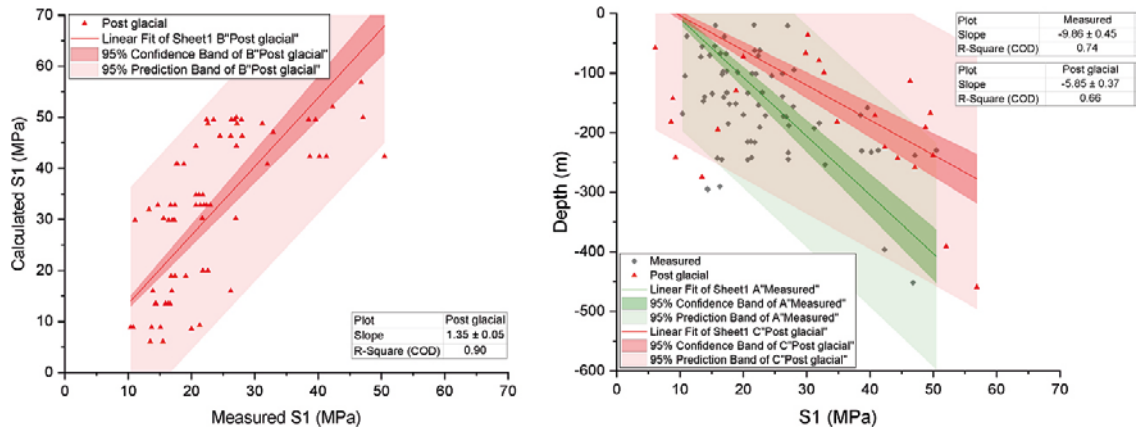


Figure A7b-37. Case 2-13, σ_1 magnitude correlation with OC stress measurements.

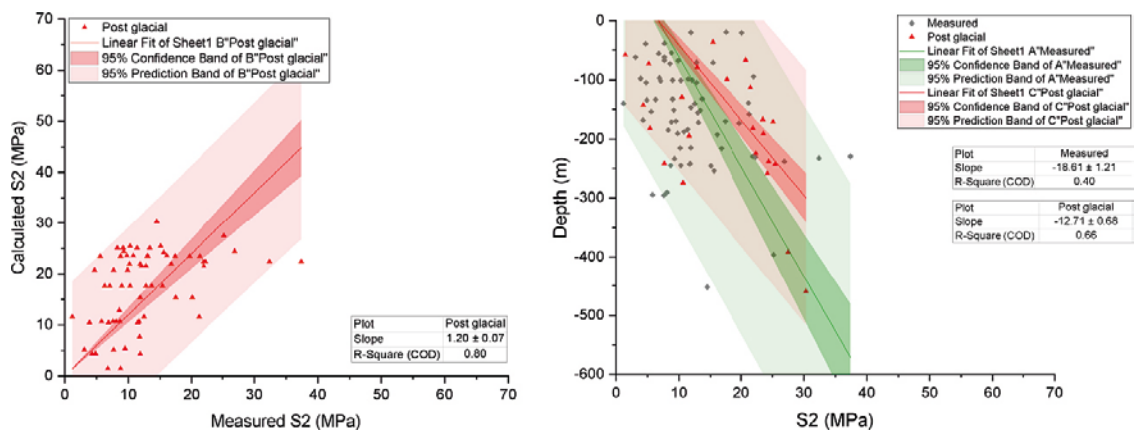


Figure A7b-38. Case 2-13, σ_2 magnitude correlation with OC stress measurements.

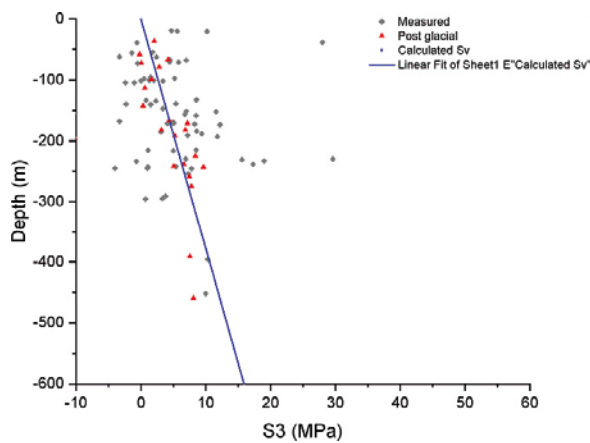


Figure A7b-39. Case 2-13, σ_3 magnitude correlation with OC stress measurements.

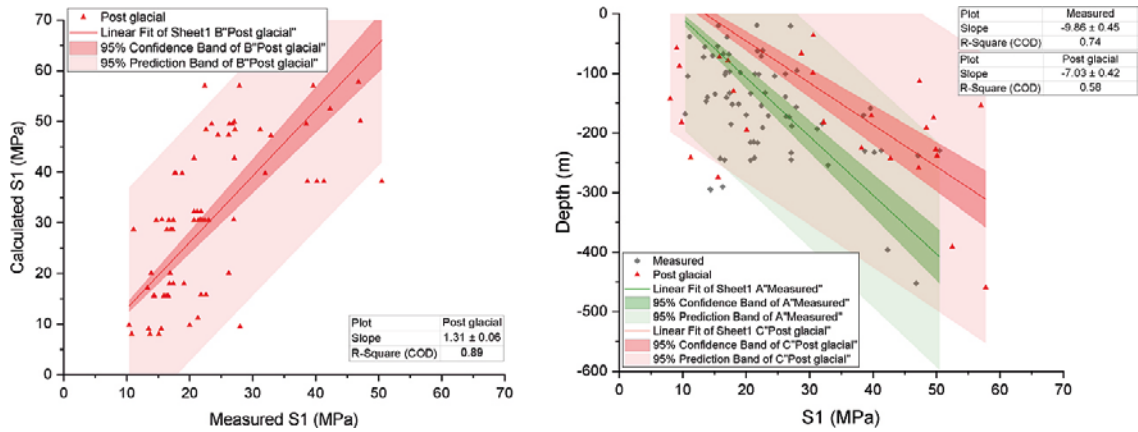


Figure A7b-40. Case 2-14, σ_1 magnitude correlation with OC stress measurements.

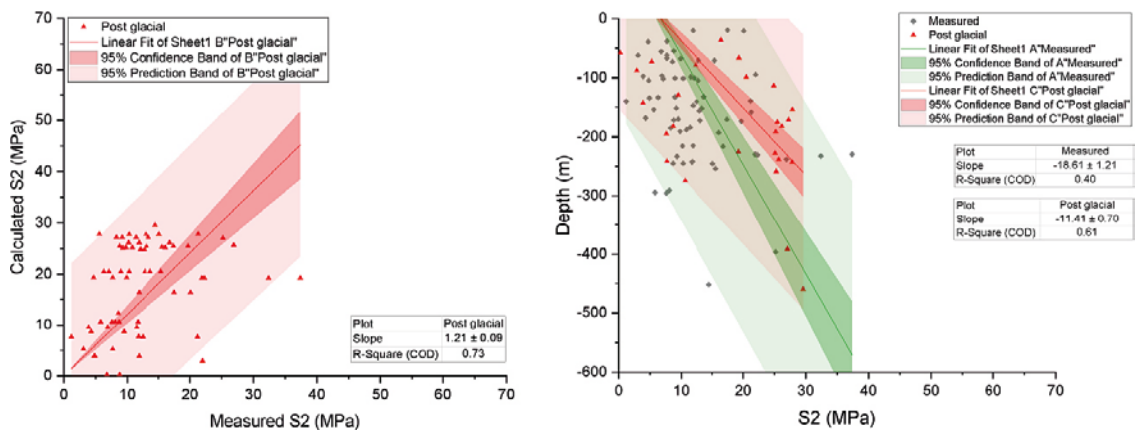


Figure A7b-41. Case 2-14, σ_2 magnitude correlation with OC stress measurements.

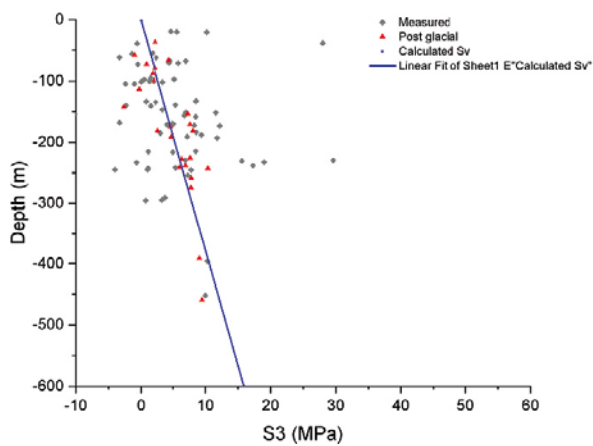


Figure A7b-42. Case 2-14, σ_3 magnitude correlation with OC stress measurements.

Simulation Phase 1

– σ_1 trend frequency based on stress measurements and stress tensors at the same location in the models

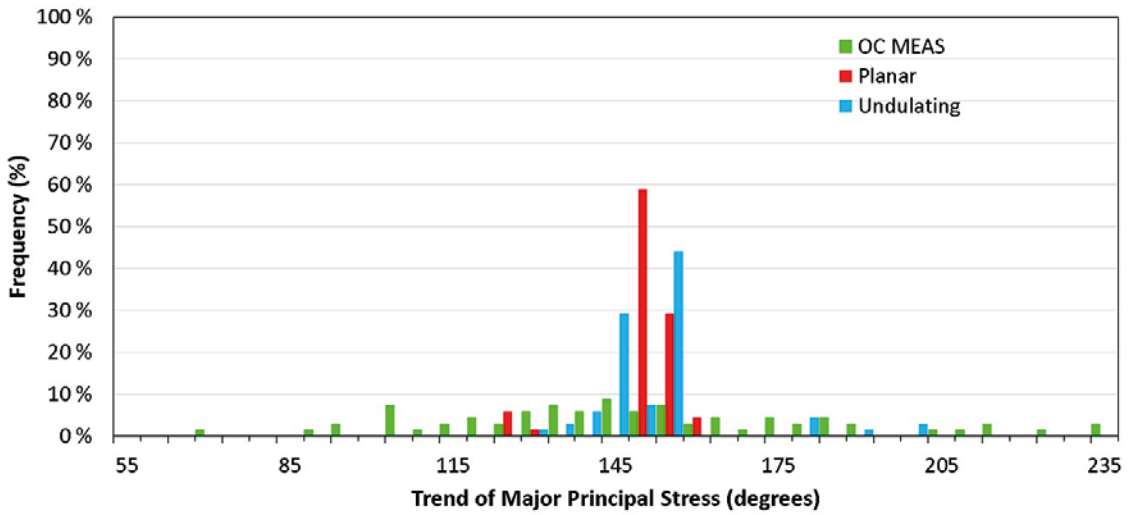


Figure A8a-1. σ_1 trend frequency based on stress measurement locations, Case 1-1.

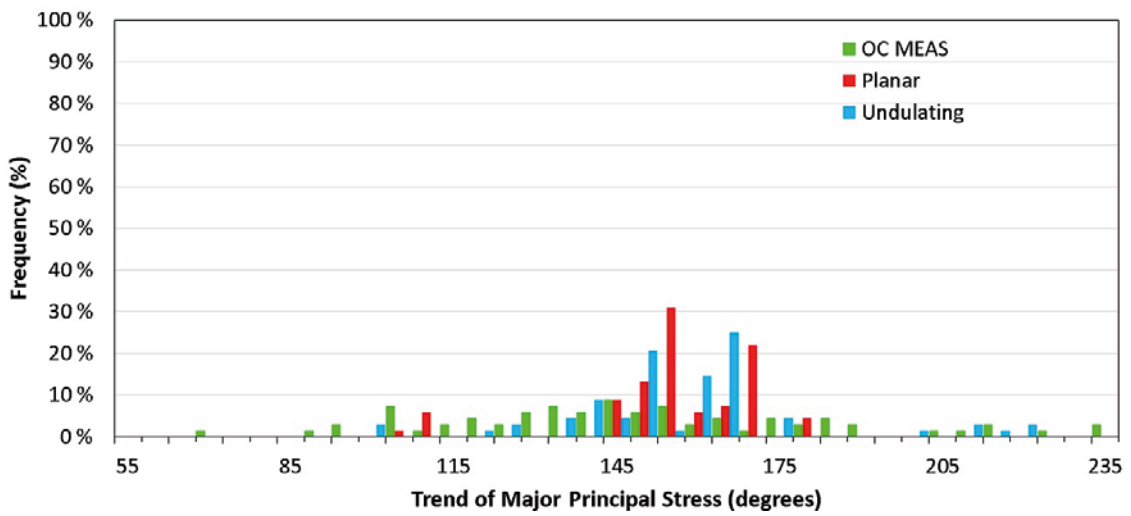


Figure A8a-2. σ_1 trend frequency based on stress measurement locations, Case 1-2.

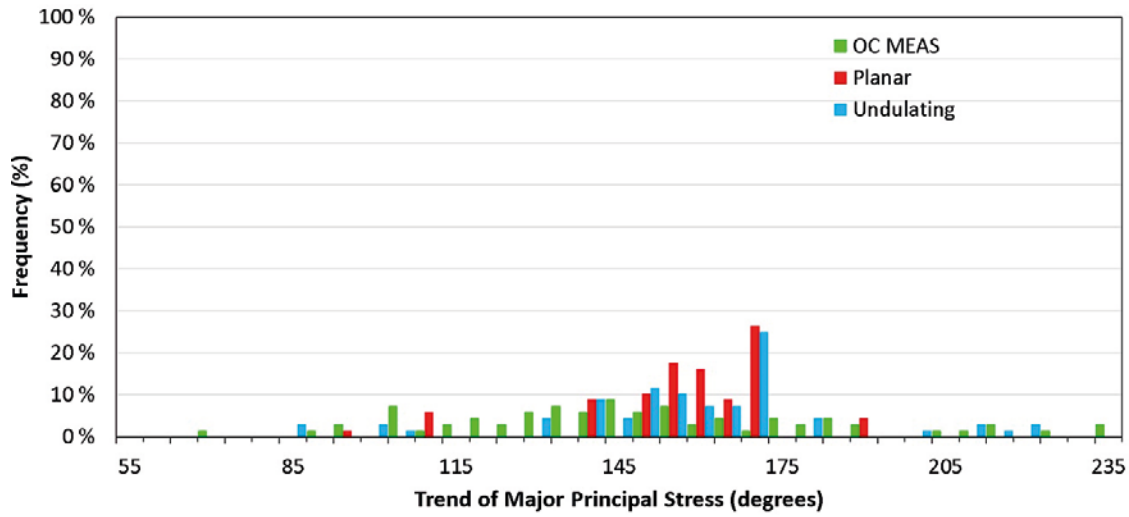


Figure A8a-3. σ_1 trend frequency based on stress measurement locations, Case 1-3.

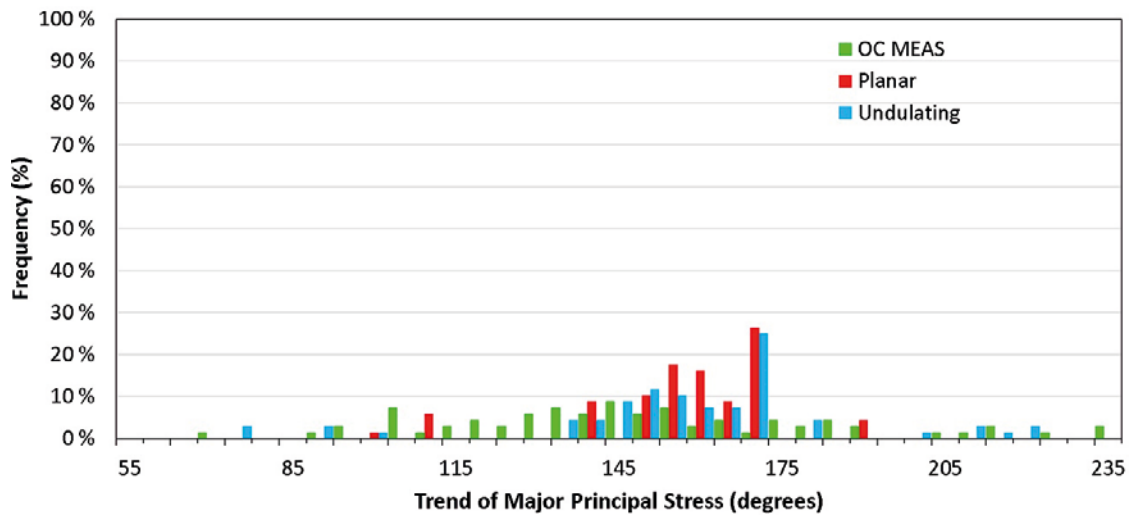


Figure A8a-4. σ_1 trend frequency based on stress measurement locations, Case 1-4.

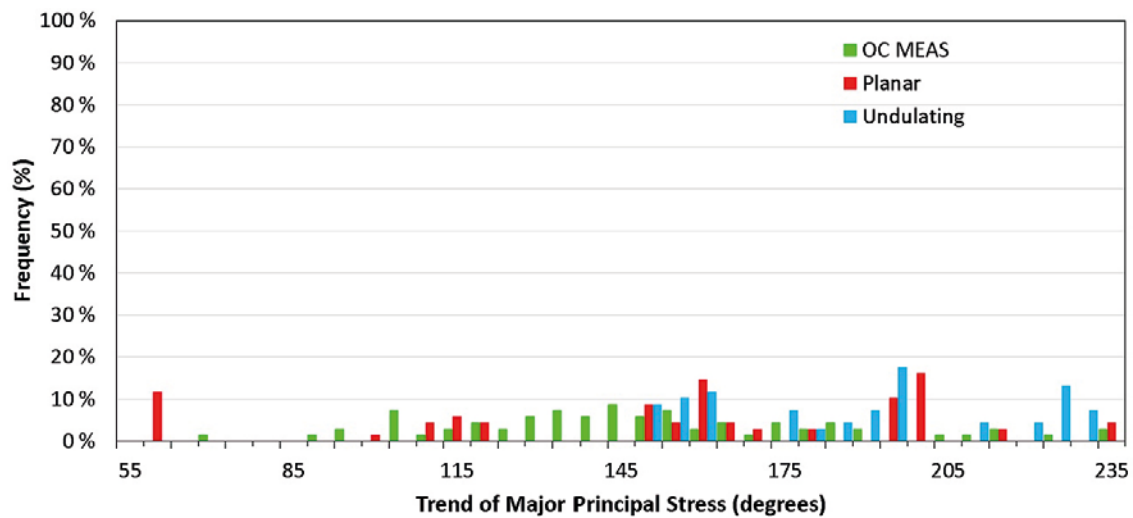


Figure A8a-5. σ_1 trend frequency based on stress measurement locations, Case 1-5.

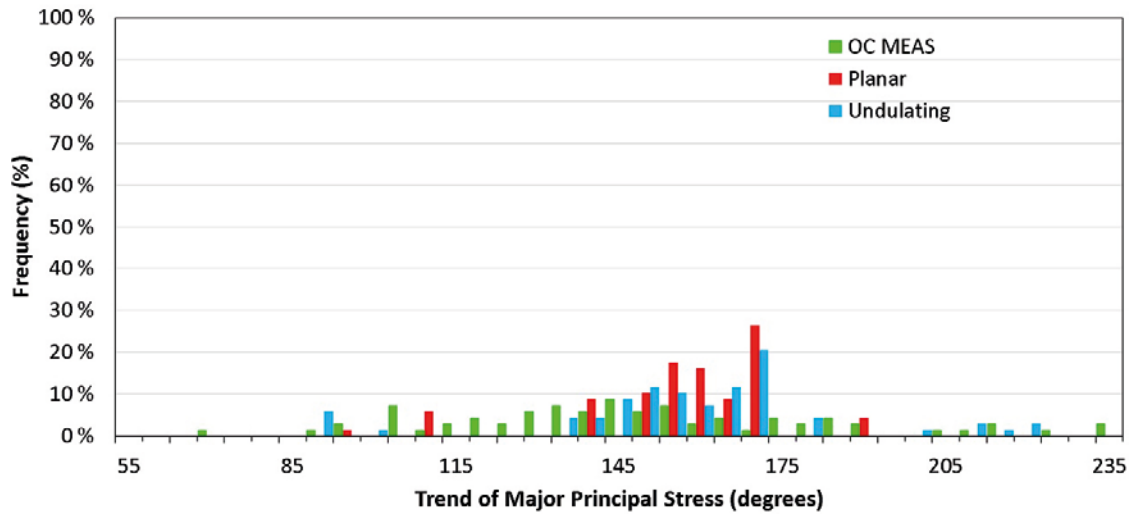


Figure A8a-6. σ_1 trend frequency based on stress measurement locations, Case 1-6.

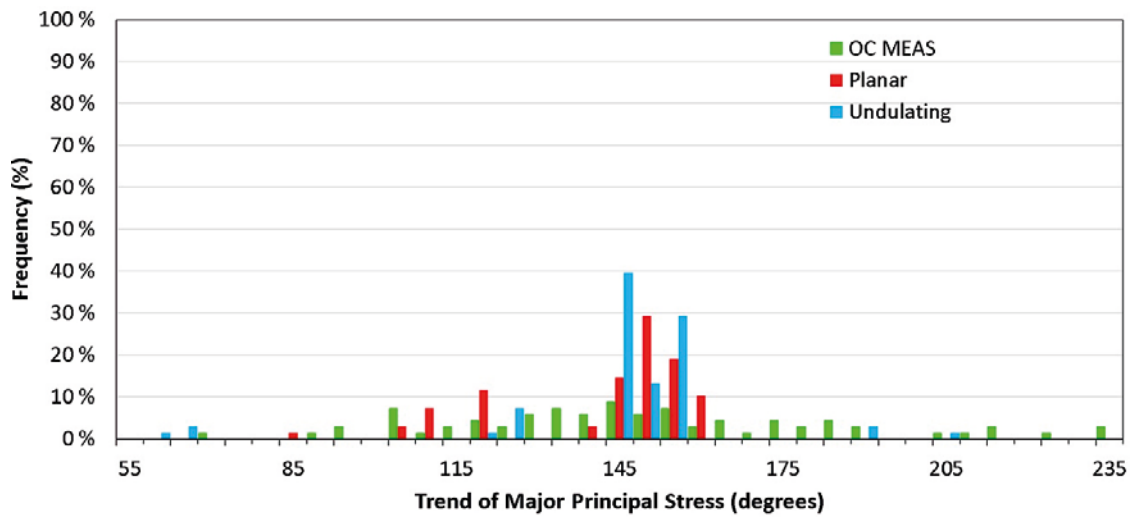


Figure A8a-7. σ_1 trend frequency based on stress measurement locations, Case 1-7.

Simulation Phase 2
– σ_1 trend frequency based on stress measurements and stress tensors at the same location in the models

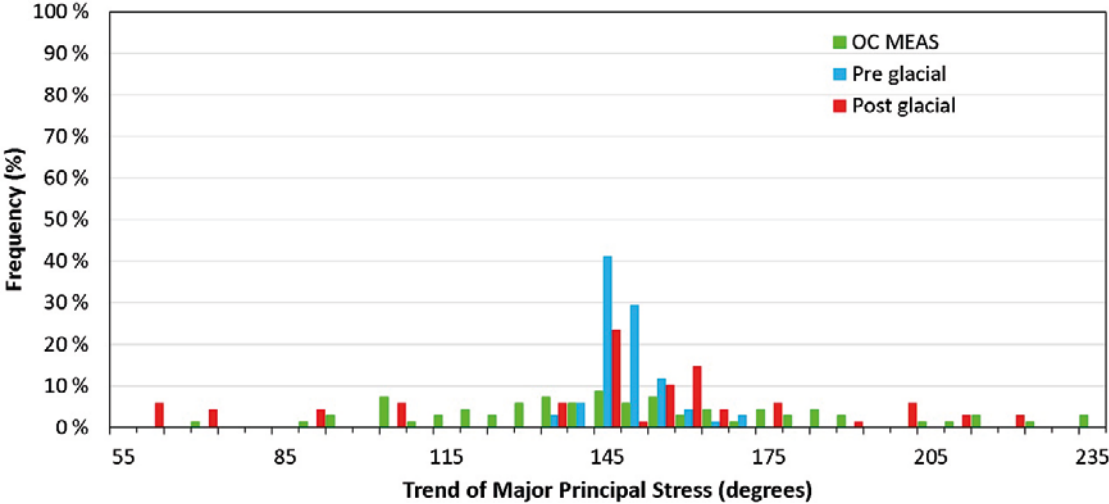


Figure A8b-1. σ_1 trend frequency based on stress measurement locations, Case 2-1.

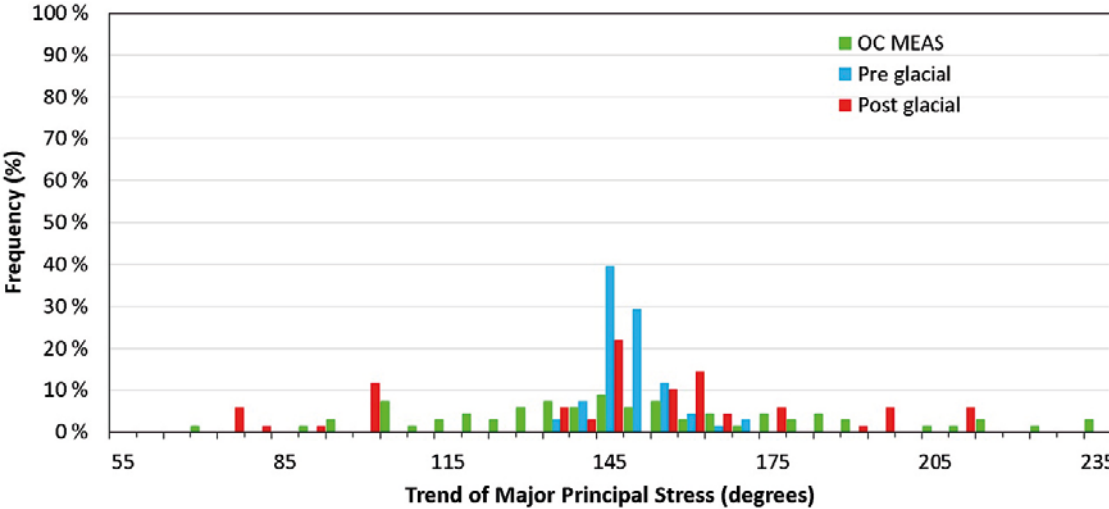


Figure A8b-2. σ_1 trend frequency based on stress measurement locations, Case 2-2.

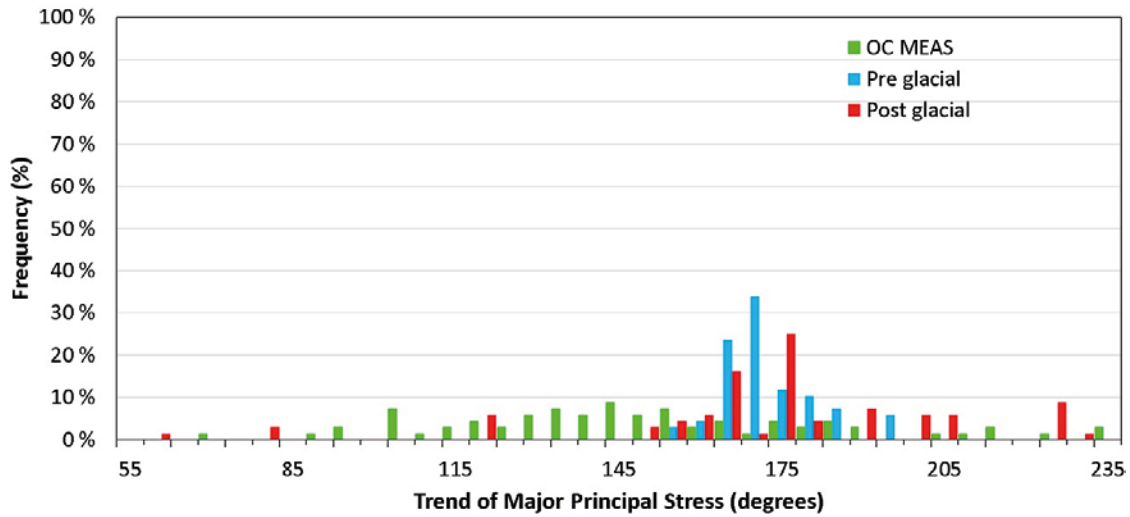


Figure A8b-3. σ_1 trend frequency based on stress measurement locations, Case 2-3.

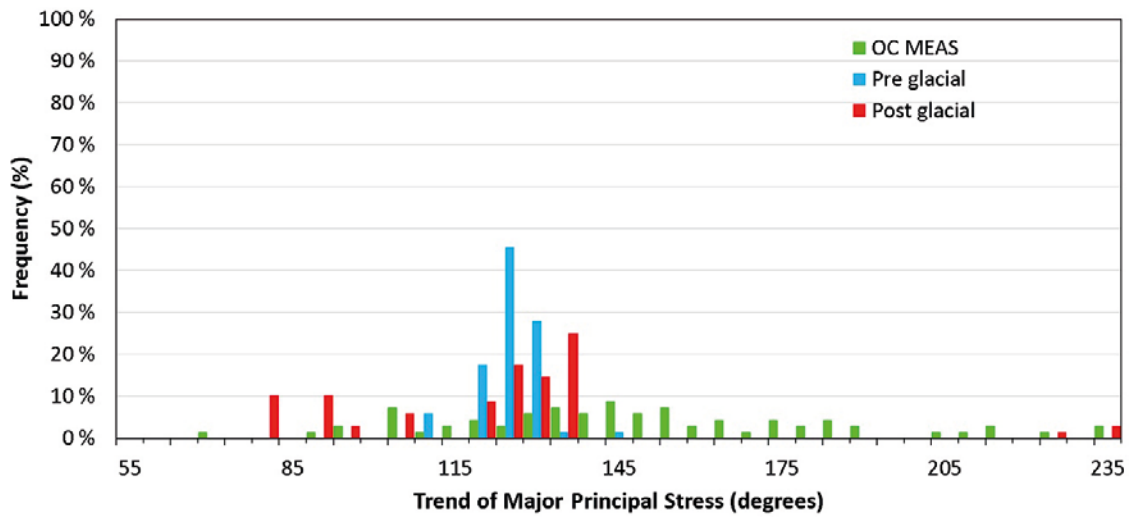


Figure A8b-4. σ_1 trend frequency based on stress measurement locations, Case 2-4.

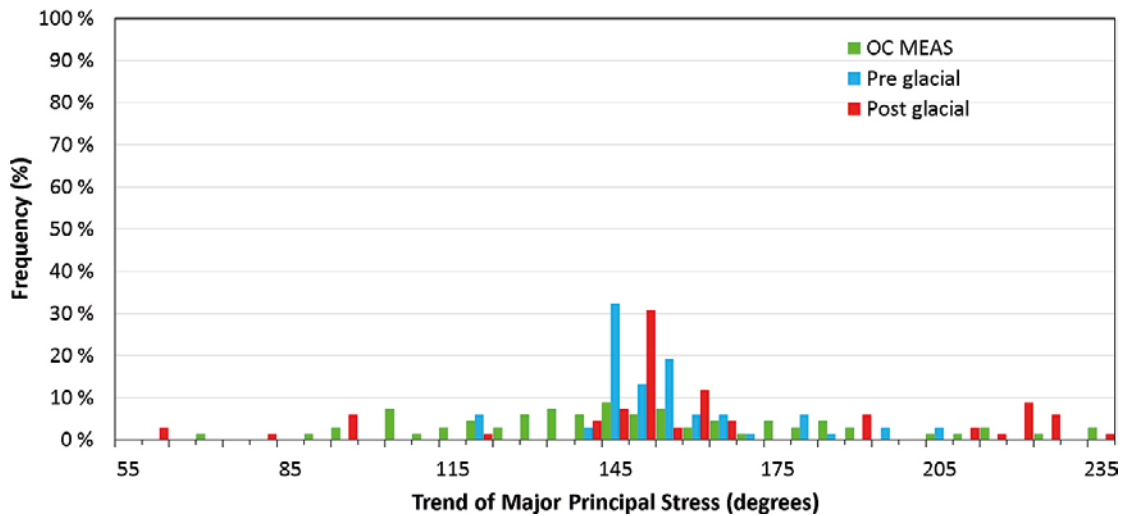


Figure A8b-5. σ_1 trend frequency based on stress measurement locations, Case 2-5.

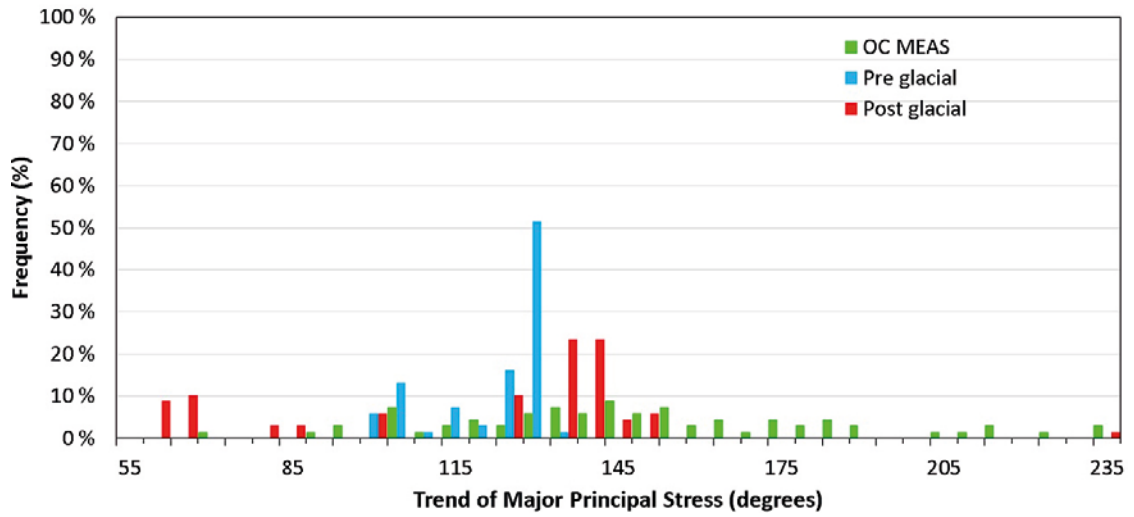


Figure A8b-6. σ_1 trend frequency based on stress measurement locations, Case 2-6.

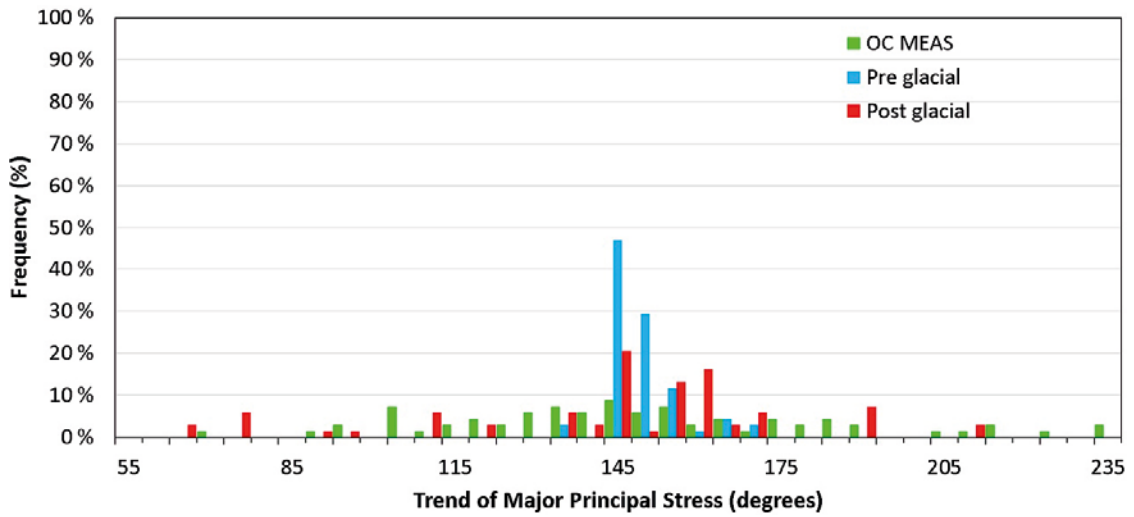


Figure A8b-7. σ_1 trend frequency based on stress measurement locations, Case 2-7.

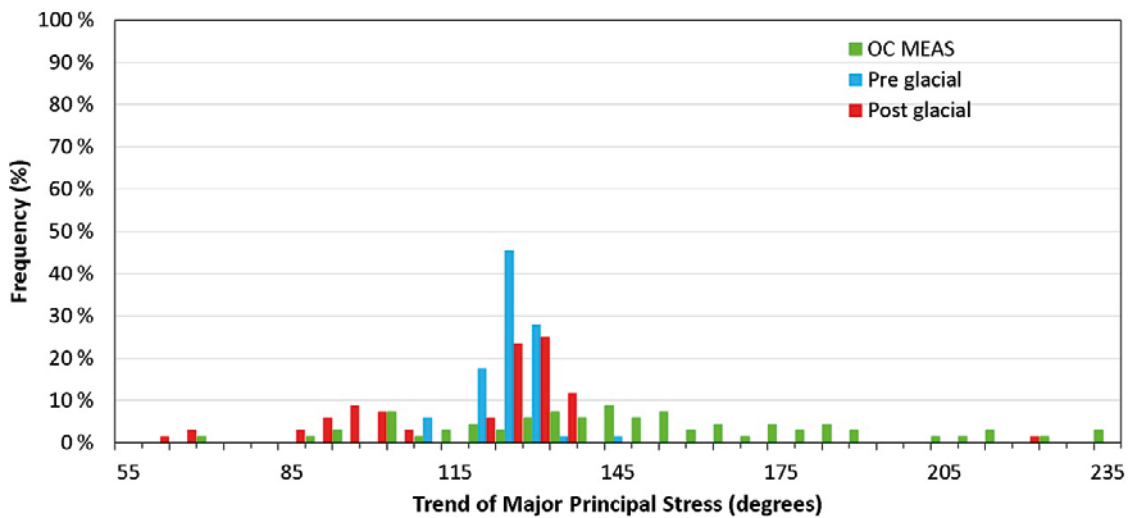


Figure A8b-8. σ_1 trend frequency based on stress measurement locations, Case 2-8.

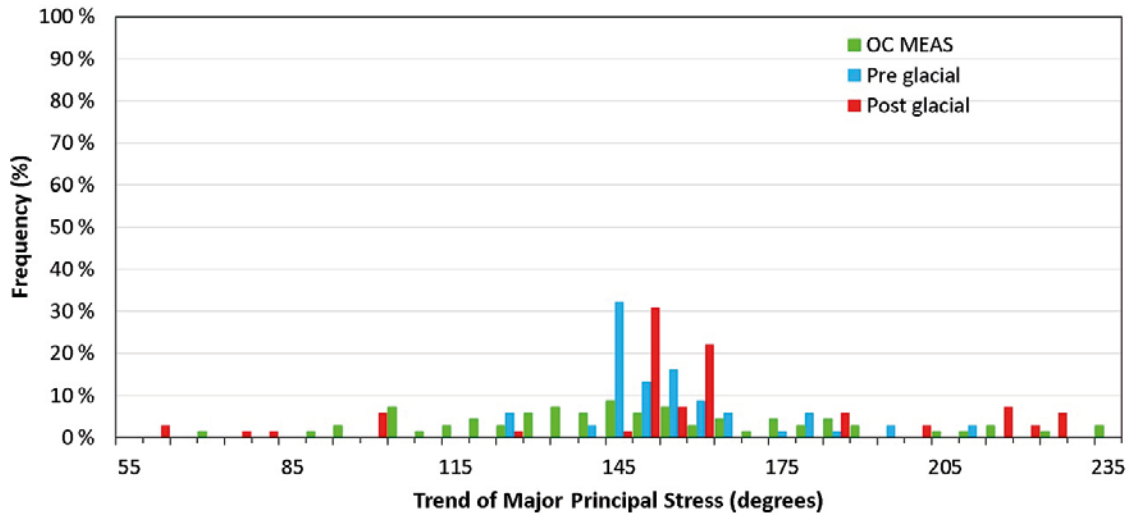


Figure A8b-9. σ_1 trend frequency based on stress measurement locations, Case 2-9.

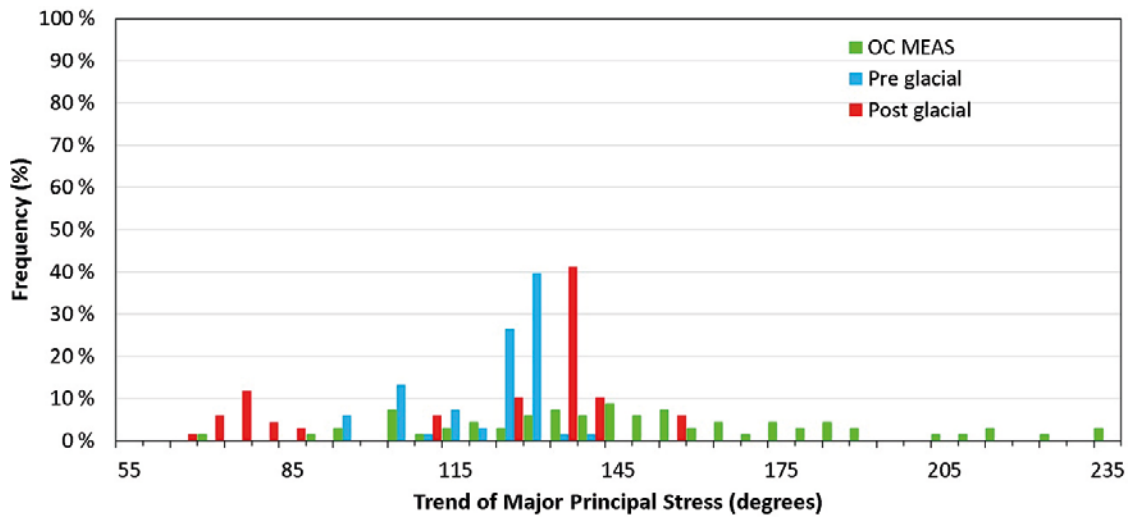


Figure A8b-10. σ_1 trend frequency based on stress measurement locations, Case 2-10.

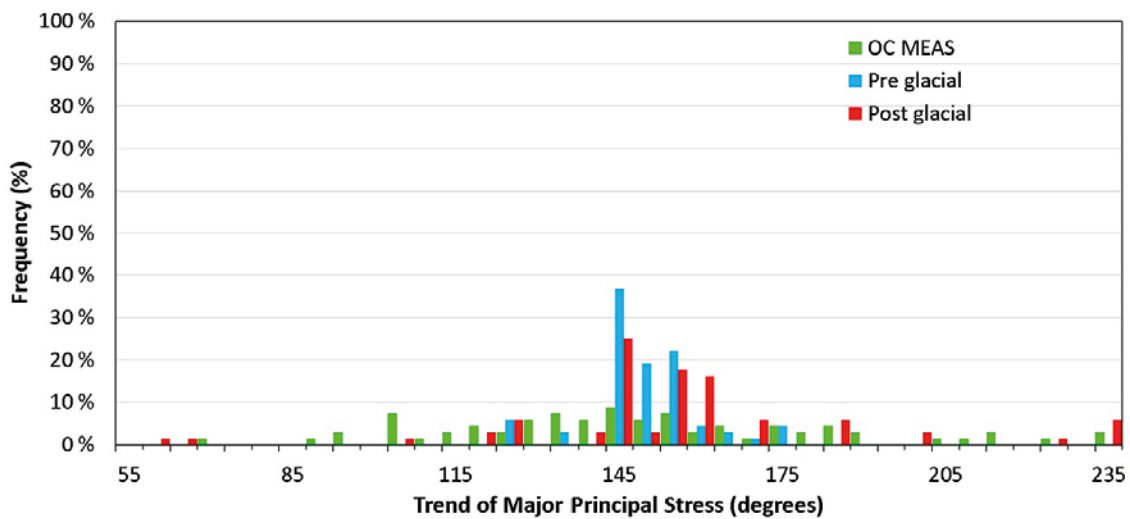


Figure A8b-11. σ_1 trend frequency based on stress measurement locations, Case 2-11.

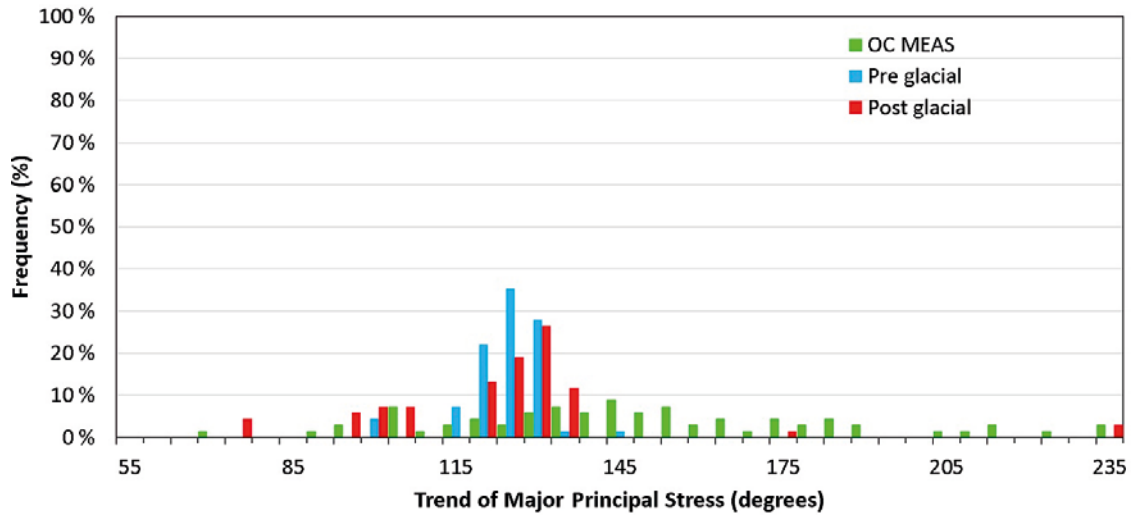


Figure A8b-12. σ_1 trend frequency based on stress measurement locations, Case 2-12.

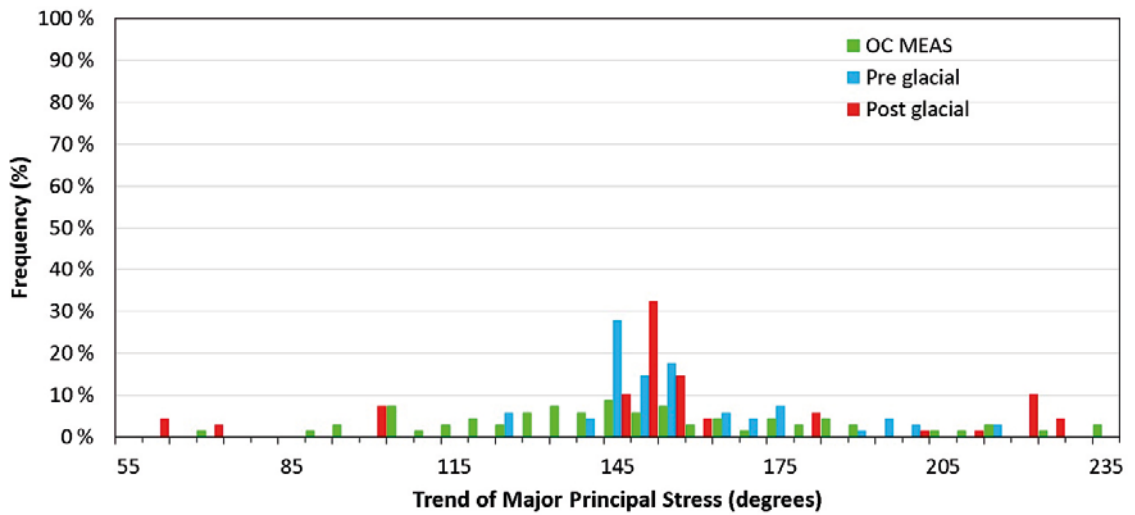


Figure A8b-13. σ_1 trend frequency based on stress measurement locations, Case 2-13.

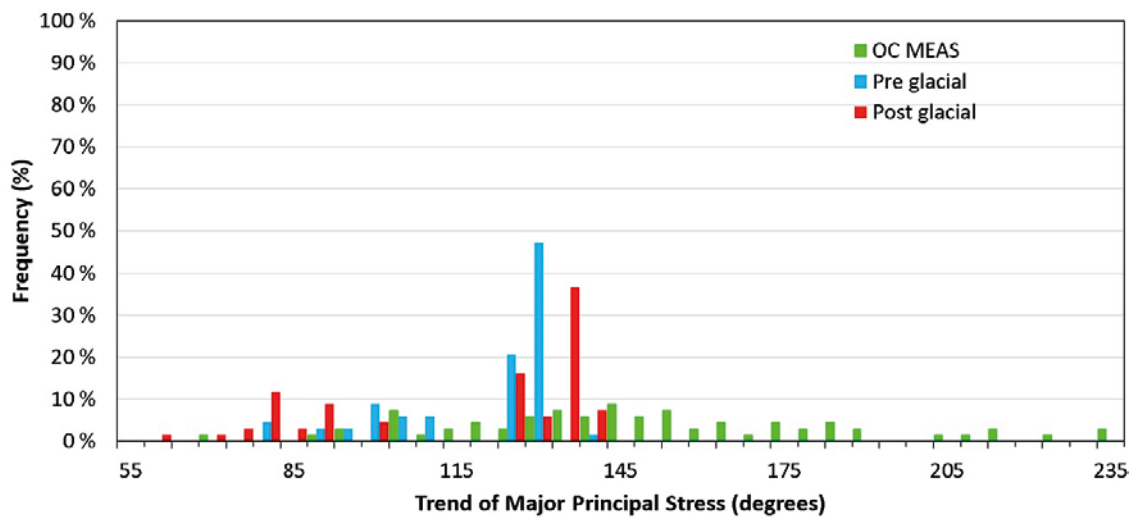


Figure A8b-14. σ_1 trend frequency based on stress measurement locations, Case 2-14.

Case 2-15

Case 2-15 was run as a supplementary analysis after the study had been completed. Only the critical result figures (Figure A9-1 to Figure A9-3) are presented within this appendix for posterity. New lower hemisphere projection figures combining principal stress magnitudes and distribution (95 % variation interval vs 90 % variation interval in original mean and variation of σ_1 figures) with orientations were also generated for Case 2-1 for comparison to the results from Case 2-15 (Figure A9-4 to Figure A9-9).

Case 2-15 made use of the same base geometry and parameters as Case 2-1. The only key difference was the target stress state: constant normal velocity boundary conditions were modified to reach an *in-situ* stress state where $\sigma_2 = \sigma_3$, at the repository depth monitoring sphere. Initially, this required thrust from all model sides after which the model was pulled from the boundaries perpendicular to σ_1 until the principal stress magnitudes were within an acceptable range of less than $\pm 5\%$ of target magnitudes. After simulating the glacial stages and reaching equilibrium, the approach had to be reapplied: σ_1 and σ_3 were over $\pm 5\%$ of the target stress magnitudes. Boundary thrust was applied in the σ_1 direction while the model was pulled in the perpendicular σ_2 direction, to reach an end result where σ_1 and σ_2 were within $\pm 3\%$, although σ_3 deviated ca 6–7 %.

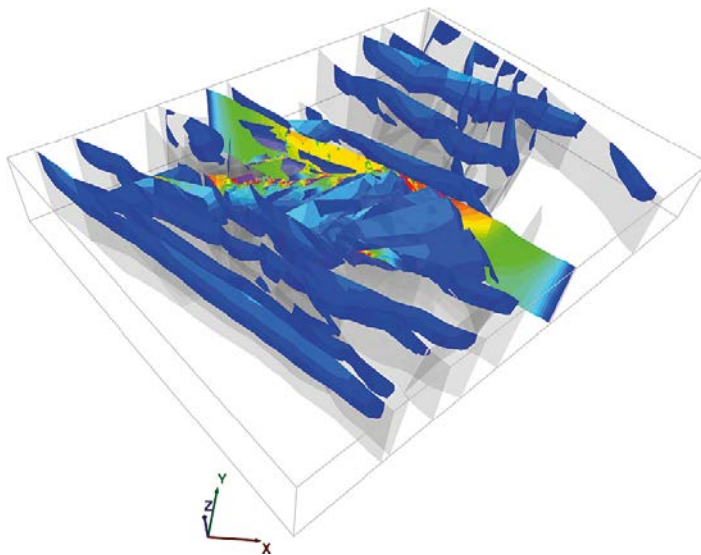


Figure A9-1. Case 2-15, DZ total shear displacements.

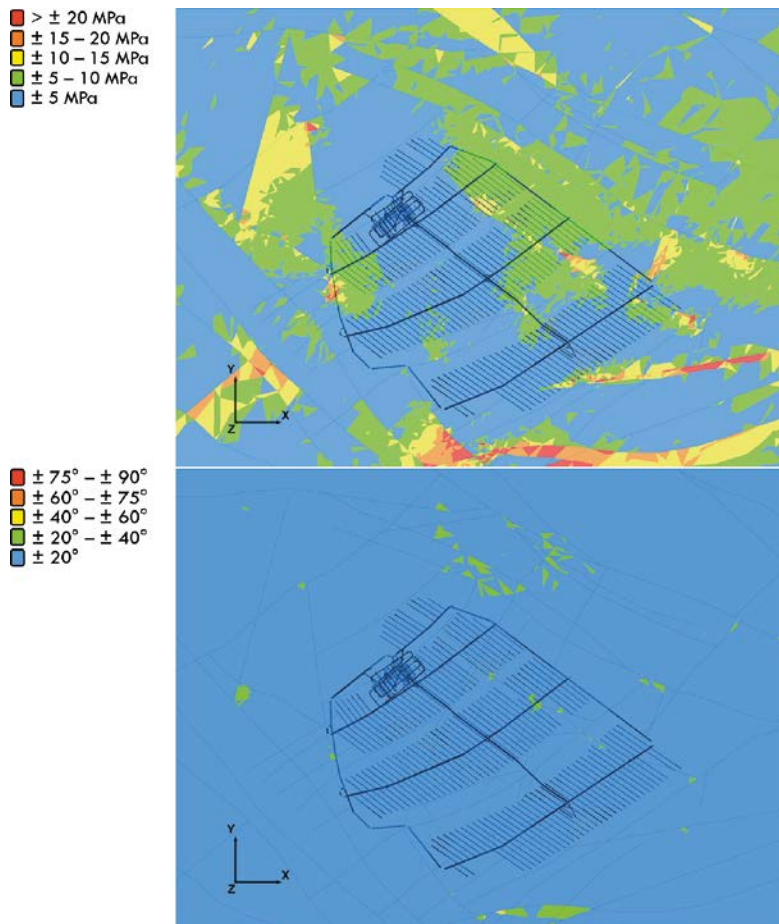


Figure A9-2. Change in σ_1 magnitude (above) and trend (below), horizontal section from repository level, Case 2-15.

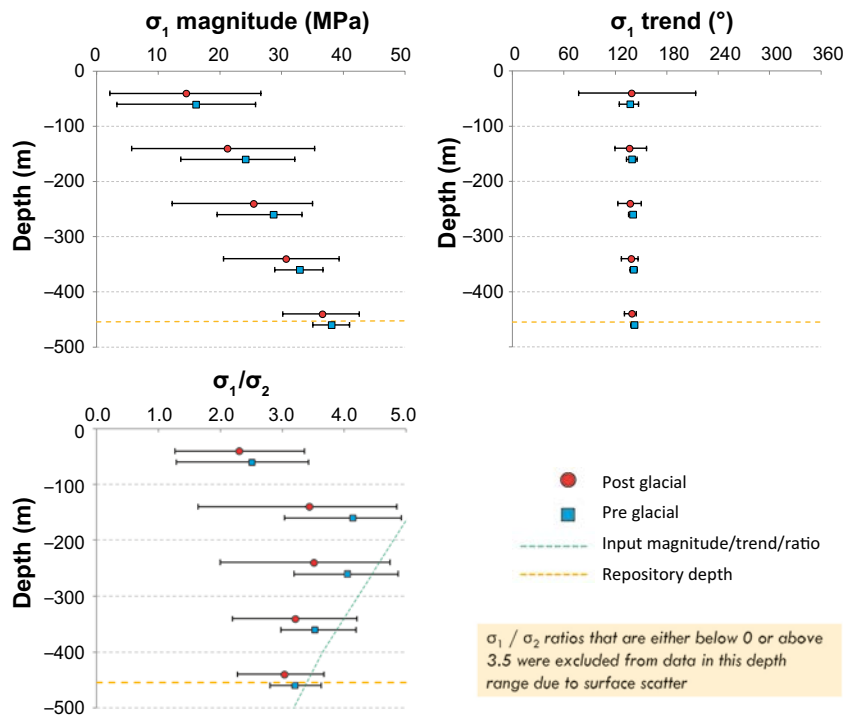


Figure A9-3. Pre/post glacial mean and variation of σ_1 magnitude, trend and σ_1/σ_2 ratio for hundred meter intervals, Case 2-15.

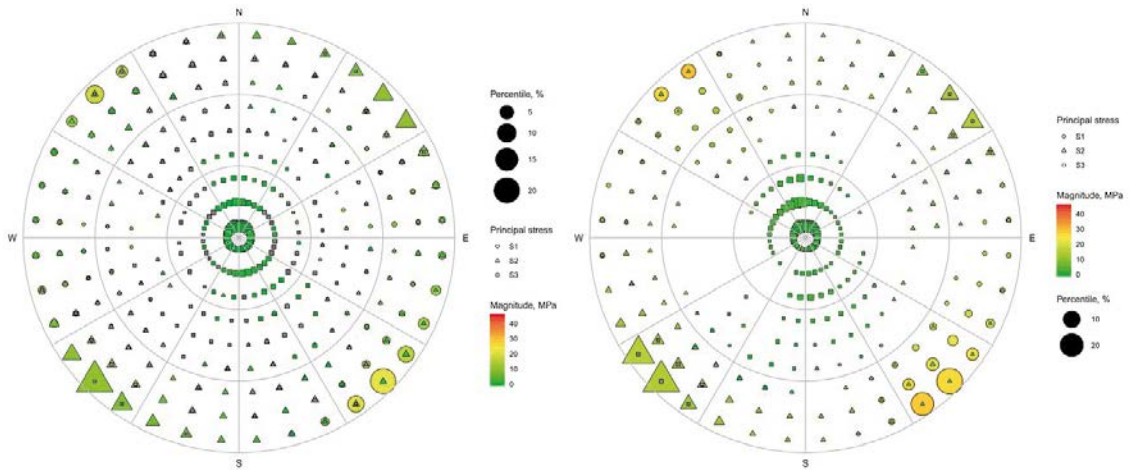


Figure A9-4. Case 2-1: Lower hemisphere projections of the principal stresses at 10° intervals, coloured according to magnitude and symbol sizes by percentile. Left: $z = 0\text{--}100$ m. Right: $z = 100\text{--}200$ m.

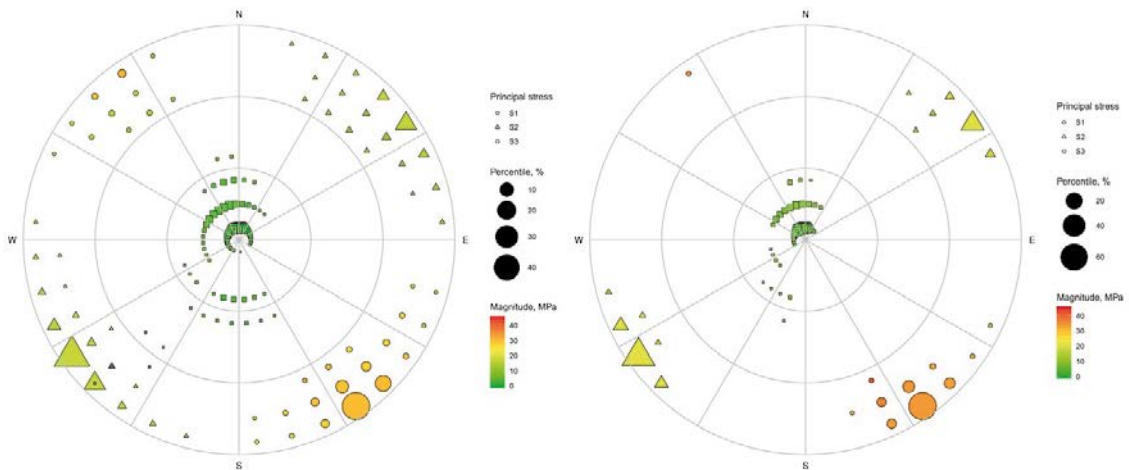


Figure A9-5. Case 2-1: Lower hemisphere projections of the principal stresses at 10° intervals, coloured according to magnitude and symbol sizes by percentile. Left: $z = 200\text{--}300$ m. Right: $z = 300\text{--}400$ m.

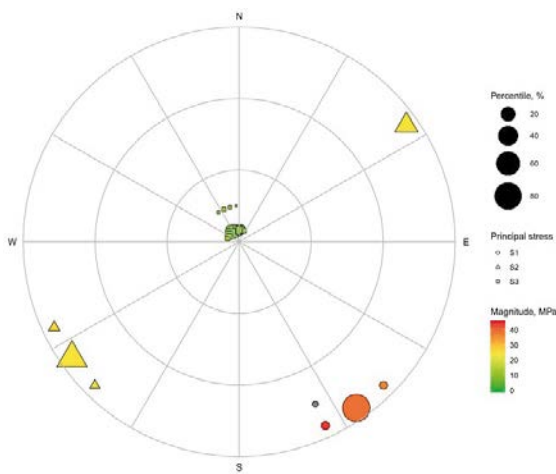


Figure A9-6. Case 2-1: Lower hemisphere projections of the principal stresses at 10° intervals, coloured according to magnitude and symbol sizes by percentile. $z = 400\text{--}500$ m.

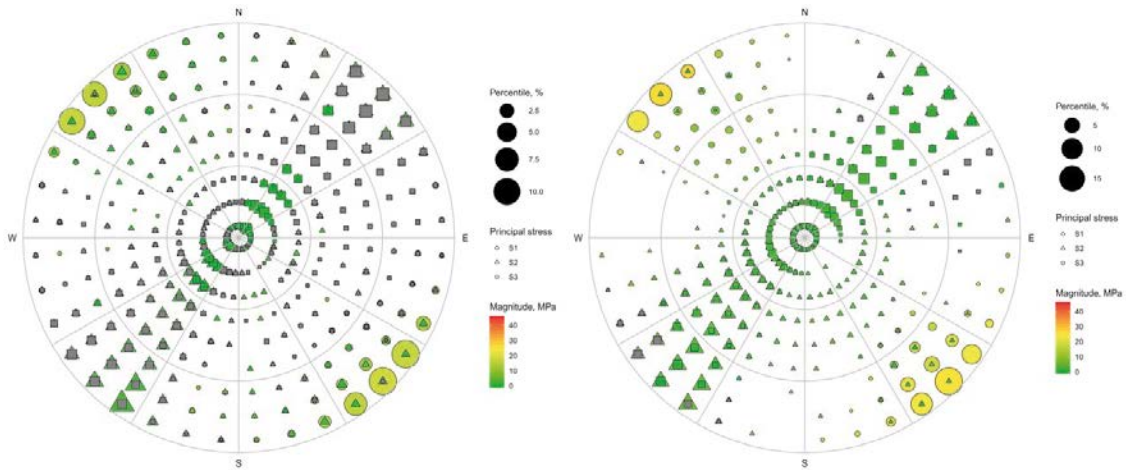


Figure A9-7. Case 2-15: Lower hemisphere projections of the principal stresses at 10° intervals, coloured according to magnitude and symbol sizes by percentile. Left: $z = 0\text{--}100$ m. Right: $z = 100\text{--}200$ m.

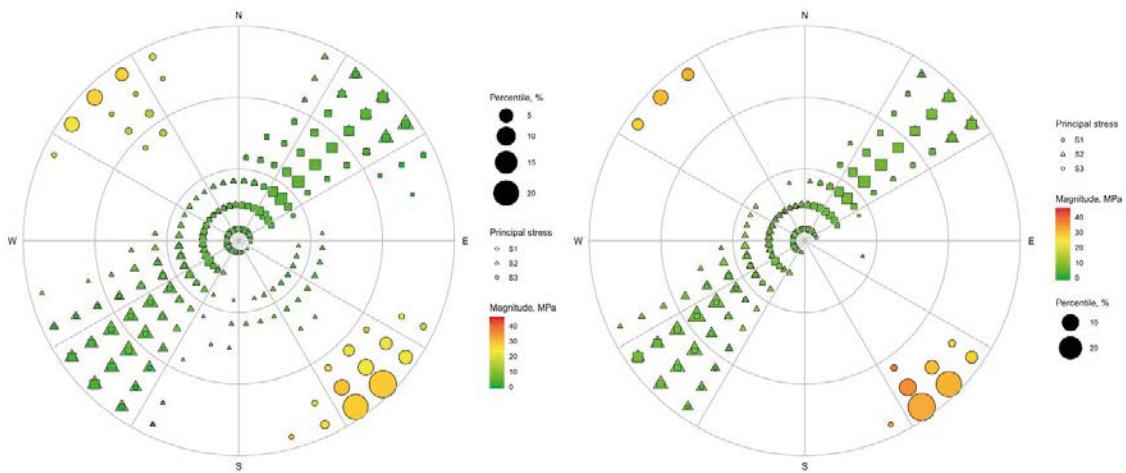


Figure A9-8. Case 2-15: Lower hemisphere projections of the principal stresses at 10° intervals, coloured according to magnitude and symbol sizes by percentile. Left: $z = 200\text{--}300$ m. Right: $z = 300\text{--}400$ m.

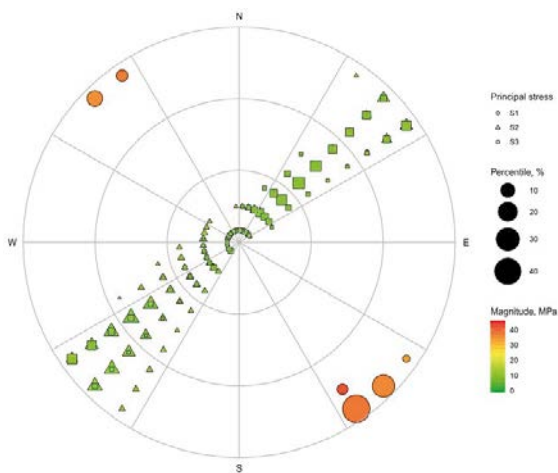


Figure A9-9. Case 2-15: Lower hemisphere projections of the principal stresses at 10° intervals, coloured according to magnitude and symbol sizes by percentile. $z = 400\text{--}500$ m.

SKB is responsible for managing spent nuclear fuel and radioactive waste produced by the Swedish nuclear power plants such that man and the environment are protected in the near and distant future.

skb.se